Observations of Transient Events with Very-High-Energy Gamma-Ray Telescopes

Deivid Ribeiro

Submitted in partial fulfillment of the
requirements for the degree of
Doctor of Philosophy
under the Executive Committee
of the Graduate School of Arts and Sciences

COLUMBIA UNIVERSITY

2022

Abstract

Observations of Transient Events with Very-High-Energy Gamma-Ray Telescopes

Deivid Ribeiro

Astrophysical events that evolve on short timescales (from milliseconds to years) are widely referred as transient events. In many cases, transient events are explosions or mergers of astrophysical objects that emit particles of all energies. This thesis focuses on very-high-energy (VHE; 100 GeV to 100 TeV) gamma rays, observed by the VERITAS telescope, to understand two types of transients, superluminous supernovae (SLSNe) and classical novae. In the first part, the background physics and technical approach of an imaging atmospheric Cherenkov technique deployed by VERITAS is reviewed in depth, including the analysis pipeline of VERITAS data, from camera data reduction to high level analysis output. In addition to supporting the ongoing work at VERITAS, the second part of this thesis describes the extensive effort to develop, commission and align the optical system of the prototype Schwarzschild-Couder telescope, also located at the VERITAS observatory. This new telescope provides an wider field of view and higher angular resolution compared with the conventional IACT design of current telescopes, and will join the next generation of VHE telescopes in the Cherenkov Telescope Array (CTA) project currently in development. The observation and analysis of two SLSNe is performed, on SN 2015bn and SN 2017egm, with both VERITAS and *Fermi*-LAT telescopes. The upper limit is reported on both events and is compared to a simple and a self-consistent model for parameter estimation. In addition, a population of sources were analyzed to estimate the future detection potential of new SLSNe with several gamma-ray observatories. Finally, the observation and

analysis of several novae were performed. These sources were observed with VERITAS and *Fermi*-LAT. The observation of Nova Herculis 2021 is noteworthy in that the overlap of both observations may constrain the cutoff energy of the nova spectral model, providing a estimate for the maximum energy of the accelerated particles in the nova's shock region.

Table of Contents

List of Figures

List of Tables

Acknowledgements

I would like to begin by thanking all those who helped me in my personal growth during this graduate experience. My parents, who have always supported me even when they never understood what I was up to. My brother, who challenges me and inspires me every day. Most importantly, my wife, who is my best friend and has always encouraged, challenged, grounded and supported me.

I want to thank the exceptional scientists who have helped me grow and learn. These include the scientists during my time at Columbia and VERITAS/CTA: Qi Feng, Ruo Shang, Marcos Santander, Daniel Nieto and Massimo Cappasso. I am very thankful for my peers Andriy, Ari and Colin, who have survived this journey with me along the way.

Before entering graduate school, I was honored to join the Columbia Bridge-to-PhD program. This program altered the course of my career, providing me with the resources to finally access a PhD program with the skills necessary to succeed. I want to thank Marcel Agueros, Summer Ash and Robyn Sanderson, who guided me along the way with regular mentorship and advice. Professor Bob Fisher first started my mentorship journey, connected to me to the Bridge program, and has guided me ever since, so I owe a huge gratitude to him.

Finally, I would like to thank the senior scientists who have played the largest roles in my scientific education. Professor Reshmi Mukherjee has taught me how to navigate the scientific world and ask the right questions to get to the bottom of a challenge right away. Professor Vladimir Vassiliev, at UCLA, provides a template of scientific tenacity and rigor that we should all aspire to, and I hope I can emulate that level of discipline.

Professor Brian Humensky, my PhD advisor, is the best advisor I could have. In the eight years we worked together, he has been tireless in providing worthwhile feedback and lessons. Since the beginning, he gave me the room to grow at my own pace and wisely guided me toward the best challenges I could handle. I want to thank him for all the support and wisdom throughout these years.

Dedication

To my family, for their unwavering support.

Chapter 1: Introduction and Background

The field of gamma-ray astrophysics is primarily concerned with the most energetic events in the universe. These events include active galactic nuclei, stellar explosions, mergers, turbulent jet structures and many others.

In many cases, the well-studied and confirmed gamma-ray sources are bright, constantly emitting sources with occasional flares. As the field developed, more sensitive and faster instruments have been able to resolve new time-dependent sources, known as transients, that appear in the sky without prior warning. Transients form the subfield of time-domain astrophysics, which is a main topic of this thesis.

Fast, high-energy, explosive events such as gamma ray bursts (GRBs) were discovered with gamma-ray detectors in the 1960's. Vela, the group of satellites meant to monitor nuclear detonations on Earth, inadvertently discovered gamma rays from the universe in 1967 [1]. This detection, and confirmation of the astrophysical nature, began the search for GRBs and other high-energy time-domain events, leading to the construction of several space-based gamma-ray detectors. Both BATSE of the Compton Gamma Ray Observatory (CGRO, [2]) and Beppo-Sax [3–5] followed up the detection of several thousands of GRBs, cataloging one of the most luminous source types in the universe at $\sim 10^{53}$ erg/s isotropic luminosity [6].

In the meantime, the development of the imaging atmospheric Cherenkov technique (IACTs) grew with the detection of very high energy (VHE; 100 GeV to 100 TeV) gamma rays from the Crab Nebula [7] in 1989. This detection was pioneered by the Whipple 10-m telescope, which used a ground-based telescope that observed the Cherenkov effect in the extensive air showers created by gamma rays interacting with the atmosphere. HEGRA, an IACT array developed on the Spanish island La Palma, joined Whipple and the gamma-ray astronomy field in 1987, introducing an array design to exploit stereoscopic reconstruction of the incoming gamma rays [8].

The Very Energetic Radiation Imaging Telescope Array System (VERITAS) was proposed in 1995, broke ground in 2003, achieved first light in 2004, and completed the full array in 2007 [9]. VERITAS followed up on the success of Whipple, constructed on the same site, and is the main telescope used in this work (see chapter 2 for a technical overview). In addition, two more IACT observatories were constructed, forming the current generation of IACT arrays around the world. The High Energy Stereoscopic System (HESS) consists of five IACTs in Namibia, which achieved first light in 2004 and construction of HESS II in 2012 [10–12]. At the same site as HEGRA, the Major Atmospheric Gamma Imaging Cherenkov (MAGIC) Telescopes (later renamed to MAGIC Florian Goebel Telescopes) achieved first light in 2004, and construction of a second telescope MAGIC-II in 2009 [13, 14].

These ground-based IACT observatories sensitive to VHE gamma rays have been aided by the additional development of gamma-ray satellites sensitive to high-energy gamma-ray photons (HE; 30 MeV to 100 GeV). The BATSE detector on the CGRO satellite was accompanied by EGRET, an important surveying detector that cataloged 271 gamma-ray sources, mapping the entire gamma-ray sky from 1991 to 2000 [2, 15]. EGRET was followed by the *Fermi* Gamma-Ray Space Telescope, a still operational satellite containing the Large Area Telescope (LAT) and Gamma-ray Burst Monitor (GBM), launched in 2008 [16–18]. *Fermi*-LAT is a crucial instrument for the work in this thesis since it surveys the sky every three hours, enabling long term monitoring of various sources. Importantly, it includes a robust public data access[1] system with user friendly data reduction and analysis tools[2] provided by the Fermi Science Support Center (FSSC) [19].

The international collaboration developed over time by these observatories have led to many physics results and many more questions. An important, open question in the field is about the origin of cosmic rays. First discovered by Victor Hess in 1912 using balloon experiments, the flux of high-energy cosmic particles from the universe reaches the highest particle energies possible, up to $\sim 10^{21}$ eV [20].

According to a recent review by Beatty and Westerhoff [21], the cosmic-ray spectrum has

[1] https://fermi.gsfc.nasa.gov/cgi-bin/ssc/LAT/LATDataQuery.cgi
[2] https://fermi.gsfc.nasa.gov/ssc/data/analysis/software/

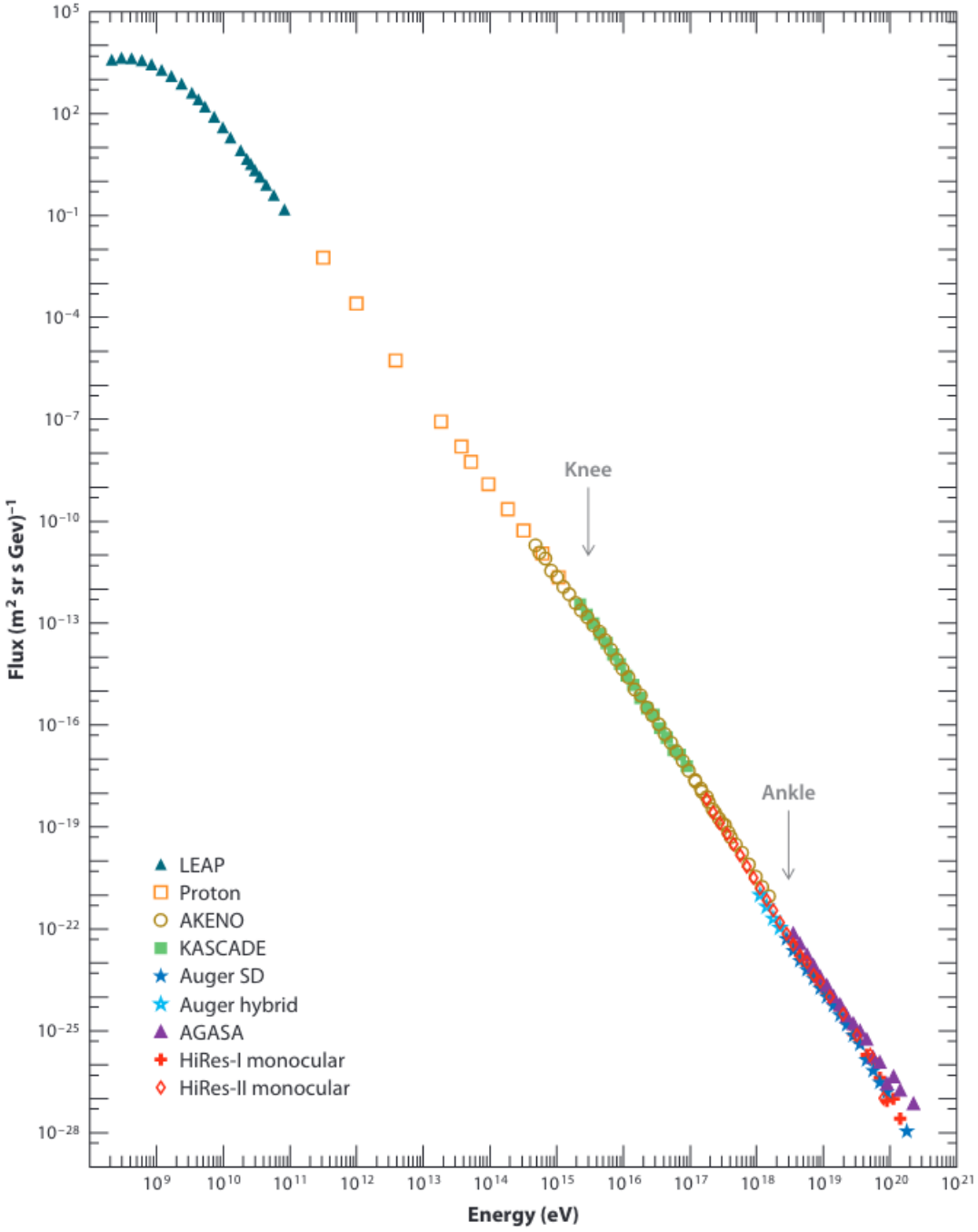

Figure 1.1: The cosmic-ray spectrum, approximating a power-law spectral model with index ~ 2.7. The “knee" and “ankle" features represent the approximate energies of the breaks in the spectrum, which may be transition points when different physical processes dominate the emission [21].

distinct features at $\sim 10^{15}$ eV and $\sim 10^{18}$ eV, known colloquially as the “knee" and “ankle" for its resemblance to a human leg (annotated on Figure 1.1). The spectrum (defining the flux $\frac{dN}{dE}$ per energy bin; see appendix C for further definitions) approximates a power law with index 2.7, while the breaks may indicate the turnover between dominant physical processes within each energy range. The particles from this cosmic ray flux may represent highest energy particles in the universe and lead to some basic fundamental questions: what are their origins? Could gamma rays reveal the acceleration mechanism? Many studies focus on specific sources of high-energy particles like active galactic nuclei (AGNs), supernova remnants, novae and GRBs to identify the physical mechanisms that accelerates particles up to 10^{21} eV and can explain the cosmic ray spectrum.

Most low-energy light from astrophysical sources consists of thermal photons, meaning that the energy radiated is proportional to the temperature of the source. This is known as blackbody radiation. For higher energy emission, the gravitational and rotational energies released by astrophysical sources power the relativistic acceleration of charged particles via processes such as shocks, reconnection, or turbulence. The relativistic, charged particles then may radiate gamma rays through various processes, both leptonic and hadronic.

The following sections are split into two parts: first, the mechanisms that accelerate charged particles are reviewed in Section 1.1; and second, the radiative processes that emit gamma rays from these high energy charged particles are reviewed in Section 1.2.

1.1 Acceleration Processes

A major acceleration mechanism is due to shocks, which is the pressurized supersonic flow created in the interface between two fluids of different velocities. These fluids are made of standard gas and matter around astrophysical objects, like hydrogen or other star ejecta, thermal and non-thermal photons, or higher energy particles and nucleons. The target medium is generally ionized, so the magnetic field of the charged particles is amplified and enhanced by self interaction. The particles in the shock are accelerated by the first and second order Fermi acceleration, described in the following sections, as summarized by [22–24].

1.1.1 Second Order Fermi Acceleration

First proposed by Fermi [25] in 1949, second order or stochastic acceleration posits that randomly scattered galactic magnetic fields moving at velocity u deposit energy into charged particles, with the average gain

$$\left\langle \frac{\delta E}{E} \right\rangle = \frac{8}{3} \left(\frac{u}{c} \right)^2 \tag{1.1}$$

In this system, charged particles interact with gas clouds in the interstellar medium with irregularities in the magnetic field. These particles are scattered inelastically, and since the cloud is moving with velocity u, individual particles gain energy. Head-on (or tail-on) collisions impart an energy gain that occurs just slightly more often than energy loss over time. The dependence on the second order v/c term leads to a smaller and less efficient energy gain than first order Fermi acceleration.

1.1.2 First Order Fermi Acceleration

The first order, or diffusive shock acceleration, was also proposed by Fermi [26] in 1954, and posits that charged particles gain energy with successive crossings of a planar shock front [22, 23, 26]. The average energy gain of a particle crossing a shock front with velocity v_s

$$\left\langle \frac{\delta E}{E} \right\rangle = \frac{4}{3} \frac{v_s}{c} \tag{1.2}$$

These collisions are effectively all head-on collisions, which impart a more regular energy gain than in second-order Fermi acceleration.

In both cases, the Fermi acceleration yields a similar energy distribution. If the fractional energy gain per interaction is β, a particle of initial energy E_0 will reach $E = E_0\beta^n$ after n interactions; if the probability of remaining per scattering event in the accelerating region is p, then after the same n interactions, only $N = N_0 p^n$ of the original N_0 particles will remain. Combining the logarithm of both equations and cancelling out the number of interactions n:

$\ln(N(E)/N_0) = \ln(E/E_0)(\ln p/\ln\beta)$ and therefore

$$\frac{dN(E)}{dE} \propto \frac{N(E)}{E} \tag{1.3}$$

$$\propto E^{-1+\frac{\ln p}{\ln\beta}} \tag{1.4}$$

This relationship yields a $\frac{dN}{dE}$ that is a power law with index $\alpha = -1 + \ln p/\ln\beta$. For strong shocks, the Rankine-Hugeniot conditions describing the fluid compression factor and mach number from the conservation of mass and energy between fluids leads to a spectral index $\simeq 2$ to $\simeq 2.5$ [23]. This power-law outcome for both first and second order Fermi accelerations is a tantalizing clue that shock environments may be a primary mechanism driving the acceleration of cosmic rays.

1.2 Radiative Processes

There are 4 main processes toward radiating photons described here, illustrated in Figure 1.2 adapted from [27]. The processes described here are synchrotron radiation, inverse Compton scattering, Brehmsstralung, and pion production. Unless otherwise specified, the derivations and discussion of these production process are given by the seminal reference text book by Longair [24].

1.2.1 Synchrotron

A basic source of the photon production is the radiation by a charged particle accelerating in a magnetic field. In the simplest form, this is the spiraling of an electron within a uniform magnetic field. The gyrofrequency of the electron in a magnetic field B moving relativistically with Lorentz factor $\gamma = 1/\sqrt{1-\beta^2}$ is $\nu_g = \frac{eB}{2\pi\gamma m_e c}$, with $\beta = v/c$. Using the Lorentz invariant radiation power $P = \frac{q^2\gamma^4}{6\pi\epsilon_0 c^3}(|a_\perp|^2 + \gamma^2|a_\parallel|^2)$, the radiation power becomes

$$P = \sigma_T c\beta^2\gamma^2 U_B, \tag{1.5}$$

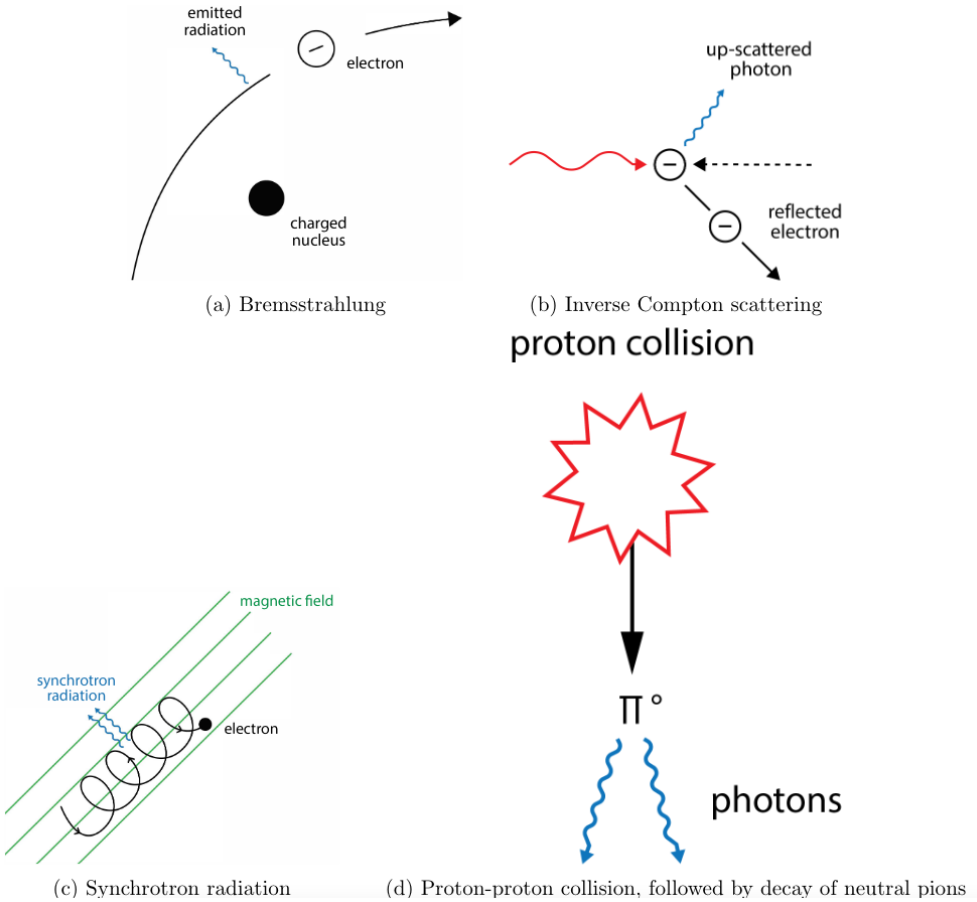

(a) Bremsstrahlung

(b) Inverse Compton scattering

(c) Synchrotron radiation

(d) Proton-proton collision, followed by decay of neutral pions

Figure 1.2: Overview of four radiative processes that emit photons [27].

where $\sigma_T = \frac{8\pi e^4}{3m_e^2c^4}$ is the Thomson cross-section, and U_B is the magnetic field density of the region, averaged over the pitch angle between the particle velocity vector and B (from $P = 2\sigma_T c\beta^2\gamma^2 U_B \sin^2\alpha$ for angle α).

The synchrotron power is $\propto -\gamma^2 U_{\rm B}/m^2$, which implies strong dependence on the energy of the spiraling electron and inverse dependence on the charged particle mass squared. This mass relationship implies that electrons will play the largest role in synchrotron power emission when compared to proton-based synchrotron emission in the same environment.

The most important result of this radiation is the combined effect on an electron sea that yields a distinguishable spectrum of the synchrotron radiation. In an extended feat of algebra by Lightman and Rybicki [28], the energy emitted by wavelength is calculated to get the emissivity of the electron as $j(\omega) \propto \nu^{1/2}\exp(\nu/\nu_c)$, where $\nu_c = \frac{3}{2}\gamma^2\nu_g \sin\alpha$, where α is the angle between the magnetic field and particle direction of motion. For an electron field with power-law distribution, $\frac{dN_e}{dE} \propto E^{-p}$, where p is the power-law index, the resulting emissivity is proportional to $J(\nu) \propto (\text{constants})B^{(p+1)/2}\nu^{-(p-1)/2}$. In this case, the synchrotron spectral index $a = (p-1)/2$. This result shows that an electron distribution with a steep power law will lead to a power-law emission spectrum.

1.2.2 Inverse Compton Scattering

In inverse Compton (IC) scattering, photons gain energy from a relativistic electron, that is:

$$e + \gamma_{\text{low energy}} \rightarrow e_{\text{low energy}} + \gamma_{\text{VHE}} \tag{1.6}$$

The typical environments contain plenty of low energy photons, whether from the cosmic microwave background (CMB), the local thermal emission or nearby bright sources – e.g. optical or UV from nearby stars or IR from dust clouds. The resulting photon is increased by the relativistic

factor γ of the electron:

$$E'_\gamma \propto \gamma^2 E_\gamma \tag{1.7}$$

The Compton power is $\propto \gamma^2 U_B / m_e^2$, implying strong dependence on the energy of the target electron and linear dependence on the local radiation field density $U_{\rm rad}$. The full expression, in the classical Thomson regime where $E_\gamma \ll m_e c^2$,

$$P = \frac{4}{3}\sigma_T c \beta^2 \gamma^2 U_{\rm rad} \tag{1.8}$$

where the Compton cross section is frequency independent, $\sigma_T = \frac{8\pi e^4}{3 m_e^2 c^4} \sim 6.65 \times 10^{-25}\,{\rm cm}^2$. In the high energy regime $E_\gamma \gg m_e c^2$, the quantum relativistic scattering cross-section is the Klein-Nishima formula,

$$\sigma_{\rm KN} = \frac{3\sigma_T}{8x}\left\{\left[1 - \frac{2(x+1)}{x^2}\right]\ln(2x+1) + \frac{1}{2} + \frac{4}{x} - \frac{1}{2(2x+1)^2}\right\} \tag{1.9}$$

where $x = E_\gamma / m_e c^2$, with ε the energy of incident photon. This reduces to the Thomson regime when $E_\gamma << m_e c^2$, and the cross section decreases $\propto 1/x$ for $x \gg 1$.

The general result is that the frequency of a photon is up-scattered by $\nu' \approx \gamma^2 \nu$. For an electron field with power-law distribution, $\frac{dN_e}{dE} \propto E^{-p}$, where p is the power-law index, it follows from a similar argument made with synchrotron radiation that the resulting IC spectral index $a = (p-1)/2$. Identifying the IC component of a source spectrum is an important part of finding the electron spectrum of the underlying source environment, providing crucial properties that will help understand the nature of these systems.

1.2.3 Bremsstrahlung

In the presence of the electric field of a nucleus, a charged particle experiences Bremsstrahlung, or "braking radiation", emitting photons that slows down the charged particle. This effect is par-

ticularly important in the production of extensive air showers, described in section 2.1.1, but also in the production of photons in dense, metal rich astrophysical environments.

The power of the nonrelativistic Bremsstrahlung is $\propto Z^2 N E_e^{1/2}$, which implies strong dependence on the metallicity and density of the environment. This is the effective behavior in astrophysical environments with relatively slow moving electrons. Relativistically (above the electron rest mass energy), the Bremsstrahlung power is $\propto E_e$, which is implies an exponential energy function rather than the polynomial relationship of the non-relativistic case. In this regime, the position dependence also enables the calculation of the radiation length, which is the distance necessary for $1/e$ energy loss. In the air, the critical energy is ~83 MeV, which is when the ionization losses equal the Bremsstrahlung losses. At this energy, the radiation length is $X_0 = 36.62\,\mathrm{gcm}^{-2}$.

1.2.4 Pions

The production of pions is a critical pathway toward radiating gamma rays. Charged and neutral pions are produced in equal amounts by the interaction between hadronic cosmic rays and protons, nucleons and photons in astrophysical environments.

The production of pions in the interaction with high-energy protons ($\backsim\ 10^{16}$ eV) and optical photons also yields neutrons, $p + \gamma \rightarrow n + \pi^+$, where the center of momentum energy of the $E_{\mathrm{photon}} * E_{\mathrm{photon}} > E_{\mathrm{n}} E_{\pi}$. In a more common interaction, both in the atmosphere and a dense astrophysical environment, the interaction of high-energy protons with a nucleon creates a shower of protons, charged and neutral pions (strange particles and antinucleons may also be created in this shower). The resulting pions decay in the following common modes:

$$\pi^0 \rightarrow \gamma + \gamma \tag{1.10}$$

$$\pi^+ \rightarrow \mu^+ + \nu_\mu \tag{1.11}$$

$$\pi^- \rightarrow \mu^- + \bar{\nu}_\mu \tag{1.12}$$

The gamma rays are the most common decay mode of the neutral pion decay (equation 1.10),

occurring more than 98% of the time with very small lifetimes ($\sim 10^{-9}$ s) [29]. Due to the direct decay of particles in these chains, a power-law distribution of the primary protons will also yield a power-law distribution of gamma rays produced.

1.3 Thesis Overview

This thesis is structured into three main parts. The first part focuses on the background physics and technical approach. In chapter 1, the basic acceleration and radiative processes are introduced. These processes are referenced throughout and are fundamental to the field of gamma-ray astrophysics. In chapter 2, the VERITAS technical approach is described in detail. This includes both the physics and processes for developing IACTs, and the data analysis pipeline of VERITAS data, from camera data reduction to high-level analysis output.

In the second part, the development of the prototype Schwarzschild-Couder telescope is discussed in chapter 3. The primary effort of this thesis was the construction, commissioning and alignment of the optical system. This effort took place in parallel with analytical and scientific work of chapters 4 and 5.

In chapter 4, the observation and analysis of superluminous supernovae (SLSNe) is discussed. This work was submitted to The Astrophysical Journal and is reproduced here verbatim. Two SLSNe were analyzed, SN 2015bn and SN 2017egm, with both VERITAS and *Fermi*-LAT telescopes. In addition, a population of sources were analyzed to estimate the future detection potential of new SLSNe with several gamma-ray observatories.

In chapter 5, the observation and analysis of several novae were discussed. These novae were observed with VERITAS and *Fermi*-LAT. The observation of Nova Herculis 2021 is noteworthy in that the overlap of both observations may constrain the cutoff energy of the nova spectral model, providing a estimate for the maximum energy of the accelerated particles in the nova shock region.

Chapter 2: VERITAS Technical Approach

2.1 Imaging Atmospheric Cherenkov Technique

Gamma rays of all energies reach the Earth, but different observational methods are necessary to detect them accurately. At very high energy (VHE; 100 GeV to 100 TeV), the atmosphere interacts directly with incoming gamma-ray photons, and while that atmospheric opacity makes it impossible to directly detect the VHE gamma ray with a ground-based detector, it provides a new opportunity for an indirect detection. The incoming photon is transformed into an extensive air shower that can be imaged by high resolution, fast triggering, ground-based optical telescopes via the imaging atmosphere Cherenkov technique (IACT), described here. In this chapter, the physics behind this technique is introduced, followed by a description of the VERITAS telescope and the analysis software necessary to process the incoming gamma-ray data.

2.1.1 Shower Cascade

A sufficiently high-energy incoming particle that interacts with the atmosphere will create a secondary particle that in turn will also interact with the atmosphere. This cascade process continues through many generations until the secondary is absorbed by the atmosphere. In this process, an extensive air shower is formed from the secondary particles.

In the presence of a nucleus, a gamma ray with a minimum energy of $2 \times m_e c^2$ (1.022 MeV) can pair produce, $\gamma\gamma \rightarrow e^+ + e^-$. If the gamma-ray energy is high enough, the resulting leptons are highly relativistic and will radiate through Bremsstrahlung in the presence of the nuclei in the atmosphere, producing further VHE photons that can also pair produce (the minimum energy required for the Bremsstrahlung process is ~84 MeV per particle). The radiation length X_0 defines the distance required for a photon to travel and lose $1/e$ of its original energy due to radiation. In

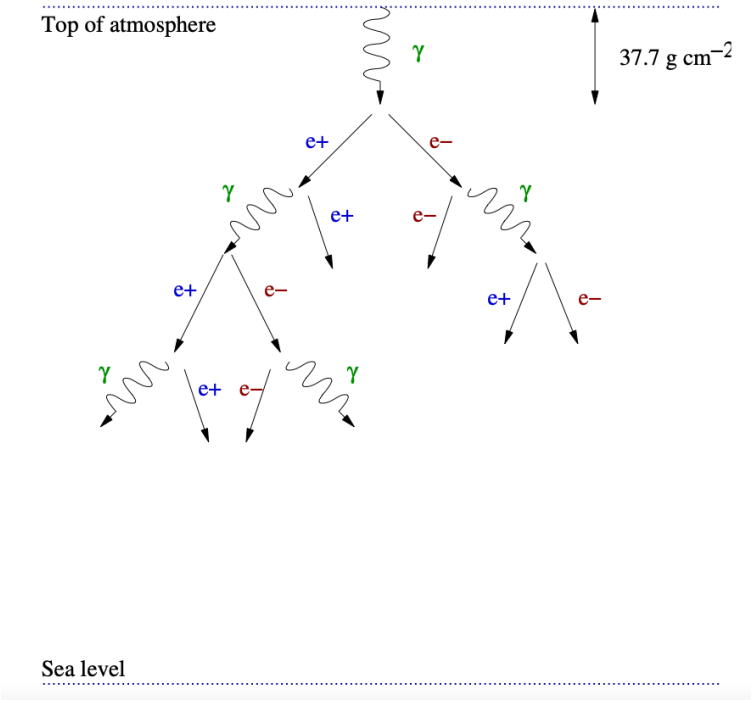

Figure 2.1: An example of the gamma-ray shower cascade from [31].

air, with Bremsstrahlung, $X_0 = 36.62\,\mathrm{g\,cm^{-2}}$, which is 7/9 of the pair production mean free path [29, 30]. This implies that the length a photon travels before pair production is a similar length to an electron undergoing Bremsstrahlung. The typical atmospheric depth is $1033\,\mathrm{g\,cm^{-2}}$ (i.e. the height of the atmosphere), so the interaction must happen near the top of the atmosphere as shown in Figure 2.1.

The number of particles grows exponentially, but at each generation energy is lost from ionization and Bremsstrahlung (~84 MeV per particle), so the process ceases when the kinetic energy is depleted. At this critical point, the critical energy $E_c = 84\,\mathrm{MeV}$, the shower has the maximum number of particles [30]. This basic model was developed by [32], which is simplified by the existence of only photons, electrons and positrons. In the air, the point at which ionization losses dominate for incoming gamma rays of energy 100 GeV to 1 TeV occurs at around 10 km above sea level [33].

There are several features to this air shower that can be directly exploited by an IACT. The only particles produced are photons, electrons and positrons, which simplifies the shower cascade (and

any subsequent simulation effort). The very high energy of the incoming photon, along with the lack of nuclear interactions, translates into most of the particle production occurring longitudinally along the path of the original gamma ray. However, due to Coulomb scattering, transverse broadening of the shower occurs by as much as 30 m. This relatively tight shower helps with the imaging and location of the shower morphology. The height of the shower maximum is proportional to the logarithm of the energy of the incoming photon, while the number of particles created is directly proportional to that energy. These two features can be mapped directly onto the image of the air shower to enable reconstruction of the true energy of the original particle.

2.1.2 Hadronic Showers

In addition to the gamma-ray extensive air shower, a significant number of hadronic cosmic-ray showers are created in the atmosphere, made up of charged, highly relativistic protons and other nuclei. In most cases, the hadrons interacting with air nuclei break off into charged and neutral pions:

$$\pi^0 \rightarrow \gamma + \gamma \tag{2.1}$$

$$\pi^+ \rightarrow \mu^+ + \nu_\mu \tag{2.2}$$

$$\pi^- \rightarrow \mu^- + \bar{\nu}_\mu \tag{2.3}$$

Hadronic cosmic-ray showers that initially decay into neutral pions quickly form into predominantly gamma-ray showers, which make them nearly indistinguishable from pure gamma-ray showers. On the other hand, showers decaying into charged pions form muons that reach the ground before decaying into the leptonic particles (ν_μ, ν_e, $\bar{\nu}_\mu$, $\bar{\nu}_e$ and $e^{+/-}$) due to time dilation. These muons lose energy through Cherenkov radiation. These strong interactions with heavy nuclei in hadronic showers produce transverse momentum, increasing the lateral length much higher than the Coulomb broadening induced in the electromagnetic showers.

The large number of decay channels complicate a general model for the hadronic cosmic-ray

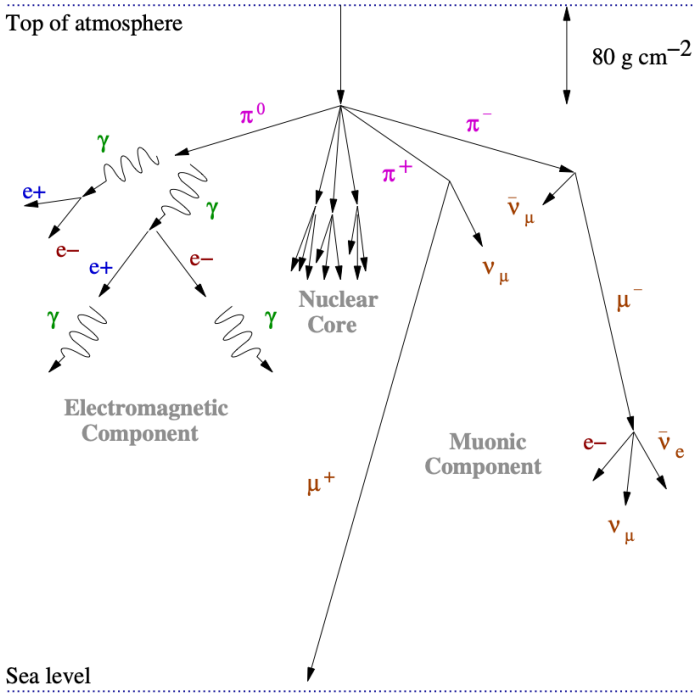

Figure 2.2: An example of the hadron cosmic-ray shower cascade from [31].

shower, which make it difficult to distinguish hadronic cosmic ray showers from pure gamma-ray incoming photons, as shown in Figure 2.2. Electron or positron cosmic rays will also induce electromagnetic showers, further complicating the true source of the incoming particle. The similarities between hadronic or leptonic cosmic-ray showers and gamma-ray showers introduce a nearly irreducible background of events that must be accounted for in the analysis.

2.1.3 Cherenkov Radiation

Once the charged particles are produced by the extensive air shower, Cherenkov radiation is the primary process converting that energy to optical light that can be detected by the IACT on the ground. In Cherenkov radiation, charged particles with phase velocity larger than the speed of light in a medium with index of refraction n will constructively polarize particles in that medium, which quickly and simultaneously radiate when the particles return to the ground state. The Cherenkov light emitted from these particles will form a cone around the trajectory of the charged particle with angle θ_C,

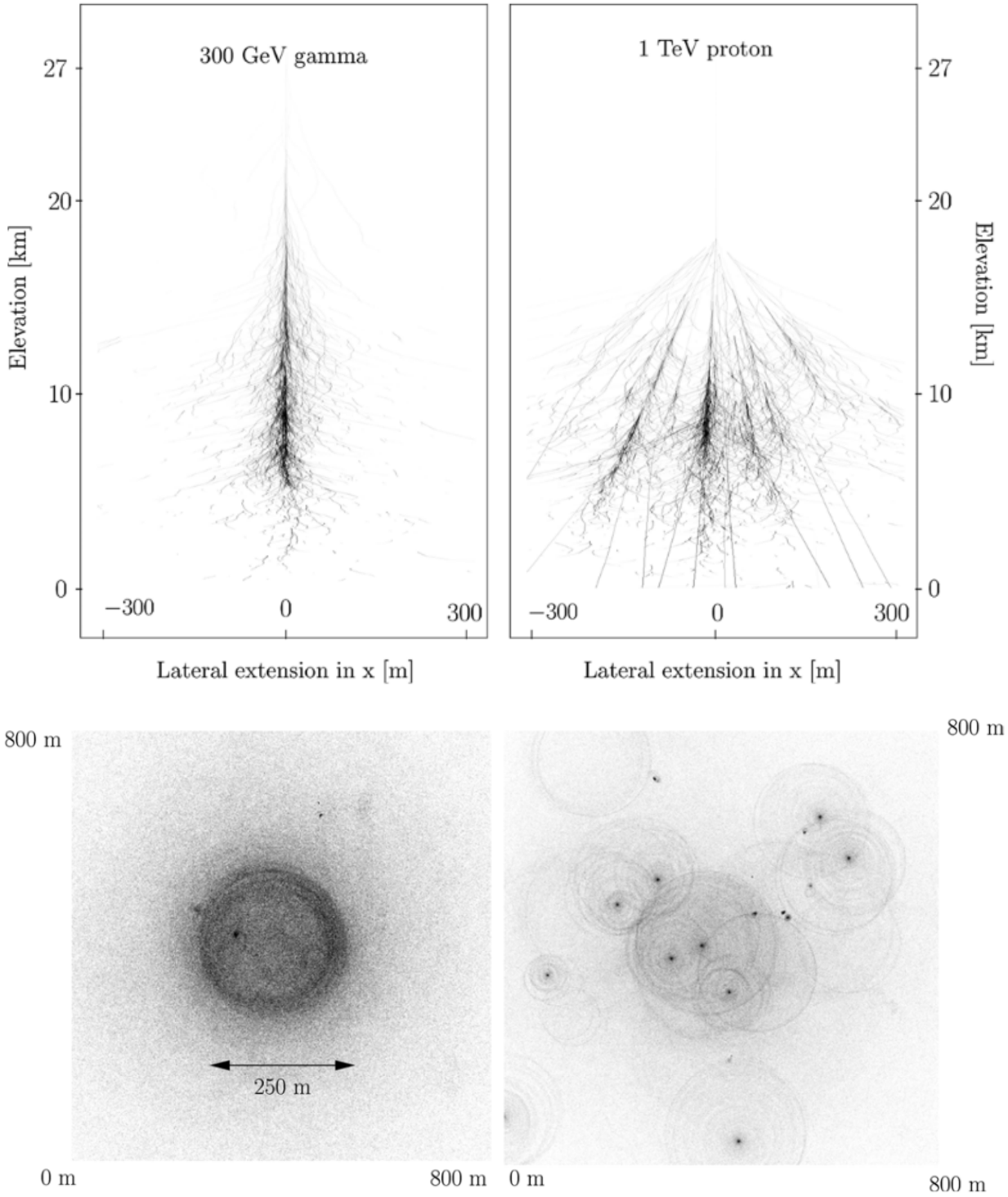

Figure 2.3: *Top*: Distribution of shower extent for a pure electromagnetic shower (from a 300 GeV gamma ray; left) and hadrons (a 1 TeV proton; right). *Bottom*: The distribution of Cherenkov light on the ground from these simulations. Both images are from Monte Carlo simulations by S. Fegan in Aharonian, Buckley, Kifune, *et al.* [34].

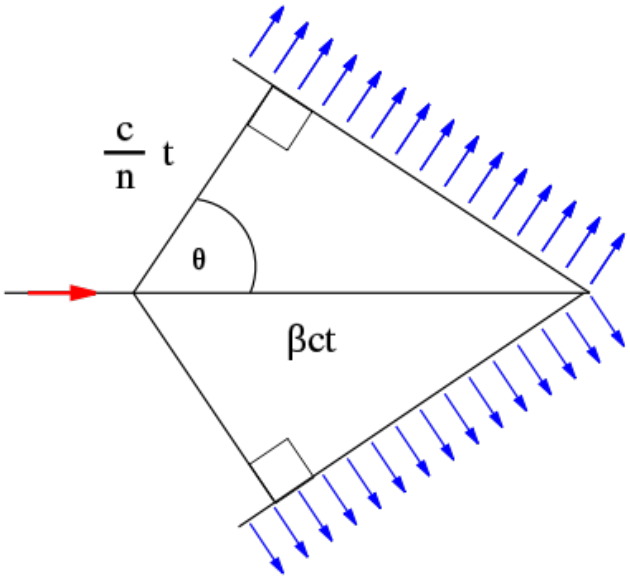

Figure 2.4: A simple Cherenkov radiation diagram. Figure from *Wikimedia* [35].

$$\cos\theta_C = \frac{1}{\beta n(\omega)} \tag{2.4}$$

The Cherenkov angle is dependent on the height of the interaction because the index of refraction depends on the density of the local medium, such that the angle decreases with increasing height. At sea level, this angle is about 1.3°, while $\simeq$ 0.74°at 8 km to 0.66°(12 mrad) at 10 km. This height dependence introduces a de-focusing effect as the altitude drops, while Coulomb broadening of the electrons in the cascade fill in the light emission turning it into a pool of light on the ground. The resulting Cherenkov light emitted at $\approx$10 km has radius of about $R \simeq 10\text{km} \times 12\text{mrad} \simeq 120\text{m}$ at ground level. VERITAS exploits this approximate shower size by placing IACTs telescopes within a baseline $\sim$100 m so that nearby telescopes can see the same shower and far enough away for stereo vision to improve direction reconstruction.

The spectrum of the resulting Cherenkov radiation is dependent on $n(\omega)$, see appendix A.1 and A.2 for discussion on the wavelength dependence. An oscillating particle forms a dielectric constant $\varepsilon(\omega)$ in equation A.10, which defines the index of refraction of the medium. This constant is then used in the application of Maxwell's equations to a moving particle in A.1. The Frank-

Tamm equation A.9 is derived in Fourier transform as a function of the frequency, and is rewritten here as a function of the wavelength:

$$\frac{d^2N}{dxd\lambda} = \frac{2\pi\alpha z^2}{\lambda^2}\left(1 - \frac{1}{\beta^2 n(\lambda)^2}\right) \tag{2.5}$$

where the critical angle is when the phase velocity $v_{\text{phase}} > c/n$, and $\cos\theta = \frac{1}{\beta n(w)}$, where $\beta = v/c$. Examples of the Cherenkov light pool generated by primary gamma rays and protons are shown in Figure 2.3.

2.2 VERITAS

The Very Energetic Radiation Imaging Telescope Array System (VERITAS) is an IACT observatory located in Southern Arizona, USA (see Figure 2.5). VERITAS has four 12 m Davies-Cotton (DC) design single-mirror telescopes, each with 350 individual mirror facets, a 499 pixel camera with 3.5°field of view. VERITAS had two major upgrades that altered the instrument sensitivity: in 2009, the T1 telescope was moved across the site, increasing the baseline distance between telescopes to $\simeq$ 100 m and improving the ground area distribution for stereo reconstruction; and in 2012, the photo-multiplier tubes (PMTs) were replaced by higher quantum efficiency PMTs to lower the energy threshold and improve the overall sensitivity. VERITAS is sensitive to gamma rays within the energy range $\sim$100 GeV to $\backsim$30 TeV, has an angular resolution (68% containment) of $\backsim 0.1°$ at 1 TeV, and an energy resolution of $\sim$15% at 1 TeV.

The many optical photons from the Cherenkov shower pass through the optical system of the IACT to a camera for conversion from analog to digital. The PMT converts light to electronic signals through the photoelectric principle, in which photons eject electrons from the surface of a photo-cathode, triggering a cascade of electrons in the presence of large electric field, and producing an output current. The electronic noise and night sky background (NSB) produce both positive and negative signal fluctuations in the output current, so an artificial signal is injected so the PMT

Figure 2.5: A photograph of VERITAS at Fred Lawrence Whipple Observatory.

signal never crosses zero. The NSB is stellar and man-made light scattered in the atmosphere that dominates over the electronic noise. The injected artificial signal is known as the pedestal, and the variation on the pedestal (the “pedvar") is directly correlated to the camera noise parameters.

The flash of light from the Cherenkov event is integrated over 2 ns samples within a custom-built flash analog-to-digital-converter (FADC) at the sampling rate of 500 MHz and stored temporarily in a 64 µs buffer. The digital signal has an 8-bit (256 digital counts per channel) dynamic range. A 32 ns window of the FADC readout is stored in a memory buffer to be sent to the data acquisition for recording, timed to compensate for the shower arrival time from each telescope. Since not all data is needed, there are hardware triggers to monitor and filter the readout of the electrical signal to the data acquisition system. The three triggers are: L1, the pixel-level trigger; L2, the telescope-level trigger; and L3 the array-level trigger. The array-level event trigger will signal to fire the memory buffer to the data acquisition [36, 37].

Specific hardware configuration is designed for each trigger level. Each PMT is connected to a constant fraction discriminator (CFD), which finds the maximum voltage of the PMT pulse. Whenever the running maximum exceeds an experimentally set threshold (generally around 45 mV), the pixel generates an L1 trigger. These pixel-level triggers can come from the NSB, which is made up of uncorrelated light of varying brightness. In order to filter out these individual flashes, L2 triggers when 3 neighboring PMTs are triggered within 5 ns of each other [38]. Further, single-telescope

events like muon rings (that cause L2 triggers) need to be filtered out. L3 triggers when 2 or more telescopes fire L2 triggers within 50 ns (experimentally optimized). A signal is sent to the FADCs to read out and record the 32 ns (16 samples) [39]. However, at this point, data is not taken during the readout period, which introduces a deadtime to the entire array. A typical dead-time percentage for the VERITAS array is around 10% at an L3 trigger rate of 300 Hz.

Observations by VERITAS are designed to optimize the data quality recorded based on the hardware considerations. The full use of the camera field of view is necessary to reconstruct events near the source position, since the shower image must be large enough to calculate image moments for each event. Additionally, observations of a background region must be taken to help set a baseline set of properties to discriminate between gamma-ray and non-gamma-ray events and to estimate the residual rate of background events at the location of interest. To accommodate this, observations are taken in a few standard ways: On/Off Tracking and wobble mode.

Each observation is taken in 30 min segments called runs. In On/Off tracking, a dedicated run is taken for the source in the center of the field of view, immediately followed by a second run taken 30 minutes (7.5°) offset from the original coordinates. This strategy allows for the direct observation of a background region in very similar and nearby sky conditions. In the wobble mode, the background and source observations are taken simultaneously by offsetting the tracking by 0.5° from the center of the camera. This offset is applied in the cardinal directions (N, E, S, W), so that the target source is always inside the camera field of view. The offline analysis of this data takes care of various observation strategies in the computation of the background, described in section 2.3.3.

2.3 VEGAS

The large amount of data generated by the array is analyzed using a clear software paradigm. In the context the next generation gamma-ray observation, the Cherenkov Telescope Array (CTA), a data organization and management was developed in anticipation of the multi-wavelength collaboration of gamma-ray data analysis [40, 41]. Although the VERITAS software predates this

Table 2.1: Mapping of data analysis stage to the responsible VEGAS tool and associated data level [40, 41].

VEGAS Tool	Data Level	Analysis stage	Description
vaStage1	DL0 → DL1	Calibration	Calculation of T0 and pedestal level.
vaStage2	DL1	Image Analysis	Trace integration. Single telescope image analysis. A deprecated vaStage3 used to perform image moment calculation, but this functionality was moved to vaStage2.
vaStage4	DL1 → DL2	Event Reconstruction	Stereo reconstruction. Energy and core position calculation. *Lookup tables* required.
vaStage5	DL2 → DL3	Background Rejection	Gamma-hadron cuts applied.
vaStage6	DL3 → DL4	Result Extraction	Spectral analysis, sky map creation, lightcurve analysis, source detection. *Effective area tables* required.

structure, it is a useful guide to understanding the data reduction strategy used here. This strategy created the gamma-ray analysis data format (GADF), which outlines the fields and file formats for each data level (DL) created from DL1 to DL5. Each data level refers to a specific responsibility: DL0 is the reduced raw camera data; DL1 is the calibrated camera data; DL2 is the reconstructed shower parameters (energy, direction, etc.) per event; DL3 are the selected gamma-like events and instrument response functions (IRFs); DL4 are the compiled spectra, skymaps, light curves from the data reduction; and DL5 are the observatory catalog or survey sky maps [40, 41].

This data management structure helps to explain the VERITAS data analysis strategy. Asserting cross-checking and validation, VERITAS maintains two independent data analysis packages to process data from DL0 to DL4: EventDisplay [42] and VEGAS [43]. In this thesis, VEGAS is used as the analysis package for all VERITAS analysis and all scientific results are confirmed by a collaborator using EventDisplay.. Each tool in VEGAS is responsible for calculations that can be mapped onto a specific data level, as outlined in Table 2.1. VEGAS is written with `C++`, relying on the CERN ROOT library for both computational methods and the file formatting [44].

Table 2.2: VEGAS image parameters calculated in stage 2.

Parameter	Definition
width	The RMS spread of light parallel to the shower image major axis.
length	The RMS spread of light perpendicular to the shower image minor axis.
distance	The angular distance of the image centroid from the center of the camera FOV.
miss	The perpendicular angular distance of the image axis from the center of the camera FOV.
azimuth-width	The RMS image width relative to an axis drawn from the image centroid to the center of the camera FOV.
size	The total number of digital counts from all the pixels making up the shower image.
nTubes	The total number of pixels that make up the shower image.

2.3.1 Calibration

The primary function of vaStage1 is the calibration of the original camera data. This includes determining the timing of the digital signal[45], the gain, and the noise level of the fluctuating NSB [46]. It also includes the identification of bad pixels within the camera. In conjunction with science data taking, every night calibration data is taken by tracking a dark patch of sky to measure the camera response to the flasher, which uniformly illuminates the camera at a fixed, high frequency rate [47].

Once the camera data from both data and flasher runs are calibrated and combined, vaStage2 applies the flasher calibration and is used to calculate the resulting image moments in the camera. Image cleaning is performed to remove bright pixels, any pixels with NSB level brightness, and truncated images [46]. A full description of this lower level analysis can be found in [48]. In brief, the Hillas parameters [49] are computed, which are summarized in Table 2.2 and shown in the diagram in Figure 2.6. In an earlier state of VEGAS, vaStage3 calculated these image moments for each event, but that functionality was merged into vaStage2 to improve the speed and efficiency of the analysis.

An important development in the image analysis is the use of templates to determine the shower parameters from the camera image. The image template method (ITM), used extensively in this

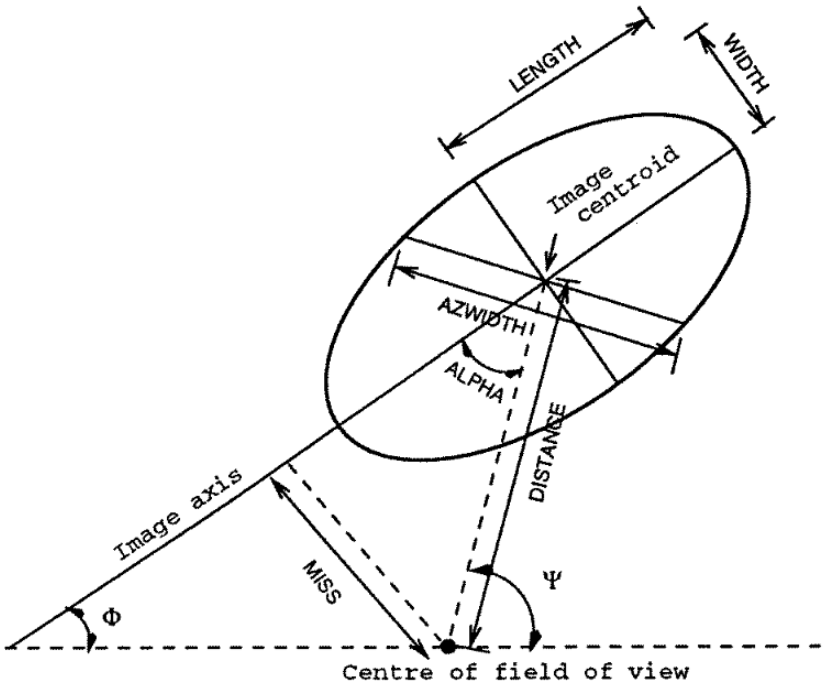

Figure 2.6: A diagram of the shower properties projected on the IACT camera from [50].

thesis, was developed by simulating gamma-ray showers in a well-tested atmosphere and detector model (incorporating the mirror model and camera electronics) [51–53]. This simulation allows the construction of a profile likelihood for every pixel in the camera, which can be fit to the data to find optimal gamma-ray shower [54]. One important cause of the improvement provided by this method is the reconstruction of truncated images at the edge of the camera, which recovers events previously thrown away in the standard method. This method has been extensively validated, including in conjunction with a BDT analysis in vaStage5 [54, 55].

2.3.2 Shower Reconstruction and Selection

In vaStage4, the stereo reconstruction of the shower using multiple telescopes is performed to calculate the direction, energy and shower core location (the hypothetical position of the light pool impact on the ground). Figure 2.7 shows this stereoscopic projection onto the ground reference frame. This stereo reconstruction enables the cutting of events with too few telescopes, or core locations that are too distant from the array.

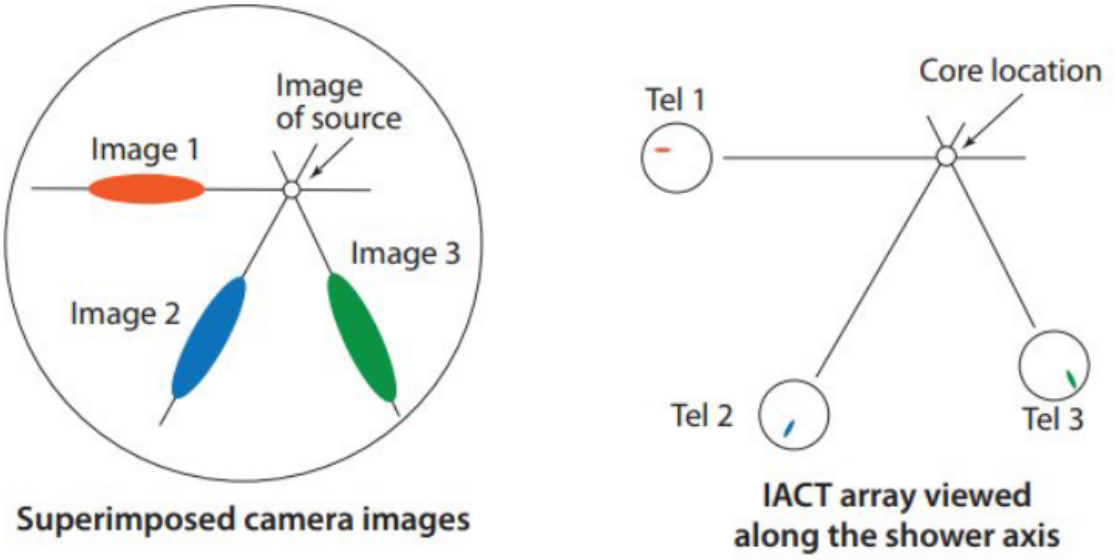

Figure 2.7: Example of the direction reconstruction using stereoscopic projection. Figure from [8].

The calculated image parameters from stage 2 do not yet connect to real showers. Using simulations, which enable the knowledge of true parameters such as the energy, to determine what a shower should look like on the camera can help create a lookup table to relate the calculated image parameters to the physical shower parameters. From these lookup tables, measured values for the length and width parameters are scaled by the lookup table values in the following form, as *mean scaled 'parameter' (MSP)* :

$$MSP = \frac{1}{N_{\text{tel}}} \sum_{i=1}^{N_{\text{tel}}} \frac{p_i}{\bar{p}_{\text{sim}}(\theta_{\text{zen}}, S_i, r_i)} \tag{2.6}$$

where p_i is the parameter of interest (length or width), and $\bar{p}_{\text{sim}}$ is the mean simulation value for that parameter given the shower zenith angle θ_{zen}, image size S_i and the impact distance r_i. Using this general equation for MSP, the specific value for mean scaled length (MSL) or mean scaled width (MSW) is calculated.

In vaStage5, the remaining cuts are applied to select the best gamma-ray candidate events. The parameter scaling is used so that uniform cuts may be applied to the entire data set to separate

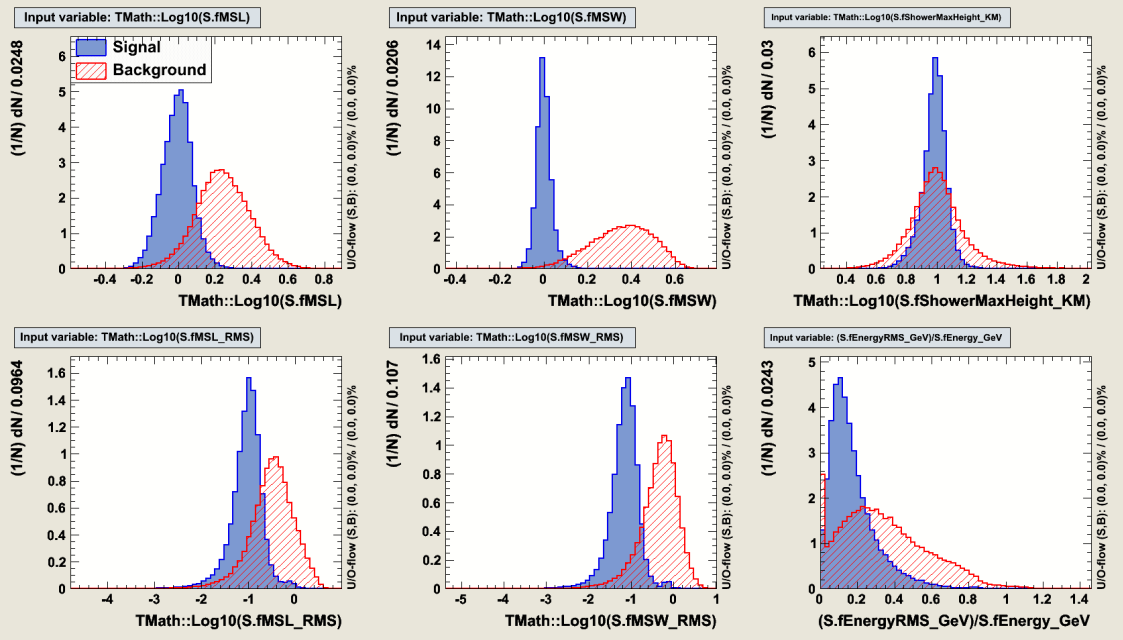

Figure 2.8: A sample distribution of parameters used for the gamma-hadron selection cuts: mean-scaled length, mean-scaled width, shower max height, mean-scaled length RMS, mean-scaled width RMS, and energy RMS for event energies above 1 TeV.

gamma rays from hadrons. The standard gamma-hadron box cuts may look like $0.05 \leq \text{MSW} \leq 1.1$ and $0.05 \leq \text{MSL} \leq 1.3$, which can be applied to the distributions in Figure 2.8.

In vaStage4, additional cuts were also applied in conjunction with the calculation of the scaled parameters. These include the minimum number of pixels in the image, $nTubes \geq 5$ and image distance to center of camera $Dist \leq 1.43$. Finally, the size (sum of charge deposited on camera) is cut in three ways, corresponding to the standard cuts used in VERITAS - soft, medium, hard - which are optimized for analysis outcomes corresponding to well-known spectral behavior.

The box cuts on scaled parameters used in vaStage5 are optimized on the analysis of known sources. However, while these cuts are easy and fast to process, there are limitations to using box cuts due to the non-linear relationships between parameters. Non-linear algorithms such as BDTs are currently being explored for VEGAS [55], while it has been robustly verified in EventDisplay [56], and known to be a component of the H.E.S.S analysis [57].

2.3.3 Analysis Summation

Background Estimation

Each candidate gamma-ray event reconstructed by the preceding analysis may originate from a different location on the sky, some of which may originate from strong gamma-ray sources. Given the uncertainty in the event reconstruction precision (the gamma-ness of an event), the creation of a large and well-observed background region affords another opportunity to statistically discriminate gamma-rays and non-gamma-rays in the data. By comparing the counts of the signal and the background regions, it is possible to estimate the difference in counts to find the source gamma-ray emission rate.

Two common background construction methods are used within both of the IACT analysis software in VERITAS: the ring background method (RBM), and the wobble or reflected region (RR) method. The observation of a source is performed by explicitly offsetting the telescope tracking position from the source position, pointed toward standard cardinal directions (i.e. wobbling around the source). This offset is tuned to balance the simultaneous measurement of the background and source positions in the same field of view while also staying within the well-behaving radius of the acceptance of the camera. The reliability of gamma-ness from event reconstruction weakens radially from the center of camera, as the Cherenkov showers are truncated from the field of view and become more difficult to analyze. Both the RBM and RR methods benefit from these wobbled observations due to the increased background observation regions and well-performing acceptance at these positions.

In the analysis of a point source (which is the primary type of source analyzed this thesis), a small circle is used to specify the region from which to count events from the target source position. This circle generally has the radius comparable in size to the point spread function (PSF) for reconstructed gamma rays, around 0.1°, and is called the *on* region. The size of this circle is given by angular radius θ from the target position, which becomes an important cut in the gamma/hadron discrimination (this cut is generally referred by the θ^2 value, since the radius

squared is linearly related to the count rate within an area and is easier to model on a histogram). For both RBM and RR methods, the counts in this *on* region are compared to the *off* region counts. Regions of the map which include bright stars, known sources, or the observational target itself, are excluded from the background estimation.

For RBM, a ring is created around the target position with upper and lower radii, forming an annulus of a given size. The top of Figure 2.9 shows the ring in light green at a random test position near the target region. This method enables the collection of a large amount of data, but with a varying acceptance that must be accounted for in the calculation. For the RR method, the bottom of Figure 2.9, a series of adjacent *off* regions are rotated around the center of the camera in each wobble observation.

Li & Ma Significance

The fundamental statistical process used in this field is the use of the optimized likelihood ratio test, formed on the assumption that count rates in the signal and background regions can be modeled (with some analytical form such as a Poisson distribution), and that the measurement of the background region gives an accurate estimate of the background rate within the signal region. This estimation is improved by increasing the background region so that the statistical uncertainty of the background is negligible compared to the uncertainty of the signal region.

$$N_{\mathrm{B}} = \alpha N_{\mathrm{off}} \tag{2.7}$$

$$N_{\mathrm{S}} = N_{\mathrm{on}} - \alpha N_{\mathrm{off}} \tag{2.8}$$

$$\alpha = \frac{A_{\mathrm{on}} t_{\mathrm{on}}}{A_{\mathrm{off}} T_{\mathrm{off}}} \tag{2.9}$$

$$f(N_{\mathrm{on}}, N_{\mathrm{off}}) = f(N_{\mathrm{on}}, N_{\mathrm{off}} | N_{\mathrm{S}}, N_{\mathrm{B}}) \tag{2.10}$$

$$= f(N_{\mathrm{on}} | \langle N_{\mathrm{on}} \rangle) f(N_{\mathrm{off}} | \langle N_{\mathrm{off}} \rangle) \tag{2.11}$$

The event counts in the *on* (N_{on}) or *off* (N_{off}) regions have background counts (N_{B}) and signal

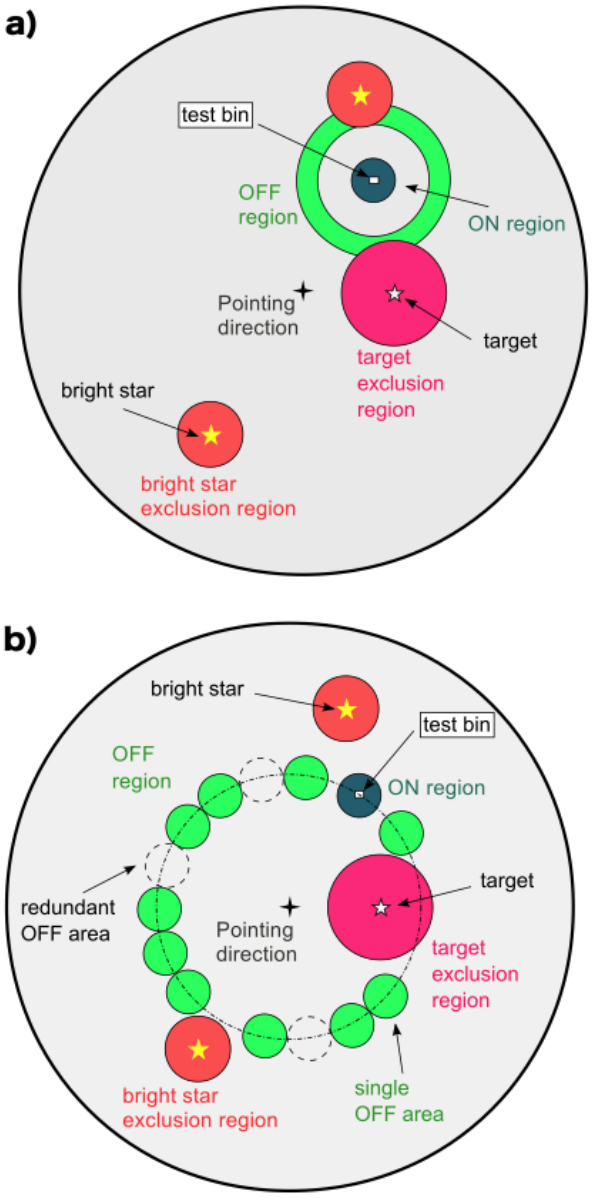

Figure 2.9: A diagram showing the RB (top, a) and reflected region (bottom, b) methods for background estimation. For both methods, the target region is wobbled to the west (right) in pink, a test *on* region is toward the top right in dark green, with its background in light green, while two exclusion regions from stars are also included. In addition to the calculating the background and excess counts for target region, the RB method is performed on test bins throughout the entire field of view, each with their own ring background, to generate a distribution of significances for the entire observation and enable map generation.

counts (N_S) from the target source. To increase the background modeling accuracy, the off region is observed with larger exposure which is scaled by α times the *on* region. The α factor is the ratio of the areas or exposures between the *on* and *off* regions; the reciprocal number of *off* regions is the α parameter in the simplest cases. The probability distribution f is modeled by the Poisson distribution of both the signal and background counts.

The strategy outlined by Li and Ma [58] assumes this probability distribution f in the likelihood $\mathcal{L}$ to form the log-likelihood ratio test λ, noting that Wilke's Theorem [59] reduces the log-likelihood to a χ^2 distribution with 1 degree of freedom when

$$\lambda = \frac{\mathcal{L}_0}{\mathcal{L}} \tag{2.12}$$

$$S = \sqrt{-2 \ln \lambda} \tag{2.13}$$

$$= \sqrt{2} \left(N_{\text{on}} \ln \left[\frac{1+\alpha}{\alpha} \left(\frac{N_{\text{on}}}{N_{\text{on}} + N_{\text{off}}} \right) \right] + N_{\text{off}} \ln \left[(1+\alpha) \left(\frac{N_{\text{off}}}{N_{\text{on}} + N_{\text{off}}} \right) \right] \right)^{1/2} \tag{2.14}$$

This derivation assumes that the signal counts are equal to the background counts in the null likelihood case $\mathcal{L}_0$, and also assumes that the number of background counts is equal to $N_B = \frac{\alpha}{1+\alpha}(N_{\text{on}} + N_{\text{off}})$.

This fundamental equation 2.14 is used throughout this work and is sometimes referred to as Equation 17 of Li & Ma [58].

Time Dependence

In the conventional analysis of sources observed by IACTs, background and signal regions are determined a priori so that an excess count can be calculated that characterizes the source count rate during an observation period. Following the criteria established, the statistical significance is calculated using Eq. 17 of Li & Ma [58]. However, in this formulation, both the source and background rates are assumed to be time independent. In the case of GRBs and other strongly time-dependent sources, the excess counts may be dominant in certain time bins within the observation and negligible in others, such that the excess counts summed over all time bins are not significant.

To solve this problem, the time dependence of the source count rate is assumed in a parameterized form $s(t)$ and the test statistic is re-derived following the strategy outlined by Li and Ma [58] [60]. The maximum likelihood estimate is used to optimize the signal and background count rates, collected within the *On* and *Off* observation regions defined as $\langle N_{on} \rangle = (\bar{b} + \bar{s}(t))T_{on}$ and $\langle N_{off} \rangle = \bar{b}T_{off}$ for observation times T_{on} and T_{off}, respectively. Again assuming a Poisson distribution of counts, the general form of the test statistic is a ratio of the likelihoods for the null and alternate hypotheses $\mathcal{L}_0$ and $\mathcal{L}$, rewritten here:

$$\frac{\mathcal{L}_0}{\mathcal{L}} = \frac{\bar{b}_0^{N_{on}+N_{off}}}{\left(\bar{b}+\bar{s}\right)^{N_{on}} \bar{b}^{N_{off}}}. \tag{2.15}$$

where $\bar{b}$ and $\bar{s}$ are the time average background and signal count rates, and $\bar{b}_0$ is the time averaged rate when all counts observed are background.

To apply the time dependence, the T_{on} observation time is split into N bins of Δt, where the probability of the number of counts for each bin is independent and $N\Delta t = T_{on}$. For a parameterized $s(t)$, at the limit of $N \to \infty$, $\Delta t \to 0$, the likelihood ratio reduces to:

$$\frac{\mathcal{L}_0}{\mathcal{L}} = \frac{b_0^{N_{on}+N_{off}}}{\left(\Pi_{t_i \in \{t_{on}\}}(b + s(t_i))\right) b^{N_{off}}} \tag{2.16}$$

where $s(t) \equiv \theta \times t^{-1}$. The time dependence of the signal was assumed to be 1/t since it is most similar to many GRBs light curves detected by *Fermi*-LAT after the burst [61], where θ is a normalization constant for the time-dependent count rate.

This modified likelihood ratio was validated with a Monte Carlo simulation. Using a toy-model MC of a GRB, with 5×10^5 observations starting 2 min after burst trigger, the time-dependent signal $s(t) = \theta \times t^{-1}$, and the typical IACT background rate (1 γ /min), the following simulation results provided evidence for some additional conclusions (see also Figure 2 of [60]). For a 35-min observation, the mean significance over all the simulated observations increased from 4σ to 5σ once time dependence is included, a 25% increase in sensitivity. For a 100-min observation: the simulated observations reveal that the overall significance improves from 3.4σ to 5.2σ with

time weighting for that observation time. Comparing 35-min and 100-min simulations, the time-independent method has a reduced sensitivity from 4σ to 3.4σ as expected with the increase in background counts, while the time-dependent model increases from 5σ to 5.2σ, indicating that the time dependence allows for an improved estimate of the background and signal rates for longer observation times.

The simulation showed that the significance is dependent on the length of the observation. The standard significance [58] peaks and then declines over time as the background rate accumulates counts toward the *On* region and dilutes the signal counts. However, the time-dependent likelihood ratio grows monotonically if events are weighted to account for the GRB's time dependence, up to as much as 10-25% increase from the time-independent significance (see Fig. 3 of [60].) Some common analysis software packages within the gamma-ray astrophysics field (e.g. CTOOLs) include a temporal model in the maximum likelihood fitting in addition to the spatial and spectral models [62].

2.3.4 Upper limit

Many of the time-domain astrophysical sources within the VHE gamma-ray range are weaker sources than measurable by current IACTs, if they emit gamma rays at all. In this case, rather than reporting the statistical flux of the source with a small statistical significance and very large relative error, an upper limit is reported. The upper limit refers to the largest possible flux attainable by the instrument given the observed background counts, calculated by finding the maximum signal counts within a specified confidence level and known measurement uncertainty. If the instrument is sensitive enough when compared to an expected model, this upper limit may even constrain the model.

Physical Reasoning

The flux upper limit is generally reported as

$$F_{>E_{\text{thr}}} = \int_{E_{\text{thr}}}^{\infty} \frac{dN}{dE} dE$$

The observations determine the threshold energy and differential flux, which define the instrument in this instance, so these must be solved for in this equation. The differential flux can take the form of a powerlaw or any other common model. For a powerlaw, the normalization needs to be computed using the effective area of the instrument.

$$\begin{aligned} \frac{dN}{dE} &= k_0 \left(\frac{E}{E_0}\right)^{-\gamma} \\ k_0 &= \frac{\langle \text{counts} \rangle}{\langle \text{time} \rangle \langle \text{area} \rangle \langle \text{energy} \rangle} \\ \langle \text{counts} \rangle &= \lambda_{\text{source}} \end{aligned}$$

The upper limit calculations (Rolke, López, and Conrad [63], Helene [64–66], and Cousins, Feldman, and Cousins [67], etc.) use the number of counts in the on and off regions, α and confidence limit (e.g. 95%) to compute the statistical number of counts possible, λ_{lim}. To estimate the largest possible upper limit, these values should use the whole observed On/Off counts and exposure of the instrument, assuming energy independence. The assumption is that these counts are from the source (not background), which follows the given physical spectral model. To calculate the number of counts from a model:

$$\begin{aligned}\lambda_{\text{source}} &= \int_{\text{instrument}} \frac{dN}{dE} A(E) dE dt \\ &= t k_0 \int \left(\frac{E}{E_0}\right)^{-\gamma} A(E) dE\end{aligned}$$

Setting $\lambda_{\text{source}} = \lambda_{\text{lim}}$, we can then find the upper limit normalization to place into the integral flux $F_{>E_{\text{thr}}}$ at the top.

$$k_0 = \frac{\lambda_{\text{lim}}}{t \int \left(\frac{E}{E_0}\right)^{-\gamma} A(E) dE}$$

Putting it all together,

$$\begin{aligned}F_{>E_{\text{thr}}} &= \int_{E_{\text{thr}}}^{\infty} \frac{dN}{dE} dE \\ &= \int_{E_{\text{thr}}}^{\infty} k_0 \left(\frac{E}{E_0}\right)^{-\gamma} dE \\ &= \int_{E_{\text{thr}}}^{\infty} \left[\frac{\lambda_{\text{lim}}}{t \int \left(\frac{E}{E_0}\right)^{-\gamma} A(E) dE}\right] \left(\frac{E}{E_0}\right)^{-\gamma} dE \end{aligned} \tag{2.17}$$

Since this upper limit is model dependent, the final value could be anything within the model parameter space $\{k_0, \gamma\}$. k_0 is dependent on the count upper limit and γ, so it is possible to vary γ to get a distribution of the range of flux upper limits. This process is approximated by trying 3 γ's to see the spread of flux upper limits, then reporting the energy at which pairs of these fluxes are close to each other (the so-called decorrelation energy). If the energies are exceptionally different ($> 30\%$), it indicates a bias due to the γ dependence. The decorrelation energy is then used in the upper limit integral, which approximates the sum of all the possible fluxes within the model parameter space $\{k_0, \gamma\}$. This is a good estimate for a parameter-independent flux upper limit.

This equation forms the strategy implemented in VEGAS in the next subsection, $F_{>E_{\text{thr}}}$ is re-

named to $\Phi_{p,int}$, and $\frac{dN}{dE}$ to $\phi(E)$.

Extragalactic Background Light

The universe is filled with extragalactic background light (EBL) that interacts with high energy photons. Unlike lower energy photons and neutrinos that pass directly through the universe unimpeded and in a straight line, VHE photons above 1 TeV interact with optical (a few eV energy) photons via photon-photon pair production. Given a probability of interacting with the EBL, VHE gamma rays traveling a larger distance increase the overall absorption factor as they are more likely to interact with light along the way [68]. The standard energy and redshift dependent EBL absorption factor $\tau(z, E)$ decreases the detected flux by $e^{-\tau(z,E)}$.

Applying the absorption formula to equation 2.17 above:

$$\phi_{p,int} = \int_{E_{\rm thr}}^{\infty} \frac{N_{UL}}{T * \left[\sum_i^N \langle A \rangle_i \int_{E_{l,i}}^{E_{u,i}} (\frac{E'}{E_0})^{-\gamma} e^{-\tau(z,E')} dE'\right]} \left(\frac{E}{E_0}\right)^{-\gamma} e^{-\tau(z,E)} dE$$

In the denominator, this changes the spectrally-averaged effective area $< A >_i$ of the instrument at the high energies by a small amount. EBL deabsorption hardens the spectrum as the energy increases, so each fine bin will increase by a small amount. Overall, it is difficult to predict the standard total change (whether greater or less than original flux) because the actual change in the spectrally-averaged effective area has to compete with the change in flux integral in the numerator.

Time Dependence

Assume there is a time dependence on the spectral model $f(t)$, generally a power law with $\beta \simeq -1.3$

$$\begin{aligned} \frac{dN}{dE} &= k_0 \left(\frac{E}{E_0}\right)^{-\gamma} f(t) \\ &= k_0 \left(\frac{E}{E_0}\right)^{-\gamma} t^{\beta} \end{aligned}$$

The estimate source counts is then

$$\begin{aligned}\lambda_{\text{source}} &= \int_{\text{instrument}} \frac{dN}{dE} A(E) dE dt \\ &= k_0 \int \left(\frac{E}{E_0}\right)^{-\gamma} t^{\beta} A(E) dE dt \\ &= \begin{cases} k_0 \frac{t^{1+\beta}}{1+\beta} \int \left(\frac{E}{E_0}\right)^{-\gamma} A(E) dE & \text{for } \beta \neq -1 \\ k_0 \ln(t) \int \left(\frac{E}{E_0}\right)^{-\gamma} A(E) dE & \text{for } \beta = -1 \end{cases}\end{aligned}$$

Fast forwarding the same analysis above to its final form (for now $E_0 = 1\ TeV$ and E in units of TeV, so that it simplifies the text):

$$\begin{aligned}\phi_{p,int} &= \int \int_{E_{\text{thr}}}^{\infty} \frac{N_{UL}}{\left[\frac{t'^{1+\beta}}{1+\beta} * \sum_i^N \langle A \rangle_i \int_{E_{l,i}}^{E_{u,i}} E'^{-\gamma} dE'\right]} (E)^{-\gamma} t^{\beta} dE dt \\ &= \int \int_{E_{\text{thr}}}^{\infty} \frac{N_{UL} * (1+\beta)}{\left[\sum_i^N \langle A \rangle_i \int_{E_{l,i}}^{E_{u,i}} E'^{-\gamma} dE'\right]} (E)^{-\gamma} \frac{t^{\beta}}{t'^{1+\beta}} dE dt\end{aligned}$$

Assuming $t = t'$, that can be integrated together

$$= \begin{cases} (1+\beta) \ln(t) \int_{E_{\text{thr}}}^{\infty} \frac{N_{UL}}{\left[\sum_i^N \langle A \rangle_i \int_{E_{l,i}}^{E_{u,i}} E'^{-\gamma} dE'\right]} (E)^{-\gamma} dE & \text{for } \beta \neq -1 \\ \int_{E_{\text{thr}}}^{\infty} \frac{N_{UL}}{\left[\sum_i^N \langle A \rangle_i \int_{E_{l,i}}^{E_{u,i}} E'^{-\gamma} dE'\right]} (E)^{-\gamma} dE & \text{for } \beta = -1 \end{cases}$$

Statistics

The upper limit of counts is found by calculating the confidence region of a distribution of signal counts. The counts are Poissonian, with some rate given by background and signal physics (all kinds of physical and instrumental reasons will define the rate itself). The signal counts are found by the difference in counts for different observing modes, *on* and *off*. With a Poissonian

distribution, likelihood functions for null and hypothesis are created, and then the confidence range is developed with these functions, whether by likelihood ratio λ or numerically. The three main upper limit calculations are Rolke [63], Feldman & Cousins [67], and Helene [64], described in the following subsections.

Rolke The Rolke method adds nuisance parameters to the basic set up of the profile likelihood to allow for statistical uncertainty. Specifically, say m events are run through a Monte Carlo (without background) and finds z events surviving. Then, the efficiency Z is modeled as a binomial random variable based on the original number of true events m and efficiency parameter e and finds the complete model to be

$$\begin{aligned} N_{\text{on}} &= \text{Poiss}(es + b) \\ N_{\text{off}} &= \text{Poiss}(b/\alpha) \\ Z &= \text{Binomial}(m, e) \end{aligned}$$

The modified log-likelihoods $L(s, b, e|N_{\text{on}}, N_{\text{off}}, Z)$ are maximized over b and e, the background counts and efficiency, respectively, eliminating the nuisance parameter Z. The log-likelihoods are used to calculate the profile likelihood function, parameterized by the signal counts. If the s counts are not small, the confidence range is found by varying s until the profile likelihood value has changed by the confidence limit (C.L). For example, if C.L. = 90%, the profile likelihood will change by 2.706 from the minimum point (at the estimator $\hat{s}$). This technique is unbounded by any constraints to the profile likelihood, so it is the default method used when computing the Rolke upper limit.

There are a few cases when the resulting signal counts upper limit is negative – that is nonphysical – which contain a few available strategies to respond. If the s counts is negative on the lower end of the uncertainty range, the s counts lower limit is set to 0. In another strategy, the profile likelihood function has a negative estimator $\hat{s}$, and the upper limit (the estimator plus the C.L. increase in profile likelihood) is also negative. One count is added to

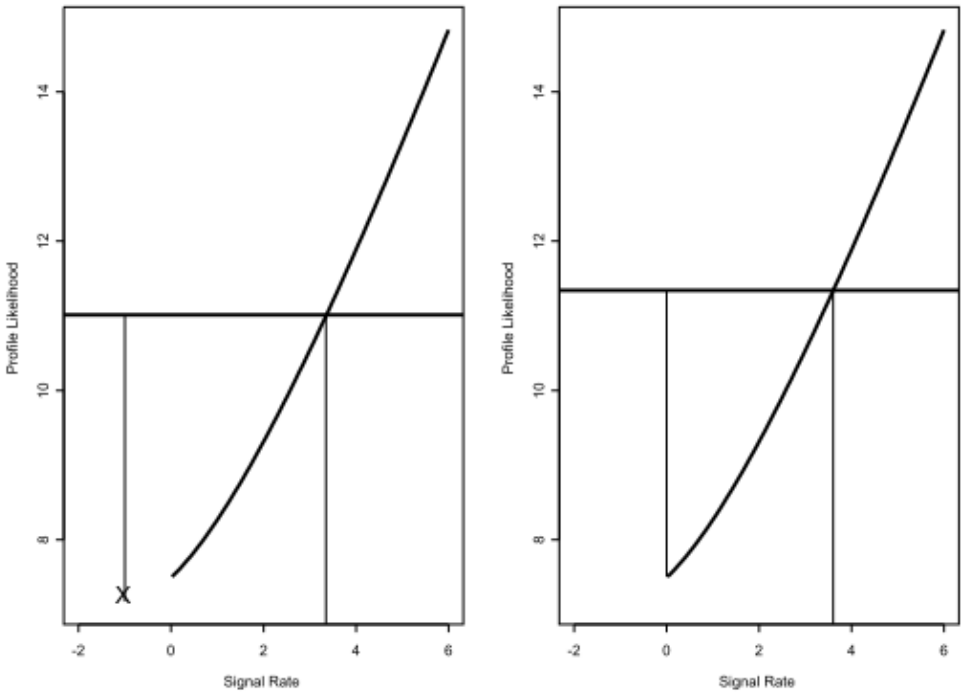

Figure 2: The case $x = 2$, $y = 15$ and $\tau = 5.0$. In the left panel we use the unbounded likelihood method and find a 95% upper limit of 3.35. In the right panel using the bounded likelihood method the 95% upper limit is 3.6.

Figure 2.10: A direct reproduction of a profile likelihood example from Rolke, López, and Conrad [63]. In both cases, the optimal signal rate s is likely below 0 and non-physical, requiring special care.

N_{on} and the profile likelihood function to find the next upper limit recomputed. This addition of one count to N_{on} is repeated until the upper limit is positive. Special care is also needed when $N_{\text{on}} = 0$ and/or $N_{\text{off}} = 0$. The simplest method adds one count to either or both N_{on} and N_{off}, and a linear extrapolation is performed on the profile likelihood to find the upper limit. See figure 2.10 for the profile likelihood example with a negative $\hat{s}$. In the computation of the "bounded" case of the Rolke method within VEGAS, the chosen strategy adds the C.L. to the profile likelihood when s is set to zero.

Feldman & Cousins Instead of using the likelihood ratio to find the confidence region, this method

uses the probability distribution of the true parameter s to find the confidence region with appropriate coverage. It uses an ordering method based on the ratio

$$R = \frac{P(N_{\text{on}}|s)}{P(N_{\text{on}}|s_{\text{best}})}$$
$$P(N_{\text{on}}|s) = \frac{(s+b)^{N_{\text{on}}} e^{-(s+b)^{N_{\text{on}}}}}{N_{\text{on}}!}$$

Cousins, Feldman, and Cousins [67] makes a lookup table for all possible s and N_{on} values, filling in $P(N_{\text{on}}|s)$ and $P(N_{\text{on}}|s_{\text{best}})$ (found by maximizing P by varying s). With the table completed for many s, the procedure then ranks the table by R. The confidence limit is found by summing all $P(N_{\text{on}}|s)$ in order of R until the confidence limit α (e.g. 90%) is reached for the measured b and N_{on}. The largest and smallest s for given N_{on} are the confidence intervals in the table.

Helene The basic assumption of Helene is to pick a probability distribution for the signal counts $P(s)$, then solve directly for the upper limit s.

$$\alpha = \int_s^\infty P(s)ds$$
$$P(s) = \begin{cases} N_1 \frac{(s+b)^{N_{\text{on}}} e^{-(s+b)^{N_{\text{on}}}}}{N_{\text{on}}!} & \text{Poisson s, known b} \\ N_2 \frac{e^{-(s-\hat{s})^2/2N_{\text{on}}}}{\sqrt{2\pi N_{\text{on}}}} & \text{Gaussian s, known b} \\ N_3 \frac{e^{-(s-\hat{s})^2/2\sigma}}{\sqrt{2\pi}\sigma} & \text{Poisson s, Gaussian b} \end{cases}$$

A key nuance: s is never 0, since the first integral is unity (note the normalizations N_1, N_2, N_3, which are set such that $\int_0^\infty P(s)ds = 1$.)

For the gaussian approximation,

$$I(z) = \frac{1}{\sqrt{2\pi}} \int_z^\infty e^{-x^2/2} dx$$
$$\alpha = \frac{I(\frac{s-\hat{s}}{\sigma})}{I(\frac{-\hat{s}}{\sigma})}$$

Out of these three upper limit methods, Rolke is most commonly use within the field due to its reliance on the log-likelihood ratio, as a natural extension of the Li & Ma significance technique [58]. It is also the default method in the VEGAS analysis package, and used throughout this thesis with the bounded method.

Chapter 3: Prototype Schwarzschild-Couder Telescope

3.1 Introduction

The recent observations of gravitational waves and detections of very-high-energy (VHE) neutrinos and gamma rays have expanded the field of multi-messenger astrophysics. To further explore the new sources found by these detectors, which encompass high-energy, transient, point-like or extended sources, improvements are necessary to allow coincident observations by VHE detectors for photons with energies greater than 100 GeV.

The present-day IACTs are based on conventional Davies-Cotton (DC) design of a single parabolic reflector [69]. The Davies-Cotton design is a well-tested design for detecting atmospherical Cherenkov light emissions; however, due to spherical and comatic aberrations the DC design is constrained to the larger pixels using photo-multiplier tubes (PMTs) with limited imaging resolution. These limitations of the DC design constrains the potential of the next-generation world-wide observatory Cherenkov Telescope Array (CTA) [70, 71].

The arrays of imaging atmospheric Cherenkov telescopes (IACTs) indirectly observe VHE photons by stereoscopic imaging of the shower cascades and reconstructing their energy and direction from the ground. Current-generation of small arrays of IACTs use prime-focus optical system (OS) based on the DC or parabolic design, which consists of a single segmented mirror with large aperture (>10 m) and f-stop ($f/\#$) in the range of $1.2 - 1.4$. As an alternative, the fast Schwarzschild-Couder (SCT) OS ($f/0.578$) uses two segmented aplanatic mirrors to achieve the best possible imaging resolution in the CTA core energy range (0.1 TeV - 10 TeV). The focal length of the fast SC OS is 5.586m. These optical improvements enable a high-resolution SiPM camera (see [72]), but require sub-mm and sub-mrad alignment precision.

The SCT OS is designed to fully correct for spherical and comatic aberrations in the full 8

degrees field of view (FoV). Astigmatism dominates the PSF at the edge of the FoV and it is minimized by implementing a curved focal plane. The choice of a two-mirror design with a de-magnifying secondary mirror reduces the focal plane (FP) plate scale to provide compatibility with the SiPM detectors [73]. The full camera has 11 328 pixels, a factor of 6 more than cameras in DC-based medium-sized telescope designs.

Located at the Fred Lawrence Whipple Observatory in Southern Arizona, the construction of the prototype SCT (pSCT) started in late 2015 at the old site of the VERITAS T1 telescope. The optical support structure (OSS) was built by August 2016. The mirrors and camera were assembled and installed by August 2018; however the current installation contains only the central backplane, consisting of 24 camera modules (rather than the full 11 328 pixels). The telescope was inaugurated and entered commissioning in January 2019. Important technical advances were made during this time period, as reported by [74–77], with many of those results represented here.

To achieve the point spread function (PSF) of the OS in the FoV compatible with the SiPM pixel size (6 mm), sub-mm and sub-mrad alignment is required [79]. The pSCT has achieved an on-axis PSF within the design goal 2.6′, allowing it to detect the Crab Nebula in 2020 [78]. The commissioning work to achieve that milestone, and the more recent activity toward global and off-axis alignment, is described in detail in this chapter.

3.2 Optical System Hardware

The SCT is a novel dual mirror optical design. The prototype SCT is built on top of the MST optical support tower with a modified counterweight to contain the larger optical support structure (OSS) needed for two mirrors. Nearby are two support trailers, a maintenance shed and a carport for protecting the camera chiller system. Within the main support trailer, the power, ethernet and optical fiber cables routed from the telescope via underground trenches meet the main computer stack, containing the alignment computer (`cta.alignment`), camera computer (`cta.camera`), database computer (`cta.database`) and network switches. Also present is the main control room containing 8 monitors and two desktop computers (`cta.sct01` and

Figure 3.1: The prototype Schwarzschild-Couder Telescope in Arizona, US [78].

`cta.sct02`) for observers.

The optical system is the largest system of the prototype SCT, containing the largest size and number of components. In this two-mirror design, each mirror is segmented into manageable sizes (approximately 1 m^2 per panel) that are identified based on their position on the telescope. Figure 3.2 describes the naming convention and shows the segmentation design of all panels. In the lower panel of Figure 3.2, a CAD diagram of the SCT shows the relative location of panel types P1, P2, S1 and S2, which refer to the primary (P) and secondary (S) inner (1) or outer (2) panel rings. The primary mirror contains 48 panels: 16 inner P1 panels and 32 outer P2 panels. The secondary mirror contains 24 panels: 8 inner S1 panels and 16 outer S2 panels. The panel types and panel numbers will be used extensively in this work. A complete list of the telescope properties is given in Table D.1.

3.2.1 Mirror Panel Module

Each panel contains the optical surface coated with Al/Cr/SiO_2/HfO_2/SiO_2 slumped in a specific radius for that panel type. The panel sits on a hexapod providing it with 6 degrees of freedom, which is controlled by an onboard mirror panel control board (MPCB) [80]. The MPCB is a custom controller that centralizes the devices on the panel: 6 actuators, 4-5 mirror panel edge sensors (MPES), internal and external temperature sensors. The term “panel" will be used liberally in this work to refer to either the optical surface responsible for star projected on the focal plane during the optical alignment work, or the entire self-contained unit with positional control. The grouping made by the mirror panel, actuators, MPES, MPCB and mounting triangle is called the mirror panel module (MPM). Figure 3.3 shows various components of the MPM during the construction and calibration.

The panel is fixed to the hexapod at three precisely machined pads, which are installed during the mirror slumping process with specially designed jigs so that the optical surface and pads are positioned in tandem for highest alignment. Aluminum joints machined to high precision are connected to both the pads on the panel and the mounting triangle, shown in Figure 3.3. Each of

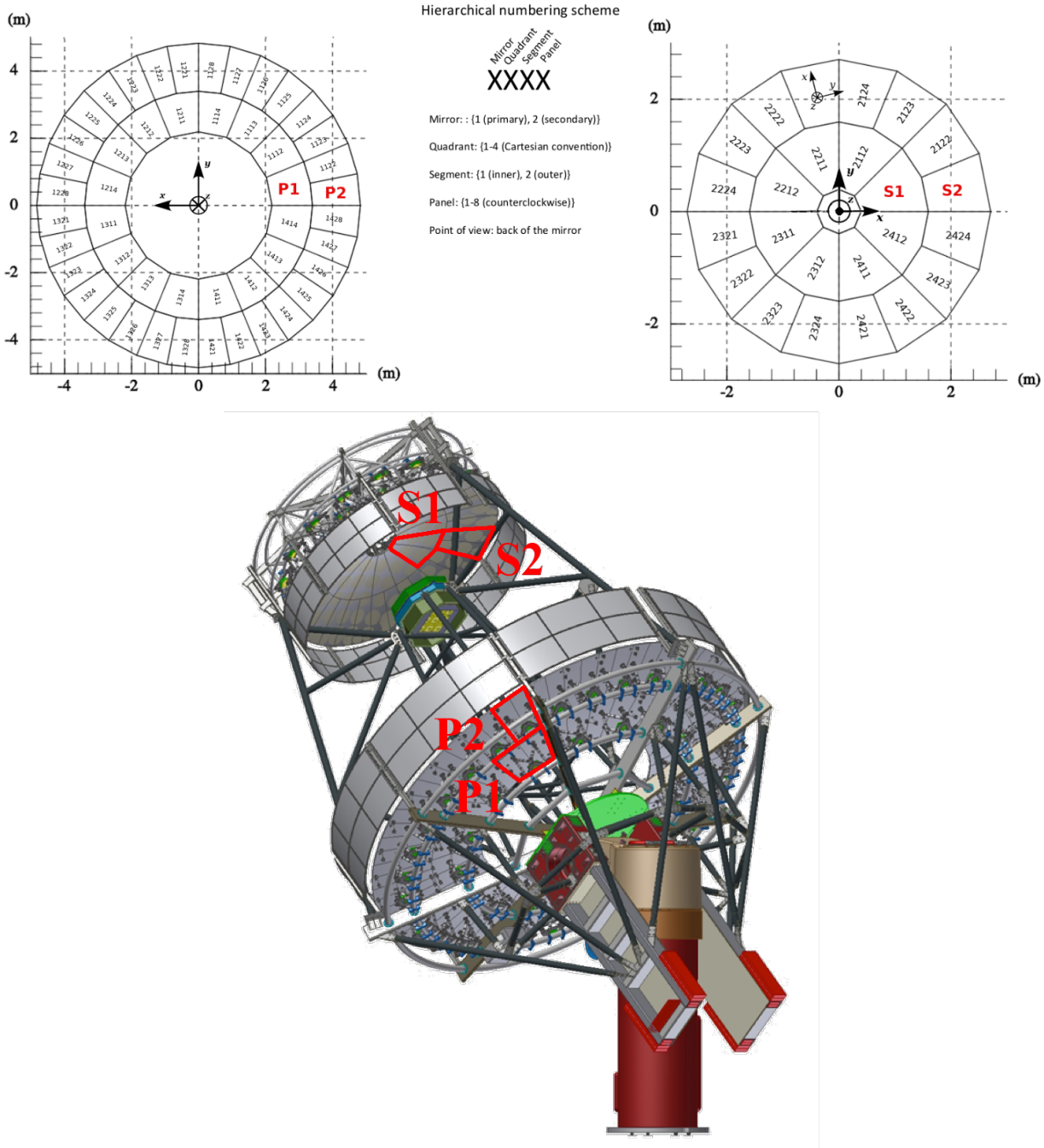

Figure 3.2: Top: mapping and naming convention for each panel on primary mirror (left) and secondary mirror (right). Each panel is named based on position, given by mirror, quadrant, segment and panel. Telescope reference frame (TRF) is denoted in the center of primary mirror diagram (left), and panel reference frame PRF is denoted on panel 2221 on secondary mirror diagram (right). Panel segments P1, P2, S1 and S2 is traced onto the CAD diagram of the SCT. Figure from [77].

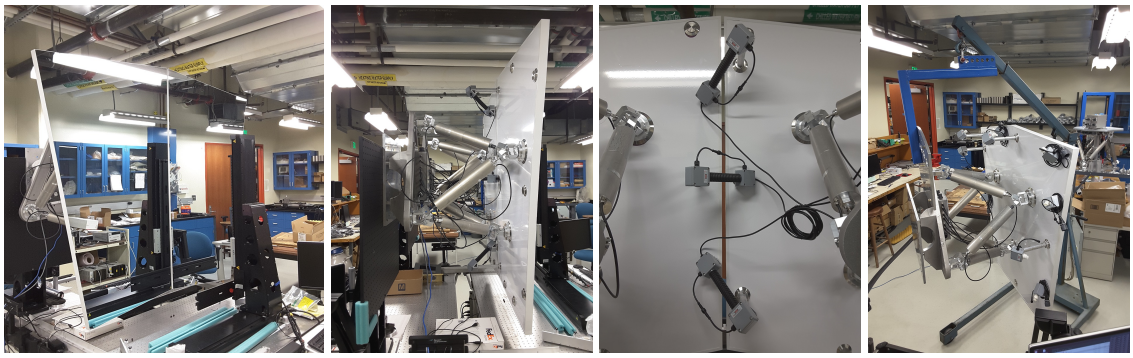

Figure 3.3: Photographs taken at the UCLA VHE Laboratory during the MPM integration tests. *Far left:* Front view of two P1 MPMs installed onto the calibration set up, facing a coordinate measuring machine. *Center left:* Lateral view of the same pair of P1 MPMs, showing the Stewart platform and attachment triangle. *Center right:* Orthogonal triad of MPESs interfacing the two P1 MPMs. *Far right:* Complete P1 MPM attached to a lifting fixture. Figure from [76].

the six actuators are attached in between, forming the hexapod system. These linear actuators have 3 µm control, which translates to 5 µm and 3″ precision to the panel physical position. The actuator has a 70 mm range. The motion is controlled by an encoder, which records up to 200 micro steps at a time and must be written to a file and the database. The platforms are installed on the OSS with up to 10 mm and 1° precision. The hexapod provides the panel control of 6 degrees of freedom. Section 3.3.3 describes the equations for the underlying software for panel control.

3.2.2 MPES

The mirror panel edge sensor (MPES) is designed to measure the relative alignment between panels and to be used for any instantaneous alignment activity. A sensor spans the gap between two panels, with one side containing a laser and the other a webcam. The laser side is on a post, which enables a 45° tilt to the camera field of view, shown in Figure 3.4. This structure, coupled with the orthogonal positioning of multiple sensors along the edge, allow the sensors to measure the misalignment along the multiple degrees of freedom for that edge. For example, with two adjacent panels there are 6 degrees of freedom from each set of actuators, and up to 3 MPES in between them. Assuming one panel is fixed, the number of degrees of freedom reduces to 6 and the sensors must provide at least 6 constraints, which is covered by the three MPES units between them. The

MPES data are the x-y coordinates captured by the webcam which give two degrees of freedom per sensor. Additionally, image quality properties are recorded like total intensity, number of saturated pixels, spot width and error along each axis.

Throughout the design of various panels (P1, P2, S1 and S2), either 8 or 10 MPES units are affiliated with each panel, in an arrangement shown in Figure 3.5 for the secondary mirror (MPES units on the primary mirror are arranged in a similar way). The total number of degrees of freedom per mirror given by the number of actuators is greater than the number of constraints given by the MPES measurements, so the panel misalignment parameter is over-determined when attempting to find the actuator motion given measured MPES alignment offsets (see Section 3.3.2 for details). This provides a redundancy in case of missing or malfunctioning sensors. Due to the installation of OSS support wedges onto the secondary mirror at the base of each of the three main support beams, three MPES units were deactivated because of the physical interference between the wedge and the MPES unit.

The calibration of the MPM includes a recording of the ideal MPES coordinates in the lab position. Figure 3.3 shows a few steps of this calibration procedure. Using a coordinate measuring device, the position of three reference points for two adjacent mirror optical surfaces are measured. Using these coordinates and the known spatial function of the optical surfaces, the two panels are positioned to form the ideal optical surface (Figure 3.3 left and center left).

Once the panels are set to form the correct optical surface, the MPES units for the edge in between these two panels are installed and activated (Figure 3.3 center right). At this setting, the coordinates from all sensors are read out and recorded - these coordinates become the reference coordinates for the lab aligned state. An exploration of this lab aligned state in Section 3.4.1 shows that unknown systematic bias in the lab is introduced and leads to a globally unaligned state (see Figure 3.16 for the outcome). However, this state is useful for positioning all panels within alignment distance. A more sophisticated alignment process can be used to record new reference coordinates for each MPES unit.

While in the aligned state, the panel is also calibrated to measure the relationship between

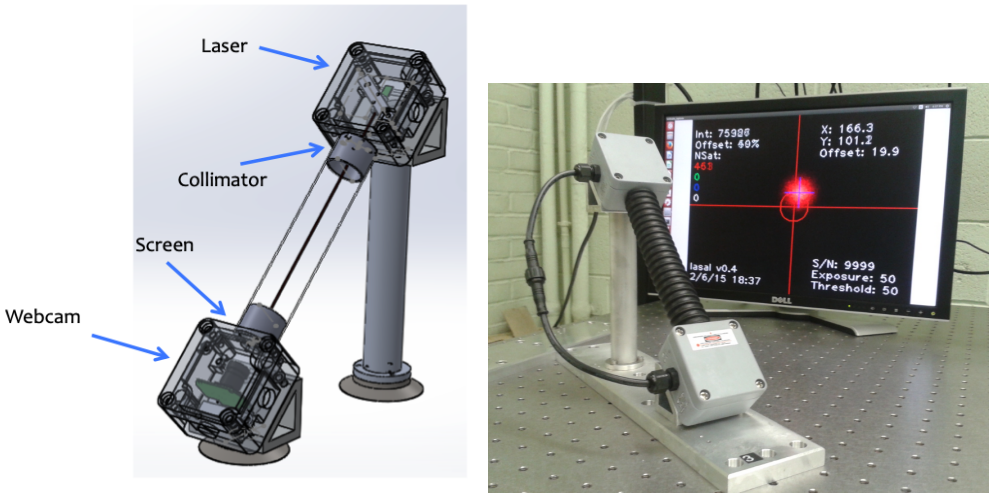

Figure 3.4: *Left)* CAD diagram of MPES unit. The functional components are highlighted, which are the webcam, screen, collimator and laser. Not pictured is the connecting tube between the laser and webcam side.*Right)* Picture of a connected and working MPES unit with tube attached. Behind is a stream of the webcam with laser positioned near the center of the field of view. The MPES tube is pictured, which is made of rubber and wire coil for structural stability. Figure from [75].

actuator motion and MPES coordinate translations. Each actuator is moved by 1 mm and the MPES coordinates are read and recorded, for all MPES on the edge and for all 6 actuators on each panel. This data forms the response matrix for the edge. Due to the linear approximation imposed on this system, small actuator motions have more predictable MPES coordinate translations. This means that MPES-based alignment is best achieved iteratively for decreasing alignment offsets.

3.2.3 Global Alignment System

In principle, the mirrors could be aligned once using some sophisticated strategy and left that way in perpetuity. However, this immediately fails since the varying gravitational load of the optical support structure deforms the telescope while moving throughout an observation, changing the relative position and orientation between every panel and destroying the original alignment. Similarly, the temperature variation imparts thermal expansion that will also non-negligibly alter the alignment. These perturbations can be monitored with additional devices that monitor the distance between mirrors and angles between them. The global alignment system (GAS) consists of these

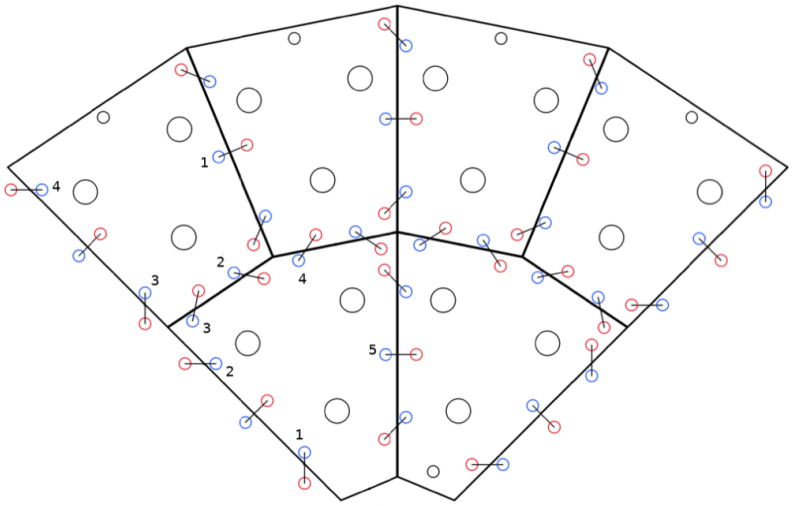

Figure 3.5: Diagram of MPES and pad layout on a secondary mirror sector consisting of 6 panels. Blue circles are the webcam side and connected red circles are the laser side of the MPES units. Larger black circles indicate the pad position connecting the panel to the Stewart platform. The number next to blue circles indicate the position of each MPES on that panel. The primary mirror layout is analogous to this set up. Figure from [74].

devices, in addition to more devices that support the alignment process and the maintenance of the alignment. Figure 3.6 is a diagram of all the devices that make up the GAS. Many of the devices are installed on the optical tables on either the primary or secondary mirror, as identified on Figure 3.7.

A selection of three panels evenly spaced on the primary and secondary mirrors are tracked for their morphology over time. These six P2 and S2 panels are nearly evenly spaced, but are selected to be visible from the optical table on the opposite mirror (see Figures 3.8 and 3.9). Each panel has a set of precisely measured LEDs along their edges that is seen by its corresponding CCD camera on the optical table. The picture taken by the CCD is analyzed for the coordinates of each of the LEDs, which is used to calculate the position and normal vector of the plane of the optical surface. By saving the coordinates of the plane of the panel over time, it is possible to monitor the structural deformation of the telescope during observation by understanding the perturbation on the coordinates of all the GAS panels.

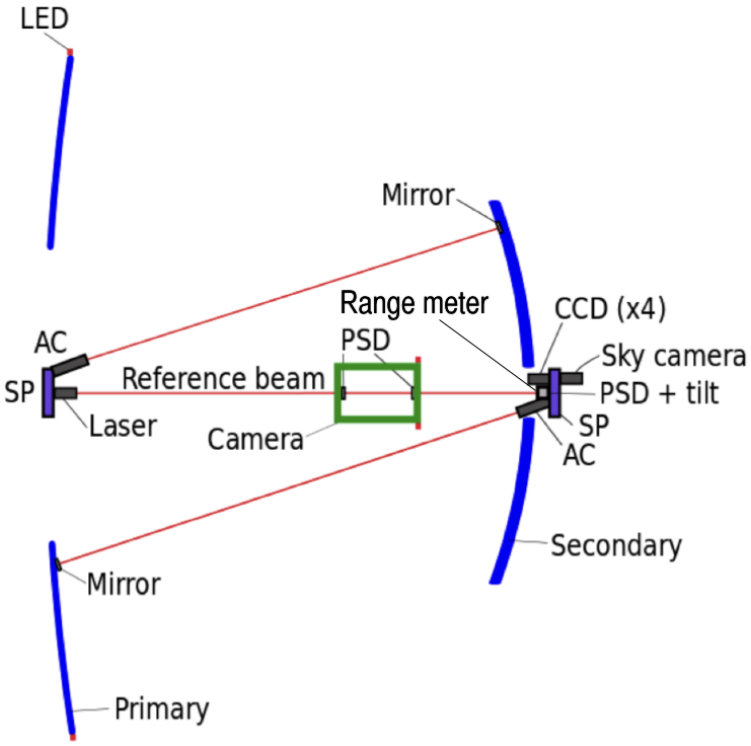

Figure 3.6: Diagram of global alignment system (GAS). Figure from [74].

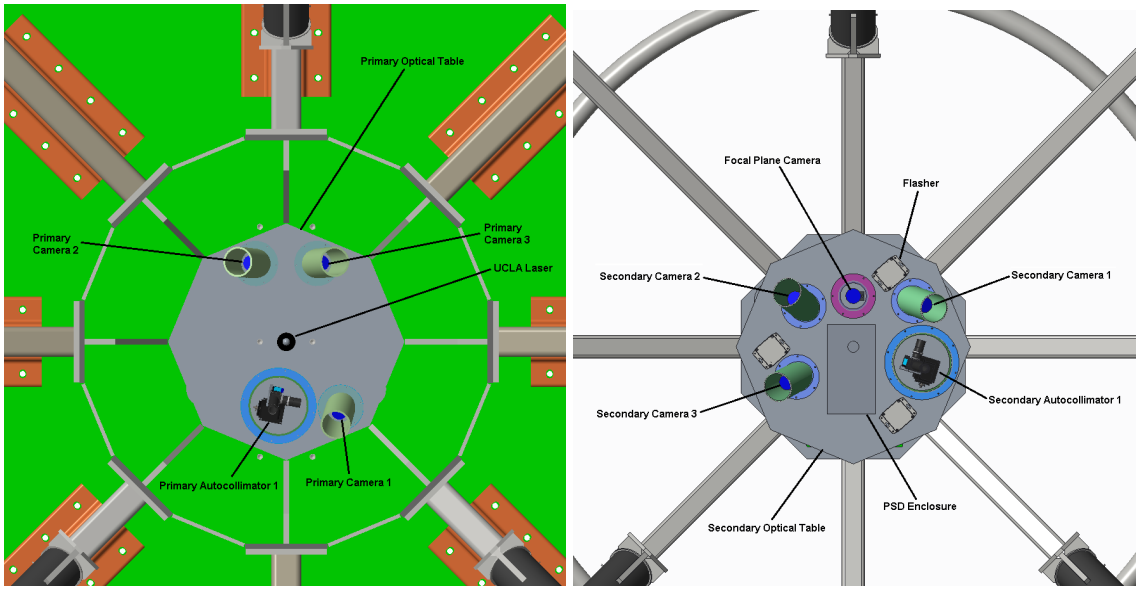

Figure 3.7: Diagram of primary (left) and secondary (right) optical tables. The cameras point to specific targets on the opposite mirror, such as panels or the focal plane. The autocollimator points to a target mirror on the opposite mirror. The position sensitive device (PSD) is semi transparent to the UCLA laser that also passes through the PSD inside the gamma-ray camera.

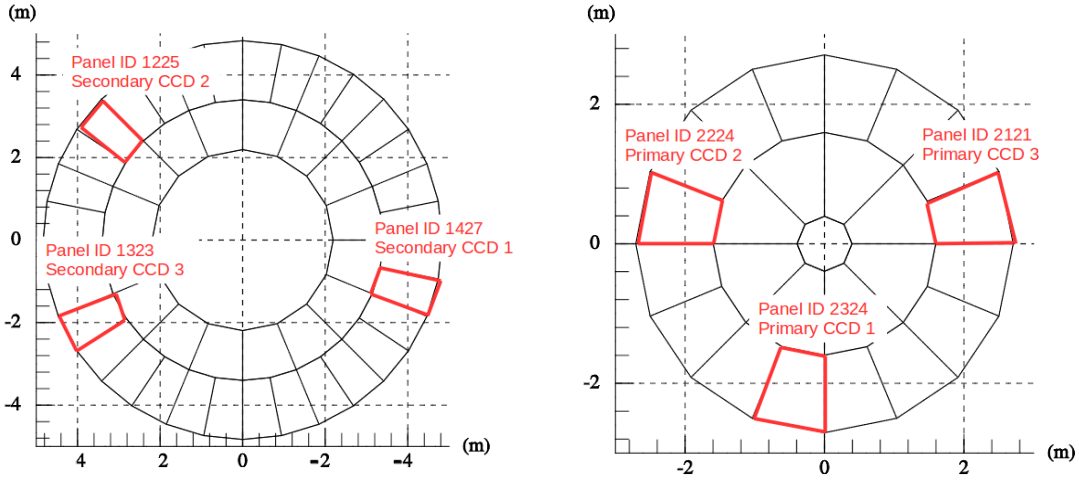

Figure 3.8: Position of the six GAS-LED panels. Each panel is paired to a CCD on the opposite optical table.

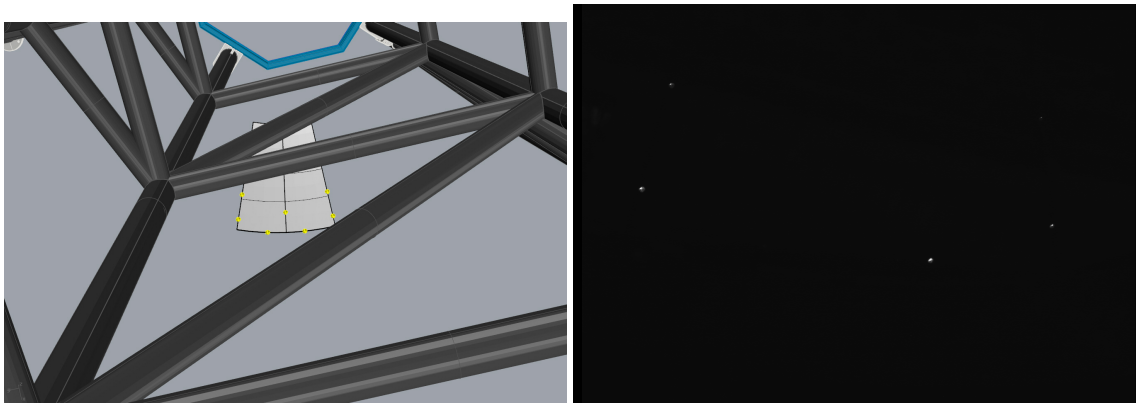

Figure 3.9: CAD drawing of panel 2324 (left) with yellow LEDs, as seen by the primary CCD 1. Telescope optical support structure is visible in CAD. Five of the six LEDs are visible in this picture.

In various alignment campaigns through 2019-2022, the GAS LED and CCD system was slowly commissioned in parallel with other alignment activities. This consisted of software development to implement the image analysis and CCD API into the client program, which had major compatibility challenges to overcome. Once installed, all six CCDs were activated and tuned to detect all the LEDs. The LEDs are focused by optical fibers passing through a 3-D printed holder, some of which were damaged over time by sunlight, weather and heat. These strings were fixed on a later trip and detected by the CCDs. Figure 3.9 shows the CAD drawing and nighttime picture of the primary GAS-CCD 1 pointed to panel 2324 on the secondary. They are yet to be used for data-taking to understand the telescope deformation, but will be used in a future campaign.

This CCD and LED pairing strategy is also used with the gamma-ray camera, which has 8 LEDs on its focal plane and a CCD camera fixed to the secondary optical table. Once commissioned, it will calculate and monitor the coordinates of the focal plane over time just like the GAS-LED panels. This set of devices were slightly modified with the development of the optical alignment strategy. By changing the optical lens on the focal plane CCD, it became possible to focus on a smaller area centered within the focal plane of the gamma-ray camera that would be used to project images of focused light. In this area, a white board is placed to help image the spots of the focused light. This setup is then used in the optical alignment strategy described in detail in Sections 3.4.3, 3.4.4, 3.4.5, 3.4.6, 3.4.7 and 3.4.8. The CCD optical lens will be replaced at a later stage of the optical alignment campaign to the original lens so that it can find the focal plane LEDs.

For the off-axis alignment campaign, a larger board will be used that extends the region for tracked stars to be projected on the focal plane. This board is machined precisely to mimic the curvature of the focal plane.

A key component to maintaining the alignment between the three primary parts of the optical system (primary mirror, secondary mirror, and gamma-ray camera) is the reference beam defining the optical axis. This beam is a laser fixed to the primary optical table that is bright enough to pass through the entire optical system. At the gamma-ray camera and secondary optical table are position sensitive devices (PSD) which measure 2-D coordinates (x and y) of the beam passing

through it. If the entire optical system is aligned, this beam will pass through both sets of PSDs, and define the center of the gamma-ray camera. Each PSD has two frames, so the combined set can be used to calculate the angle of the beam normal to the PSD frame. The laser and PSDs were commissioned and software was developed to implement into the client. The optical tables were calibrated to relate each table's position to the laser coordinate on the PSD, creating a response matrix that will be used to maintain the alignment of the entire system.

Two remaining devices measure the relative position between the primary and secondary mirrors. The autocollimator (AC) on each optical table are laser/camera pairs that point to a small target mirror on each structure. The light beam from the AC reflects on the target mirror, and if aligned correctly, points back into the AC's camera. This enables the alignment between the pair to make sure each beam is always visible. These set of devices are yet to be commissioned at this time.

The range meter on the secondary optical table measures the distance to two targets: a point on the primary mirror structure, or the center of the focal plane. It was used extensively to record the best measurement of the focal plane distance to the secondary mirror (see section 3.4.3 and 3.4.8 for full description of how that was measured).

Finally, the sky camera device on the other end of the secondary optical table will point outward along the pointing direction of the telescope. This camera is operated by an external program that streams a live feed of the stars in the sky in the field of view, calculating the exact coordinates at the center of the camera. This calculated coordinate should be parallel with the optical axis of the telescope, which should also match the telescope pointing direction derived from the telescope's tracking system. Any offset between the tracking system and sky camera is recorded and used during the offline analysis of the gamma-ray data.

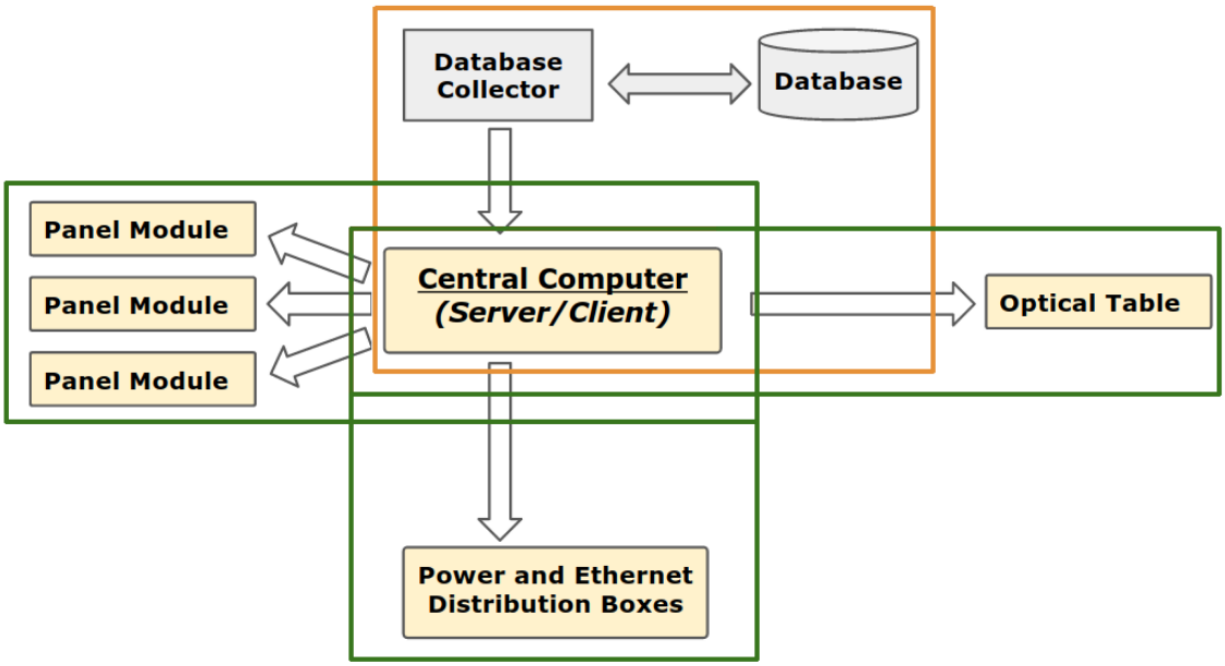

Figure 3.10: Overall software components and database communication. Adapted from [55].

3.3 Optical System Software

3.3.1 OPC-ua Architecture

To accommodate the many hardware and software requirements of the SCT, in addition to the CTA software requirements for observatory level standardization, the industry standard `OPC-ua` protocol with `C++` is used. This protocol enables direct hardware implementation with the appropriate API, while also providing the network communication framework between server and client objects. The overall software strategy is described in Figure 3.10, which shows the client, server and database components.

Each panel contains an instance of the server object, which controls the hardware described in section 3.2, primarily the actuators, MPES and temperature sensors. The optical tables (OT) are functionally identical to the panel; however MPES units are replaced by various GAS devices described in section 3.2.3, depending on whether it is a primary OT or secondary OT. The servers measure data directly from the hardware and control the mechanical components, but in turn these

commands are managed and fired by a central client computer. Up to 74 server objects are simultaneously active (72 panels and 2 OTs), each with a statically defined IP address in the SCT namespace that is mapped to that panel and saved in the database.

The client object is a single program running on the alignment machine (`cta.alignment`) in the SCT trailer, with which the observers and technicians primarily interact. Alignment commands concerning one or multiple devices are organized by the client and sent by the `OPC-ua` protocol to the intended devices. This interaction layer bypasses any hardware specific needs since the hardware implementation is at the server level and provided by the hardware API, while the client only needs to communicate with the `OPC-ua` controllers. This strategy enables the ease of replacement of hardware with minimal software disruption to the entire system.

Both the server and client objects interact with the database, also located at the SCT trailer on a separate machine (`cta.database`). This database contains all hardware data for configuration, calibration and mapping, in addition to lookup tables and status updates from several devices. All servers and the client connects to the database with the `MySQL C++ Connector`[1], with connections created and destroyed as needed. Most connections are made during hardware startup, when configuration parameters are queried and loaded. This database also contains the various tables needed for the performance of the SCT camera, which are not discussed here.

The specific software diagram relating all devices in the optical system are described in Figure 3.11. The `OPC-ua` protocol allows the creation of a hierarchical structure, which is used to identify parent-child relationships between various controllers shown in Figure 3.11. Each controller may be either a direct software implementation of a hardware device, or a composite device. Composite devices are abstractions of human-understandable systems which have specific needs such as properties, data entries, and unique methods, but are made of multiple hardware devices. “Edges" are clear examples since they are made up of two adjacent panels, the MPES units between them, and have unique methods such as `AlignEdge` or `FindMatrix`. Hardware controllers are simpler since they map directly to the API for that device and have well defined purpose and scope.

[1] https://dev.mysql.com/doc/connector-cpp/8.0/en/

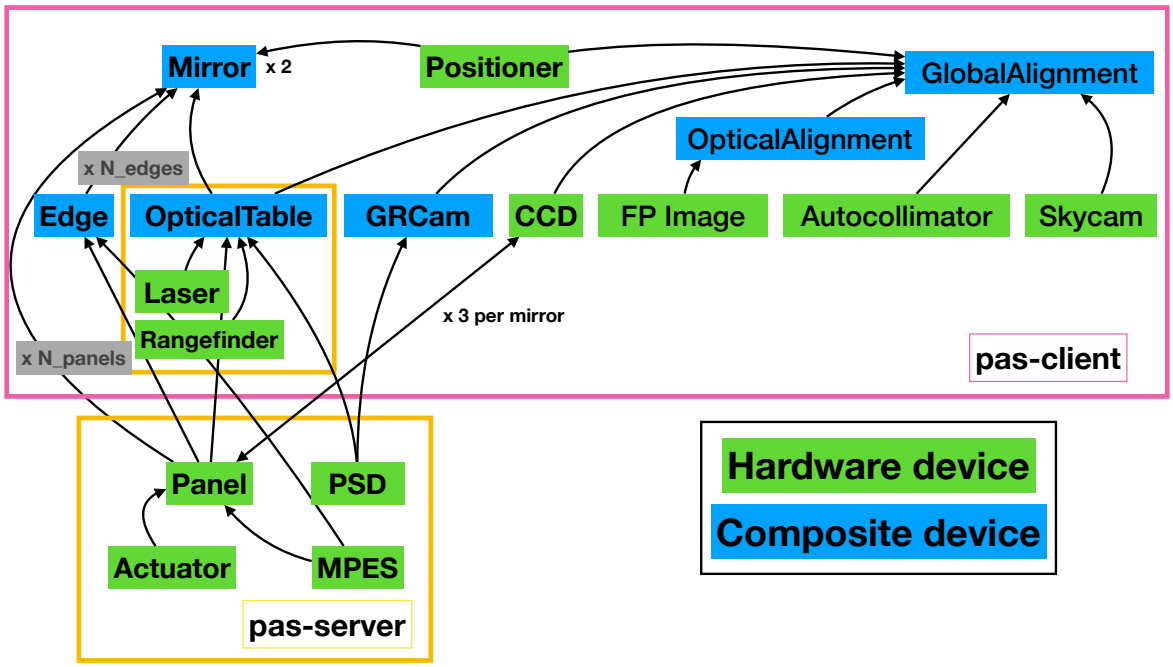

Figure 3.11: Controller diagram.

A full technical diagram of both the server and client software objects are reviewed in Appendix D.2. All methods and properties for each device are also enumerated.

The software was designed and implemented in multiple stages. During the first stage, in parallel with the original mirror calibration work, the basic panel motions, edge alignment and MPES reading was developed. Once the panels were installed and the initial alignment was achieved, improved methods were developed to align more edges and panels together, and to improve full mirror control.

Most of the controllers in Figure 3.11 were added after this stage during the initial development of the global alignment system. At this current time, the autocollimator and skycam devices are not yet fully implemented into the alignment process. Commissioning has begun on the laser, rangefinder and PSD devices, although not all are yet part of the full alignment process while the optical alignment work continues (described in sections 3.4.3, 3.4.4, 3.4.5, 3.4.6, 3.4.7 and 3.4.8). An extensive database of alignment states is being measured and recorded from the optical alignment process. This database of states will replace the tedious and time-costly process of

star-tracking-based alignment, by providing the panels with internal measurements (either actuator lengths or MPES nominal coordinates) that can be loaded quickly to achieve alignment.

Some software limitations were found during testing and on-site implementation. In one major issue, the number of servers that a single client could connect to was limited to 24, which is significantly less than the number of panel servers in the system (72 panels and 2 OTs). This issue was resolved by creating 4 intermediate clients that funneled its data to a top level client, allowing up to 96 available server connections. A second major resolution came with the proper implementation of multi-threading, which was made possible by creating a device `State` class (`On`/`Off`/`Busy`/`Error`) that could be checked while asynchronous calls were made to the system. This device class is implemented throughout, so that parallel processing calls (such as `Move` or `Read` methods to all devices) cycle through available devices until they have all been controlled.

Many other issues were resolved by staging the development inside a docker container that simulated the network of servers in the telescope within a single test computer. This sandbox environment permitted destructive actions such as panel motions or database calls in safe virtual space so that bugs could be found and internal logic could be tested, without moving any actual panels on the telescope or altering real database records. The development of this docker container also enables the future creation of a full simulation of the telescope, where any activity could be tested and passed into an optical ray-tracing program to evaluate the impact of the optical PSF. This work is in progress.

3.3.2 Alignment Parameter Minimization

The main computation within the client software is the fitting of the panel positions toward an alignment state. Measurements from the MPES units, along with nominal MPES coordinates from an aligned state, are used to align adjacent panels by moving the panel actuators and minimizing the difference between the MPES measurements and nominal coordinates.

The panel's misalignment parameter is $\chi^2_m = \chi^2_{m,\mathrm{MPES}} + w_{GAS}\chi^2_{m,\mathrm{GAS}}$, where $\chi^2_{m,\mathrm{MPES}}$ is its misalignment coming from MPES readings, $\chi^2_{m,\mathrm{GAS}}$ comes from global misalignment, and w_{GAS} is

a weight that treats global misalignment more or less stringently than panel-to-panel misalignment. This can be written in simplified notation as minimizing

$$\sum_m \chi^2 = \sum_m \left[\sum_{\text{MPES}} \left(\delta\vec{\sigma}_m(\text{MPES}) + \hat{R}_m \delta\vec{L}_m \right)^2 + w_{\text{GAS}} \sum_{\text{GAS}} \left(\delta\vec{\sigma}_m(\text{GAS}) + \hat{M}_m \delta\vec{L}_m \right)^2 \right] \tag{3.1}$$

Here, for a given panel m, $\delta\vec{\sigma}_m$ are its positional readings coming from the MPES or the global alignment system; $\delta\vec{L}_m$ are the actuator displacements that bring it to its nominal position; $\hat{R}_m$ and $\hat{M}_m$ are the actuator response matrices that connect positional readings with physical motions of actuators. A straightforward inversion of this combined misalignment parameter matrix can be done with linear algebra, primarily by solving the single value decomposition (SVD). Even with some hardware failing, χ^2 can still be minimized to a satisfactorily small value because of the large number of MPES units and degrees of freedom in the system. The weight parameter is still to be explored, and may be tuned after experimentation on site. Since the alignment software is multi-threaded, collecting sensor data $\delta\vec{\sigma}_m$ and requesting actuator movements by necessary displacements $\delta\vec{L}_m$ is done simultaneously for each individual panel.

More precisely, since the alignment of panels using the MPES units are so fundamental to the future alignment of optical system (that is, without the optical alignment strategy of star tracking and tedious star defocusing described in sections starting in 3.4.3), it is worth expanding the misalignment parameter explicitly. Let j and k denote two neighboring panels with arbitrary lengths of actuators $\vec{L}_j$ and $\vec{L}_k$, respectively. The measurement of the MPES coordinates along this edge form the vector $\vec{\sigma}_{j,k}$. The response matrix is defined as $R_{j,k} = \delta\vec{\sigma}_{j,k}/\delta\vec{L}_k$, so that it transforms small displacements of the actuators $\delta\vec{L}_k$ of a panel k to the corresponding changes of the MPES readings for the edge between panels j and k, i.e., $\delta\vec{\sigma}_{j,k} = R_{j,k}\delta\vec{L}_k$.

The nominal MPES coordinates are $\vec{\sigma}^{\text{ref}}_{j,k}$ for a given aligned state, whether measured in the laboratory or from the optical alignment work. This reference data then forms the relative misalignment of an edge as the difference between the reference and actual MPES coordinates $\Delta\vec{\sigma}_{j,k} = \vec{\sigma}^{\text{ref}}_{j,k} - \vec{\sigma}_{j,k}$. The remaining computation for the panel-to-panel alignment then becomes finding a

set of $\delta\vec{L}_k$, which defines the motions for all panels k that lead to ideal alignment $\Delta\vec{\sigma}_{j,k} = 0$ for all panels j, k.

Before the panels were installed onto the OSS of the SCT, every edge between two adjacent panels was aligned on an optical table in the lab with the help of a coordinate measuring machine. Then the MPES units for each aligned edge were installed, and the reference MPES coordinates $\vec{\sigma}^{\text{ref}}_{j,k}$ were recorded. Finally, the response matrix $R_{j,k}$ (and $R_{k,j}$) was measured by extending and retracting each actuator for panel k (and j) and recording the change in MPES readings $\delta\vec{\sigma}_{j,k}$. Additional $\vec{\sigma}^{\text{ref}}_{j,k}$ are also measured for aligned states derived from the optical alignment work.

The alignment of a sector of an arbitrary number of panels (denoted as Ω), is formulated as follows:

$$\left[\sum_m R_{m,k}\delta\vec{L}_k\right]_{k\in\Omega} = [\Delta\vec{\sigma}_{j,k}]_{j,k\in\Omega}, \tag{3.2}$$

where the summation index m represents the neighbors of panel k. One arbitrary panel, e.g., l, in the sector is fixed so that $\delta\vec{L}_l = 0$, as the extra constraints.

After actuator motion vectors $\delta\vec{L}_k$ in Equation 3.2 are solved for selected panels $k \in \Omega$, one can move the panels accordingly to align the edges, and read the MPES units to verify $\Delta\vec{\sigma}_{j,k} = 0$ for all edges $\forall j, k \in \Omega$.

The math described above is implemented within the Edge and Mirror controllers. These are the main controllers used to move panels based on the MPES reading. Within the Mirror controller, the `AlignSector` is a primary method used with an arbitrary number of panels and external MPES units to align that sector.

3.3.3 Mirror Control

The second main computation in the optical software is the transformation between actuator lengths on each panel to global mirror coordinates. The six linear actuators on a panel are arranged to form a 3D stewart platform, or hexapod [80]. On one end, one pair of actuators are attached to a joint on the triangle below, and at the other end to two separate joints below the optical surface pad joints. A CAD drawing of this arrangement is shown in Figure 3.12.

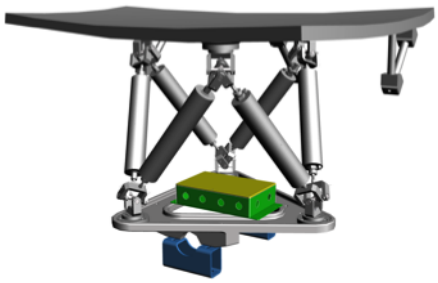

Figure 3.12: A CAD drawing of a single panel. The six linear actuators connect the three triangle pad joints to the three panel pad joints in an arrangement to form a 3D hexapod. A yellow and green control board sits above the triangle, and the blue optical support structure brackets are connected below with long bolts. A single MPES unit is included on the top right for reference. Figure from [77].

Given that every panel is constructed the same way, a straightforward calculation is used. Both sets of pad coordinates are measured to high precision, so it is possible to find the panel normal vector given the six actuator lengths. The circle that contains the three coordinates of the optical surface pad positions is calculated (which has radius 320 mm), so that the center of that circle is the position of the panel normal vector and the plane of that circle is the plane of the panel. This vector is calculated by minimizing the position parameter,

$$\chi^2(\vec{a}) = \sum_{i=0}^{6} \left[\left(\vec{P}_i(\vec{t}, \vec{\xi}) - \vec{B}_i \right)^2 - l_i^2 \right] \tag{3.3}$$

where the panel physical coordinates $\vec{a} = (x, y, z, R_x, R_y, R_z)$, the panel pad coordinate $\vec{P}_i(\vec{t}, \vec{\xi})$ for position $\vec{t}$ and orientation $\vec{\xi}$, triangle pad positions $\vec{B}_i$ and actuator lengths l_i, over all six actuators. The resulting panel coordinate vector $\vec{a}$ relates to the actuator lengths l_i. An extensive derivation of the hexapod geometry and coordinate transformations are described in [55]. The resulting panel physical coordinates $\vec{a}$ describe the panel's normal vector, are in the reference frame of the panel's triangle and may be computed for either primary or secondary mirror panels. These coordinates may then be transformed in to the telescope reference frame.

Naturally, it follows that the construction of multiple panel coordinates in a 3D space form a mirror surface. The coordinate system and panel identification was shown in Figure 3.2. The

ideal surface, the Schwarzschild-Couder solution, is calculated by the optical ray tracing library ROBAST [81, 82], based on the mirror properties described in Table D.1. This library is built into the alignment client software.

Given a panel's pad coordinates $\vec{P}_n^w$ ($\vec{P}_i(\vec{t},\vec{\xi})$ above), where n = MQSP is the mirror, quadrant, segment, panel identifier of the panel and w = P1, P2, S1, S2 is the type of the panel, the transformed coordinates in telescope reference frame is

$$\vec{r}_n^w = R_z(\phi_n^w)\left(\vec{T}^w + R_y(\theta^w)\vec{P}_n^w\right) \tag{3.4}$$

where $R_z(\phi_n^w)$ is the rotation matrix in the telescope z-axis for angle ϕ_n^w, $R_y(\theta^w)$ is the rotation matrix in the telescope y-axis for angle θ^w, and $\vec{T}^w$ is the translation to the telescope reference frame, each for that specific panel w. The angle ϕ_n^w is the angle between the x-axis of the telescope reference frame and the projection of the x-axis of the panel reference frame onto the x-y plane of the telescope reference, while the angle θ^w is the angle between the z axes of the telescope and panel reference frames. Each panel in Figure 3.4 has a different rotation to define its position.

These coordinate transformations are straight-forward to apply to the panel object within the mirror class in the client software, which enables mirror-level control. To move a panel or sector of panels by translation T and rotation R, a set of transformations are applied. First, the panel's starting actuator lengths are transformed to panel coordinates. These coordinates are transformed to telescope reference frame $\vec{r}_n^w$ via equation 3.4. These are the coordinates that are operated on by the intended T and R transformations. With the new coordinates in the telescope reference frame, the reverse transformation is applied to return to panel reference frame, and the new actuator lengths are calculated. This routine has been successfully tested in the field to first order, but precision is limited due to the assumption of linearity on a non-linear system. A full treatment of the coordinate transformation is derived in [55].

3.3.4 Focal Plane Software

In the optical alignment work, the optical light passing through the optical system while the telescope is tracking a planet or star is projected onto the focal plane. This projection forms an image that is necessary to analyze in order to understand the optical system. A second package was developed to make images of this spot projection on the focal plane and analyze the image for various properties.

This image analysis package, named `focal_plane`, is written in python and uses the following libraries: `numpy, matplotlib, astropy, pandas` and `SourceExtractor` (imported as `sewpy)`. The main underlying library, `SourceExtractor`, a well-tested program used in astronomy, is written to efficiently analyze star field images to identify all stars in a picture, their brightness and higher order moments, and the field background [83]. In the optical alignment work, specific patterns of images are created on the focal plane that correspond to specific alignment states, and each image can be attributed to a given panel pair in the optical system.

A main component of the image analysis package is to identify the star image and its associated panel in the picture, then report all the relevant properties for further analysis. In the simplest case, one image on the picture is identified and its coordinates are reported, then the associated panel is moved and the new image coordinates are reported – this outcome can be used to help identify panels on a crowded field, or determine the exact relation between 3D panel motion and 2D image position on the image. This software is capable of simultaneously identifying multiple images projected from the misaligned mirrors while tracking a single star or planet, and associating those images to the appropriate panels responsible for the images. In more advanced uses, high-order moments of each image (coordinates, eccentricity, skewness, etc.) are compiled for analysis described in sections 3.4.3, 3.4.4, 3.4.5, 3.4.6, 3.4.7 and 3.4.8.

3.4 Alignment Strategies

The primary goals of the optical alignment system of the Schwarzschild-Couder telescope are two-fold: align the optical components of the telescope to achieve the optical point spread function within the CTA design requirements for both on-axis and off-axis conditions; and maintain this alignment throughout an observing period given fluctuations in gravitational load due to telescope pointing direction, temperature variations or other perturbations to the mirror alignment.

As described in the previous sections, the alignment process will harness the measurements from the mirror panel edge sensors (MPES), panel actuator lengths, image analysis of the patterns made by stars or planets imaged on the focal plane of the gamma-ray camera (GAS-CCD-GR) and various global alignment system (GAS) devices throughout the telescope to determine and update the alignment status. Due to the novel nature of this telescope, several of the strategies mentioned will be experimental, so that they will be evaluated for ease of reproducibility and efficiency in attaining an aligned state. The goal of this work is to not only achieve the desired alignment state, but to compile a series of well-tested strategies that are useful to the alignment process and can be shared with the greater field of optical instrumentation and astronomy.

3.4.1 MPES Alignment

In an early attempt at full optical alignment, only the MPES units were used to determine misalignment between panels. As described in sections 3.2.2 and 3.3.2, each MPES unit was attached to the mirror panel and calibrated with the appropriate edge. Each panel was placed to optimize the shape of the optical surface based on the position of three reference points on the optical surface of that panel. Once both panels were optimized to the ideal position, the MPES units between them were activated and their coordinates were saved as the laboratory nominal coordinates.

The nominal coordinates were used to align the entire mirror by minimizing the alignment offsets – the difference between the measured MPES coordinates and nominal coordinates. In

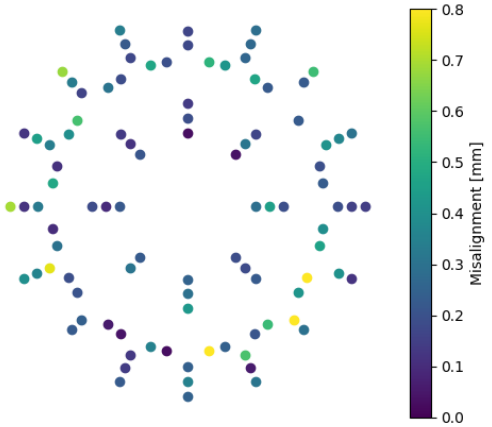

Figure 3.13: MPES alignment offsets of the secondary mirror.

principle, minimizing all of the MPES offsets would lead to a maximally aligned mirror.

The procedure to align each mirror using the MPES units and alignment offset minimization was iterative and attempted in multiple ways. In the simplest case, each successive edge was aligned by fixing one panel and moving the other, all the way around the mirror. At the end of this strategy, it was found that systematic biases introduced by the laboratory calibration compounded to form a large offset between initial and final panels. This offset was as large as 20 mm, which is large enough to cause a collision between panels or disconnect the MPES tubes.

After some modification to the minimization algorithm (section 3.3.2), the edge alignment was expanded to sector alignment that minimized the motion of several panels based on the reading of all MPES units internal to the sector and along the boundary edges. This method sidesteps the systematic bias evident in the successive ring alignment. Multiple sector alignment steps were taken to minimize the distribution of all sensor offset on the mirror. These include alignment per mirror ring (inner or outer), per mirror quadrant (1-4), per full mirror with evenly distributed fixed panels, and so on. Figure 3.13 shows the relative misalignment offsets for all MPES units on the secondary mirror in a well-aligned state.

To fulfill the second goal of the SCT alignment work, the MPES alignment offset was measured based on temperature and pointing variations to evaluate how well the telescope is capable of

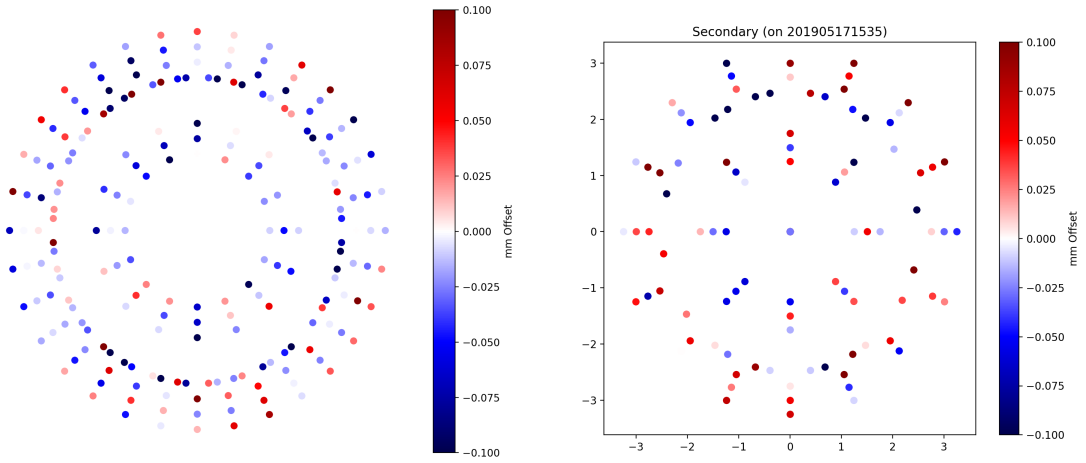

Figure 3.14: Testing of the changes in panel-to-panel alignment of the SCT under different conditions without moving the optical components. The differences in the panel-to-panel alignment of the primary mirrors (*left*) were calculated from two readings of the MPES measurements nine hours apart at 10° C and 20° C, when the SCT was parked at 20° elevation. The ongoing commissioning alignment for the secondary mirrors, with a mean and standard deviation of the misalignment being 0.3 ± 0.2 mm (*right*). Figure and caption from [74].

maintaining its alignment. Figure 3.14 shows the difference between MPES alignment offsets for the primary mirror at temperatures 10° C and 20° C (left) taken at 20° elevation, and for the secondary mirror at elevations 20° and 60° (right) taken at 20° C. These deviations are greater than MPES image resolution (0.05 mm/pixel) and the target optical design angular offset (10^{-4} rad) to reach the target PSF, indicating that these deviations are non-negligible and must be incorporated in the design of the alignment procedure.

Following an iterative process, the alignment offset for every edge was minimized using the sector alignment routine. The distribution of the best alignment achieved with the MPES units is shown in figure 3.15, for both the primary mirror and the secondary mirror. In this state, the alignment offset averages ~300 µm.

One outstanding detraction to this strategy is that while there are enough MPES measurements to constrain the degrees of freedom required for the motion of all of the panels, the MPES alone do not constrain the remaining 6 degrees of freedom for the aligned mirror (conceptualized as a solid body) in the telescope reference frame. A couple of techniques may be employed to generate

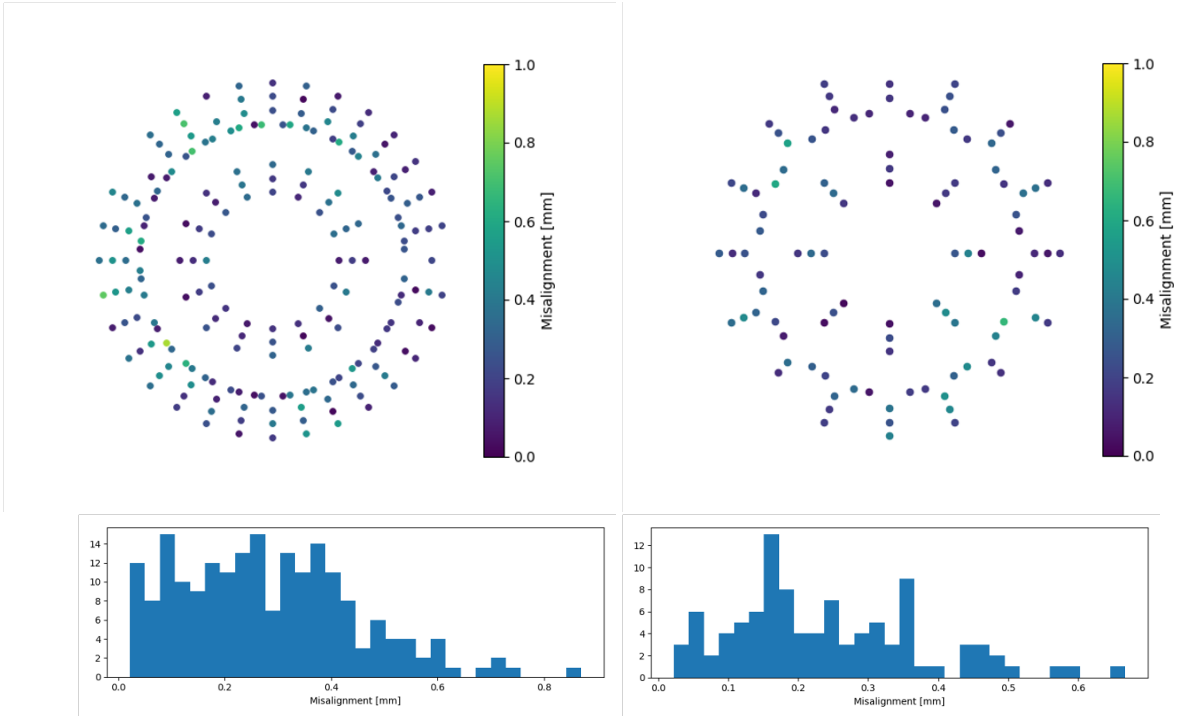

Figure 3.15: Best alignment of M1 (*left*) and M2 (*right*) mirrors using the MPES units alone. Top panels show the amount of the MPES units' displacement with respect to the nominal coordinates measured in the laboratory. The positions of the filled circles correspond to the installed locations of each MPES, and the color scale shows the amount of misalignment. The bottom panels are histograms of the displacements shown in the top panels. Figure from [84].

the required measurements to fully constrain the system: 1) add new sensors between the panels and telescope optical support structure (OSS) to constrain panels to fix locations (in effect, create new “edges" between panels and the OSS), 2) rely on the devices that make up the global alignment system (GAS) to measure the relative translation and rotation between the primary mirror, secondary mirror and focal plane and 3) use an optical alignment strategy to evaluate the relative position of each panel based on the properties of images projected on the focal plane. Strategy 3 is discussed extensively in the following sections since it has the largest potential toward achieving the optical PSF design goals, while strategy 2 has only begun the commissioning phase.

3.4.2 Panel Identification and Response Matrix

The MPES-based alignment of the mirror panels may succeed in minimizing the alignment offset between individual panels to <300 μm, however, it will not impact the relative misalignment between the primary mirror, secondary mirror and focal plane. The most effective method to assess whether the optical surfaces will achieve the optical design PSF is to literally pass light through the entire optical system and image it onto the focal plane. This method will reveal any components missing from the consideration of the optical design, and will best mimic the normal observing conditions of the telescope.

As described in section 3.2.3, the optical table on the secondary contains a CCD intended for detecting the LEDs on the focal plane to use in calculating the relative translation and rotation between the optical table on the secondary and the focal plane. This CCD can also be used to detect the images of stars or planets projected on the focal plane, which can be analyzed for properties such as position and higher image moments (see section 3.3.4 for software description).

The sizes of the pSCT “imaging” pixel is an angular scale of 4 arcmin, and the pSCT “trigger” pixel (8 arcmin), and for each CCD pixel of the focal plane image, the plate scale is 0.241 pix/mm. This converts to ~27 pix (6.5 mm) and ~54 pix (13 mm) for the pSCT “imaging" and “trigger" pixels, respectively, on a picture of the focal plane shown here. Therefore, the pSCT camera pixels are very small in these focal plane pictures, but a similar in size to the imaged stars. A direct

comparison both pSCT camera pixels is shown in figure 3.22.

At first pass, the telescope tracked a single star to assess how well the MPES-aligned optical surface was projected onto the focal plane. Figure 3.16 show several images in a disorganized pattern, where each point represents the end of a light path after traveling through a primary and secondary panel pair. This pattern is the result of the MPES aligned state, which is not yet ideal.

Calibration

To identify the panel pair responsible for each image on the focal plane, Figure 3.16 was carefully assessed by moving one panel at a time and cataloging every corresponding spot that moved. At the same time, each motion was also measured precisely on the image to generate a response matrix that relates panel rotations (motions R_x and R_y) to pixel changes on the image. This 2D response matrix was measured for every panel on the P1-S1 pair. The plate scale relates the CCD pixel size to the physical size represented by the pixel, which was measured to 0.241 px/mm.

The ideal configuration of panel pairs is shown in Figure 3.18. This graphic was generated by following the ray tracing of parallel light traveling from infinity, reflecting onto the primary, secondary and projecting onto the focal plane. The primary (purple) and secondary (green) mirrors overlap relative to each other in different sizes, while in the ideal configuration (where the relative global translation and rotation between mirrors are centered and parallel), the two sets are co-centered. The area of the overlapping regions approximate the light collection area for each panel pair, which indicate the brightness of the star imaged on the focal plane.

Given this structure, the natural strategy for panel calibration forms three concentric rings of defocused stars. The pair of panels that form each image are identified in Table 3.1, along with the name used for each ring in this work and their relative brightness to each other. After calibrating every panel on the focal plane, all three rings were created to begin the optical alignment strategy. Figure 3.19 summarizes the general steps to the optical alignment routine. In brief, the panels are moved from some starting configuration (say that of the starting state in Figure 3.16) to the defocused star pattern of three rings, where the primary and secondary mirrors can then be rotated

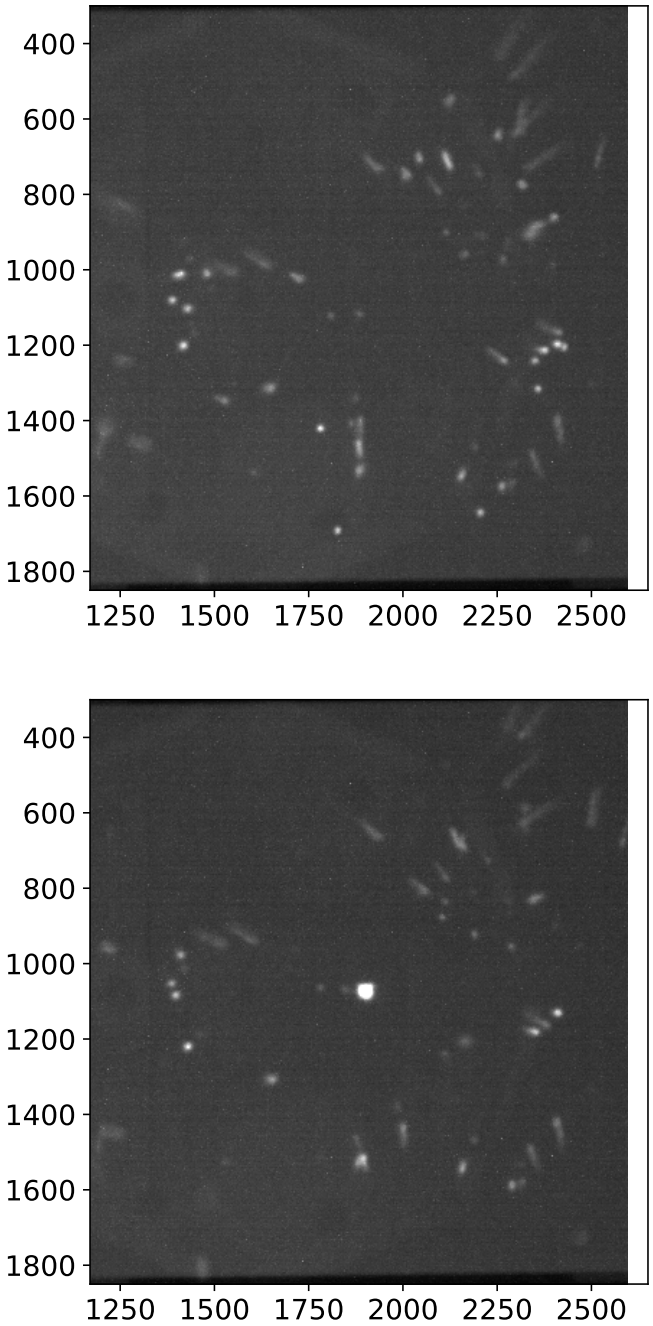

Figure 3.16: Starting state of star tracking using only the MPES alignment. Disorganized pattern of spots (from the projection of a single star) indicate misalignments between panels. Following P1 panel identification and response matrix calibration, the P1 panels are aligned and collapsed to single focus point. Images shown cover about a 3.5° field with the focal point and the pSCT camera roughly in the center. The sizes of the pSCT "imaging" pixel is an angular scale of ~27 pix (6.5 mm), and for the pSCT "trigger" pixel it is ~54 pix (13 mm). Figure from [84].

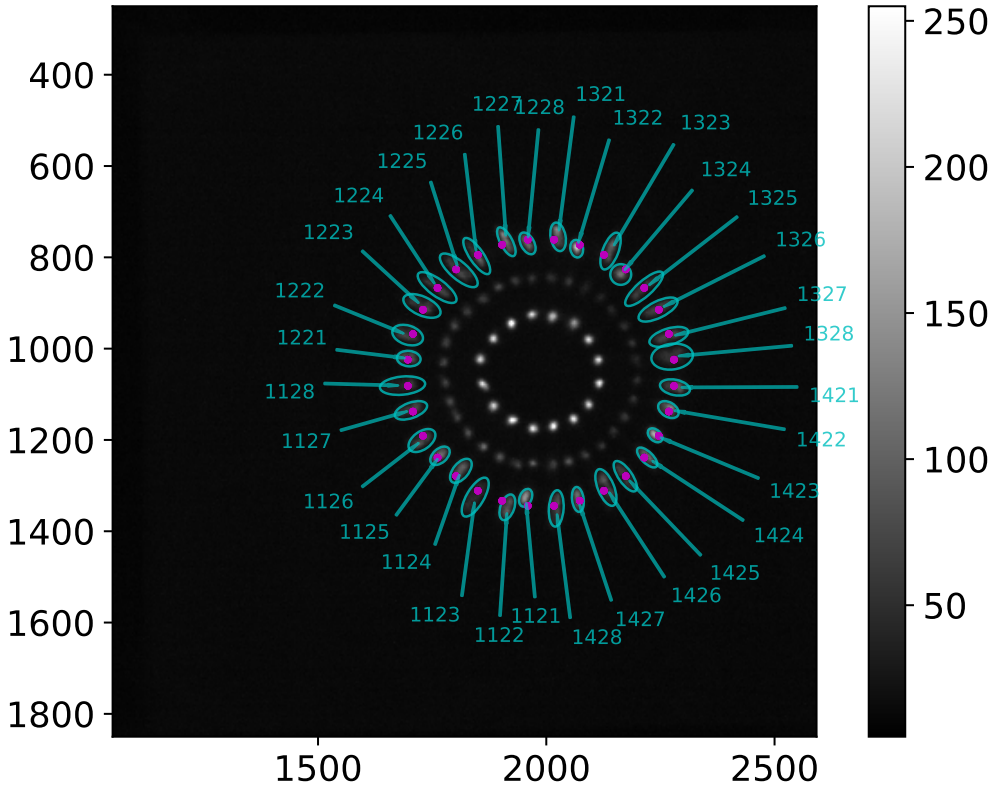

Figure 3.17: Identification of S2 panels. All three defocused star ring patterns (P1, S1 and S2) are set and visible in this picture. Figure from [84].

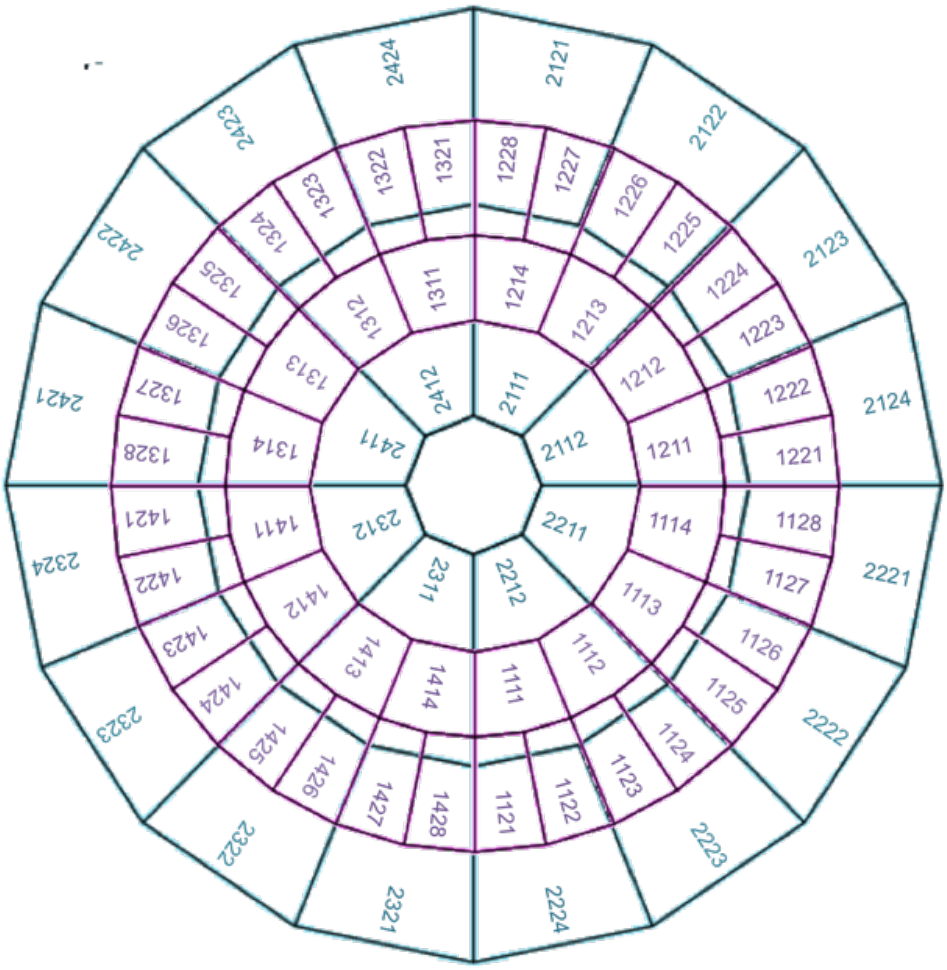

Figure 3.18: Overlapping panels for an aligned mirror. Reflection are based on light from infinity travelling in parallel to optical axis. Rotating a panel in x or y axis has the effect of translation in this image, while z-axis motion has the effect of changing panel area. You can map this image to a focal plane figure of the defocused star pattern by flipping all labels horizontal (i.e. panel 1211 is at 9 o'clock with increasing in number in clockwise direction.)

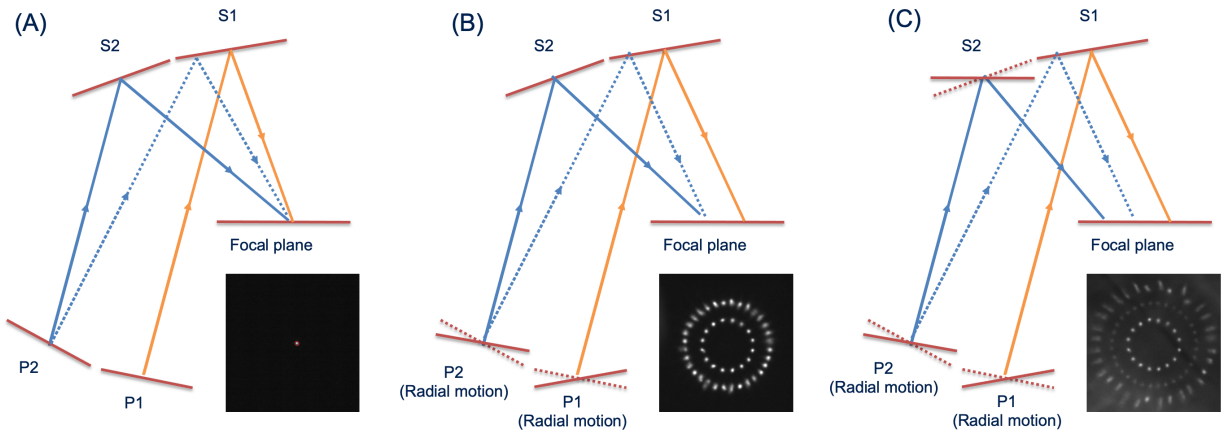

Figure 3.19: A general overview of the alignment process using a defocused star projected on the focal plane. The diagram perspective shows a cross-section of primary mirror panels P1 and P2; secondary mirror panels S1 and S2; and the focal plane. The telescope is pointing toward a star along optical axis (upward in diagram). A) The aligned panels project a single focus point of the star. B) Primary panels P1 and P2 are rotated radially outward to de-focus the star into two concentric rings, projecting the individual panels from each P1 and P2 sectors reflecting off the aligned secondary panels. C) Secondary panels S2 are rotated radially outward to defocus the star even further, separating the projection of P2 panels from their S1 and S2 counterparts. Figure from [85].

by a uniform amount to collapse into a single, focused point and the PSF can be measured.

Primary	Secondary	Name	Ring Radius (px)	Brightness Rank
P1	S1	P1 Ring	130	1
P2	S1	P2 Ring	200	3
P2	S2	S2 Ring	290	2

Table 3.1: Names and configurations of defocused star patterns projected onto focal plane.

3.4.3 Mirror Position Optimization

The properties of the individual images in the defocused star pattern will help determine the global translations and rotations between the primary mirror, secondary mirror and focal plane. These properties include position, first and higher order moments, eccentricity, elongation, image area and brightness. They are measured while the panels are aligned in the defocused star pattern so that any position-based correlations can be understood.

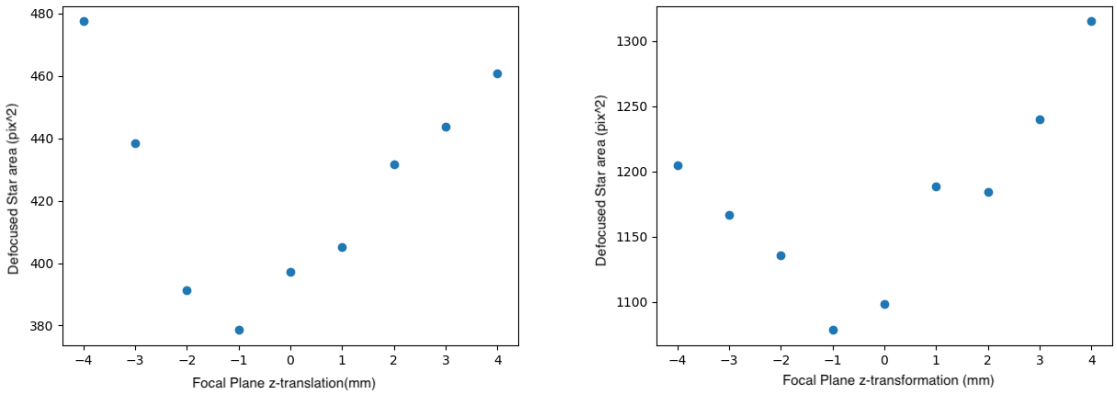

Figure 3.20: The average area (~80% containment) of individual images on the focal plane produced by P1-S1 panels (*left*) and P2-S2 panels (*right*) with the defocused configuration (as shown in the right panel of Figure 3.17) with respect to the distance between the focal plane and the secondary mirror. The defocused images from P1-S1 form the inner circle shown in Figure 3.17, and those from P2-S2 form the outer circle. Each data point is derived from an image similar to Figure 3.17 when the distance between focal plane and secondary mirror is at one of the nine relative values in 1-mm increments shown in the plots. At the "-1 mm" relative distance between the secondary mirror and the focal plane, the defocused images of the star reach a minimal area, and the OS is the closest to true focus. Figure from [84].

In the simplest case, the distribution of image size is directly related to the distance between the secondary mirror and the focal plane. Optimizing this distance for the smallest size will yield a good approximation of the best focal plane and secondary mirror separation. While the creation of each ring may indicate a relatively acceptable alignment between the panels within that ring, separate rings are decoupled and may have different global translations and rotations. Therefore, the measurement of the mean size must be done independently for each ring.

Figure 3.20 contains the evolution of the mean area (a proxy for image resolution and size) for the specified ring pattern as a function of the z-axis distance. In both cases, the smallest area is achieved when the panel is moved by -1 mm from the default in the z-axis. This distance was saved as a first-order estimate for the ideal separation, to be used whenever the gamma-ray camera was moved to focus position.

An additional measurement was made at the same time to evaluate the Fourier decomposition of both the eccentricity and flux area as a function of the z-axis translation along the phase of the panel position. In this Fourier decomposition, only the first harmonic is extracted, which can indicate

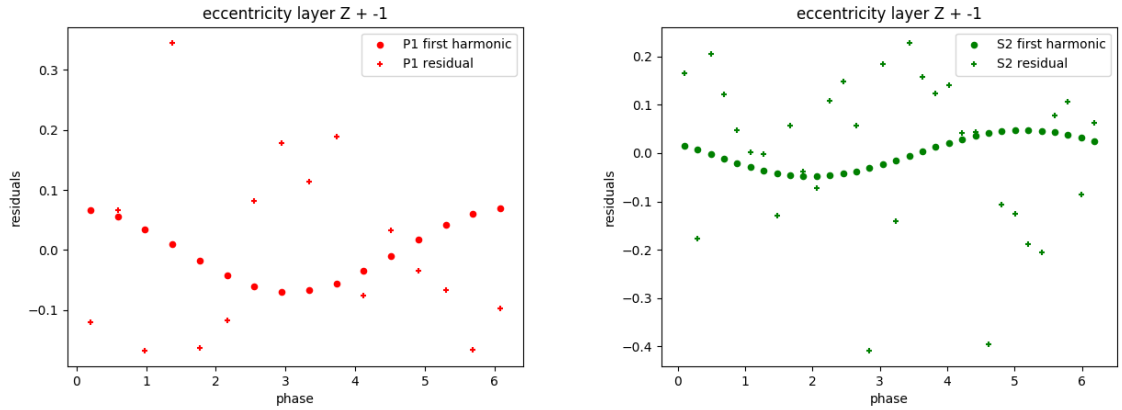

Figure 3.21: First harmonic of the eccentricity property of P1 ring panels (left) and S2 ring panel (right). Residuals between panel eccentricity value and first harmonic are also plotted with '+' marker. No obvious harmonic is evident, which indicates minimal global rotation between the secondary mirror and the focal plane.

a global rotation between the mirror and the telescope reference frame. For example, uniformly large eccentricity on opposite sides of the ring, with small eccentricity on the perpendicular axis, can indicate that the mirror is rotated along the perpendicular axis.

The net evaluation of the first harmonic as a function of z-axis show that no strong harmonics are present anywhere in either the P1 or S2 rings. The first harmonic and residuals of Figure 3.21 are similar in size, while in strongly periodical data the residuals would be significantly smaller than the first harmonic. This was an encouraging sign that the global translations and rotations were not excessively large. A higher precision measurement of the global translation and rotation is measured in a later section using (section 3.4.8) higher-order moments from each image.

3.4.4 Point Spread Function

The optical point spread function (PSF) is a main result to be measured throughout remaining alignment work. In standard astronomical instrumentation, the PSF is a direct measure of the capability of an instrument, defining the resolving power of the optical system for a set of observation

conditions. It is defined as follows:

$$PSF = 2 \times \max\left(\sigma_x, \sigma_y\right) \tag{3.5}$$

where σ_x and σ_y are found by fitting the image with a 2-D Gaussian. The fit parameters are peak height, x, y, σ_x, σ_y, θ, and background pixel size. The original image is cropped to contain just the single image, isolating it from other images in the full field of view, but large enough to estimate a uniform background underneath the 2D Gaussian distribution. The width σ represents the 68% containment of the Gaussian distribution. The angle of rotation θ defines the angle between the horizontal axis of the full image and the largest orthogonal axis of the image (the semi-major axis). Twice the maximum σ provides the largest width of the image, which defines the smallest size that is resolvable by the optical instrument.

This work will measure the PSF derived from several contexts: the image formed from the alignment of the entire optical system; the image formed from the alignment of a selection of panels (e.g. by forming an image by rotating just the P1 ring, made up of P1 and S1 panels); and the image from individual panels. These measurement will be performed on-axis, where the star or planet being tracked is centered in the field of view, and off-axis, where an field angle is applied in some direction offsetting the star or planet from the center of the field of view. The performance of the off-axis PSF is expected to be an important improvement provided by the design of the Schwarzschild-Couder telescope over conventional IACT telescopes [73].

During the initial alignment campaign in 2019, the star Capella was tracked while performing the optical alignment data taking and calibration tasks. During this extended campaign, starting from the MPES aligned state, the following tasks were accomplished: the panels were identified on the focal plane; all response matrices were measured; the optimized focal plane to secondary mirror separation distance was found; the defocused ring patterns and best ring radii were determined; and the ideal panel rotation angle to achieve the focus point was found. Once completed, the best on-axis PSF was measured and is shown in Figure 3.22. This PSF is 2.9′, well within the SCT on-axis

design goals [84, 86].

The technique developed to carefully align all panels from some starting position to the focus point for measuring the PSF consists of many steps, which takes about half an hour to achieve in the current state of the optics software. Through trial and error, there is now a database of actuator lengths for all panels in given patterns that can be loaded for the panels to move toward. From there, a snapshot is taken to evaluate the position of every image within the three rings so that they can be corrected. The ideal ring positions are determined based on the pattern center and ring radius, where every panel is evenly spaced along that circle in the correct panel order. With the ideal and measured position now compiled, the panels are moved by this correction to their best positions.

In this nearly perfect pattern, the panels can begin to rotate toward the focus point. First, the P1 ring panels are moved using R_y and z motions toward the center. A snapshot is taken to measure the position of the remaining P2 and S2 rings, which will be corrected as needed. Then, P2 and S2 rings are moved in the same way, one ring at a time with a snapshot and ring correction in between. The panel states and ring-to-focus motion files are saved in between every step. Figure 3.19 reviews the reverse of these steps from subfigures A) to C) detailing the focus-to-ring motion, but this is directly applicable to the ring-to-focus motion if taken in the opposite direction.

3.4.5 PSF per elevation

The gravitational load on the optical support structure (OSS) can distort the optical PSF in non-neglible ways. These distortions are most evident between large motions, such that the alignment made at zenith is significantly degraded when observing at low elevation, for example. Temperature variations also lead to measurable thermal expansions throughout the structure that will distort the optical PSF. From these two environmental conditions, it is clear that the alignment must be measured and constantly monitored throughout these conditions. It is not yet clear how often corrections must be applied throughout an observing period, and further experimentation and software development will be needed.

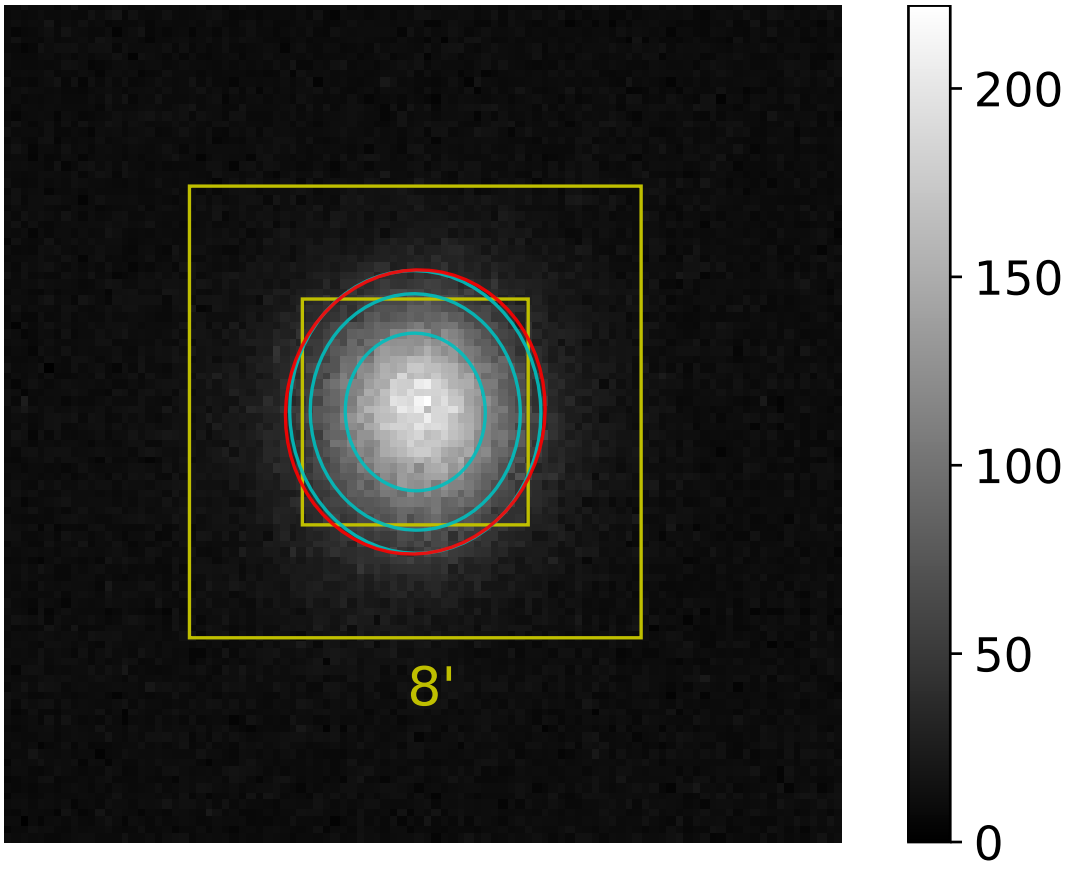

Figure 3.22: The PSF of the SCT, illustrated by an image of the star Capella on the focal plane, as achieved during the initial commissioning campaign concluded in December 2019. From inner to outer, the three cyan ellipses show the 1-σ (~39% containment), 1.5-σ (~68% containment), and 1.8-σ (~80% containment) contours from the best 2D Gaussian fit, respectively. The red contour is the extension solution obtained from the `astrometry.net` tool, roughly corresponding to 80% light containment without reliance on the 2D Gaussian fit. The inner and outer yellow unfilled squares illustrate the sizes of the SCT "imaging" pixel (an angular scale of 4 arcmin) and the SCT "trigger" pixel (8 arcmin), respectively. Figure from [84].

Using the best alignment methods developed at that time, the PSF was measured as a function of elevation to evaluate the effect of pointing on the PSF [85]. This process also formed a testing stage to experiment with the interpolation of actuator lengths between the measured elevation states, which proved successful.

Following the extensive steps outlined in Section 3.4.4, 8 distinct elevations were used to set up and measure the PSF. These states were recovered on a later night to confirm that the interpolation of the states was possible. These 8 elevations form the first version of a pointing-based database of alignment states, which contains the actuator lengths for all panels taken when aligned to form the focus point.

Table 3.2 contains the PSF and pointing direction, denoted by both the elevation during the time of the measurement of the alignment state and at the time of the PSF measurement. Figure 3.24 shows the PSF for up-going and down-going elevations. The PSF is consistent with the elevation in either up-going or down-going directions. The best PSF is achieved at the highest elevations, which is consistent with the gravitational symmetry present when the telescope is pointing directly upward. The PSF denoted by the purple point is measured at 40° elevation, but using an alignment set at 77° elevation. In this case, the deviation reveals the worst case PSF if the wrong alignment setting is used, which degrades the PSF from $\sim 3'$ to $>4'$.

A newer version of this database to be measured in a future alignment campaign will incorporate higher-order corrections applied to the motions and an improved S1 ring alignment. It will also include the measurement of all MPES coordinate readings, to be used as the pointing-based nominal coordinates so that panels can be internally aligned at a faster frequency. Finally, the temperature will be another primary key alongside elevation and azimuth.

3.4.6 S1 Alignment

The alignment configuration patterns of a defocused star described in Table 3.1 is not able to internally align the S1 ring on its own. This ring couples to the other rings such that any misalignment internally to it will be built into the alignment of the other rings. To make sure

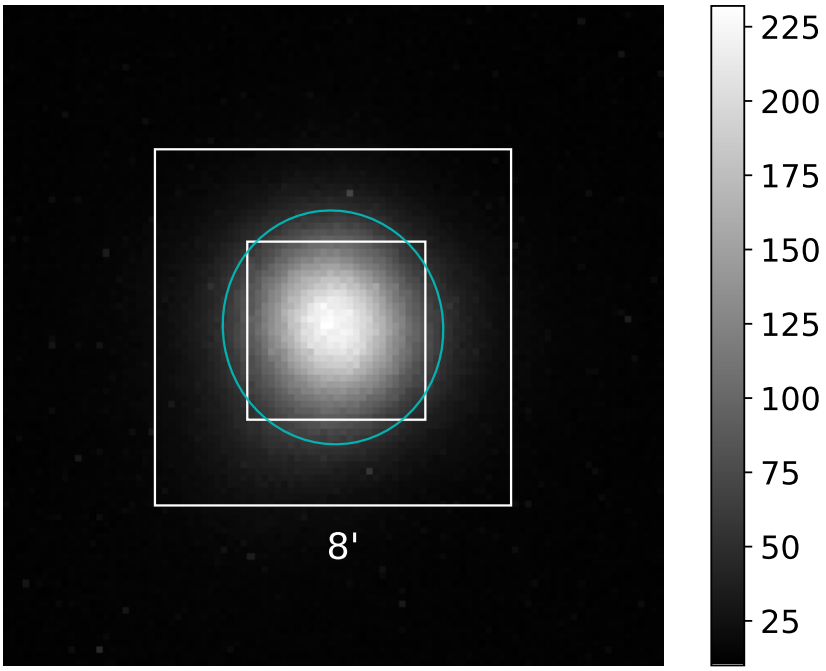

Figure 3.23: Picture of Arcturus at 76° elevation. The PSF is 2.93'. The boxes indicate the relative size of the imaging (8') and trigger (4') pixels of the SiPM camera. Figure from [85].

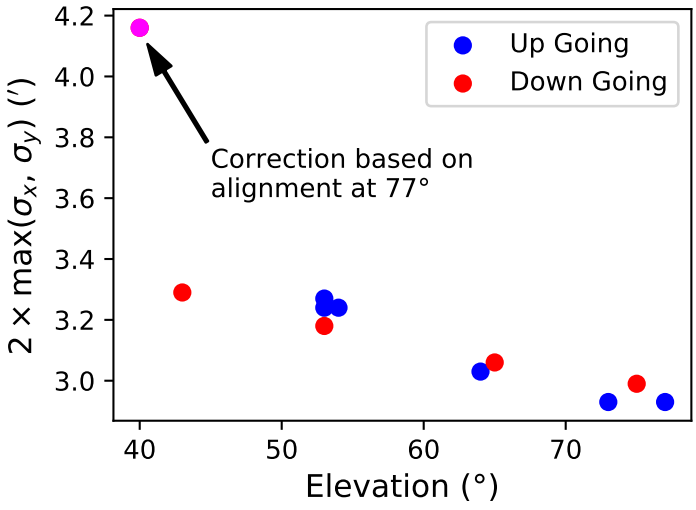

Figure 3.24: PSF measured per elevation. PSF is defined as $2 \times \max(\sigma_x, \sigma_y)$. At 40°, the panel alignment setting from 77° was loaded to measure the largest PSF deviation from the optimal setting, shown in purple. Panel alignment settings derived without corrections for all elevations. Figure from [85].

Table 3.2: Elevation dependent PSF measurements. Alignment setting made before PSF was measured, so both pointing directions are denoted for each PSF.

El$^{(a)}$	Az$^{(a)}$	El$^{(b)}$	Az$^{(b)}$	PSF ($'$)
49	97	53	100	3.24
49	97	53	100	3.27
49	97	54	102	3.24
60	108	64	113	3.03
69	123	73	134	2.93
76	155	77	175	2.93
77	198	75	216	2.99
70	234	65	244	3.06
56	256	53	260	3.18
46	264	43	267	3.29
77	198	40	269	4.16

$^{(a)}$at alignment;$^{(b)}$at PSF measurement.

all the panels will be aligned, a separate technique was developed to align just the S1 ring by correcting small misalignment between the panels, as described in Figure 3.25.

The S1 correction will exploit the “ghost" spots to minimize the misalignment between S1 panels. Rotating P1 panels tangentially with respect to Fig. 3.18 (inner purple shapes), will lead to part of the P1 panels overlapping two S1 panels and the other part continuing to overlap the original S1 panels. In the perfectly aligned state, each P1 overlaps exactly on one S1, while one S1 overlaps with two P1s within the same sectors.

In this S1 correction, the two S1 panel overlap is exploited by rotating all P1s until the “ghost" image appears in alternating P1-S1 pairs, shown in the right of Figure 3.25 . In this case, a single P1 overlaps with two S1s, and if the overlap is not symmetric, the “ghost" spot is the smaller overlap region. If the two S1 panels in this overlap are perfectly aligned, no ghost will appear. Instead, a misalignment between S1 panels is deliberately inserted to measure the response matrix of S1 to the ghost, and then simultaneously minimize all ghosts. This procedure is reviewed in Figure 3.25.

To simultaneously align all P1-S1 panels, the P1 panels are rotated in alternating x-axis rotation. This maximizes the measurement on the respective S1-S1 edge, since two sets of ghost images will appear. Then, both P1 ghosts can be minimized by the motion of the S1 edge. For example, the S1-S1 edge 2112 + 2211 is aligned with the 4 spots created by 1211 + 2112, 1211

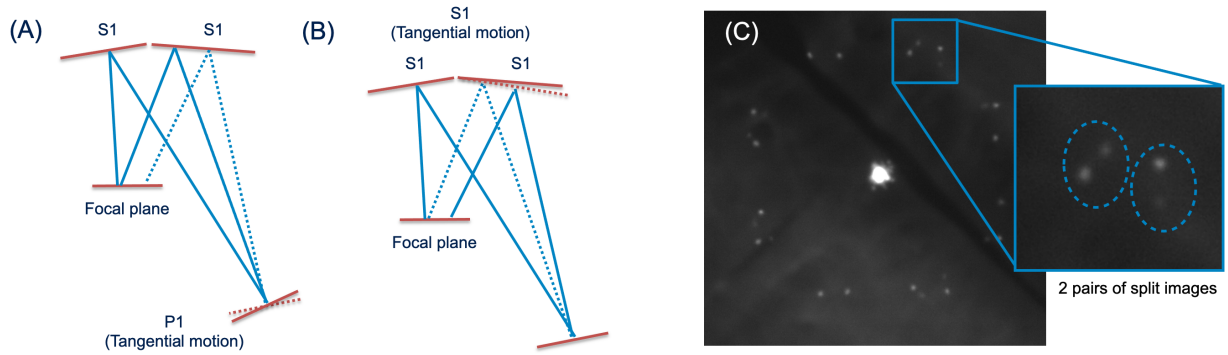

Figure 3.25: A general overview of the S1 alignment process. A) Assuming that S1 panels are misaligned, P1 panels are rotated tangentially to create a second set of centroids on the focal plane. B) S1 panels are rotated tangentially to remove the new centroids, therefore aligning the S1 panels. C) Focal plane picture of the projected centroids. Inset: 2 pairs of split images visible by the misalignment of S1 panels, to be merged and corrected. Figure from [85].

+ 2211, 1114 + 2112, 1114 + 2211. The spots generated by 1211 + 2211 and 1114 + 2112 are the “ghosts", which are moved to the 1211 + 2112 and 1114 + 2211 positions. An example of alternating R_x + /−1 mm rotation applied to P1 is shown in fig. 3.26, which have the reordered panel identification in red.

After aligning five of the 8 S1 edges, it was found that edges 2121 + 2424, 2211 + 2212 and 2311 + 2312 produced no ghosts. This was caused by the occultation of the structure between the primary and secondary mirror. One solution is to apply the same technique to a wobble offset: point the telescope 1.5 degrees away from the star or planet in several directions rotated in ϕ. To maximize the appearance of the ghost, the sector in between the edges were brought to a focused point, labelling each S0, S1 and S2. The wobbled results showed no new ghosts or deformation at the center spot, indicating good off-axis alignment up to 1.5 degree offset. An example is shown in fig 3.27.

3.4.7 First-order Correction to Panel Motion

The systematic errors introduced by the response matrix affect the motion of the image on the focal plane from its original position to its target position. This systematic error makes it so that moving a panel from its pattern position to the focal point will be off by a few pixels, which then

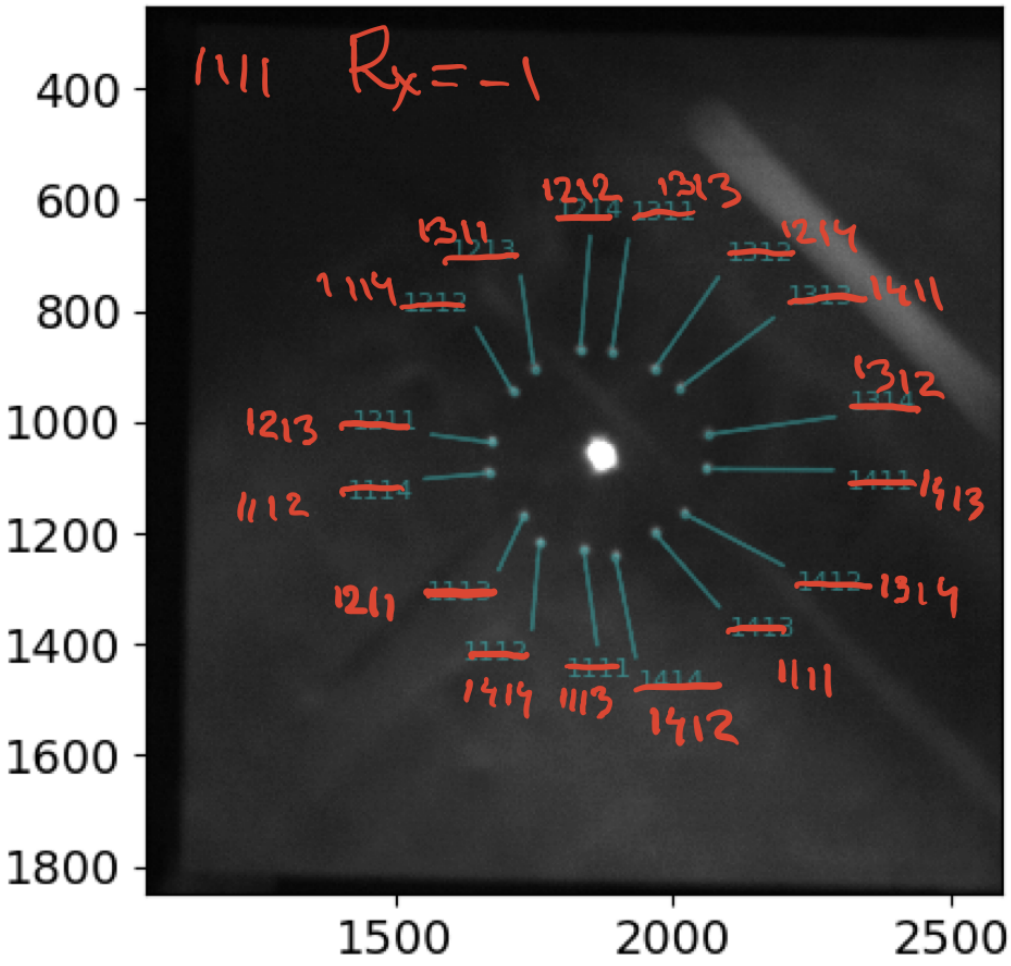

Figure 3.26: Perturbed P1 with alternating $R_x +/-1$ (mm). Note the placement of the labels, which is an effect of the perturbation that alternates the panel placement by 1 panel.

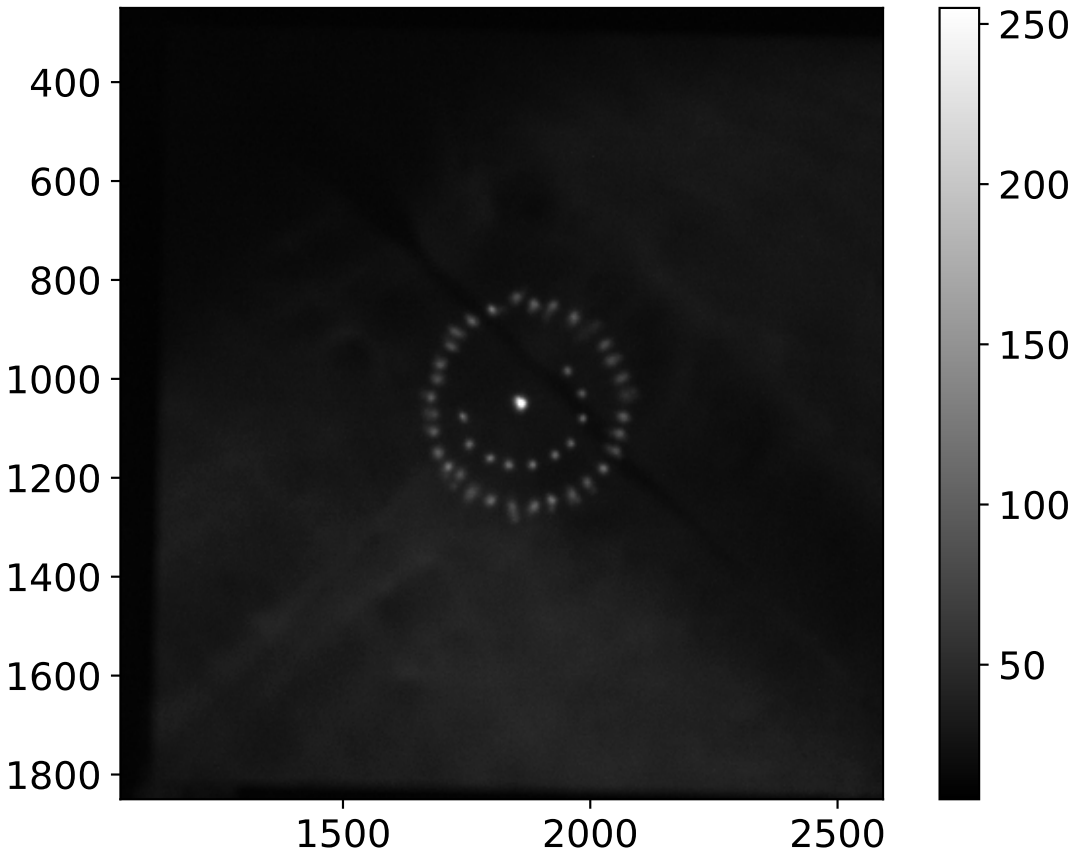

Figure 3.27: S2 Sector aligned to focal point. No wobble applied; Capella at center. No deformation or ghost visible at center point.

have to be corrected with one or two more motions. This is the first-order correction. For each panel, move to the target position, calculate the difference from that position to where it actually landed, and iterate motions until that delta is minimized. The sum total corrective motion is then saved to a table mapped to this motion. Ideally, this first-order correction should be analytically understood.

Through trial and error, it was discovered that the tubes between MPES units (which are vital for providing a constant and uniform dark background so the MPES camera can identify its laser) provide non-negligible torque between panels. The tube – pictured on the right side of Figure 3.4 – is made of rubber and an internal wire coil, which provides for structural stability and also a spring force between panels. There are between 2 and 3 MPES units along each edge, and it is evident during panel motions that adjacent image on the focal plane are also moving even when the panels responsible for those image are not given motion commands. The panels are pushed or pulled by the MPES tubes, and removal of these tubes stops the unexpected motion. This tube-dragging effect plays a large role in the systematic bias in the motion uncertainty.

One largely successful strategy to measure the first correction and counter the MPES tube dragging built on previous technique already well tested. Instead of measuring the corrections to individual panel motions, which is a laboriously and time consuming effort, it was decided to move all panels together at the same time in a way that all could still be identified by the image analysis software.

From a ring position (whether P1 or P2 rings), the already well measured rotation toward the focal point was used twice, recreating the ring but with all panels reversed from their original position. In the ideal case, without the systematic bias from the tube dragging, all panels move to the opposite end of the ring while maintaining the full ring properties such as shape, radius and center. This was measured and verified with the tubes removed from all MPES using the P1 ring. With MPES tubes reinstalled, the offset from expected and measured position for each panel was recorded as two times the systematic bias. Additionally, the general panel motion also included a compensation along that panel's z-axis to minimize any action along the offending edge. These

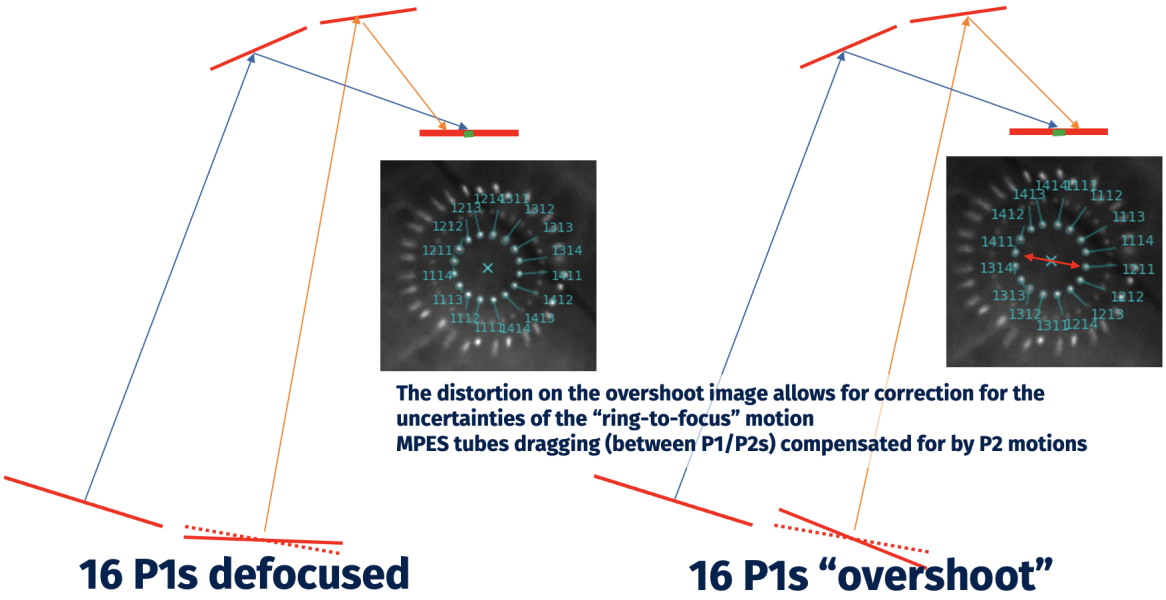

Figure 3.28: First order correction to P1 panels by moving the P1 ring toward the focus point twice to measure the systematic bias. The offset between start and final motion is the measurement of the uncertainty, which is applied to the ring-to-focus motion. This is was also known as the "overshoot method", since the panels move past the focus point on the way to their final positions.

two steps combined created a first-order correction that was applied to future motions. Figure 3.28 is a diagram of this motion for the P1 panels.

3.4.8 Global Alignment

Following the improvements to both S1 alignment and first correction to panel motions, a major remaining component of the alignment is to make sure the global translation and rotation components of the primary mirror, secondary mirror and focal plane are aligned (see Figure 3.29 for details). Global misalignment becomes evident on the images through position-based behavior, such as phase-dependent brightness that increases and decreases within a ring of panels, or image-property-based behavior, such as the systematic effect on image skewness. Both of these were explored in section 3.4.3.

Higher-order moments measured on each image probe different properties of the global behavior. Zeroth-order (brightness) and first-order (position) have been the primary moments used so far. The second order measurement of the P1 and S2 rings yield no global misalignments as seen

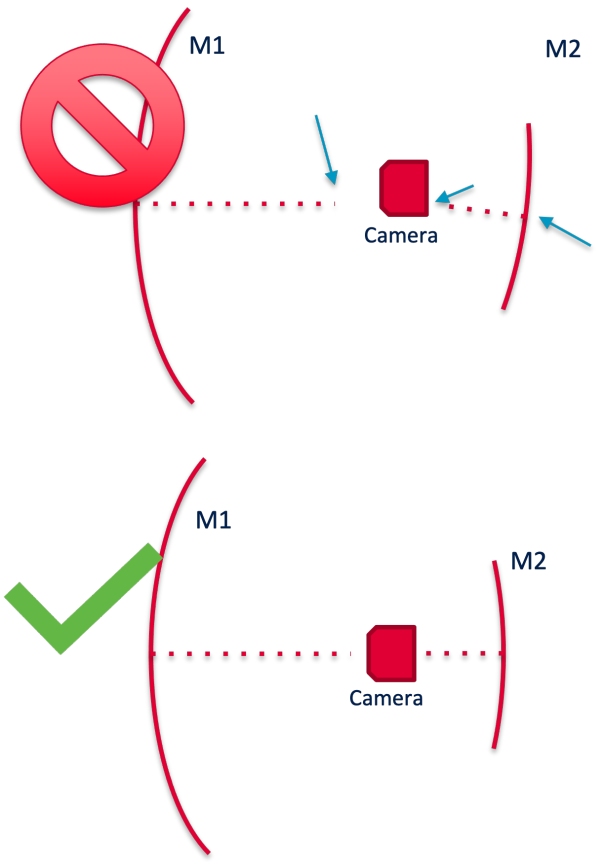

Figure 3.29: Diagram of global alignment strategy, consisting of major components: primary mirror (M1), secondary mirror (M2) and focal plane (camera). Highlighted in the upper panel, from left to right: translation offset from primary mirror optical axis to camera optical axis; translation offset from secondary mirror optical axis to camera optical axis; and rotation offset between secondary mirror and focal plane. Lower panel shows aligned optical axis throughout components in translation and rotation dimensions.

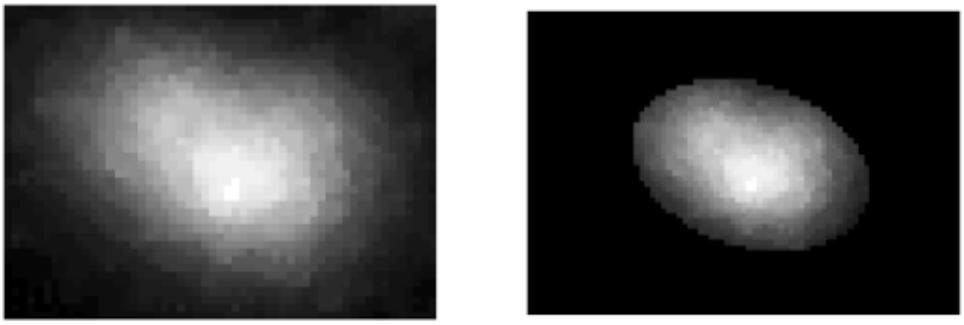

Figure 3.30: Selection and cropping of an individual image for use in calculating high-order moment.

in Figure 3.21, which involved calculating the first harmonic of the second moment (eccentricity) along the panel phase in the ring. In this section, the third-order moment were calculated and measured for S2 rings to achieve a higher-precision measurement.

Third-Order Moment Derivation

For each image, the analysis initially crops and removes the background from the nearby region. On the remaining image, the right side of Figure 3.30, the following moments are calculated:

$$M_{00} = \sum_{i \in S} p_i \tag{3.6}$$

$$\overline{x} = \sum_{i \in S} (p_i x_i) / M_{00} \tag{3.7}$$

$$\overline{y} = \sum_{i \in S} (p_i y_i) / M_{00} \tag{3.8}$$

$$dx_i = (x_i - \overline{x}) \tag{3.9}$$

$$dy_i = (y_i - \overline{y}) \tag{3.10}$$

First Moment

$$M_{11} = \sum_{i \in S} (p_i dx_i) / M_{00} \tag{3.11}$$

$$M_{12} = \sum_{i \in S} (p_i dy_i) / M_{00} \tag{3.12}$$

Second Moment

$$M_{20} = \sum_{i \in S} (p_i (dx_i^2 + dy_i^2)) / M_{00} \tag{3.13}$$

$$M_{21} = \sum_{i \in S} (p_i (dx_i^2 - dy_i^2)) / M_{00} \tag{3.14}$$

$$M_{22} = \sum_{i \in S} (p_i (2dx_i dy_i)) / M_{00} \tag{3.15}$$

Third Moment

$$M_{31} = \sum_{i \in S} (p_i (dx_i^3 + dy_i^2 dx_i)) / M_{00} \tag{3.16}$$

$$M_{32} = \sum_{i \in S} (p_i (dx_i^2 dy_i + dy_i^3)) / M_{00} \tag{3.17}$$

$$M_{33} = \sum_{i \in S} (p_i (dy_i^3 - 3dx_i^2 dy_i)) / M_{00} \tag{3.18}$$

$$M_{34} = \sum_{i \in S} (p_i (dx_i^3 - 3dy_i^2 dx_i)) / M_{00} \tag{3.19}$$

Fourth Moment

$$M_{40} = \sum_{i \in S} (p_i (dx_i^2 + dy_i^2)^2) / M_{00} \tag{3.20}$$

$$M_{41} = \sum_{i \in S} (p_i (dx_i^4 - dy_i^4)) / M_{00} \tag{3.21}$$

$$M_{42} = \sum_{i \in S} (p_i (2dx_i dy_i^3 + 2dx_i^3 dy_i)) / M_{00} \tag{3.22}$$

$$M_{43} = \sum_{i \in S} (p_i (dx_i^4 - 6dx_i^2 dy_i^2 + dy_i^4)) / M_{00} \tag{3.23}$$

$$M_{44} = \sum_{i \in S} (p_i (4dx_i^3 dy_i - 4dx_i dy_i^3)) / M_{00} \tag{3.24}$$

Measurement of Net Asymmetry

For the S2 ring, the sum of the M_{31} and M_{32} terms were reported, indicating the net skewness vector for that ring. To fully align that ring with the corresponding P2 panels, and focal plane, the (M_{31}, M_{32}) vector was minimized by moving the secondary panels along the global z-axis. As the global z-axis position decreased, the skewness in each image transitioned from positive to negative around $dx = -3$ mm, indicating that a critical transition point was passed as seen in the two states of Figure 3.31.

Measurement Using Off-Axis Plane

With the measurement and minimization of the net asymmetry complete, the off-axis PSF can be measured. This is performed by using a larger focal plane target segment that mimics the curvature of the camera SiPM modules. This larger target is precisely machined nylon, installed in the center backplane of the gamma-ray camera and capable of rotating to arbitrary axial angles. Figure 3.32 shows this curved focal plane segment before and after installation.

In a simulation study to assess the alignment tolerances of the SCT OS, perturbations in rotation and translation were applied to each primary and secondary mirrors and the output PSF was measured [87]. The simulation results determined the PSF design goals of the pSCT for both on-

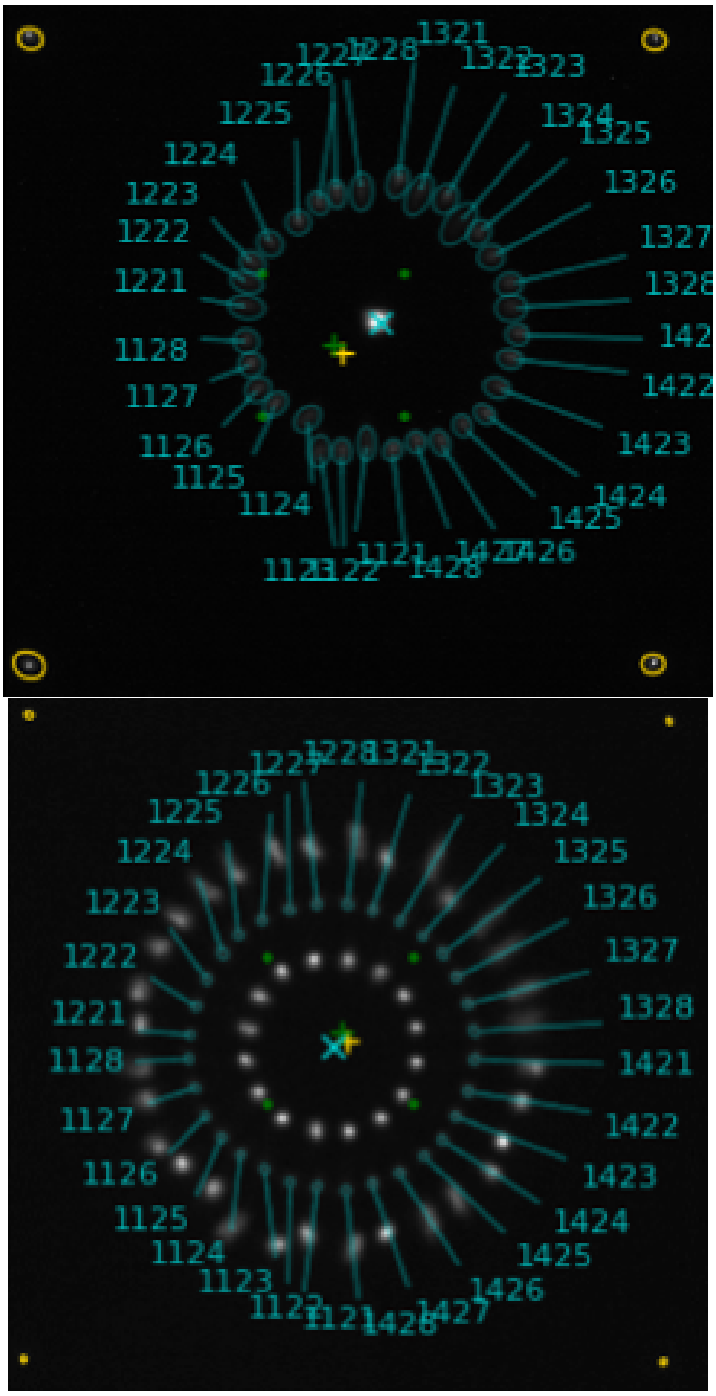

Figure 3.31: In the *top* figure, a slight asymmetry in the skewness is evident, where top and bottom S2 panels have large skewness, while left and right panels have small skewness. In the *bottom* figure, the total skewness asymmetry is decreased after moving by −3 mm from the position of the top image.

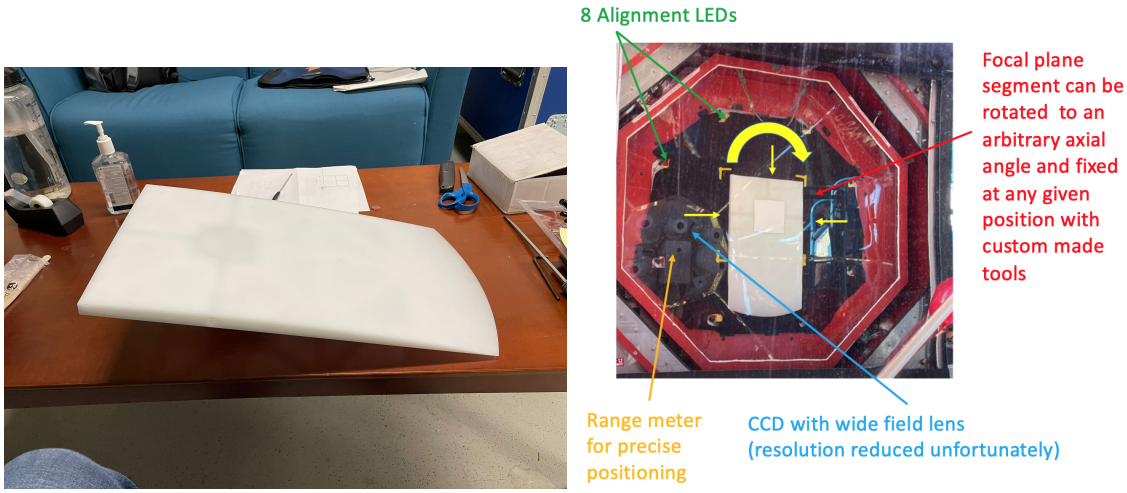

Figure 3.32: The curved focal plane segment precisely machined and made of nylon. The installation in the center backplane allows it rotate freely for various axial angles.

axis and off-axis observations, using the exact parameters described in Table D.1. The result of these perturbations are shown in Figure 3.33 for up to 4° field angle (the off-axis angle). In addition to the ideal design, the study assumed realistic degradations from panel rotational misalignment of 0.1 mrad and 0.2 mrad, and combined 1 arcmin mirror degradation.

In a preliminary measurement, a significant number of wobble offsets (field angles) were observed while tracking either Arcturus or Vega. The optical system was aligned with the net-asymmetry-minimized state at 70° elevation, which provides a useful median elevation to use that does not requiring constant elevation-dependent correction. In this state, the preliminary measurement of the off-axis PSF is confirmed, achieving ~3.8 arcmin at 3° field angle [87]. A future campaign will incorporate improved global alignment, online pointing correction and elevation-dependent alignment states for each measurement of the PSF per field angle.

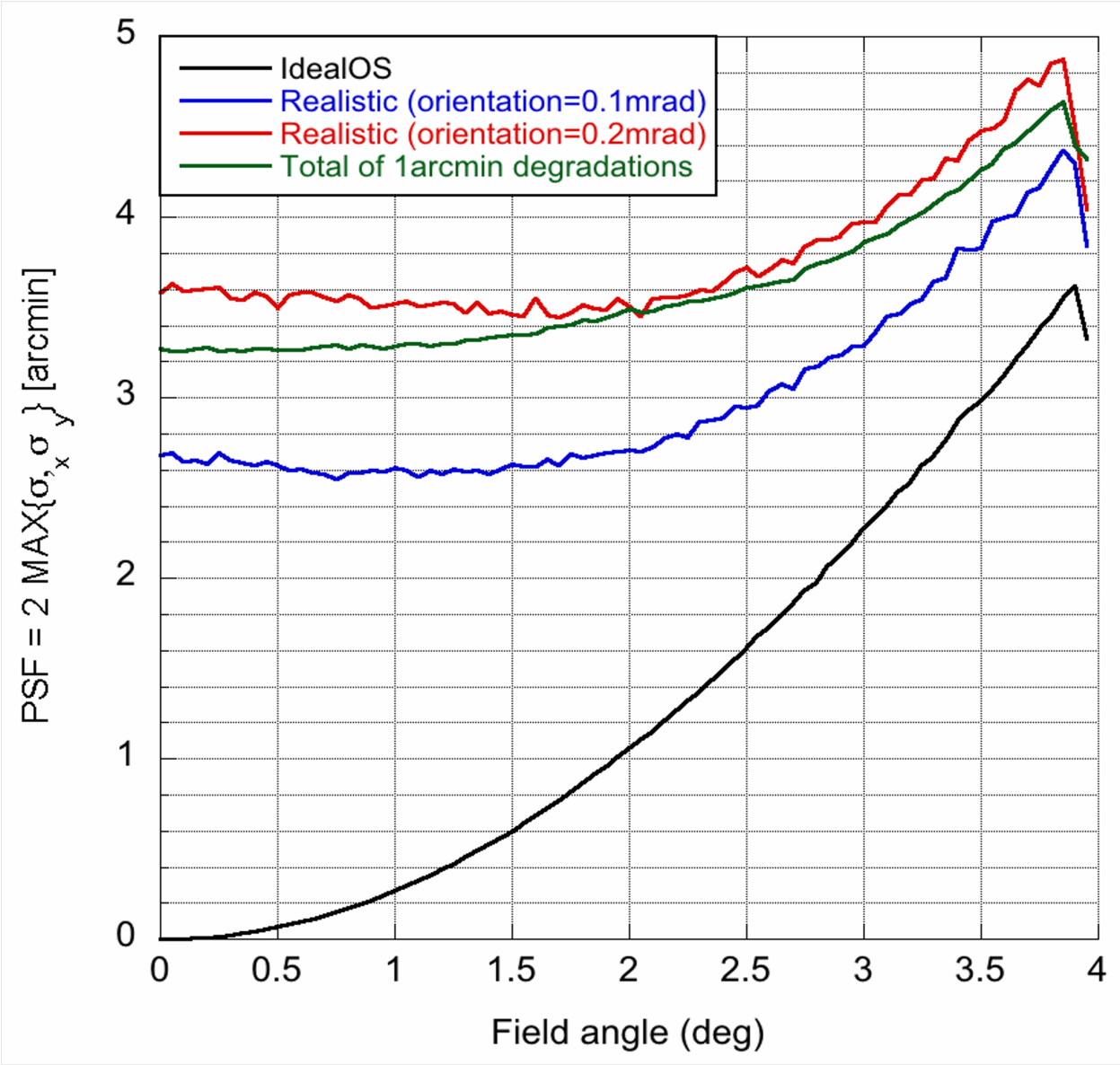

Figure 3.33: Full PSF simulation study of the SCT assuming ideal, 0.1 mrad, 0.2 mrad and 1 arcmin degradations. The simulation results determined the PSF design goals of the pSCT for both on-axis and off-axis observations. Reproduced from [87].

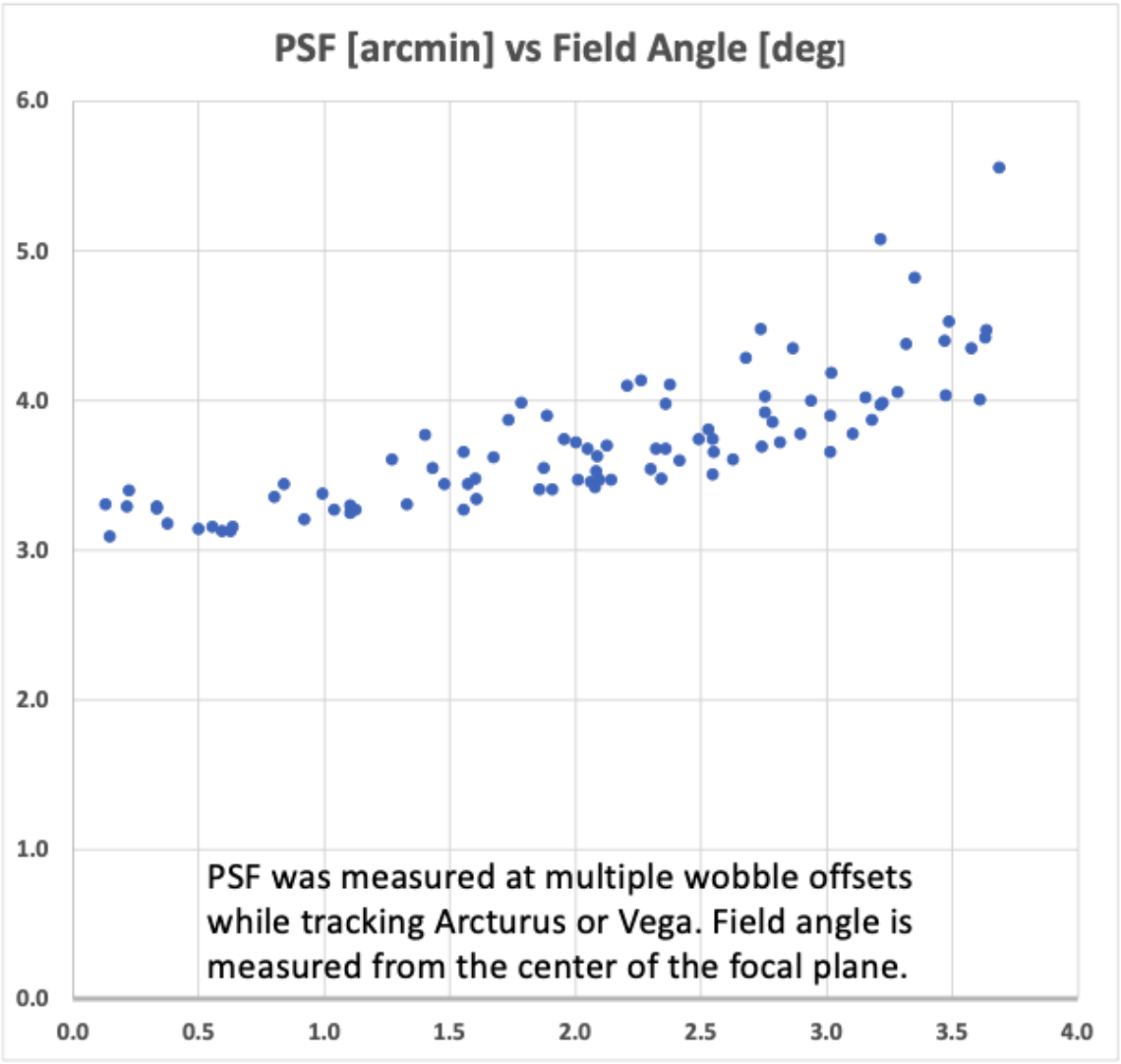

Figure 3.34: A preliminary measurement of the off-axis PSF as a function of the field angle (in degrees). The general behavior follows the off-axis PSF realistic design goal [87].

Chapter 4: Superluminous Supernovae

The following chapter was submitted to Astrophysical Journal on June 7, 2022 for publication. It is reproduced here as submitted before completion of the review process, with introductory material that has already been introduced in this thesis.

4.1 Introduction

The recent growth of sensitive optical time-domain surveys has revealed and expanded exciting new classes of stellar explosions. These include superluminous supernovae, which can be up to 10–100 times more luminous than ordinary massive star explosions (e.g. [88–94]; see [95] for a recent review). Conventionally, the optical emission from most core-collapse supernovae is powered by the radioactive decay of ^{56}Ni (Type Ib/c) and by thermal energy generated via shock heating of the stellar envelope (Type IIL, IIp). However, the peak luminosities of SLSNe greatly exceed the luminosity expected from those conventional mechanisms, and the origin of the energy is still debated.

A popular model for powering the time-dependent emission of SLSNe, particularly the hydrogen - poor Type I class (SLSN-I), involves energy input from a young central engine, such as a black hole or neutron star, formed in the explosion. For example, the accretion onto the compact object from bound debris of the explosion could power an outflow which heats the supernova ejecta from within ([96–99]). Alternatively, the central engine could be a strongly magnetized neutron star with a millisecond rotation period, whose rotationally powered wind provides a source of energetic particles which heat the supernova ejecta [100–104]. The magnetar[1] model provides a good fit to the optical light curves of most SLSNe-I [90, 105]. Furthermore, analyses of the nebular spectra of hydrogen-poor SLSNe [106, 107] and Type-Ib SNe [108] support the presence of a persistent central energy source, consistent with an energetic neutron star.

The details of how the magnetar would couple its energy to the ejecta are uncertain. Several models consider that the rotationally powered wind from a young pulsar inflates a nebula of relativistic electron/positron pairs and energetic radiation behind the expanding ejecta [109–111]. At the wind termination shock, the pairs are heated and radiate X-rays and gamma rays with high efficiency via synchrotron and inverse-Compton processes. Photons which evade absorption via γ-γ

[1]To remain consistent with the SLSNe literature, the term magnetar is used throughout this paper. Magnetars generally have large dipole magnetic fields $B \simeq 10^{13}$ G to 10^{15} G with a rotation period of a few seconds. In the case of the SLSN magnetar model, the radiation is extracted from the rotational energy of the young millisecond pulsars, but with large magnetic fields characteristic of magnetars.

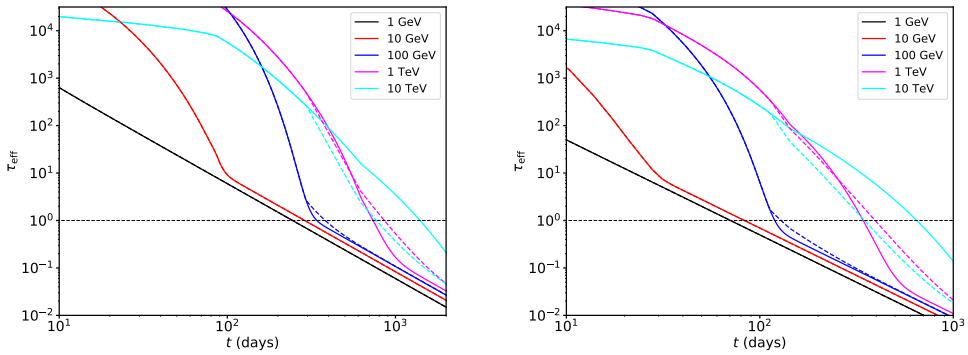

Figure 4.1: Optical depth at different photon energies as a function of time, calculated for ejecta properties (mass $M_\odot$, mean velocity, etc) derived from observations of SN2015bn [115] and SN2017egm [116] shown in Table 4.1. Top: SN2015bn. Bottom: SN2017egm. The horizontal dotted line represents $\tau_{\rm eff} = 1$. The cross-sections for photon-photon and photon-matter pair production opacities are taken from Zdziarski and Svensson [117]. The solid lines correspond to target blackbody radiation temperature $T_{\rm eff} = (L_{\rm opt}/4\pi R^2)^{1/4}$, where $L_{\rm opt}$ and R are the optical luminosity and ejecta radius, respectively. The dashed lines are computed with a temperature floor of $T = 4000$ K, to mimic the approximate spectrum in the nebular phase. Below ~10 GeV the opacity is dominated by photon-matter pair production at all times. Above 100 GeV, pair production on the thermal target radiation field dominates up to a few years.

pair creation in the nebula can be “absorbed" by the ejecta further out, thermalizing their energy and directly powering the supernova’s optical emission (e.g. [110, 112]).

Thermalization of the nebular radiation will be most efficient at early times, when the column through the ejecta shell and “compactness” of the nebula are at their highest. At these times one would expect the optical light curve to faithfully track the energy input of the central engine. However, as the ejecta expand, the radiation field dilutes and the shell becomes increasingly transparent to high-energy and very-high-energy photons. The increasing transparency, and correspondingly decreasing thermalization efficiency, eventually causes the supernova’s optical luminosity to drop below the rate of energy injection from the central engine [113, 114], with the remaining radiation escaping directly from the nebula as gamma rays or X-rays (the putative “missing" luminosity).

As the ejecta expand and the spin down luminosity weakens, the conditions for various processes responsible for photon energy loss change and impact the effective optical depth. Within a few months, the effective optical depth to high-energy (HE; 100 MeV to 100 GeV) photons

emitted from the central engine nears unity, and at several hundred days it reaches unity for very-high-energy (VHE; 100 GeV – 100 TeV) photons.

Figure 4.1 shows examples of the effective optical depth through the ejecta for photons of various energies as a function of time. They have been calculated using time-dependent properties for the supernova ejecta and radiation field motivated by the observations of SN2015bn and SN2017egm, both particularly well-studied SLSNe-I explored in [112].

The dominant processes involved in the calculation of the gamma-ray optical depth include photon-matter and photon-photon interactions, particularly pair production on the nuclei and soft radiation fields in the ejecta. An accurate treatment considering the radiation transport is discussed in depth in Vurm and Metzger [112]. The standard version of the magnetar model [100, 101, 105] does not consider this time-dependent calculation and relies on constant effective opacities to optical and high-energy photons. Figure 4.1 provides a useful guiding timescale for when to consider gamma-ray emission at various energies, calculated with the model in Vurm and Metzger [112] using the ejecta properties fit to the optical data in Table 4.1.

Given its comparatively nearby distance at z=0.1136, SN2015bn is an excellent candidate event to test the magnetar hypothesis. The optical light curve shows a steepening from $\propto t^{-2}$ decay to $\propto t^{-4}$ around ~200 days [115]. This behavior is consistent with a leakage of high-energy radiation from a magnetar nebula [115]. A deep search in the ~0.1 – 10 keV X-ray band resulted in non-detections [118], eliminating the possibility that leakage from the nebula occurs in the softer X-ray bands.

Margutti, Chornock, Metzger, *et al.* [119] present a similar search for late-time X-ray emission from a larger sample of SLSNe-I, mostly resulting in upper limits; however, see Levan, Read, Metzger, *et al.* [120] for an X-ray detection of the SLSN-I SCP 06F6 that could still support the magnetar hypothesis. X-ray non-detections are not surprising, because the ejecta are likely to still be opaque in the $\lesssim$ 10 keV band due to photoelectric absorption in the hydrogen-poor ejecta [121]. Intriguingly, Eftekhari, Berger, Margalit, *et al.* [122] detected radio emission from the location of the SLSN PTF10hgi at 7.5 years after the explosion and argued that the emission could be

synchrotron emission from an engine-powered nebula.

Some effort has been underway to search for nebular leakage in the gamma-ray band. Renault-Tinacci, Kotera, Neronov, *et al.* [123] obtained upper limits on the 0.6 – 600 GeV luminosities from SLSNe by a stacked analysis of 45 SLSNe with *Fermi*-LAT. The majority of their sample were SLSNe-I, the most likely class to be powered by a central engine; however the results were dominated by a single, extremely close Type II event (SLSN-II), CSS140222. Hydrogen-rich SLSNe make up the Type II class (SLSN-II), which are suggested to be powered by the interaction of the circumstellar medium with the supernova ejecta. Nevertheless, even with CSS140222 included, the upper limits are at best marginally constraining on the inferred missing luminosity.

In this paper, the search is expanded to gamma-ray emission from SLSNe-I in the HE to VHE bands using the *Fermi* Gamma-Ray Space Telescope and the ground-based VERITAS observatory. In particular, observations of SN2015bn and SN2017egm are presented here. SN2017egm is the closest SLSN-I to date in the Northern Hemisphere at z=0.0310 [116, 124]. Observations of young supernovae with gamma-ray telescopes have been few, with no detections so far. Some tantalizing candidates like iPTF14hls and SN 2004dj have been explored with *Fermi*-LAT but are unconfirmed due to large localization regions overlapping with other gamma-ray candidates [125, 126]. MAGIC carried out observations of a Type I SN [127]. HESS observed a sample of core-collapse SNe [128], and later obtained upper limits on SN 1987A [129]. Our observations are the first of superluminous supernovae.

Throughout this paper, a flat ΛCDM cosmology is used, with $H_0 = 67.7\,\mathrm{km\,s^{-1}\,Mpc^{-1}}$, $\Omega_M = 0.307$, and $\Omega_\Lambda = 0.6911$ [130]. The corresponding luminosity distances to SN2015 bn and SN2017 egm are 545.37 Mpc (z=0.1136) [131] and 139.29 Mpc (z=0.0310) [124].

4.2 Observations & Methods

The superluminous supernovae SN2015bn and SN2017egm were observed with *Fermi*-LAT and VERITAS during 2015–2016 and 2017–2020, respectively. SN2015bn is a SLSN-I explosion from 23 Dec 2014 (MJD 57014) and it peaked optically on 19 Mar 2015 (MJD 57100) [132].

Table 4.1: Properties of the SLSNe considered in this paper. The quantities P_0, B, $M_{\rm ej}$, κ, $E_{\rm SN}$, $v_{\rm ej}$, κ_γ and $M_{\rm NS}$ were obtained from a best-fit to the UVOIR supernova light curves.

Parameter	[unit]	SN2015bn	SN2017egm
RA	$^\circ$	173.4232	154.7734
Dec	$^\circ$	0.725	46.454
z	-	0.1136	0.0310
$t_0^{(a)}$	MJD	57014	57896
$t_{pk}^{(b)}$	MJD	57100	57922
$P_0^{(c)}$	ms	2.50	5.83
$B^{(d)}$	10^{14} G	0.26	0.94
$M_{ej}^{(e)}$	$M_\odot$	10.8	2.99
$\kappa^{(f)}$	cm^{2}g^{-1}	0.18	0.12
$v_{ej}^{(h)}$	10^8 cm s^{-1}	5.68	10.3
$\kappa_\gamma^{(i)}$	cm^{2}g^{-1}	0.008	0.080
$M_{\rm NS}^{(j)}$	$M_\odot$	1.84	1.57

$^{(a)}$Epoch of explosion; $^{(b)}$Epoch of optical flux peak; $^{(c)}$Initial spin-period; $^{(d)}$magnetic field strength of magnetar; $^{(e)}$Total mass, $^{(f)}$effective opacity; $^{(g)}$kinetic energy; $^{(h)}$mean velocity of supernova ejecta; $^{(i)}$gamma-ray effective opacity; and $^{(j)}$neutron star mass.

SN2017egm is a SLSN-I explosion from 23 May 2017 (MJD 57896) and it peaked optically on 18 Jun 2017 (MJD 57922) [124]. Some properties of the SLSNe are given in Table 4.1. Details regarding the optical, *Fermi*-LAT and VERITAS observations and the data-analysis methods are below.

4.2.1 *Fermi*-LAT

The Large Area Telescope (LAT) on board the *Fermi* satellite has operated since 2008 [17]. It is sensitive to photons between ~20 MeV and ~300 GeV and has ~60° field of view, enabling it to survey the entire sky in about three hours.

The data were analyzed using the publicly available *Fermi*-LAT data with the `Fermitools` suite of tools provided by the *Fermi* Science Support Center (FSSC). Using the `Fermipy` analysis package [19] [2], the data were prepared for a binned likelihood analysis in which a spatial spectral model is fit over the energy bins. The data were selected using the SOURCE class of events, which

[2] https://fermipy.readthedocs.io/en/latest/ ; v0.19.0

are optimized for point-source analysis, within a region of 15° radius from the analysis target position. Due to the effect of the Earth, a 90° zenith angle cut was applied to remove any external background events. The standard background models were applied to the test model, incorporating an isotropic background and a galactic diffuse emission model without any modifications. The standard 4FGL catalog was then queried for sources within the field of view and their default model parameters [16].

Additional putative point sources were added to each field of view as needed to support convergence of the fit. These sources were added for all analysis time scales. This process continued until the distribution of test statistics for the field of view was Gaussian with standard deviation near 1 and mean centered at zero, and the residual maps were near uniformly zero without strong features. These conditions indicate the appropriate coverage of spectral sources within the analysis was reached and no putative sources are missing. The fitting process is performed in discrete energy bins while optimizing the spectral shape, but the distribution of test statistics is evaluated with the stacked data spanning the full energy range. With the improvements to *Fermi*-LAT low-energy sensitivity in PASS8 reconstruction, the low energy bin covering 100 – 612 MeV was also added.

In the case of both SN2015bn and SN2017egm, the data were fitted with a power-law spectral model, $N(E) = N_0 E^{\Gamma}$, with a free prefactor and a fixed photon index Γ of -2. From the fit, the reported flux upper limit was found using a 95% confidence level with the bounded Rolke method [63].

SN2015bn was observed from 23 Mar 2015 to 23 Mar 2018. This observation period begins $\sim$ 4 days after the supernova optical peak, a total of $\sim$ 90 days after the explosion, thus accounting for the absorption of low-energy gamma rays by the ejecta prior to this time (Figure 4.1). The data were thereafter binned in time intervals of six months to maximize observation depth and sensitivity to time dependent variation. SN2017egm was observed 21 Aug 2017 to 21 Aug 2020. This period covers three years from the discovery date, also split into six 6-month bins starting $\sim$ 90 days after the explosion. The three-year observation period is selected to cover approximately 1000 days after the explosion. After this period, it is expected that the predicted luminosity will have

decreased below the *Fermi*-LAT detectable limit.

SN2015bn is within 5° of the Sun each year in August, so a one-month time cut is applied to each relevant time bin (to cover a $\sim$ 15° radius field of view). SN2017egm is not near the the path of the Sun, so this cut was not applied.

4.2.2 VERITAS

The Very Energetic Radiation Imaging Telescope Array System (VERITAS) is an imaging atmospheric cherenkov telescope (IACT) array at the Fred Lawrence Whipple Observatory (FLWO) in southern Arizona, USA [133, 134]. It consists of four 12-m telescopes separated by approximately 100 m, and the observatory is sensitive to photons within the energy range $\backsim$100 GeV to $\backsim$30 TeV. The instrument has an angular resolution (68% containment) of $\backsim$0.1° at 1 TeV, an energy resolution of $\backsim$15% at 1 TeV, and 3.5° field of view.

VERITAS serendipitously observed SN2015bn for a total of 1.01 hours between 7 May 2015 and 22 May, 2015, approximately 135 days from explosion (49 days from the date of peak magnitude), as a part of an unrelated campaign. Another 1.7 hours were taken between 25 May 2016 and 30 May 2016. Data were taken in good weather and dark sky conditions. Since SN2015bn was not the target source, its sky position averages 1.4° from the center of the camera.

VERITAS directly observed SN2017egm for 8.7 hours between 24 Mar 2019 and 5 Apr 2019, under dark sky conditions, as part of a Directors Discretionary Time (DDT) campaign, approximately 670 days from explosion. This target was triggered based on the predicted gamma-ray luminosity (see section 4.4.1 and appendix 4.7 for a description) derived from the optical observation. Although it was almost two years after the explosion, the nearby distance yielded a gamma-ray luminosity prediction still within reach of VERITAS, making this an enticing target to follow up.

The SN2017egm data in this paper were taken using “wobble" pointing mode, where the source is offset from the center of the camera by 0.5°. This mode creates space for a radially symmetric off region to be used for background estimation in the same field of view, saving time from targeted

Table 4.2: Results from VERITAS observations for both epochs of SN2015bn, and SN2017egm. Shown are the quality selected livetime, number of gamma-ray-like events in the on and off-source regions, the normalization, the observed excess of the gamma-rays and the statistical significance. The integral flux upper limit is shown for the given energy threshold, without EBL absorption correction, integrated up to 30 TeV.

Parameter	[unit]	SN2015bn$_1$	SN2015bn$_2$	SN2017egm
Start (MJD)	[day]	57149	57533	58566
End (MJD)	[day]	57164	57538	58578
Livetime	[hour]	1.0	1.8	8.7
On	[event]	4	10	49
Off	[event]	179	188	596
$\alpha^{(a)}$	-	0.0286	0.0299	0.0634
Excess	[event]	-1.1	4.4	11.2
Significance	[σ]	-0.5	1.7	1.6
Flux UL	[10^{-13} cm^{-2} s^{-1}]	29	28	10
$E_{\text{threshold}}$	[GeV]	> 320	> 420	> 350

$^{(a)}$ Ratio of relative exposure for On and Off regions.

background observations that contain the same data observing conditions. The data were processed with standard VERITAS calibration and reconstruction pipelines, and then cross-checked with a separate analysis chain [42, 43].

Using an Image Template Method (ITM) to improve event angular and energy reconstruction [54], analysis cuts are determined with a set of a priori data selection cuts optimized on sources with a moderate power-law index (from -2.5 to -3).

Unfortunately, the large offset on SN2015bn due to the serendipitous observation precludes us from using ITM in the analysis, so in that case SN2015bn is analyzed without templates by calculating image moments directly from candidate images triggered by the camera [42, 43].

The upper limit is calculated for both SN2015bn and SN2017egm. The bounded Rolke method for upper limit calculation is used, assuming a power law spectrum with index of -2.0 and 95% confidence level [63]. In both cases, the signal and background counts are determined using the reflected region method.

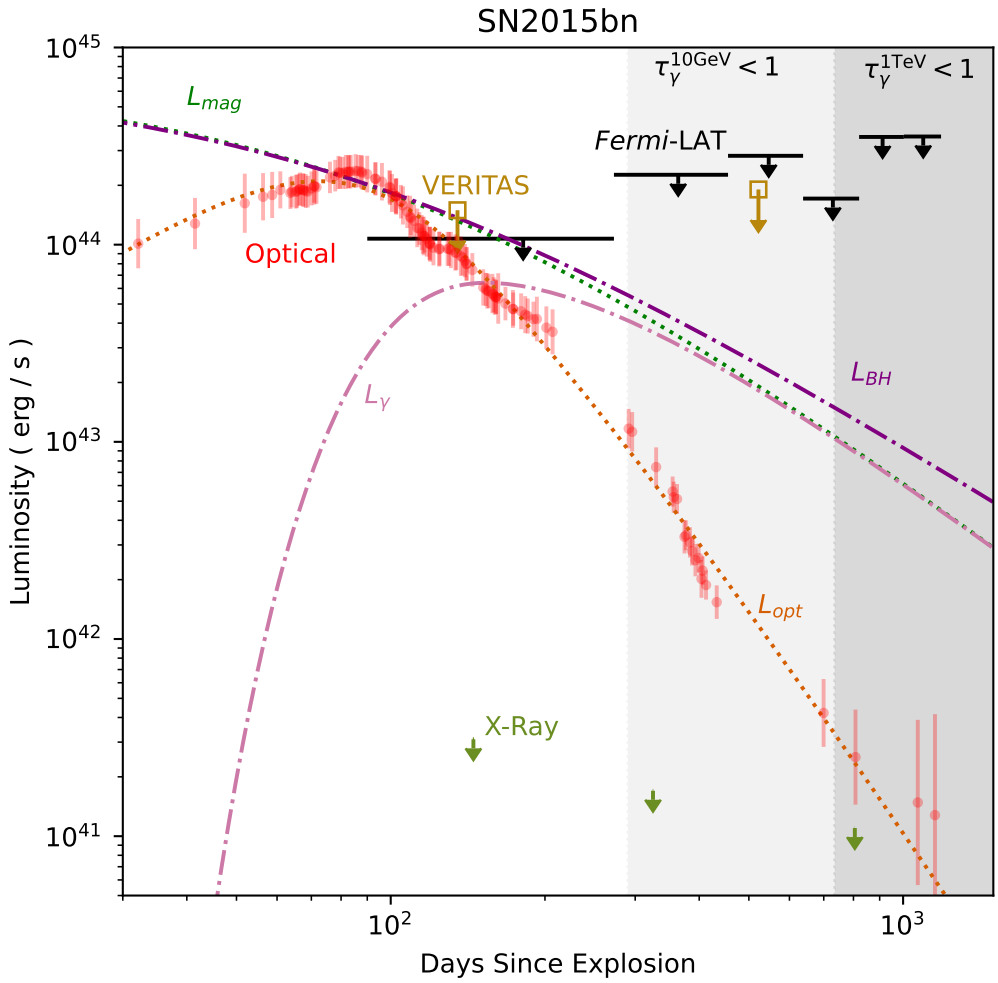

Figure 4.2: Light curves of SN2015bn spanning 30 to 1500 days after explosion. Curves shown include (1) the (thermal) supernova luminosity, $L_{\rm opt}$, fit to UVOIR bolometric luminosity data (in red; [115]) to obtain the magnetar parameters; (2) magnetar spin down luminosity, $L_{\rm mag}$ (green dotted lined); and (3) predicted gamma-ray luminosity that escape the ejecta, L_γ (pink dot-dashed line; Equations 4.2, 4.4 and 4.5). Black bars show *Fermi*-LAT upper limits reported for six 180 day bins starting ~90 days after explosion. The olive open box shows the VERITAS upper limit taken ~135 days after the explosion, with EBL absorption correction applied. Upper limits on the 0.2-10 keV X-ray luminosity from *Chandra* are from Bhirombhakdi, Chornock, Margutti, *et al.* [118] in green. Grey shaded regions labeled "$\tau_\gamma < 1$" show the approximate time after which gamma rays of the indicated energy should escape ejecta, based on Figure 4.1. A purple dot-dashed line shows the engine luminosity, $L_{\rm BH}$ (Eq. 4.1), in an alternative model in which the supernova optical luminosity is powered by fall-back accretion onto a black hole. All upper limits denote the 95% confidence level.

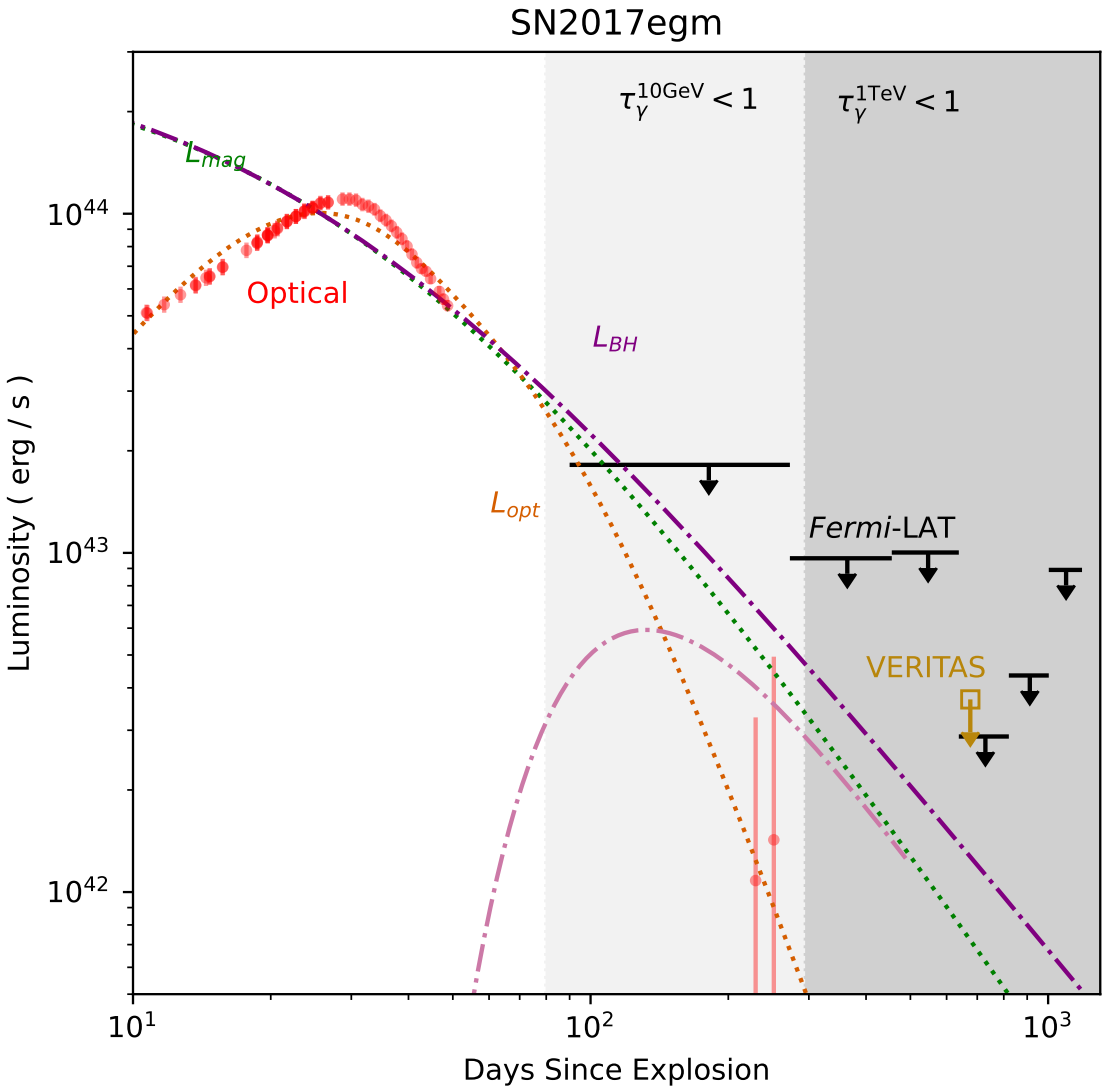

Figure 4.3: The SN2017egm light curve spanning 10 to 1300 days after explosion, following the same format as Figure 4.2. UVOIR data are shown in red [116, 124]. Upper limits from *Fermi*-LAT are reported for six 180 day bins starting ~90 days after the explosion. Upper limits are shown for VERITAS data taken ~670 days after explosion, with EBL absorption correction applied. The maximum luminosity of the black hole accretion model L_{BH} (Eq. 4.1) is shown in purple. All upper limits denote the 95% confidence level.

4.3 Results

No statistically significant detections were made of either SN2015bn or SN2017egm across the energy range 100 MeV to 30 TeV. Upper limits are reported. Figure 4.2 and Figure 4.3 show the *Fermi*-LAT and VERITAS upper limits in comparison to the supernova optical light curves and the theoretically-predicted escaping luminosity from the magnetar model.

4.3.1 Optical

The SN2015bn integrated ultraviolet-optical-infrared (UVOIR) light curve data are reproduced here from previous analyses [115, 131, 132]. To produce these bolometric light curves, the multi-band optical data were interpolated and integrated at each epoch using the code `superbol` [135].

Similarly, the SN2017egm UVOIR data are also reproduced here with `superbol` [116, 124].

4.3.2 *Fermi*-LAT

Both SN2015bn and SN2017egm are not statistically significant sources in the first 6-month bin starting 90 days after the explosion. These sources also remain undetected in any subsequent 6-month bins, and in the multi-year data sets.

SN2015bn is found to have test statistic (TS) of 0.06, with 12 predicted events above the isotropic diffuse background $\simeq 4.8 \times 10^4$ events. The flux upper limit is 1.6×10^{-6} MeV cm^{-2} s^{-1} over the energy range 100 MeVto 500 GeV. For the first 6-month period, when the signal is most likely, the flux upper limit is 1.9×10^{-6} MeV cm^{-2} s^{-1} for $TS \simeq 0$, consistent with a non-detection. All of the following 6-month bins reported non-detections with $TS < 2$.

SN2017egm is found to have $TS = 4.4$, with 43 predicted events above the isotropic diffuse background $\simeq 5.9 \times 10^4$ events. The flux upper limit is 1.2×10^{-6} MeV cm^{-2} s^{-1} over the energy range 100 MeVto 500 GeV. For the first 6-month period, when the signal is most likely, the flux upper limit is 4.9×10^{-6} MeV cm^{-2} s^{-1} for $TS = 10.1$, consistent with a non-detection. All of the following 6-month bins reported non-detections with $TS < 1$.

4.3.3 VERITAS

Table 4.2 reports the results from VERITAS observations of SN2015bn and SN2017egm. Each observation is consistent with a non-detection. The significance of each excess of observed events above background is below 2 standard deviations (sigma). The flux upper limits are also given.

The statistical significance of an excess is estimated using Equation 17 of Li & Ma [58]. SN2015bn has significance value of -0.5σ in the first epoch observation. The integral flux upper limit from 0.32 TeV to 30 TeV for SN2015bn is 2.9×10^{-12} cm^{-2} s^{-1}, which corresponds to an upper limit on the luminosity of 1.3×10^{44} erg s^{-1} at a redshift of 0.1136. Due to the serendipitous nature of the observation, SN2015bn is significantly off-axis, which lowers the instrument sensitivity at the energy threshold of 320 GeV. Additionally, a 10% systematic uncertainty is added to the flux normalization and reported energy threshold due to instrument degradation during the period of 2012-2015 [136]. This uncertainty is derived empirically from the observation of the Crab Nebula over the same period. During the second observation in 2016, SN2015bn was found to have a significance of 1.7. The integral flux upper limit from 0.42 TeV to 30 TeV for SN2015bn is 2.8×10^{-12} cm^{-2} s^{-1}, which corresponds to an upper limit on the luminosity of 1.6×10^{44} erg s^{-1}.

For SN2017egm, the Li & Ma significance value is 0.2σ and an integral upper limit from 0.35 TeV to 30 TeV is 1.0×10^{-12} cm^{-2} s^{-1}, which corresponds to an upper limit on the luminosity of 3.5×10^{42} erg s^{-1} above the energy threshold of 350 GeV at redshift z=0.0310. The systematic correction due to instrument degradation during the period of 2012-2019 is applied automatically with the use of the throughput-calibrated analysis templates [136].

VHE photons are absorbed by the extragalactic background light (EBL) throughout the universe, so the flux must be corrected to account for the missing photons. This absorption is energy and redshift dependent. Deabsorption is applied to the flux using the model of Domínguez, Primack, Rosario, *et al.* [68]. The EBL deabsorption factor was convolved with the upper limit calculation, assuming the same spectral shape (a power law with the photon index of -2.0). The deabsorbed integral photon upper limit for SN2015bn within the energy range 0.32 TeV to 30 TeV, is 3.4×10^{-12} cm^{-2} s^{-1}, which corresponds to a luminosity upper limit of 1.5×10^{44} erg s^{-1}. For the

second observation, the deabsorbed integral photon upper limit for SN2015bn within the energy range 0.42 TeV to 30 TeV, is 3.3×10^{-12} cm^{-2} s^{-1}, which corresponds to a luminosity upper limit of 1.9×10^{44} erg s^{-1}. For SN2017egm, with a slightly smaller energy range 0.35 TeV to 30 TeV, the deabsorbed integral photon flux is 1.1×10^{-12} cm^{-2} s^{-1}, which corresponds to a luminosity upper limit of 3.7×10^{42} erg s^{-1}. These EBL corrected values are plotted in Figure 4.2 and Figure 4.3.

4.4 Discussion

The source of the extra luminosity powering SLSNe-I may be found in the signature of its late time gamma-ray emission. This section explores the HE to VHE emission hundreds of days after the explosion. The following models with a gamma-ray emission component for the powering mechanism are discussed: 1) magnetar central engine (see section 4.4.1), 2) black hole central engine (see section 4.4.2), and 3) circumstellar interaction (see section 4.4.3).

4.4.1 Magnetar Central Engine

The most promising mechanism for powering SLSNe-I is the rotational energy input from a central magnetar. In this scenario, a young pulsar or magnetar inflates a nebula of relativistic particles, which radiate high-energy gamma rays and X-rays. This section initially explores a simple implementation of the magnetar model (see Appendix 4.7 for full description), followed by a more complete, self-consistent model described in detail in Vurm and Metzger [112] for both SN2015bn and SN2017egm.

At early times after the explosion (around and immediately after the maximum in the optical emission) the gamma rays are absorbed and thermalized by the expanding supernova ejecta. At these times, the luminosity and shape of the optical light curve can be used to constrain the parameters of the magnetar. In this model, the radiation of an input energy reservoir (the spin down luminosity of a rotating magnetar) diffuses through the ejecta following the analytical solution by Arnett [137] (equation 4.4).

The time evolution of the magnetar's spin-down luminosity can be modeled by assuming a rotating dipole magnetic field whose energy loss is dominated by emission of radiation in the gamma-ray and X-ray bands (see Appendix 4.7 for details).

This luminosity depends on the magnetar initial spin period, surface dipole magnetic field strength, and neutron star mass, $L_{\rm mag}(t, P_0, B, M_{\rm NS})$ (equation 4.2). The emitted radiation thermalizes as it diffuses through the ejecta. The conditions of the ejecta determine the optical and gamma-ray outputs, dominated by the values of the ejecta mass, ejecta velocity, and optical and gamma-ray opacities to form $L_{\rm opt}(t, M_{\rm ej}, v_{\rm ej}, \kappa, \kappa_\gamma)$ (equation 4.5) and $L_\gamma(t, M_{\rm ej}, v_{\rm ej}, \kappa, \kappa_\gamma)$ (equation 4.6).

For SN2015bn and SN2017egm, the parameters for the magnetar and the supernova ejecta properties were found by fitting their integrated ultraviolet-optical-infrared (UVOIR) light curves, shown with red points in Figure 4.2 and Figure 4.3. All fits were conducted using non-linear least squares minimization[3]. The best-fit parameters for the magnetar model are given in Table 4.1. These are consistent with the results of previous fits [115, 116] that took into account both the optical spectral energy distribution and light curve using the open source code `MOSFiT` [4]. The redshifts and time of peak optical magnitude are shown in the table as listed in The Open Supernova Catalog [138][5].

A particularly important shortfall of this model is the constant effective opacity to both optical and gamma-ray photons, rather than a time-dependent treatment of the opacity. TeV gamma rays interact preferentially with optical photons, so at the time of the peak optical emission, $\gamma\gamma$ absorption by optical photons will be high, reducing any predicted gamma-ray emission by this model. Equation 4.5 is a bolometric luminosity, so it does not take into account the energy and time dependent opacity, instead fitting a constant effective κ and κ_γ to generate the time dependent optical depth.

Therefore, Figure 4.1 is used as a guide for when to expect L_γ to provide an appropriate es-

[3] `scipy.optimize.curve_fit`
[4] https://mosfit.readthedocs.io/en/latest/
[5] https://sne.space

timate for the gamma-ray emission. The shaded regions in Figures 4.2 and 4.3 estimate the time periods when photons of the given energies can escape.

Following the methodology in Appendix 4.7 with the magnetar parameters for each SLSN, $L_{\rm mag}(t)$, $L_{\rm opt}(t)$, and $L_\gamma(t)$ were calculated and are shown in comparison to the gamma-ray limits in Figures 4.2 and 4.3.

For SN2015bn (Figure 4.2), neither the *Fermi*-LAT upper limits nor the VERITAS upper limit constrain the predicted escaping luminosity. Similarly, for SN2017egm (Figure 4.3), both the VERITAS and *Fermi*-LAT upper limits are not deep enough to constrain the predicted escaping luminosity. An important caveat to these upper limits is that the escaping luminosity may also be emitted at energies not explored here, such as hard X-rays or gamma-rays greater than 30 TeV.

The optimal time to observe with a pointed instrument sensitive at a particular photon energy results from a trade-off between the dropping ($\propto t^{-2}$) magnetar luminosity and the rising transparency of the ejecta; predicting the optimal time post-peak to observe requires knowledge of the evolution of the optical spectrum. It is possible to accumulate enough optical data within a few weeks after the optical peak to fit the magnetar model for a reliable prediction of the gamma-ray luminosity. In the case of SN2017egm, the gamma-ray luminosity prediction was anchored by the late optical data points about 1 year after the explosion. This means that had the VERITAS observations been taken at that point (more than a year earlier than the original observation), they would have been deeply constraining to the magnetar model.

Going beyond these relatively model independent statements to compare to a more specific spectral energy distribution for the escaping magnetar nebula requires a detailed model for the nebula emission and its transport through the expanding supernova ejecta. Such a model offers preliminary support that a significant fraction of L_γ may come out in the VHE band [112]. In this case, the VHE limits on SN2015bn and SN2017egm do not strongly constrain the parameters of the magnetar model, such as the nebular magnetization.

The model of Vurm and Metzger [112] self-consistently follows the evolution of high-energy electron/positron pairs injected into the nebula by the magnetar wind and their interaction with the

broadband radiation and magnetic fields. They found that the thermalization efficiency and the amount of gamma-ray leakage depends strongly on the nebular magnetization, ε_B, i.e. the fraction of residual magnetic energy in the nebula relative to that injected by the magnetar.

The model is simulated for dimensionless ε_B values set between 10^{-6} and 10^{-2}; the higher magnetizations lead to greater synchrotron efficiencies, which dominate within a few hundred days, and lead to the optical emission tracking the spin-down luminosity. Lowering the magnetization to 10^{-7} – 10^{-6} for SLSN-I events like those in this work delays the transition to synchrotron-dominated thermalization, so that the predicted optical emission actually tracks the observed data.

The theoretical light curves and gamma-ray upper limits are shown in Figure 4.4. Vurm and Metzger [112] concluded that the predicted low magnetizations constrained by the optical data alone presents new challenges to the theoretical framework regarding the dissipation of the nebular magnetic field. This may invoke magnetic reconnection ahead of the wind termination shock or near the termination shock through forced reconnection of alternating field stripes described in Komissarov [139], Lyubarsky [140], Margalit, Metzger, Thompson, *et al.* [141]. It is also possible that the true luminosity of the central engine decreases faster in time than the simpler $\propto t^{-2}$ magnetic spin down, such that escaping VHE emission is not necessary to explain the model. These VHE upper limits do not rule out this model, and do not settle the challenges inferred by the low magnetization required to fit the optical data. Further observations are needed to probe the nebular magnetization and synchrotron efficiency, and deep VHE observations will contribute to these constraints.

4.4.2 Black Hole Central Engine

Instead of forming a neutron star like a magnetar, a SLSN-I might form a black hole, in which case the optical peak of the light curve could be powered by energy released from the fallback accretion of ejecta from the explosion (e.g. [142]). Even if a black hole does not form immediately, it could form at late times once the magnetar accretes enough fallback material [143]. The main practical difference as compared to a magnetar in section 4.4.1 is that the black hole central engine

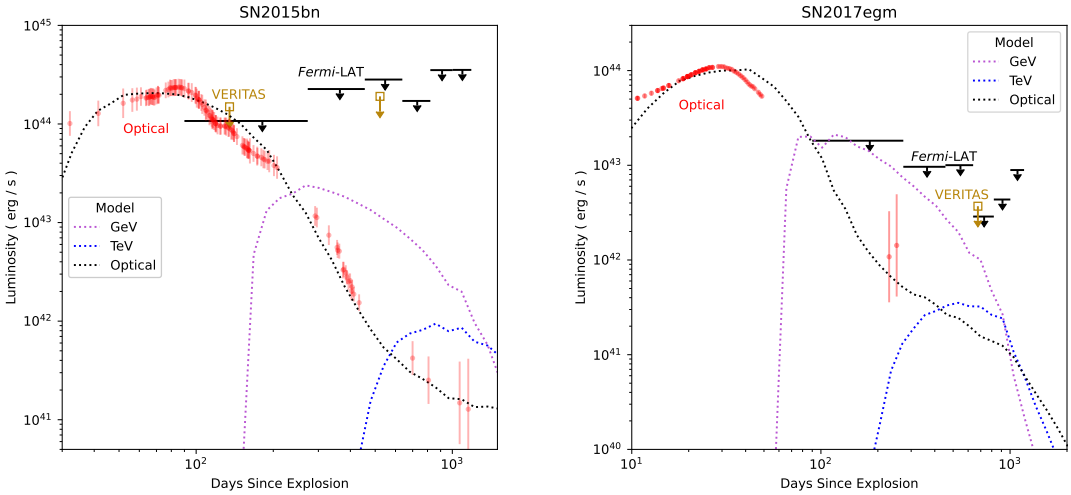

Figure 4.4: Model light curve for nebular magnetization (from [112]) for SN2015bn with $\varepsilon_B = 10^{-7}$ (top panel) and SN2017egm with $\varepsilon_B = 10^{-6}$ (bottom panel).

power would be predicted to decay with the fall-back accretion rate $\dot{M}_{\rm fb} \propto t^{-5/3}$ instead of $\propto t^{-2}$. Thus, in principle, for the same luminosity at the time of the optical maximum $t_{\rm pk}$, the central engine output at times $t \gg t_{\rm pk}$ could be enhanced by a factor $\propto (t/t_{\rm pk})^{1/3} \sim 2$ for $t \sim 1$ year and $t_{\rm pk} \sim 1$ month, thus tightening our constraints.

In Figures 4.2 and 4.3, a rough estimate of the maximal engine luminosity in the BH accretion scenario is shown, which is calculated as

$$L_{\rm BH} = \frac{2^{5/3} L_{\rm opt}^{\rm pk}}{\left(1 + \frac{t}{t_{\rm pk}}\right)^{5/3}}, \tag{4.1}$$

where $L_{\rm opt}^{\rm pk}$ is the peak optical luminosity, scaled so that $L_{\rm BH} = L_{\rm opt}$ around the optical peak.

On the other hand, while gamma rays are naturally expected from the ultra-relativistic spin-down powered nebula of a magnetar, it is less clear this would be the case for a black hole engine. For instance, the majority of the power from a black hole engine could emerge in a mildly relativistic wind from the black hole accretion disk instead of an ultra-relativistic spin-down powered pulsar wind.

As seen in both Figure 4.2 (SN2015bn) and Figure 4.3 (SN2017egm), the gamma-ray emission in the black hole scenario is not constrained in the *Fermi*-LAT and VERITAS energy bands.

4.4.3 Circumstellar Interaction

An alternative model for powering the light curve of SLSNe is to invoke the collision of the supernova ejecta with a slower expanding circumstellar shell or disk surrounding the progenitor at the time of the explosion (e.g. [144–146]). Features of this circumstellar model (CSM), such as the narrow hydrogen emission lines that indicate the interaction of a slow-moving gas, provide compelling evidence for this being a powering mechanism for many but not all of the hydrogen-rich class of SLSNe (SLSNe-II; e.g. [147, 148]).

Shock interaction could in principle also power some hydrogen-poor SLSNe (SLSNe-I), particularly in cases where the circumstellar interaction is more deeply embedded and less directly visible (e.g. [149, 150]). There is growing evidence for hydrogen-poor supernovae showing hydrogen features from the interaction in their late-time spectra [151–156]. The light echo from iPTF16eh [93] implies a significant amount of hydrogen-poor circumstellar medium in a SLSN-I at $\sim 10^{17}$ cm. However, this material is too distant for the ejecta to reach by the time of maximum optical light and hence cannot be responsible for boosting the peak luminosity.

In principle, the gamma-ray observations of SLSNe can constrain shock models. In many cases, this may not work out since most of the emission from shock-heated plasma is either expected to: (1) come out in the X-ray band, as is well studied in other CSM-powered supernovae such as SNe IIn like SN 1998S [157], SN 2006jd [158], and SN 2010jl [159], and SNe Ib/c [160]; or (2) be absorbed by the surrounding ejecta and reprocessed into the optical band. Thus, these VHE limits on SLSNe do not constrain the bulk of the shock power.

Higher-energy radiation can be produced if the shocks accelerate a population of non-thermal relativistic particles which interact with ambient ions or the supernova optical emission to generate gamma rays (e.g. via the decay of π^0 generated via hadronic interactions with matter and radiation; e.g., [161]). However, because shocks typically place a fraction $\epsilon_{\rm rel} \lesssim 0.1$ of their total power into

relativistic particles (or even less; [162, 163]), the predicted gamma-ray luminosities (matching the same level of optical emission as magnetar models) would be at least 10 times lower than L_γ predicted by the magnetar nebula scenario, thus rendering our VHE upper limits unconstraining on non-thermal emission from shocks on SN2015bn and SN2017egm. This is consistent with upper limits from the Type IIn SN 2010j from *Fermi*-LAT, which Murase, Franckowiak, Maeda, *et al.* [164] used to constrain $\epsilon_{\rm rel} \lesssim 0.05 - 0.1$.

4.5 Future Prospects

These results demonstrate that high-energy gamma-ray observations of SLSN-I are on the brink of enabling constraints on the light curves and even spectral energy distribution of magnetar models. Given the rarity of bright, nearby SLSN-I, and the need to take observations in the optimal window (when L_γ is near maximum), careful planning will be required to make progress going ahead [88, 165, 166]. The strategy outlined below will focus only on SLSN-I, as type II SLSN are likely to be powered by a mechanism that requires a different consideration of the temporal and spectral evolution of the gamma-ray emission.

Standard arrays of IACTs provide an improved instantaneous sensitivity to gamma-ray emission over *Fermi*-LAT due to 10^4 to 10^5 larger effective area, counterbalanced in part by the pointed nature of their observations. To propose a strategy, we firstly re-visited the characteristics of a large sample of observed SLSNe and performed a systematic study.

Nicholl, Guillochon, and Berger [105] fit a sample of 38 SLSNe light curves using MOSFiT to obtain a distribution of magnetar model parameters. This sample is a selection of SLSNe with well observed events classified as Type-I with published data near the optical peak, forming a representative sample of good SLSNe-I for a population study. For each event in this sample, the following was calculated: the escaping gamma-ray luminosity L_γ following the procedure outlined in Appendix 4.7 and the flux $F_\gamma = L_\gamma / 4\pi D_{\rm L}^2$ based on the source luminosity distance D_L. In performing this analysis, rather than fitting the value of κ_γ individually to each optical light curve (as done in [105]), the value $\kappa_\gamma = 0.01\,{\rm cm^2 g^{-1}}$ is fixed in all events, based on the best-fit to

SN2015bn (given its particularly high-quality late-time data, which provides the most leverage on κ_γ).

The results for $F_\gamma(t)$ are shown in the top panel of Figure 4.5. In the magnetar model, the predicted gamma-ray flux could emerge anywhere across the HE to VHE bands and hence it represents an upper limit on flux in the bands accessible to *Fermi*-LAT and IACTs. The bottom two panels of Figure 4.5 show the distribution of the peak escaping flux $F_{\gamma,\mathrm{max}}$ and time of the peak flux relative to the explosion. For most SLSNe-I presented here, $F_{\gamma,\mathrm{max}}$ is well below the sensitivity of VERITAS and even the future Cherenkov Telescope Array (CTA) [71]. Also note that the characteristic timescale to achieve the peak gamma-ray flux is $\approx 2-3$ months from the explosion. This timescale occurs approximately at the same time as when the optical depth of the ejecta to VHE emission falls below unity, when the VHE photons can escape (Figure 4.1).

Figure 4.6 shows $F_{\gamma,600\mathrm{d}}$ as a function of the peak optical magnitude of the SLSNe-I from the same sample as in Figure 4.5. The selection of fluxes at 600 d approximates the time when the effective opacity to 1 TeV photons reaches 1, based on Figure 4.1. The top axis also gives the all-sky rate of SLSNe-I above a given peak optical magnitude, which is estimated using the magnitude distribution of SLSNe-I and assuming they occur at a comoving volumetric rate of $R(z) = 19(1+z)^{3.28}\,\mathrm{Gpc^{-3}\,yr^{-1}}$ following De Cia, Gal-Yam, Rubin, *et al.* [92], Lunnan, Chornock, Berger, *et al.* [93], and Nicholl, Williams, Berger, *et al.* [167]. This estimation captures the general volumetric rate of events, but is unreliable for exceptionally bright events such as SN2017egm due to the small population for estimating the magnitude normalization. A bright event like SN2017egm may actually happen more often than once a century.

Shown for comparison in Figure 4.6 are the integral sensitivities of various gamma-ray instruments for different exposures. For IACT instruments such as VERITAS and the future CTA, sensitivity is defined as the minimum flux necessary to reach 5σ detection of a point-like source, requiring at least 10 excess gamma rays and the number of signal counts at least 5% of the number of background counts. For VERITAS, the sensitivity was calculated using observed Crab Nebula data to estimate the rates of signal and background photons with cuts optimized for a $\Gamma = -2.5$

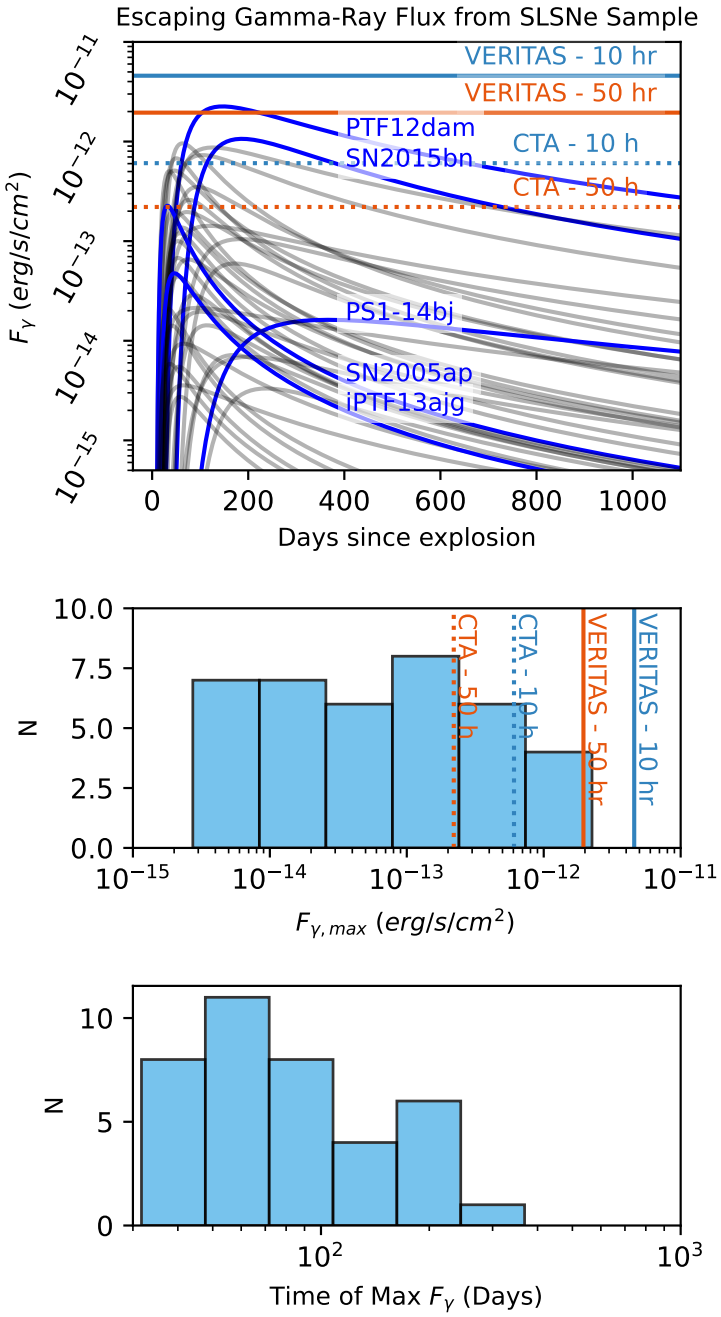

Figure 4.5: Top: Escaping gamma-ray luminosity $L_\gamma(t)$ for the sample of SLSNe fit by Nicholl, Guillochon, and Berger [105]. Five well studied SN are highlighted in blue, including SN2015bn. Overplotted are the VERITAS and CTA sensitivity curves for various exposures. Middle: Distribution of peak escaping gamma-ray flux $F_{\gamma,\max} = \max[L_\gamma]/4\pi D^2$, for the light curves from the top panel where D is the distance to each source. Again, VERITAS and CTA sensitivities for different exposures are shown as vertical dashed lines. Bottom: Distributions of times since explosion to reach the maximum gamma-ray flux $F_{\gamma,max}$ from F_γ above.

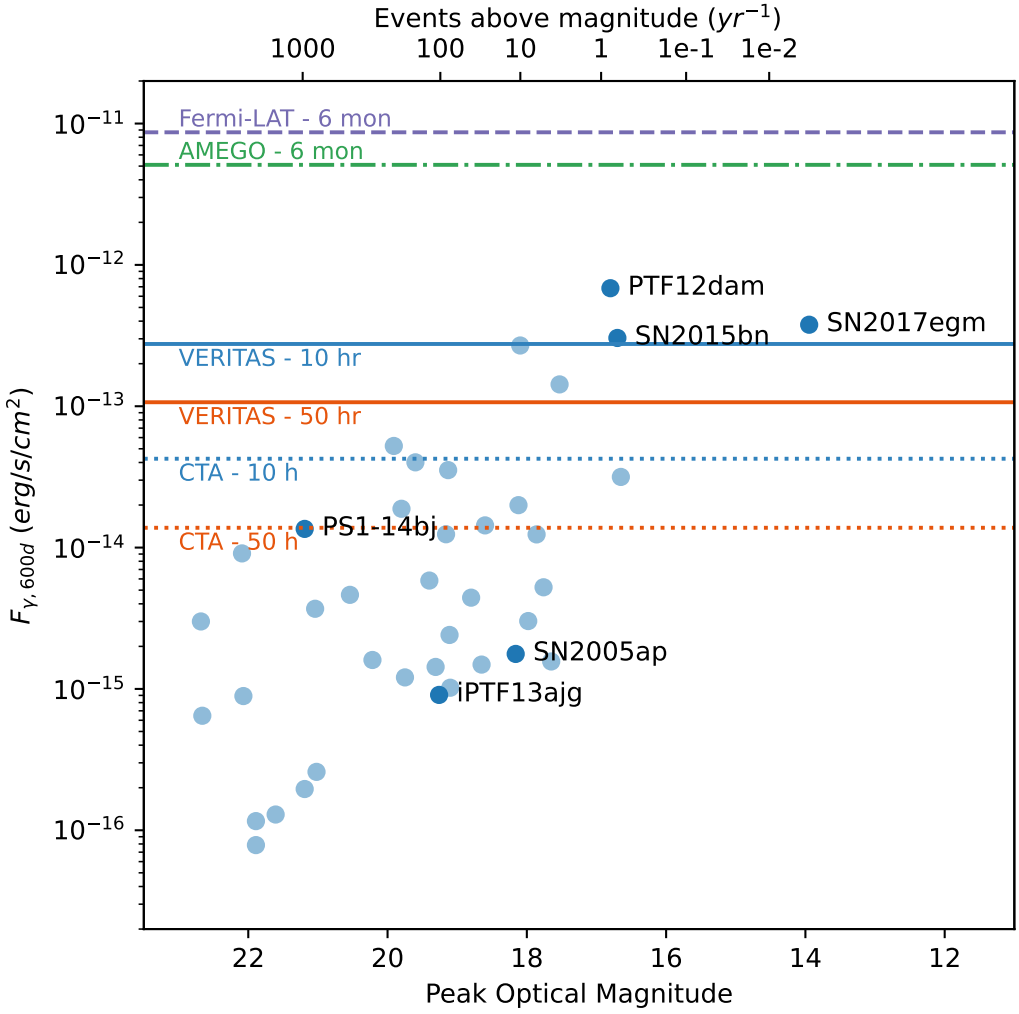

Figure 4.6: Blue dots show the peak optical apparent magnitudes of a sample of SLSNe-I [105] as a function of their predicted maximum gamma-ray luminosity at 600 days after explosion ($F_{\gamma,600d}$). The top axis shows the approximate rate of events above the given peak optical magnitude, calculated using the method described in the main text. Peak maximum gamma-ray luminosities are calculated from fits of optical data with fixed $\kappa_\gamma = 0.01$ cm^2 g^{-1}. Integral sensitivities of various instruments are overplotted for different exposures. Solid lines: VERITAS 10 and 50 hour integral sensitivities above 220 GeV. Dotted lines: CTA (in development) 10 and 50 hour integral sensitivities above 125 GeV as estimated from 50 hour Monte Carlo simulations of the southern array [71] and extrapolated to 10 hours. Similar extrapolation is done for *Fermi*-LAT from 10 years to 6 months [18] (dashed line). Proposed project AMEGO integral sensitivity above 100 MeV for 6 month observation window is also plotted (dash-dot line) [168].

power-law spectrum, and then re-scaled for the appropriate observation time [169]. For CTA, Monte Carlo simulations were used to derive angular resolution, background rates and energy dispersion features – the instrument response functions (IRF) – based on the Prod3b-v2 telescope configuration for the Southern site and its atmosphere [170]. These IRFs are publicly available and were analyzed using the open-source CTOOLS[6] [171]. A power law spectral model was used to estimate the integral sensitivity above 0.125 TeV and 1 TeV each for observations of 10 h and 50 h (see [172] for further discussion on CTA integral sensitivity).

Based on this systematic study, we propose the following observation strategy: 1) Receive automated public alert and Type I classification of SLSN from a survey instrument such as the Zwicky Transient Facility (ZTF). Classification is generally determined by identification of early spectral components such as OII absorption features. 2) During the multi-day rise and fall of bolometric optical light curve, fit the magnetar model ($L_{\rm opt}$, yielding parameters for $L_{\rm mag}$ and L_γ) 3) Compare L_γ to the telescope sensitivity at the appropriate day when the effective γ-γ opacity falls below ~ 1 for the telescope's sensitive energy range (see Figure 4.1). In the case of IACTs sensitive to energies above 100 GeV, the gamma rays will escape the magnetar a few hundred days after explosion, requiring a bright SLSN-I that will power gamma rays for as much as two years.

Estimating ~35% of all-sky visibility at VERITAS due to Sun, Moon, and seasonal weather cut, and above 60° elevation, VERITAS is capable of detecting up to ~0.4 and ~4 SLSNe-I per year for 10 h and 50 h exposures, respectively. The next-generation CTA observatory will be able to detect as many as ~8 and ~80 events for 10 hr and 50 h, respectively, assuming a larger sky visibility fraction of ~80% when both North and South arrays are included. On the other hand, SLSNe at greater distances also imply a stronger role of $\gamma - \gamma$ interactions on the EBL in suppressing the $\gtrsim$ TeV emission, decreasing the observed integral flux by as much as 60 times at redshifts near 0.5 in the VERITAS energy range.

Figure 4.7 shows the distribution of fluxes at 200 d and 600 d which are approximate average dates when the opacity to 100 GeV and 1 TeV photons falls below 1, respectively, and they are

[6] http://cta.irap.omp.eu/ctools/

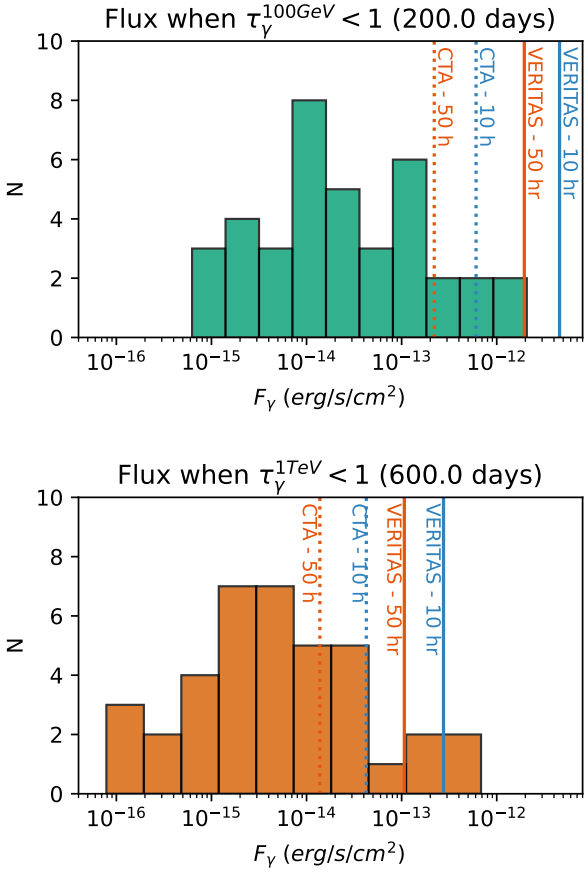

Figure 4.7: Distribution of gamma-ray luminosities L_γ at $t = 200\,\mathrm{d}$ (top) and $t = 600\,\mathrm{d}$ (bottom), when the optical depth for 100 GeV and 1 TeV photons drops below 1, calculated for a sample of 38 SLSNe [105]

able to escape the ejecta. Accounting for this time delay for the opacity to drop, the expected rate of bright events drops by another 3 to 15 times. While past observations have not been followed up until this publication, the distribution of predicted gamma-ray fluxes hints that, particularly for 100 GeV photons, future SLSN-I will be observable with current and planned observatories.

4.6 Conclusion

SLSN-I are potential gamma-ray emitters, and this paper provides the first upper limits at different times after the optical outburst for two good candidates. The reported upper limits approach the magnetar spin-down luminosity limit of SN2015bn and SN2017egm. While the expected gamma-

ray luminosity in either the magnetar central-engine scenario or the shock-acceleration scenario is not constrained by these limits, a relativistic jet powered by fall-back accretion onto a black hole is disfavored in both cases. We explore prospects for obtaining improved VHE gamma-ray constraints in the future by current and planned IACTs. We estimate the Type-I SLSNe rate for VERITAS and CTA, considering observation constraints and the time delay due to the optical depth. For sufficiently nearby and bright SLSN-I, 0.4 and 4 events per year can be observed by VERITAS from 10-hr and 50-hr observation, respectively, and similarly rates of 8 and 80 events per year can be expected by CTA.

4.7 Magnetar Light Curve Model

Following Woosley [101] and Kasen and Bildsten [100], the spin-down power of a strongly magnetized, young neutron star ("magnetar") at a time t after its birth is given by the magnetic dipole luminosity,

$$L_{\rm mag}(t) = \frac{E_{\rm rot}}{\tau_p}\frac{2}{(1+2t/\tau_p)^2}. \tag{4.2}$$

Here, $E_{\rm rot} = (1/2)I_{\rm NS}\Omega_i^2 \approx 2.6\times10^{52}(M_{\rm NS}/1.4M_\odot)^{3/2}P^{-2}$ erg is the magnetar rotational energy, $I_{\rm NS}$ is its moment of inertia, and $M_{\rm NS}$ is the neutron star mass. The spin-down time is given by $\tau_p = (6I_{\rm NS}c^3/B^2R_{\rm NS}^6\Omega_i^2) \approx 1.3\times10^5 B_{14}^{-2}P^2\,(M_{\rm NS}/1.4M_\odot)^{3/2}\sin^{-2}\left(\theta_{B_\perp}=90^\circ\right)$ s, where $B = 10^{14}B_{14}$ G is the dipole magnetic field strength, P (ms) is the birth spin period ($\Omega = 2\pi/P$ is the birth angular velocity), and $\theta_{B_\perp}$ is the inclination angle of the magnetic dipole axis relative to the rotation axis.

Magnetar energy deposited behind the ejecta shell is assumed to thermalize and then diffuse outwards through the ejecta as electromagnetic radiation. This occurs over a characteristic diffusion time [137]

$$\tau_m = \left(\frac{2\kappa M_{\rm ej}}{\beta c v}\right)^{1/2}, \tag{4.3}$$

where $M_{\rm ej}$, v, and κ are the total mass, mean velocity, and (optical wavelength) opacity of the supernova ejecta, respectively, and $\beta \approx 13.7$ is a constant. In most cases, $\tau_{\rm m}$ sets the peak timescale of the supernova light curve.

To allow for the possibility that high-energy photons from the central magnetar nebula can escape instead of thermalizing, one can apply a trapping coefficient $(1-e^{-\tau_\gamma})$ where the optical depth of the ejecta to gamma-rays can be written as $\tau_\gamma = At^{-2}$, where $A \equiv (3\kappa_\gamma M_{\rm ej}/4\pi v_{\rm ej}^2)$ and

κ_γ is an effective gamma-ray opacity [173, 174]. For large $\tau_\gamma \gg 1$ (early times), the effects of gamma-ray leakage are small and the optical light curve (after the optical peak, at times $\gtrsim \tau_{\rm m}$) will follow the spin-down luminosity, i.e. $L_{\rm opt} \approx L_{\rm mag}$. However, at late times when $\tau_\gamma \ll 1$, one has $L_{\rm opt} \ll L_{\rm mag}$, with the remaining luminosity $L_\gamma = L_{\rm tot} - L_{\rm opt}$ escaping as gamma rays.

More precisely, the luminosity of the magnetar (eq. 4.2) that escapes the ejecta via photon diffusion by time t is calculated by [90, 137]

$$L_{\rm tot}(t) = \frac{2}{\tau_m} e^{-\left(\frac{t}{\tau_m}\right)^2} \times \int_0^t {\rm d}t' L_{\rm mag}(t') e^{\left(\frac{t'}{\tau_m}\right)^2} \frac{t'}{\tau_m} \tag{4.4}$$

Of this total luminosity, only a fraction is able to thermalize and hence power the optical supernova light curve,

$$L_{\rm opt}(t) = (1 - e^{-At^{-2}}) L_{\rm tot}(t), \tag{4.5}$$

with the remainder instead escaping as gamma-rays,

$$L_\gamma = L_{\rm tot} - L_{\rm opt} = e^{-At^{-2}} \frac{2E_p}{\tau_{\rm p}\tau_m^2} e^{-(\frac{t}{\tau_{\rm m}})^2} \int_0^t {\rm d}t' \frac{2}{(1 + 2t'/\tau_{\rm p})^2} e^{\left(\frac{t'}{\tau_{\rm m}}\right)^2} t' \tag{4.6}$$

Chapter 5: Novae

The following chapter is a draft manuscript of a VERITAS paper to be submitted. Elements of the analysis and discussion are still in development.

5.1 Introduction

Determining the origin of cosmic-rays has long been a goal of high-energy astrophysics. The cosmic-ray spectral energy distribution follows a power-law model that hints at shock-driven acceleration of particles. These shock environments accelerate relativistic lepton and hadron particles and can produce non-thermal radiation via inverse-Compton (IC) and synchrotron processes to very high energy (VHE; E >100 GeV). Novae are candidate sources that can contribute to the cosmic-ray spectrum.

Classical novae are a sub-type of cataclysmic variables (CV), which are binary star systems composed of a white dwarf star and a low mass, main sequence companion star [175]. In this system, hydrogen accretes onto the surface of the white dwarf that the bottom layer gets hot enough to begin nuclear fusion. The heat from the fusion triggers a thermonuclear runaway (TNR) that drives the ejection of mass along the accretion disk, generating a shock between the ejected mass and either the companion star's wind or other ambient material. High energy (HE; E >100 MeV) and VHE photons detected from these bursts may indicate indicate that particle acceleration is going on at the shock, despite it being a very different kind of environment (e.g. much higher density) than other shocks where particle acceleration was already known to occur, like in supernova remnants.

Observations by the *Fermi* Large Area Telescope have shown that many classical novae emit in the HE range [176–178]. The ratio of gamma-ray to optical flux of ASASSN-16ma measured by [179] shows remarkable stability, suggesting the optical flux is reprocessed emission from the same population of shock-accelerated particles that produce the gamma rays.

Further modeling power was gained by the VHE observation of V407 Cyg by VERITAS, which constrained the maximum energy of synchrotron and IC relativistic particles [180]. The derived upper limit of the VHE observation of V339 Del by MAGIC constrained the ratio of proton to electron luminosities to $L_p \lesssim 0.15 L_e$ [181].

Contrasted with classical novae, dwarf novae are generally less bright outbursts (about 100

times weaker) with different burst timescales [182]. Dwarf novae have a low-mass secondary, such as a red dwarf, accreting onto the white dwarf through an inner Lagrange point. The magnetic fields are weaker than other CVs, while the orbital period between the white dwarf and companion star are a few hours due to the close binary separation.

In recent years, objects with large-amplitude outbursts (typically $\backsim$ 8 mag, at least greater than 6 mag) that exhibit early superhumps at least for several days during the early stage of long outbursts have been unambiguously classified as WZ Sge-type dwarf novae [182]. AT2021afpi was discovered and classified as a WZ Sge-type dwarf novae, following a serendipitous follow-up on an IceCube neutrino event.

Observations of classical and dwarf novae with gamma-ray telescopes have not led to many unambiguous detections of VHE photons. Similar to the difficulty in detecting GRBs, statistically significant detections of classical novae emission by VHE observatories have not yet occurred due to the challenge of fast follow-up of these rare events ($5\,\mathrm{yr}^{-1}$ to $15\,\mathrm{yr}^{-1}$) after optical triggering. Luck and timing play a significant role in observing the brightest event at the earliest time possible.

On the other hand, a separate class of cataclysmic variable has been observed in the VHE. A recent detection of TeV photons from RS Oph, a symbiotic nova, was made by HESS and MAGIC [183, 184]. This is the first significant detection of a nova by a VHE telescope, and although it is a different nova subtype, it generates enthusiasm in the possible detection of VHE photons in classical novae. This work is an effort to follow up the most promising candidates observed by VERITAS since the observation of Nova V407 Cyg in Aliu, Archambault, Arlen, *et al.* [180].

5.2 Observations & Methods

The three events reported here are Nova Perseus 2020, Nova Herculis 2021 and AT2021afpi. Both Nova Perseus 2020 and Nova Herculi 2021 were classified as classical novae which triggered VERITAS follow-up observation. The VERITAS observation of Nova Her 2021 was triggered by a very bright *Fermi*-LAT detection [185].

Nova Per 2020 was discovered on 2020-11-27 05:31:12.000 UTC (59 180.23 MJD) at 04 29

18.85 +43 54 23.0 within the Perseus constellation. Nova Her 2021 was discovered on 2021-06-12 12:53:16.800 UTC (59 377.54 MJD) at 18 57 30.98 +16 53 39.6 within the Herculis constellation. AT2021afpi was a dwarf nova discovered on 2021-11-26 19:48:59.616 UTC (59 544.83 MJD) at 03 02 27.34 +19 17 54.7 [186].

5.2.1 Nova Per 2020

The optical observation is summarized with AAVSO data in appendix Table B.1. Nova Perseus 2020 is also known as *TCP J04291884+4354232* and V1112 Per. [AAVSO Page[187] and WIS-TNS catalog entry.]

Nova Per 2020 is a classical nova with blue shifted velocity of ~500 km s^{-1} [188, 189]. The velocity increased on the following day to ~1500 km s^{-1} [190–192].

5.2.2 Nova Her 2021

Nova Her 2021 is the fastest nova on record, with velocities reaching 11 000 km s^{-1} [193–196]. It peaked at 6 mag and was ultimately classified as a neon classical nova following additional detections of FeII emission lines [197–200]. Two additional features are remarkable: the early detection of X-rays by Swift led to a classification as a supersoft source (SSS) [201, 202], and the detection of a periodic signal lasting ~500 s in the r-band and in X-rays [196, 201, 203–206].

It is interpreted to be an intermediate polar system (IP). The near-infrared measurement of early multiple coronal line emission on day 28 implied parcels of gas in the ejecta having widely different velocities [207]. In addition, the detection spanned radio [208, 209] to gamma-rays [185, 210]. The variation in periodic signal between optical and X-ray measurements implies either the loss of angular momentum due the ejection of mass, shock height modulation due to the thermonuclear runaway (TNR) in the WD envelope, or the co-rotation of the WD and the photosphere at different angular velocities due to the weakening magnetic field radially along the WD envelope [196].

The optical observation is summarized with AAVSO data in appendix Table B.2. Nova Herculi 2021 is also known as V1674 Her. Below are snippets of the ATels. [AAVSO Page and Lasair

Page (ZTF).]

5.2.3 AT2021afpi

Originally, there was an IceCube GCN for event IceCube-211125A, with event energy at 117 TeV [211]. [AAVSO Page and WIS-TNS catalog entry] While following up the IceCube source candidate, MASTER optical telescope found a coincident source nearby that was brightening at the same time to 10 magnitude [186]. The optical source was initially considered a possible counterpart to the IceCube event, but the optical data showed a spectrum containing strong Balmer lines, HeI and HeII, suggesting a young He/N classical nova of Galactic origin[1] [212]. Further optical follow up classified AT2021afpi as a WZ Sge-type dwarf nova [213, 214]. Neither ANTARES nor HAWC found significant emission, de-associating from the original IceCube candidate source [215–218], but X-ray emission was detected [219–221]. The original VERITAS upper limit results based on 1.5 hr pointed at IceCube-211125A and 4.0 hr on AT2021afpi were reported [222].

5.2.4 *Fermi*-LAT

The Large Area Telescope (LAT) on board the *Fermi* satellite has operated since 2008 [17]. It is sensitive to photons between ~20 MeV to ~300 GeV and has a ~ 60° field of view, enabling it to survey the entire sky in about three hours.

The data was analyzed using the publicly available *Fermi*-LAT data with the `Fermitools` suite of tools provided by the *Fermi* Science Support Center (FSSC). Using the `Fermipy` analysis package [19] [2], the data were prepared for a binned likelihood analysis in which spatial and spectral models are fit over the field of view and energy bins. The data were selected using the SOURCE class of events, which are optimized for point-source analysis, within a region of 15° radius from the analysis target position. Due to the effect of the Earth, a 90° zenith angle cut was applied to remove any external background events. The standard background models were applied to the test model, incorporating an isotropic background and a Galactic diffuse emission model provided by

[1] https://www.wis-tns.org/object/2021afpi
[2] https://fermipy.readthedocs.io/en/latest/

Fermi-LAT without any modifications. The standard 4FGL catalog was then queried for sources within the field of view and their default model parameters [16].

Additional putative point sources were added to each field of view as needed to support convergence of the fit. These sources were added to the relevant six-month time bins and full observation period. This process continued until the distribution of test statistics for the field of view was Gaussian with standard deviation near 1 and mean centered at zero, and the residual maps were near uniformly zero without strong features. These conditions indicate the appropriate coverage of spectral sources within the analysis was reached and no putative sources are missing. The fitting process is performed in discrete energy bins while optimizing the spectral shape, but the distribution of test statistics are evaluated with the stacked data spanning the full energy range.

5.2.5 VERITAS

The Very Energetic Radiation Imaging Telescope Array System (VERITAS) is a ground-based Imaging Atmospheric Cherenkov Telescope (IACT) at the Fred Lawrence Whipple Observatory (FLWO) in southern Arizona, USA [134]. It consists of four 12-m Davis-Cotton telescopes sensitive to 100 GeV to >30 TeV photons. With the 100-meter separation between telescopes, the original gamma-ray Cherenkov shower is reconstructed through the images in each camera with a stereoscopic projection technique, resulting in key photon parameters energy and direction. The instrument has an angular resolution of $< 0.1°$at 1 TeV, an energy resolution of 15 – 25% and 3.5°field of view.

VERITAS observed Nova Per 2020 for 9.20 h, starting on 59 179.44 MJD for 30 minutes, then 59 189.19 MJD to 59 197.33 MJD. Data were taken in good weather and dark sky conditions. VERITAS observed Nova Her 2021 for 1.56 h, from 59 378.38 MJD to 59 378.45 MJD. Data were taken in good weather and dark sky conditions. VERITAS observed AT2021afpi for 5.45 h, from 59 546.24 MJD to 59 547.31 MJD. Data were taken in good weather and dark sky conditions.

Table 5.1: Vegas 2.5.8 ITM Soft - with GT corrections.

Parameter	Unit	Nova Per 2020	Nova Her 2021	AT2021afpi
Start	[MJD]	59 179.44	59 378.38	59 546.24
End	[MJD]	59 197.33	59 378.45	59 547.31
Livetime	[hr]	9.25	1.56	4.71
On	[ph]	309	40	228
Off	[ph]	3374	350	2223
α	-	0.09	0.09	0.09
Excess	[ph]	8.44	8.18	25.91
Significance	[σ]	0.47	1.33	1.70
E_{thresh}	[GeV]	240	263	240
Flux UL$^{(a)}$	[cm^{-2}s^{-1}]	2.07×10^{-12}	3.97×10^{-12}	3.60×10^{-12}

$^{(a)}$ 99% confidence level using the bounded Rolke method [63].

5.3 Results

5.3.1 Optical

The optical data provides the best estimate of the velocity and temperature profile for each event as a function of time. Using AAVSO data for all outbursts described here, V magnitudes were extracted by averaging over 1 day bins, shown in Tables B.1, B.2 and B.3 in the appendix.

5.3.2 VERITAS

The results of the VERITAS observations are summarized in Table 5.1. The reflected region background method [223] was used to calculate upper limits on the flux from all events with the method described by Rolke, López, and Conrad [63] and the assumption of a Gaussian-distributed background. In all cases, the nova was not detected. Upper limits were reported with 99% confidence level, assuming a power law spectral model with index 2.5.

5.3.3 *Fermi*-LAT

For each burst, the *Fermi*-LAT data was binned into either daily or weekly bins for the entire energy range ~100 MeV to ~500 GeV. These data were fit with either power-law or exponential

cutoff spectral models. The results of each analysis follows.

5.3.4 Nova Per 2020

Nova Per 2020 was observed with *Fermi*-LAT in weekly bins for four months following the optical trigger. These large observation periods were selected to increase the HE sensitivity since no detections were claimed in the 1-day bins during the week immediately after the burst. A power-law spectral model was used in the fit with normalization and spectral index free parameters. In the follow-up VHE observation by VERITAS, the upper limit was derived using a power-law spectral model with index 2.5 and a 99% confidence level. HE and VHE limits will be compared to the optical brightness in Section 5.4.2.

5.3.5 Nova Her 2021

Nova Her 2021 was modeled with a power-law spectral model to find the best fit over the *Fermi*-LAT data, from 2021-06-12 15:24:36 UTC to 2021-06-22 14:30:00 UTC. The observation period of 10 d was chosen since it is a typical length of time for a LAT-detected nova to remain detectable. The power-law spectral index found on the fit of the entire data is about -2.8, but this is not well constrained since only one energy bin is statistically significant, as shown the spectral energy distribution (SED) in Figure 5.1. Over this large time period, the statistically significant emission of the first day is overwhelmed by the cumulative background from the remaining days, weakening the overall detection. The overall TS for the entire data is 5.25.

During the first day (between 2021-06-12 15:24:36 UTC and 2021-06-13 15:24:36 UTC), there was a statistically significant detection between $TS = 23$ and $TS = 27$ for two different spectral models tested, a power law and a power law with an exponential cutoff, respectively; these results are consistent with the *Fermi*-LAT Astronomer's Telegram [185]. The cutoff energy is estimated from the fit. The fit result are summarized in Table 5.2, while the two fits are shown over the data in Figure 5.2. The exponential cutoff model is favored, with a cutoff at 370 MeV.

Separately, this single-day bin overlapped with the VERITAS observation. The joint fit of the

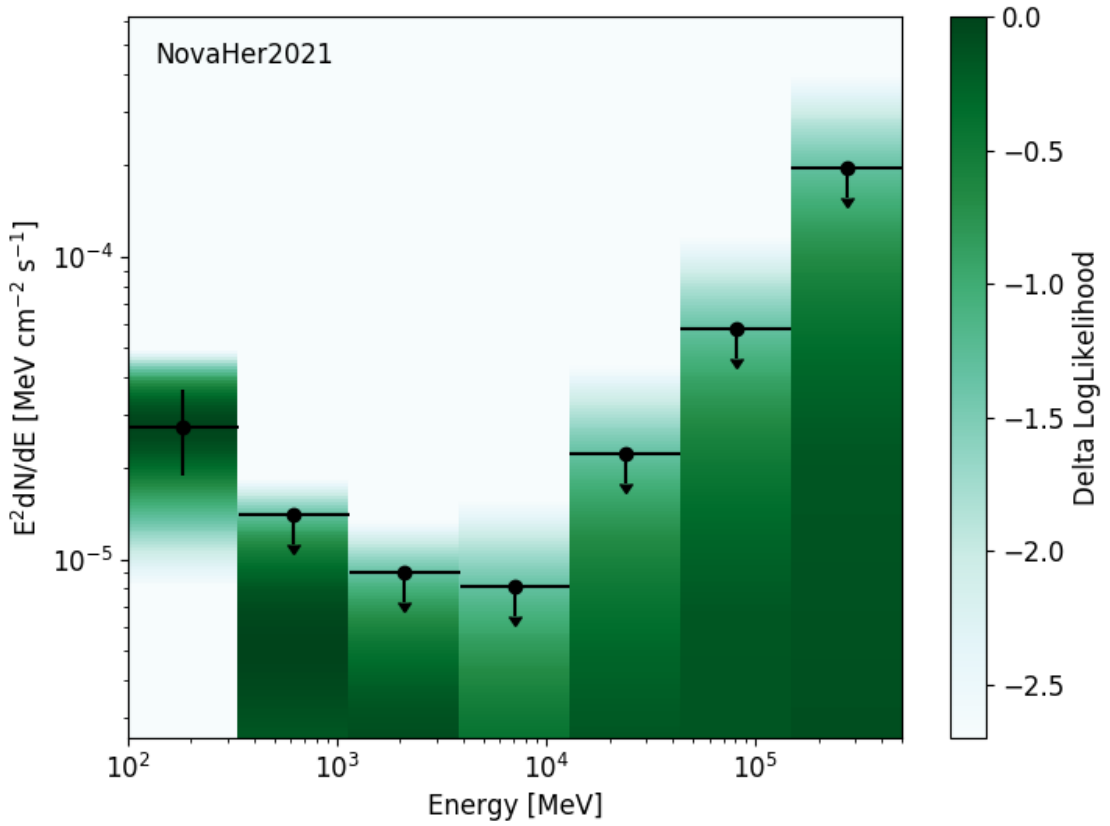

Figure 5.1: Nova Her 2021 SED in Fermi for data taken over 10 days, from 2021-06-12 15:24:36 UTC to 2021-06-22 14:30:00 UTC. Over this large time period, the statistically significant emission of the first day is overwhelmed by the cumulative background from the remaining days, weakening the overall detection. Attempting to fit with a power law, the model has a TS of 5.25, a weak and not statistically significant detection.

Fermi-LAT and VERITAS data required some exploration. Except for a few low-energy bins in the *Fermi*-LAT spectral range as can be seen in Figure 5.2, all of the remaining spectral energy bins were not statistically significant. Instead of using the 2 energy bins per decade in the larger 10 d fit, the *Fermi*-LAT data were fit with 4 energy bins per decade to allow for better fitting the spectral model in the energy range 100 MeV to 10 GeV. For the VERITAS data, all bins where less than 10 counts were observed were discarded, and the remaining spectral energy bins were not statistically significant. The fluxes (and limits) were extracted in energy bins so that `gammapy` could perform a joint fit of the SED, rather than a full likelihood analysis of the combined event lists described

Table 5.2: The SED model fit results of Nova Her 2021 during the first day, which overlaps with VERITAS observation. This full field of view analysis was performed with `fermipy`.

	Unit	power law	ExpCutoff
TS	σ^2	23.06	26.28
Improvement	σ	-	1.80
Index	-	2.30 ± 0.26	0.77 ± 0.32
Prefactor	$\mathrm{MeV}^{-1}\mathrm{cm}^{-2}\mathrm{s}^{-1}$	$(5.76 \pm 0.02) \times 10^{-11}$	$(99.998 \pm 0.004) \times 10^{-11}$
Cutoff	MeV	-	366 ± 72

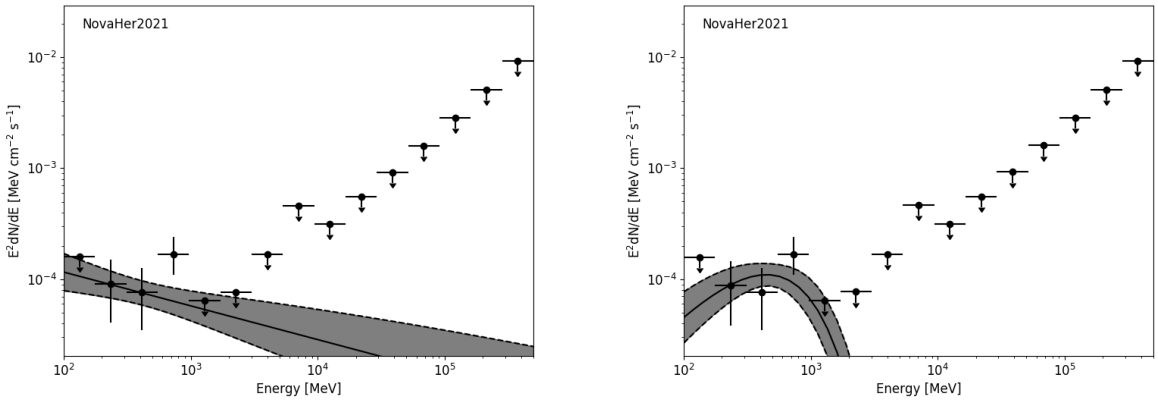

(a) Power law.

(b) Exponentially cutoff power law.

Figure 5.2: The SED model fit results of Nova Her 2021 during the first day. This full field of view analysis was performed with `fermipy`, assuming a power law model in Figure 5.2a and an exponentially cutoff power law in Figure 5.2b. The fit parameters are summarized in Table 5.2.

above.

In the resulting combined data set, the attempt to fit was met with computational challenges. The available spectral fitting programs do not account for upper limits; only flux points (with TS above some threshold) are included in the fit, while upper limits are discarded, biasing any resulting fit. Properly handling upper limits in the joint fit requires a full and careful software development effort to adjust the code to incorporate "censoring", which is the statistical framework necessary to work with upper limits in individual data points while fitting [224, 225]. Alternatively, tools are in development for a future pipeline that will allow the calculation of the joint analysis of *Fermi*-LAT and IACT event lists via a maximum likelihood optimization process that properly accounts for the underlying counts in each energy bin (analogous to `fermipy` [19]) [226, 227]. This joint

likelihood is likely a more statistically sensible way to handle multi-instrument analysis.

The standard gamma-ray astronomy package `gammapy` is used in this part of the work and it follows the convention of discarding upper limits during spectral model fitting [226]. A plugin is in development to convert VEGAS outputs into a format that `gammapy` can process in a joint likelihood analysis at the counts level (more like `fermipy`), but is not ready for this analysis. A kludge alternative – attempted here – is to explicitly replace the upper limit points by lowering the TS threshold to an unrealistic value (say $\sqrt{TS} = 0.5$), which then forces `gammapy` to use the weak flux points and errors rather than upper limits for some energy bins, allowing the fit to be computed.

In principle, this is a reasonable plan. Replacing the previously discarded points so that the fit can proceed will enable a computation that could yield results that are already visible by eye. The power law fit in Figure 5.2a should be steeper to account for the upper limits in the VERITAS range, as evident by the dotted line in Figure 5.3. It is then apparent that a power law will be constrained by the upper limits in the VERITAS band, so converting those bins to flux points so that the software will not discard them will help ensure this result. The fit results of Figure 5.2 were computed with `fermipy`, which performed a full likelihood optimization of the underlying counts in each energy bin and the upper limits were properly included in the analysis.

However, there is a key limitation to this kludge plan when applied to this specific data. The *Fermi*-LAT energy bins between 0.97-5.30 GeV are strictly upper limits that may play a significant role in constraining the spectral model over the entire energy range. Lowering the TS threshold activates the energy bin directly above this range (centered at 7 GeV), which unfairly biases the analysis toward higher energies (whether a smaller power-law index or higher cutoff energy), while ignoring the strong limits in the 1-3 GeV range. Only a joint maximum likelihood optimization will avoid this bias. Nonetheless, this kludge plan is attempted here as a precursor to a full analysis to illustrate the power of the additional VERITAS data in constraining the SED.

The result of the combined *Fermi*-LAT and VERITAS SED fit, with a threshold of $\sqrt{TS} = 0.5$, might indicate a preference for the exponential cutoff model. The reduced-chi-squared statistic

Table 5.3: Summary of the joint *Fermi*-LAT and VERITAS fit performed with `gammapy` using different TS threshold values. The lower threshold of $TS = 0.5$ enables `gammapy` to use weaker flux points, rather than discarding upper limits, in the fitting process.

Model	$TS_{\rm th}^{(a)}$	$\chi^2_{\rm red}{}^{(b)}$	Index	$E_{\rm cp}$(GeV)
Power law	0.5	7.3	2.67 ± 0.11	-
	2.0	0.5	1.25 ± 0.84	-
Exponential Cutoff	0.5	1.5	1.76 ± 0.24	39.12 ± 0.13
	2.0	1.9×10^{-7}	4.5 ± 3.7	-0.14 ± 0.16

$^{(a)}$ TS threshold for data selection; $^{(b)}$ Reduced χ^2 of spectral fit.

for the power-law model was 7.35 and for the exponential cutoff model was 1.51. These results are summarized in Table 5.3, separated by the spectral model type and TS threshold. Figure 5.3 contains the combined *Fermi*-LAT and VERITAS SED with both sets of model fit results. The green lines are a joint fit of both VERITAS and *Fermi*-LAT data with the reduced TS threshold, while the dotted lines were computed in `fermipy` with the full likelihood estimation on the *Fermi*-LAT data alone, for each power law and exponential cut off models. The flux is plotted if the bin has $\sqrt{TS} > 2$, and otherwise the upper limit is plotted.

It is readily apparent in Figure 5.3 that the `fermipy` power law model could be constrained by the VERITAS data toward a steeper index, even before this biased kludge plan is attempted. In the reduced TS threshold power law model fit, the power-law index is 2.67 ± 0.11, steeper than the `fermipy` result for the *Fermi*-LAT data alone, but not yet ideal since it could be less steep.

For the exponential cutoff model, preferred best fit result has the index of 1.76 ± 0.24 with a cutoff energy of (39.11 ± 0.13) GeV. This energy is higher than the result fit by the *Fermi*-LAT data alone with `fermipy` (~0.37 GeV), since this is explicitly fitting to the highest possible energy constrained by the VERITAS upper limit. However, it is unfairly biased toward the higher energies since the fit is ignoring the stringent limits given by the bins in the 1-3 GeV range.

5.4 Discussion

From the reported telegrams, Table 5.4 summarizes the estimates of nova properties. The parameters presented refer to basic physical conditions of the shock environment. This includes

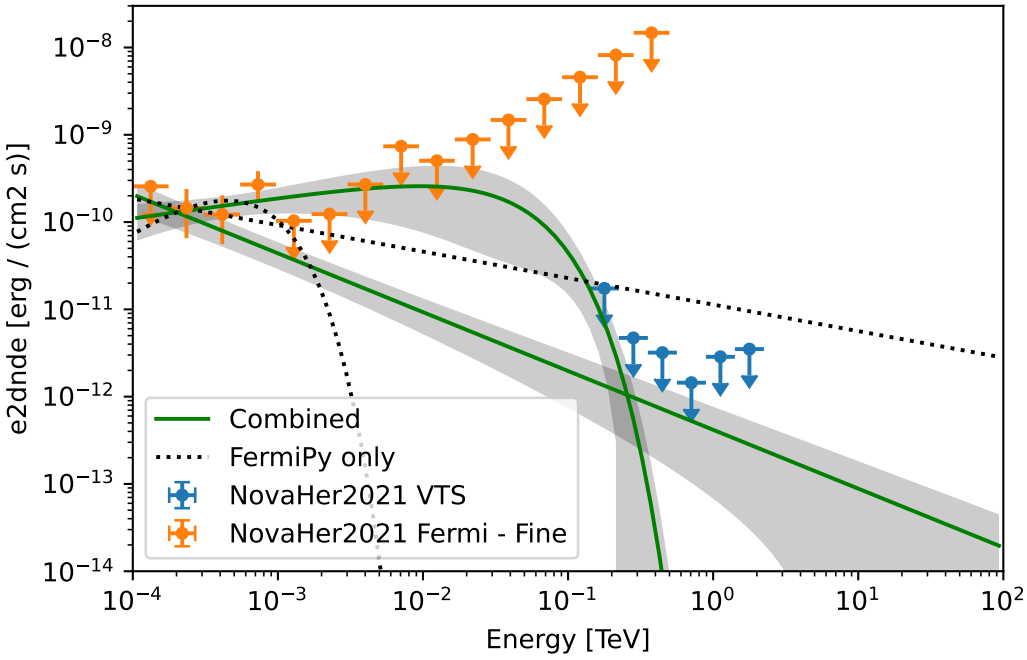

Figure 5.3: Combined spectra of Nova Her 2021 for *Fermi*-LAT and VERITAS. The plotted models in black are derived from the original *Fermi*-LAT fit using *Fermi*-LAT data only, reproducing the models in Figure 5.2 with parameters in Table 5.2. In green are the model fit result from the combined *Fermi*-LAT and VERITAS data. The flux points are plotted with the standard $\sqrt{TS} = 2$ threshold.

the mass loss rate $\dot{M}_f$ of the medium's fast outflow, the fast and slow velocities v_f and v_s, and the cool gas velocity of the central shell v_{cs}, with ξ as the factor relating the slow velocity to the cool gas velocity $v_{cs} = \xi v_s$. The efficiency of the magnetic energy density is ϵ_B, which is the fraction of the spherical magnetic field energy available in shock region. The time it takes for the nova light curve to reduce by 2 magnitudes is t_2. The distances are either reported directly in the telegrams reporting the original detection, or estimated from the emission properties.

5.4.1 Estimation of Distance

The estimation of the distance is critical to converting apparent magnitude to luminosity measurements. In this section, the distance estimates are summarized.

For Nova Per 2020, no distance is reported, but it may be possible to estimate the distance

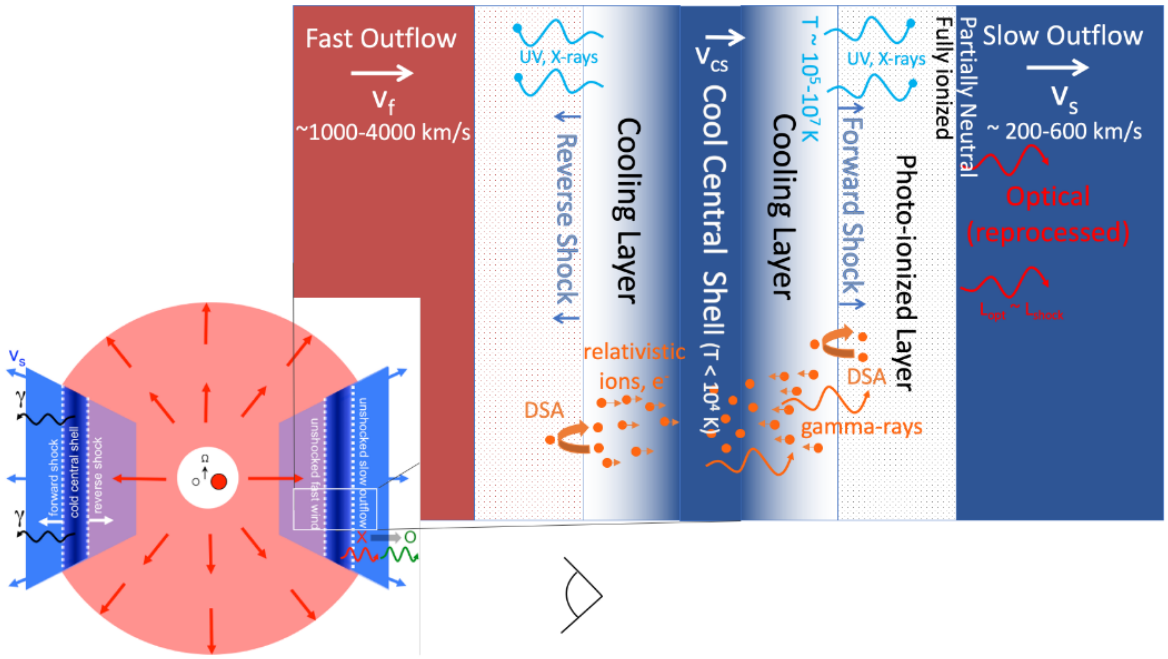

Figure 5.4: Direct reproduction of a nova emission diagram relevant to the calculations here, from [228]: “Anatomy of a radiative internal shock, zoomed in on a small patch where a fast outflow of velocity v_f collides with a slower outflow of velocity v_s. A forward shock is driven forward into the slow outflow, while a reverse shock propagates backwards into the fast outflow. Each shock heats the gas immediately behind it to temperatures $\gtrsim 10^6 - 10^7$ K, but the gas quickly cools via UV/X-ray emission in a narrow cooling layer. The cool gas collects into a thin central shell that will be corrugated on a scale of order its thickness due to thin-shell instabilities (not drawn). UV/X-rays from the shocks are absorbed by the partially neutral upstream flow or by the cool central shell, and their emission is reprocessed into the UVOIR and contributes to the optical light curve. Most of the relativistic particles (electrons and ions; orange dots) accelerated at the shocks are advected into the cold central shell, where they emit gamma-rays. Both optical and gamma-ray production occur with little delay, resulting in correlated optical and gamma-ray light curves. Figure adapted from [229]."

Table 5.4: Estimates of parameters for the shock dynamics from the respective Astronomer's Telegrams: Nova Per 2020 [188–192, 230], Nova Her 2021 [185, 193–195, 197–206, 208–210, 231–234], AT2021afpi [186, 211–222, 235–237],

Parameter	Units	Nova Per 2020	Nova Her 2021	AT2021afpi
$\dot{M}_f$ [(a)]	$M_\odot yr^{-1}$	1.6e-5 to 9e-5	2e-9 to 5e-7	-
v_f [(b)]	km s^{-1}	−1200	9000	500
v_s [(c)]	km s^{-1}	−600	3000	250
v_{cs} [(d)]	km s^{-1}	-	11 000	500
ϵ_B [(e)]	-	1.40	1.40	1.40
ξ [(f)]	-	1	1	1
t_2 [(g)]	d	50 hrs to 9 days	-	-
distance	kpc	5 to 10	1.50	-

[(a)] Mass rate of fast outflow; [(b)] fast velocity; [(c)] slow velocity; [(d)] cool central shell velocity; [(e)] magnetic efficiency; [(f)] slow velocity factor; [(g)] 2-mag reduction time.

using the apparent magnitude light curve and the maximum magnitude - rate of decline relation, as discussed in [179, 238]. The model from [179] relates the t_2 to the absolute magnitude:

$$M_V = (-11.32 \pm 0.44) + (2.55 \pm 0.32) \log t_2 \tag{5.1}$$

[188] notes that "At the time of writing the nova is still quickly rising in brightness, going from V=10.331 to V=8.594 is 43 hours." Estimating a round value for $t_2 \approx 50$ hr, then $M_V = -7$. The approximate maximum of 8.2 apparent magnitude, with this absolute magnitude, returns the distance ≈ 10 kpc. The shape of the lightcurve fluctuates and complicates the estimation of t_2. The light curve rises fast, then plateaus before rising a bit more, so t_2 (the time for the flux to decrease by 2 magnitudes) could be as high as 9 days, ($M_V \simeq -5.36$, $d \approx 5$ kpc). With this range of t_2, the distance is approximately 5 kpc to 10 kpc.

For Nova Her 2021, the [209] radio detection concludes the distance is about 1.7 kpc based on a probabilistic analysis of the parallax relationship derived in [239]. Using a simultaneous fit to both visual extinction value $A_v = 1.82$ to the correct the V apparent magnitudes and the distance from the MMRD relation, [207] estimates $d = 4.7^{+1.3}_{-1.0}$ kpc. [239, 240] list $d = 6.0^{+3.8}_{-2.8}$ kpc based on Gaia EDR3, while [196] adopts a distance of 5 kpc. A distance of 5 kpc is adopted here as a

compromise between the larger distance estimates and the adopted distance by [196].

Nova AT 2021afpi does not have a published distance estimate. Additionally, the decline relation above may not even apply to a WZ Sge-Type Dwarf nova, so it is not estimated.

5.4.2 Gamma-to-Optical Ratio

The GeV detection of ASASSN-16ma with tight correlation between optical and gamma-ray fluxes showed that the γ-to-optical ratio of 10^{-2} constrains the shock acceleration efficiency [179]. Using a range of previously measured, typical gamma-ray to optical luminosity ratios, an attempt is made to place the gamma-ray fluxes and limits in context of the optical flux. The shock efficiency is the fraction of the optical luminosity processed into non-thermal power $\epsilon_{\rm nth} = \frac{1}{\epsilon_\gamma}\frac{L_\gamma}{L_{\rm opt}}$, with some estimate of the efficiency of processing non-thermal radiation into gamma rays ϵ_γ. [229] estimates a general gamma-ray efficiency ϵ_γ at $20-30\%$, depending on the spectrum of the accelerated protons and the trapping timescale. Observations of the Tycho supernova remnant found $\epsilon_{\rm nth} \simeq 0.1$, suggesting the upstream magnetic fields were quasi-parallel to the shock normal direction [229, 241]. This bright observation suggested a great environment for producing gamma rays, placing a relative upper limit on the non-thermal shock efficiency. Furthermore, [229] argues that simulation of leptonic and hadronic scenarios coupled with observed supernova remnants motivates an efficiency range $\epsilon_{\rm nth} \simeq 10^{-5} - 10^{-3}$.

Figures (5.5, 5.6 and 5.7) show the optical and expected gamma-ray flux over the optical observation time, with the Fermi-LAT and VERITAS flux points over-plotted. In all those cases, the expected gamma-ray flux is simply a scale of 10^{-2} to 10^{-4} times the optical flux, which is motivated by the observations of *Fermi*-LAT detected novae summarized in [228], including V339 Del, V1324 Sco, V5856 Sgr and V5855 Sgr, rather than smaller range above motivated by simulations. These ratios provide a reference for constraining the shock efficiency $\epsilon_{\rm nth}$, if at all possible in these observations.

For Nova Per 2020 (Figure 5.5), early *Fermi*-LAT upper limits are below the 10^{-2} scale, but is above all the 10^{-4} scales. For all remaining data, *Fermi*-LAT upper limits are above the 10^{-2} scale.

For the VERITAS upper limit, it is just above the 10^{-4} scale. These upper limits, at least at the early time, may constrain the nova shock efficiency to 10^{-2}, and possibly to a few $1e{-}4$ for VHE photons.

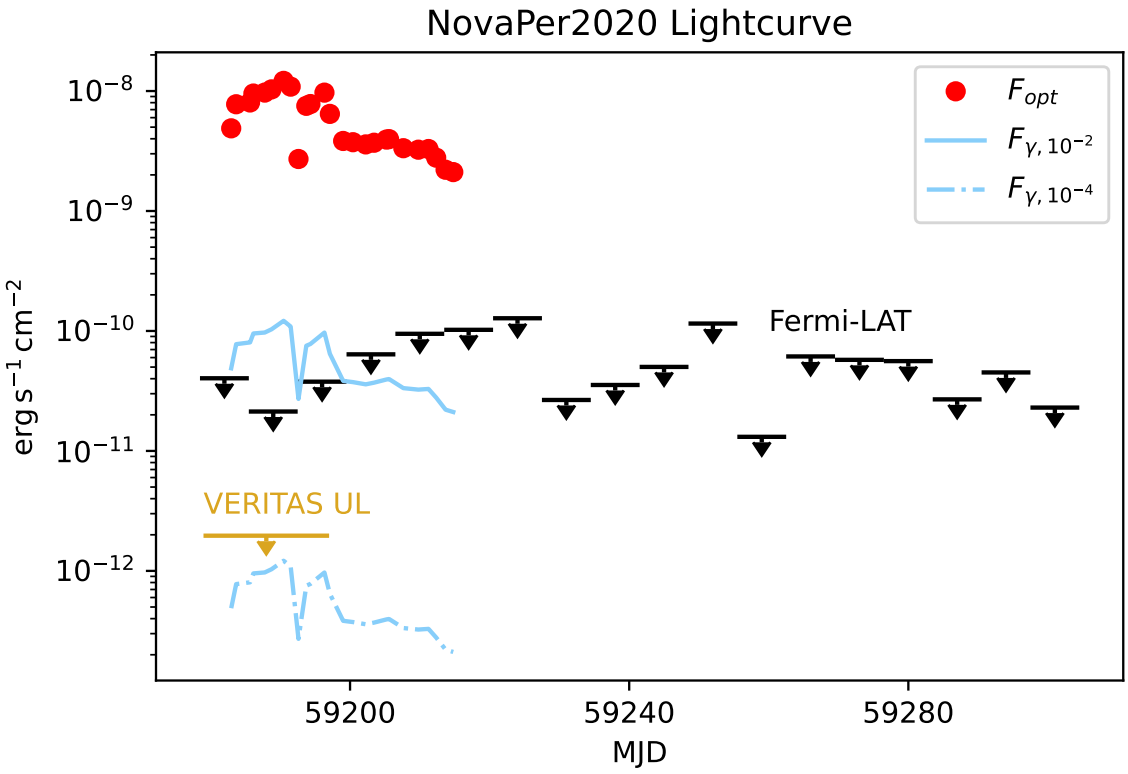

Figure 5.5: Nova Per 2020 light curve, assuming a distance of 5 kpc, indicating the expected gamma-ray luminosity range at a factor of 10^{-4} – 10^{-2} below the optical.

In the case of Nova Her 2021 (Figure 5.6), the predicted gamma-ray luminosity (at a few 10^{-2}) is detected by *Fermi*-LAT in the first time bin. The VERITAS upper limit is above the 10^{-4} gamma-ray prediction. This difference of about two orders of magnitude between HE and VHE emission may imply a decreasing shock efficiency for higher energy photon production, or may be reveal shock conditions that were unable to accelerate primary particles to energies that could produce VHE photons downstream.

In the case of AT2021afpi, the predicted gamma-ray luminosity (at 10^{-2}) is near the VERITAS upper limit. This limit does not constrain the shock efficiency below 10^{-2}.

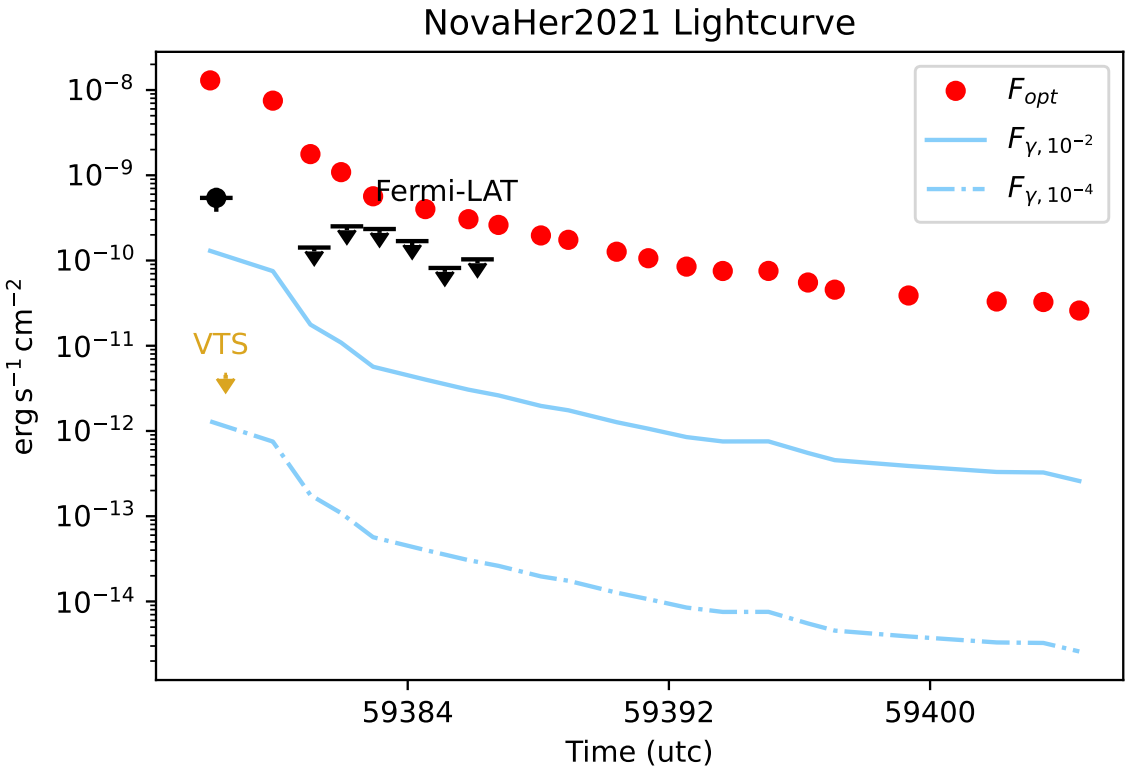

Figure 5.6: Nova Her 2021 light curve, assuming a distance of 5 kpc, indicating the expected gamma-ray luminosity range at a factor of $10^{-4} - 10^{-2}$ below the optical.

5.4.3 Maximum Particle Energy

A standard approach [228] to determine the maximum energy of the particles in the shock region entails comparing the energy-dependent timescales for particle acceleration, diffusion, and energy loss. Particle diffusion is modeled with the magnetic field behind the shock accelerating particles through the medium at characteristic time $t_{\rm diff} \approx D/v_{cs}^2$, where $D = r_{\rm g}c/3$, $r_{\rm g} = E/eB_{\rm sh}$. The magnetic field is

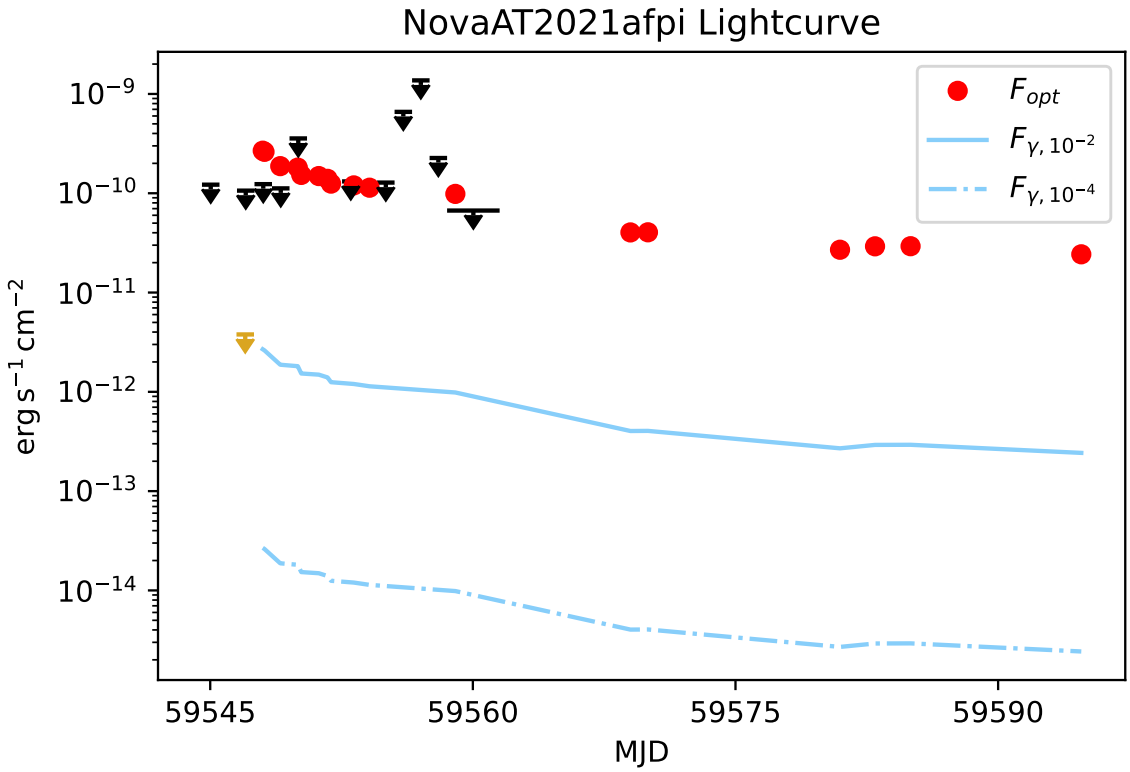

Figure 5.7: AT2021afpi light curve, assuming a distance of 5 kpc, indicating the expected gamma-ray luminosity range at a factor of $10^{-4} - 10^{-2}$ below the optical.

$$B_{sh} \simeq (6\pi\epsilon_B m_p n_f v_{cs}^2)^{1/2} \simeq \left(\frac{3}{2}\frac{\epsilon_B \dot{M}_f}{v_f t^2}\right)^{1/2}$$
$$\simeq 0.07\,\mathrm{G}\,\epsilon_{B,-2}^{1/2}\left(\frac{\dot{M}_f}{10^{-6}\,\mathrm{M}_\odot\,\mathrm{yr}^{-1}}\right)^{1/2} \times$$
$$\left(\frac{v_f}{5500\,\mathrm{km\,s}^{-1}}\right)^{-1/2}\left(\frac{t}{1\,\mathrm{wk}}\right)^{-1}$$

This magnetic field is calculated assuming that a fraction B of the shock-dissipated energy is placed into the magnetic field B, i.e. $B^2/8\pi = (3/4)\epsilon_B \rho v_{sh}^2$. This fraction is the magnetic efficiency ϵ_B, which is a comparison of magnetic energy density to the thermal pressure of the shell.

The mass loss rate is found from a naive estimate of the particle flow based on the bolometric luminosity:

$$L_{\rm bol}(t) \simeq L_{sh}(t) \simeq \frac{1}{2}\dot{M}_f v_f^2$$
$$\simeq 8\times10^{36}\,{\rm erg\,s^{-1}}\frac{\dot{M}}{10^{-6}\,{\rm M_\odot yr^{-1}}}\left(\frac{v_f}{5500\,{\rm km\,s^{-1}}}\right)^2$$

where the assumption is made that $v_f \gg v_s$ and treating the fast outflow as a wind of mass-loss rate $\dot{M}_f$.

This energy-dependent diffusion timescale can be set to either the downstream advection time $t_{adv} \approx z_{acc}/v_{cs}$, where z_{acc} is the width of the acceleration zone, or (in hadronic scenarios) the pion creation timescale $t_\pi = (n_f \sigma_\pi c)^{-1}$, where $\sigma_\pi \approx 2\times10^{26}\,{\rm cm^2}$ is the inelastic cross section for p-p interactions.

With $t_{\rm diff} = t_{{\rm ad}v}$:

$$E_{\rm max} \simeq \frac{3eB_{sh}v_{cs}z_{acc}}{c}$$
$$\approx 340\,{\rm TeV}\left(\frac{z_{acc}}{R_{cs}}\right)\left(\frac{\xi}{2}\right)^2\epsilon_{B,-2}^{1/2}\left(\frac{\dot{M}_f}{10^{-6}\,{\rm M_\odot yr^{-1}}}\right)^{1/2}\times$$
$$\left(\frac{v_f}{5500\,{\rm km\,s^{-1}}}\right)^{-1/2}\left(\frac{v_s}{2700\,{\rm km\,s^{-1}}}\right)^2$$

On the other hand, with $t_{\rm diff} = t_\pi$:

$$E_{\rm max} \approx \frac{3e}{c^2}\frac{v_{cs}^2 B_{sh}}{n_f\sigma_{pi}} \simeq 12\pi\frac{m_p}{\sigma_\pi}\frac{e}{c^2}\frac{B_{sh}v_f v_{cs}^4 t^2}{\dot{M}_f}$$
$$\simeq 2\times10^7\,{\rm TeV}\left(\frac{\xi}{2}\right)^4\epsilon_{B,-2}^{1/2}\left(\frac{\dot{M}}{10^{-6}\,{\rm M_\odot yr^{-1}}}\right)^{-1/2}\times$$
$$\left(\frac{v_f}{5500\,{\rm km\,s^{-1}}}\right)^{1/2}\left(\frac{v_s}{2700\,{\rm km\,s^{-1}}}\right)^4\left(\frac{t}{1\,{\rm wk}}\right)^2$$

Using the estimates of the velocities v_f and v_s in Table 5.4, the estimated luminosity from the optical data is used to find the mass loss rate $\dot{M}_f(t)$. This has a dependence on the distance, and

is combined to find $E_{\gamma,max} \approx 0.1 E_{\rm max}$. In the pion timescale method, the time t is taken to be the time elapsed between the nova eruption and the time of the VERITAS observation. The scale of these characteristic energies is different by several orders of magnitude, implying that at these conditions, the minimum $E_{\rm max}$ estimate is given by the advection timescale $t_{\rm adv}$.

Nova Per 2020

The distance is 5−10 kpc, so the optical luminosity is 6.40×10^{36}–3.60×10^{37} erg s^{-1} for 5 kpc. The VERITAS observation is centered approximately 15 d after the nova event. The velocities are 600 km s^{-1} and 1200 km s^{-1}. This yields $\dot{M}_f(t) \approx 1.60 \times 10^{-5}$ M$_\odot$ yr^{-1}. Then, the $E_{\gamma,max}$ is in the range of 7 − 17 TeV. With the distance doubled to 10 kpc, the luminosity is 0.25×10^{38} – 1.40×10^{38} erg s^{-1} and $\dot{M}_f(t) \approx 0.66 \times 10^{-4}$ – 4×10^{-4} M$_\odot$ yr^{-1}. This yields an $E_{\gamma,max}$ in the range of 14 − 34 TeV. The resulting range of maximum energy is 7 − 34 TeV.

The flux upper limit derived by VERITAS during the first day of the *Fermi*-LAT observation shown in Figure 5.5 implies a soft spectrum or possibly a cutoff at a few GeV energy. Figure 5.3 show the spectral model fit on the combined data.

Nova Her 2021

The adopted distance is 5 kpc, so the luminosity is 7.70×10^{34}–3.90×10^{37} erg s^{-1}. The velocities are 3000 kms^{-1} and 9000 km s^{-1}. This yields $\dot{M}_f(t) \approx 3.60 \times 10^{-9} - 1.80 \times 10^{-6}$ M$_\odot$yr^{-1}. At the time of the VERITAS observation, only 11 hours after the burst, the $E_{\gamma,max}$ is around 20 TeV. Based on numerical plasma simulations in [228], it is reasonable to assume that the magnetic efficiency may be as low as 10^{-4}, which lowers the maximum energy to about 2 TeV.

The resulting range of maximum energy is 2 TeV to 20 TeV. The exponential cutoff model fit to the VERITAS and *Fermi*-LAT SED with the unrealistic threshold of $\sqrt{TS} = 0.5$ yielded an energy cutoff of 39.12 GeV, which is about fifty times smaller than the lower bound of the maximum energy estimated by the criteria above. The best-fit result on the *Fermi*-LAT data alone with the same reduced TS threshold yields an even lower maximum energy of 3.41 GeV, while the `fermipy`

maximum likelihood optimization yields the lowest maximum energy of (366 ± 72) MeV. The combined *Fermi*-LAT and VERITAS cutoff provides a higher maximum particle energy allowed by the upper limit derived by VERITAS, although it was biased by the flawed reduced TS threshold plan discussed in Section 5.3.5. The large energy estimates calculated from the derived shock velocities indicates that although the nova may have accelerated particles the TeV energy range, the gamma-ray telescopes were not sensitive enough to observe them.

Further, a full chi-square minimization was attempted to find the 90% confidence upper limit of the energy cutoff using the reduced TS threshold data. While this kludge plan is biased toward higher energies and the results here may not be completely reliable, this procedure is performed anyway to illustrate the utility of the technique. Figure 5.8 shows the confidence region of the fit based on the exponential cutoff and spectral index. When combining both the *Fermi*-LAT and VERITAS data, the 90% region limits the exponential cutoff energy to ~90 GeV at index 2.20. This result is constrained because of the addition of the VERITAS data, while the *Fermi*-LAT data alone only constrains the spectral index to 1.9 at 90%, with no constraint evident on the maximum cutoff energy. At the low end, the combined *Fermi*-LAT and VERITAS 90% confidence region limits the smallest exponential cutoff energy to 0.45 GeV, which is smaller than the prediction above based on the velocity estimate (2 TeV to 20 TeV).

There is not enough data for AT2021afpi to estimate the velocity profile.

5.5 Conclusion

The analysis of both Nova Per 2020 and AT 2021afpi lacked a significant detection in the HE-VHE range covered by VERITAS and *Fermi*-LAT. The weak fluxes represented here, along with a small subset of published multi-wavelength data, pose significant challenges in estimating the maximum particle energy accelerated in their respective shock regions.

The noteworthy case of Nova Her 2021 presents a tantalising upper limit provided by VERITAS that may constrain the maximum particle energy. The addition of the VERITAS upper limit to the *Fermi*-LAT parameter space in the joint fit reduced the 90% confidence region of the photon cutoff

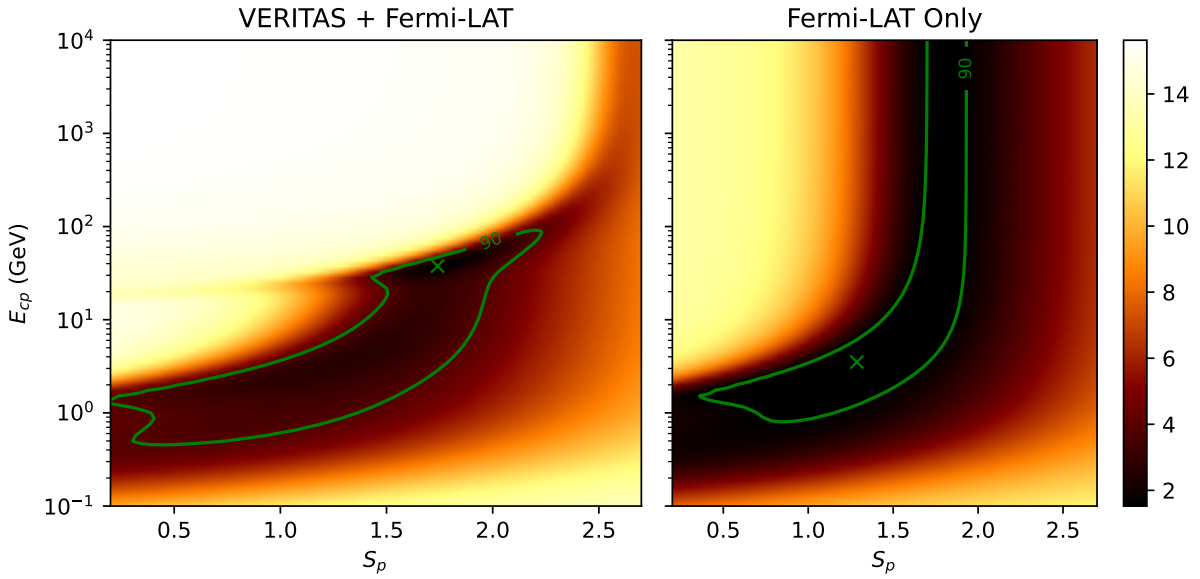

Figure 5.8: The chi-square distribution based on spectral index and energy cutoff, taken for *Fermi*-LAT alone (right) and combined VERITAS and *Fermi*-LAT on Nova Her 2021. The 90% confidence region is highlighted in green. The green "x" are the best fit value reported in the text, where the joint fit finds the exponential cutoff energy at 39.12 GeV at index 1.76, and the *Fermi*-LAT fit find the cutoff energy at 3.41 GeV and index $\backsim$ 1.3. The joint fit maximally constrains the allowed cutoff energy to $\sim$90 GeV at the 90% confidence region.

energy to range of 0.45 GeV to 90 GeV. This reduced cutoff energy, compared to the higher 2-20 TeV derived from the analytical estimate, implies that the shock efficiency may be decreased at the VHE range, as indicated by the $\sim 10^{-4}$ gamma-to-optical ratio measured by VERITAS in Figure 5.6. Future observations in other bands may constrain the shock efficiency and better determine the acceleration conditions to produce HE and VHE photons.

References

[1] R. W. Klebesadel, I. B. Strong, and R. A. Olson, "Observations of Gamma-Ray Bursts of Cosmic Origin," *The Astrophysical Journal*, vol. 182, p. L85, Jun. 1973.

[2] G. Kanbach, D. L. Bertsch, C. E. Fichtel, *et al.*, "The project EGRET (energetic gamma-ray experiment telescope) on NASA's Gamma-Ray Observatory GRO," *Space Science Reviews*, vol. 49, pp. 69–84, Jan. 1, 1989.

[3] G. Boella, L. Chiappetti, G. Conti, *et al.*, "The medium-energy concentrator spectrometer on board the BeppoSAX X-ray astronomy satellite," *Astronomy and Astrophysics Supplement Series*, vol. 122, pp. 327–340, Apr. 1, 1997.

[4] G. Boella, R. C. Butler, G. C. Perola, *et al.*, "BeppoSAX, the wide band mission for X-ray astronomy," *Astronomy and Astrophysics Supplement Series*, vol. 122, pp. 299–307, Apr. 1, 1997.

[5] E. Costa, F. Frontera, J. Heise, *et al.*, "Discovery of an X-ray afterglow associated with the γ-ray burst of 28 February 1997," *Nature*, vol. 387, no. 6635, pp. 783–785, Jun. 1997.

[6] R. D. Preece, M. S. Briggs, R. S. Mallozzi, *et al.*, "The BATSE Gamma-Ray Burst Spectral Catalog. I. High Time Resolution Spectroscopy of Bright Bursts Using High Energy Resolution Data," *The Astrophysical Journal Supplement Series*, vol. 126, no. 1, pp. 19–36, Jan. 2000.

[7] T. C. Weekes, M. F. Cawley, D. J. Fegan, *et al.*, "Observation of TeV Gamma Rays from the Crab Nebula Using the Atmospheric Cerenkov Imaging Technique," *The Astrophysical Journal*, vol. 342, p. 379, Jul. 1, 1989.

[8] HEGRA Collaboration and A. D. et Al, "First Results on the Performance of the HEGRA IACT Array," *Astroparticle Physics*, vol. 8, pp. 1–19, February Apr. 11, 1997.

[9] G. Maier, *VERITAS: Status and Latest Results*, Oct. 3, 2007.

[10] J. A. Hinton and HESS Collaboration, "The status of the HESS project," *New Astronomy Reviews*, vol. 48, pp. 331–337, Apr. 1, 2004.

[11] P. Hofverberg, R. Kankanyan, M. Panter, *et al.*, "Commissioning and Initial Performance of the H.E.S.S. II Drive System," vol. 33, p. 3092, Jan. 1, 2013.

[12] A. Förster, "Gamma-ray astronomy with H.E.S.S," *Nuclear Instruments and Methods in Physics Research Section A: Accelerators, Spectrometers, Detectors and Associated Equipment*, vol. 766, pp. 69–72, Dec. 2014.

[13] J. Aleksić, E. A. Alvarez, L. A. Antonelli, *et al.*, "Performance of the MAGIC stereo system obtained with Crab Nebula data," *Astroparticle Physics*, vol. 35, no. 7, pp. 435–448, Feb. 2012.

[14] J. Cortina, "Status and First Results of the Magic Telescope," *Astrophysics and Space Science*, vol. 297, no. 1-4, pp. 245–255, Jun. 2005.

[15] J. M. Casandjian and I. A. Grenier, "A revised catalogue of EGRET γ-ray sources," *Astronomy and Astrophysics*, vol. 489, pp. 849–883, Oct. 1, 2008.

[16] S. Abdollahi, F. Acero, M. Ackermann, *et al.*, "Fermi Large Area Telescope Fourth Source Catalog," *The Astrophysical Journal Supplement Series*, vol. 247, no. 1, p. 33, Mar. 10, 2020.

[17] W. B. Atwood, A. A. Abdo, M. Ackermann, *et al.*, "The large area telescope on the fermi gamma-ray space telescope mission," *Astrophysical Journal*, vol. 697, no. 2, pp. 1071–1102, 2009.

[18] P. L. Nolan, A. A. Abdo, M. Ackermann, *et al.*, "Fermi large area telescope second source catalog," *Astrophysical Journal, Supplement Series*, vol. 199, no. 2, p. 31, 2012.

[19] M. Wood, R. Caputo, E. Charles, *et al.*, "Fermipy: An open-source Python package for analysis of Fermi-LAT Data," in *Proceedings of Science*, ser. International Cosmic Ray Conference, vol. 301, Jan. 2017, p. 824.

[20] V. F. Hess and C. D. Anderson, "Physics 1936," in *Physics 1922–1941*, Elsevier, 2013, pp. 351–377, ISBN: 978-1-4831-9745-6.

[21] J. J. Beatty and S. Westerhoff, "The Highest-Energy Cosmic Rays," *Annual Review of Nuclear and Particle Science*, vol. 59, no. 1, pp. 319–345, Nov. 1, 2009.

[22] A. R. Bell, "The acceleration of cosmic rays in shock fronts - II," *Monthly Notices of the Royal Astronomical Society*, vol. 182, no. 3, pp. 443–455, Jan. 1978.

[23] ——, "The acceleration of cosmic rays in shock fronts - I," *Monthly Notices of the Royal Astronomical Society*, vol. 182, no. 2, pp. 147–156, Feb. 1, 1978.

[24] M. S. Longair, *High Energy Astrophysics*. Cambridge university press, 2010.

[25] E. Fermi, "On the Origin of the Cosmic Radiation," *Physical Review*, vol. 75, no. 8, pp. 1169–1174, Apr. 15, 1949.

[26] E. Fermi, "Galactic Magnetic Fields and the Origin of Cosmic Radiation.," *The Astrophysical Journal*, vol. 119, p. 1, Jan. 1, 1954.

[27] A. J. B. Chromey, "New developments for a multidimensional maximum likelihood approach to analyzing VERITAS data," Iowa State University, Ames, Iowa, 2022.

[28] A. P. Lightman and G. B. Rybicki, "Inverse Compton reflection - Time-dependent theory," *The Astrophysical Journal*, vol. 232, p. 882, Sep. 1979.

[29] P. A. Zyla *et al.*, "Review of particle physics," *PTEP*, vol. 2020, no. 8, p. 083C01, 2020.

[30] P. K. Grieder, *Extensive Air Showers: High Energy Phenomena and Astrophysical Aspects ; a Tutorial, Reference Manual and Data Book*. Berlin: Springer, 2010, ISBN: 978-3-540-76941-5 978-3-540-76940-8.

[31] S. Gammel, "A Search for Very High Energy Gamma-ray Emission from Active Galactic Nuclei using Multivariate Analysis," University College Dublin, Oct. 2004.

[32] W. Heitler, *Quantum Theory of Radiation*. Jan. 1, 1954.

[33] T. C. Weekes, *Very High Energy Gamma-Ray Astronomy*. CRC Press, 2003.

[34] F Aharonian, J Buckley, T Kifune, *et al.*, "High Energy Astrophysics with Ground-Based Gamma Ray Detectors," *Reports on Progress in Physics*, vol. 71, no. 9, p. 096 901, Sep. 1, 2008.

[35] W. Commons, *File:Cherenkov.svg — Wikimedia Commons, the free media repository*, 2020.

[36] E. Hays, "VERITAS Data Acquisition," Oct. 11, 2007.

[37] P Cogan, "Analysis of flash ADC data with VERITAS," in *30th International Cosmic Ray Conference (ICRC 2007)*, vol. 3, 2008, pp. 1369–1372.

[38] B. Zitzer, "The VERITAS Upgraded Telescope-Level Trigger Systems: Technical Details and Performance Characterization," version 1, 2013.

[39] A. Weinstein, "The VERITAS trigger system," in *Proceedings of the 30th International Cosmic Ray Conference, ICRC 2007*, vol. 3, Sep. 2007, pp. 1539–1542.

[40] G. Lamanna, L. A. Antonelli, J. L. Contreras, *et al.*, *Cherenkov telescope array data management*, 2015.

[41] C. Deil, C. Boisson, K. Kosack, *et al.*, "Open high-level data formats and software for gamma-ray astronomy," in *AIP Conference Proceedings*, vol. 1792, Oct. 6, 2017, p. 070 006, ISBN: 978-0-7354-1456-3.

[42] G. Maier and J. Holder, "Eventdisplay: An Analysis and Reconstruction Package for Ground-based Gamma-ray Astronomy," in *Proceedings of Science*, ser. 35th International Cosmic Ray Conference (ICRC2017), vol. 301, Sissa Medialab Srl, Jan. 2017, p. 747.

[43] P. Cogan, "VEGAS, the VERITAS Gamma-ray Analysis Suite," in *Proceedings of the 30th International Cosmic Ray Conference, ICRC 2007*, vol. 3, 2008, pp. 1385–1388.

[44] R. Brun and F. Rademakers, "ROOT — An object oriented data analysis framework," *Nuclear Instruments and Methods in Physics Research Section A: Accelerators, Spectrometers, Detectors and Associated Equipment*, vol. 389, no. 1-2, pp. 81–86, Apr. 1997.

[45] J. Holder, "Exploiting VERITAS Timing Information," version 1, 2005.

[46] P. T. Reynolds, C. W. Akerlof, M. F. Cawley, *et al.*, "Survey of candidate gamma-ray sources at TeV energies using a high-resolution Cerenkov imaging system - 1988-1991," *The Astrophysical Journal*, vol. 404, p. 206, Feb. 1993.

[47] D. Hanna, A. McCann, M. McCutcheon, *et al.*, "An LED-based flasher system for VERITAS," *Nuclear Instruments and Methods in Physics Research Section A: Accelerators, Spectrometers, Detectors and Associated Equipment*, vol. 612, no. 2, pp. 278–287, Jan. 2010.

[48] P Cogan, "Nanosecond Sampling of Atmospheric Cherenkov Radiation Applied to TeV Gamma-Ray Observations of Blazars with VERITAS.," University College Dublin, Dec. 2006.

[49] A. M. Hillas, "Cerenkov light images of EAS produced by primary gamma," in *Goddard Space Flight Center 19th Intern. Cosmic Ray Conf.*, vol. 3, Aug. 1985, pp. 445–448.

[50] D. J. Fegan, "/hadron separation at TeV energies," *Journal of Physics G: Nuclear and Particle Physics*, vol. 23, no. 9, pp. 1013–1060, Sep. 1, 1997.

[51] M. de Naurois and L. Rolland, "A high performance likelihood reconstruction of γ-rays for imaging atmospheric Cherenkov telescopes," *Astroparticle Physics*, vol. 32, no. 5, pp. 231–252, Dec. 2009.

[52] S. Le Bohec, B. Degrange, M. Punch, *et al.*, "A new analysis method for very high definition Imaging Atmospheric Cherenkov Telescopes as applied to the CAT telescope," *Nuclear Instruments and Methods in Physics Research Section A: Accelerators, Spectrometers, Detectors and Associated Equipment*, vol. 416, no. 2-3, pp. 425–437, Nov. 1998.

[53] R. Parsons and J. Hinton, "A Monte Carlo template based analysis for air-Cherenkov arrays," *Astroparticle Physics*, vol. 56, pp. 26–34, Apr. 2014.

[54] J. Christiansen, "Characterization of a Maximum Likelihood Gamma-Ray Reconstruction Algorithm for VERITAS," in *Proceedings of Science*, Trieste, Italy: Sissa Medialab, Aug. 16, 2017, p. 789.

[55] A. Petrashyk, "Advancements in Very-High-Energy Gamma-Ray Astronomy with Applications to the Study of Cosmic Rays," Columbia University, 2019, 194 pp., ISBN: 6103544947.

[56] M. Krause, E. Pueschel, and G. Maier, "Improved γ /hadron separation for the detection of faint γ -ray sources using boosted decision trees," *Astroparticle Physics*, vol. 89, pp. 1–9, Mar. 2017.

[57] S. Ohm, C. van Eldik, and K. Egberts, "γ/hadron separation in very-high-energy γ-ray astronomy using a multivariate analysis method," *Astroparticle Physics*, vol. 31, no. 5, pp. 383–391, Jun. 2009.

[58] T.-P. Li and Y.-Q. Ma, "Analysis methods for results in gamma-ray astronomy," *The Astrophysical Journal*, vol. 272, p. 317, Sep. 1983.

[59] S. S. Wilks, *Mathematical Statistics*. New York-London: Wiley, 1962, 0173–45805.

[60] O. M. Weiner, T. B. Humensky, R. Mukherjee, *et al.*, "Estimating significance in observations of variable and transient gamma-ray sources," *Astroparticle Physics*, vol. 93, pp. 1–7, Supplement C Jul. 2017.

[61] M. Ackermann, M. Ajello, K. Asano, *et al.*, "The First *fermi* -Lat Gamma-Ray Burst Catalog," *The Astrophysical Journal Supplement Series*, vol. 209, no. 1, p. 11, Oct. 23, 2013.

[62] J. Knödlseder, M. Mayer, C. Deil, *et al.*, *Ctools: Cherenkov Telescope Science Analysis Software*, 2016.

[63] W. A. Rolke, A. M. López, and J. Conrad, "Limits and confidence intervals in the presence of nuisance parameters," *Nuclear Instruments and Methods in Physics Research, Section A: Accelerators, Spectrometers, Detectors and Associated Equipment*, vol. 551, no. 2-3, pp. 493–503, Mar. 9, 2005.

[64] O. Helene, "Upper limit of peak area," *Nuclear Instruments and Methods In Physics Research*, vol. 212, no. 1-3, pp. 319–322, Jul. 1983.

[65] ——, "Errors in experiments with small numbers of events," *Nuclear Instruments and Methods in Physics Research Section A: Accelerators, Spectrometers, Detectors and Associated Equipment*, vol. 228, no. 1, pp. 120–128, Dec. 1984.

[66] ——, "Determination of the upper limit of a peak area," *Nuclear Instruments and Methods in Physics Research Section A: Accelerators, Spectrometers, Detectors and Associated Equipment*, vol. 300, no. 1, pp. 132–136, Jan. 1991.

[67] R. D. Cousins, G. J. Feldman, and R. D. Cousins, "A Unified Approach to the Classical Statistical Analysis of Small Signals," *Physical Review D - Particles, Fields, Gravitation and Cosmology*, vol. 57, no. 7, pp. 3873–3889, Nov. 21, 1997.

[68] A. Domínguez, J. R. Primack, D. J. Rosario, *et al.*, "Extragalactic background light inferred from AEGIS galaxy-SED-type fractions," *Monthly Notices of the Royal Astronomical Society*, vol. 410, no. 4, pp. 2556–2578, Feb. 1, 2011.

[69] J. M. Davies and E. S. Cotton, "Design of the quartermaster solar furnace," *Solar Energy*, vol. 1, no. 2-3, pp. 16–22, Apr. 1957.

[70] The CTA Consortium, M. Actis, G. Agnetta, *et al.*, "Design concepts for the Cherenkov Telescope Array CTA: An advanced facility for ground-based high-energy gamma-ray astronomy," *Experimental Astronomy*, vol. 32, no. 3, pp. 193–316, Dec. 2011.

[71] The CTA Consortium, *Science with the Cherenkov Telescope Array*. World Scientific, Mar. 2019, ISBN: 978-981-327-008-4 978-981-327-009-1.

[72] L. Taylor and CTA SCT Project, "Design and performance of the prototype Schwarzschild-Couder Telescope camera," in *Proceedings of 37th International Cosmic Ray Conference — PoS(ICRC2021)*, Berlin, Germany - Online: Sissa Medialab, Aug. 4, 2021, p. 748.

[73] V. Vassiliev, S. Fegan, and P. Brousseau, "Wide field aplanatic two-mirror telescopes for ground-based γ-ray astronomy," *Astroparticle Physics*, vol. 28, no. 1, pp. 10–27, Sep. 2007.

[74] C. Adams, G. Ambrosi, M. Ambrosio, *et al.*, "Prototype schwarzschild-couder telescope for the cherenkov telescope array: Commissioning status of the optical system," in *Proceedings of Science*, vol. 358, Trieste, Italy: Sissa Medialab, Jul. 22, 2019, p. 672.

[75] D. Nieto, S. Griffiths, B. Humensky, *et al.*, "Construction of a medium-sized schwarzschild-couder telescope as a candidate for the cherenkov telescope array: Development of the optical alignment system," *Proceedings of Science*, vol. 30-July-20, arXiv:1509.02463, Sep. 2015.

[76] D Nieto Castaño, T. B. Humensky, P Kaaret, *et al.*, "Prototype 9.7m Schwarzschild-Couder telescope for the Cherenkov Telescope Array: Status of the optical system.," in *35th International Cosmic Ray Conference (ICRC2017)*, ser. International Cosmic Ray Conference, vol. 301, Jan. 2017, p. 815.

[77] J Rousselle, K Byrum, R Cameron, *et al.*, "Toward the construction of a medium size prototype Schwarzschild-Couder telescope for CTA," in *Society of Photo-Optical Instrumen-*

tation Engineers (SPIE) Conference Series, ser. Society of Photo-Optical Instrumentation Engineers (SPIE) Conference Series, vol. 9603, Sep. 2015, p. 960 305.

[78] C. B. Adams, R. Alfaro, G. Ambrosi, *et al.*, "Detection of the Crab Nebula with the 9.7 m Prototype Schwarzschild-Couder Telescope," *Astroparticle Physics*, vol. 128, p. 102 562, Dec. 15, 2020.

[79] A. N. Otte, J. Biteau, H. Dickinson, *et al.*, "Development of a SiPM Camera for a Schwarzschild-Couder Cherenkov Telescope for the Cherenkov Telescope Array," version 1, 2015.

[80] D. Stewart, "A Platform with Six Degrees of Freedom," *Proceedings of the Institution of Mechanical Engineers*, vol. 180, no. 1, pp. 371–386, Jun. 1965.

[81] A. Okumura, M. Hayashida, H. Katagiri, *et al.*, "Development of Non-sequential Ray-tracing Software for Cosmic-ray Telescopes," version 1, 2011.

[82] A. Okumura, K. Noda, and C. Rulten, "ROBAST: Development of a Non-Sequential Ray-Tracing Simulation Library and its Applications in the Cherenkov Telescope Array," version 2, 2015.

[83] E. Bertin and S. Arnouts, "SExtractor: Software for source extraction," *Astronomy and Astrophysics Supplement Series*, vol. 117, no. 2, pp. 393–404, Jun. 1996.

[84] C. Adams, R. Alfaro, G. Ambrosi, *et al.*, "Verification of the optical system of the 9.7-m prototype Schwarzschild-Couder Telescope," vol. 1148805, p. 3, August 2020 2020.

[85] C. B. Adams, G. Ambrosi, M. Ambrosio, *et al.*, "Prototype Schwarzschild-Couder Telescope for the Cherenkov Telescope Array: Commissioning the Optical System," Oct. 14, 2021.

[86] C. B. Adams, R. Alfaro, A. G.~ Ambrosi, *et al.*, "Alignment of the optical system of the 9.7-m prototype Schwarzschild-Coulder Telescope," 2020, p. 96, ISBN: 978-1-5106-3677-4.

[87] J. Rousselle and V. Vassiliev, "pSCT alignment tolerances and specifica4ons," presented at the CTA SCT Design Review 2013 (Warsaw, Poland), Sep. 28, 2013.

[88] R. M. Quimby, S. R. Kulkarni, M. M. Kasliwal, *et al.*, "Hydrogen-Poor Superluminous Stellar Explosions," *Nature*, vol. 474, no. 7352, pp. 487–489, Jun. 2011.

[89] M. Nicholl, S. J. Smartt, A. Jerkstrand, *et al.*, "Slowly Fading Super-Luminous Supernovae That Are Not Pair-Instability Explosions," *Nature*, vol. 502, no. 7471, pp. 346–349, Oct. 2013.

[90] C. Inserra, S. J. Smartt, A. Jerkstrand, *et al.*, "Super-Luminous Type Ic Supernovae: Catching a magnetar by the tail," *Astrophysical Journal*, vol. 770, no. 2, Apr. 11, 2013.

[91] D. A. Howell, D. Kasen, C. Lidman, *et al.*, "Two superluminous supernovae from the early universe discovered by the supernova legacy survey," *Astrophysical Journal*, vol. 779, no. 2, p. 98, Dec. 2013.

[92] A. De Cia, A. Gal-Yam, A. Rubin, *et al.*, "Light Curves of Hydrogen-poor Superluminous Supernovae from the Palomar Transient Factory," *The Astrophysical Journal*, vol. 860, no. 2, p. 100, Jun. 2018.

[93] R. Lunnan, R. Chornock, E. Berger, *et al.*, "Hydrogen-poor Superluminous Supernovae from the Pan-STARRS1 Medium Deep Survey," *The Astrophysical Journal*, vol. 852, no. 2, p. 81, Jan. 2018.

[94] R. M. Quimby, A. D. Cia, A. Gal-Yam, *et al.*, "Spectra of Hydrogen-poor Superluminous Supernovae from the Palomar Transient Factory," *The Astrophysical Journal*, vol. 855, no. 1, p. 2, Mar. 2018.

[95] A. Gal-Yam, "The Most Luminous Supernovae," *Annual Review of Astronomy and Astrophysics*, vol. 57, pp. 305–333, Nov. 2019.

[96] E. Quataert and D. Kasen, "Swift 1644+57: The longest gamma-ray burst?" *Monthly Notices of the Royal Astronomical Society: Letters*, vol. 419, no. 1, pp. L1–L5, Jan. 2012.

[97] S. E. Woosley and A. Heger, "Long gamma-ray transients from collapsars," *Astrophysical Journal*, vol. 752, no. 1, p. 32, Jun. 2012.

[98] B. Margalit and B. D. Metzger, "Time-dependent models of accretion discs with nuclear burning following the tidal disruption of a white dwarf by a neutron star," *Monthly Notices of the Royal Astronomical Society*, vol. 461, no. 2, pp. 1154–1176, Sep. 2016.

[99] T. J. Moriya, M. Nicholl, and J. Guillochon, "Systematic Investigation of the Fallback Accretion-powered Model for Hydrogen-poor Superluminous Supernovae," *The Astrophysical Journal*, vol. 867, no. 2, p. 113, May 31, 2018.

[100] D. Kasen and L. Bildsten, "Supernova light curves powered by young magnetars," *Astrophysical Journal*, vol. 717, no. 1, pp. 245–249, Jul. 2010.

[101] S. E. Woosley, "Bright Supernovae from Magnetar Birth," *Astrophysical Journal Letters*, vol. 719, pp. L204–L207, 2 PART 2 Aug. 3, 2010.

[102] L. Dessart, D. John Hillier, R. Waldman, *et al.*, "Superluminous supernovae: 56Ni power versus magnetar radiation," *Monthly Notices of the Royal Astronomical Society: Letters*, vol. 426, no. 1, pp. L76–L80, Oct. 11, 2012.

[103] B. D. Metzger, B. Margalit, D. Kasen, *et al.*, "The diversity of transients from magnetar birth in core collapse supernovae," *Monthly Notices of the Royal Astronomical Society*, vol. 454, no. 3, pp. 3311–3316, Dec. 2015.

[104] T. Sukhbold and S. E. Woosley, "The Most Luminous Supernovae," *The Astrophysical Journal*, vol. 820, no. 2, p. L38, Apr. 2016.

[105] M. Nicholl, J. Guillochon, and E. Berger, "The Magnetar Model for Type I Superluminous Supernovae. I. Bayesian Analysis of the Full Multicolor Light-curve Sample with MOSFiT," *The Astrophysical Journal*, vol. 850, no. 1, p. 55, Nov. 2017.

[106] M. Nicholl, E. Berger, P. K. Blanchard, *et al.*, "Nebular-phase Spectra of Superluminous Supernovae: Physical Insights from Observational and Statistical Properties," *The Astrophysical Journal*, vol. 871, no. 1, p. 102, Jan. 2019.

[107] A. Jerkstrand, S. J. Smartt, C. Inserra, *et al.*, "Long-Duration Superluminous Supernovae at Late Times," *The Astrophysical Journal*, vol. 835, no. 1, p. 13, Jan. 16, 2017.

[108] D. Milisavljevic, D. J. Patnaude, R. A. Chevalier, *et al.*, "Evidence for a Pulsar Wind Nebula in the Type Ib Peculiar Supernova SN 2012au," *The Astrophysical Journal*, vol. 864, no. 2, p. L36, Sep. 2018.

[109] K. Kotera, E. S. Phinney, and A. V. Olinto, "Signatures of pulsars in the light curves of newly formed supernova remnants," *Monthly Notices of the Royal Astronomical Society*, vol. 432, no. 4, pp. 3228–3236, Jul. 2013.

[110] B. D. Metzger, I. Vurm, R. Hascöet, *et al.*, "Ionization break-out from millisecond pulsar wind nebulae: An X-ray probe of the origin of superluminous supernovae," *Monthly Notices of the Royal Astronomical Society*, vol. 437, no. 1, pp. 703–720, Jan. 2014.

[111] K. Murase, K. Kashiyama, K. Kiuchi, *et al.*, "Gamma-Ray and Hard X-Ray Emission From Pulsar-Aided Supernovae As a Probe of Particle Acceleration in Embryonic Pulsar Wind Nebulae," *Astrophysical Journal*, vol. 805, no. 1, p. 82, May 2015.

[112] I. Vurm and B. D. Metzger, "Gamma-Ray Thermalization and Leakage from Millisecond Magnetar Nebulae: Toward a Self-consistent Model for Superluminous Supernovae," *The Astrophysical Journal*, vol. 917, no. 2, p. 77, Aug. 1, 2021.

[113] S. Q. Wang, L. J. Wang, Z. G. Dai, *et al.*, "Superluminous Supernovae Powered by Magnetars: Late-Time Light Curves and Hard Emission Leakage," *Astrophysical Journal*, vol. 799, no. 1, p. 107, Jan. 2015.

[114] T. W. Chen, S. J. Smartt, A. Jerkstrand, *et al.*, "The host galaxy and late-time evolution of the superluminous supernova PTF12dam," *Monthly Notices of the Royal Astronomical Society*, vol. 452, no. 2, pp. 1567–1586, Sep. 2015.

[115] M. Nicholl, P. K. Blanchard, E. Berger, *et al.*, "One Thousand Days of SN2015bn: HST Imaging Shows a Light Curve Flattening Consistent with Magnetar Predictions," *The Astrophysical Journal*, vol. 866, no. 2, p. L24, Sep. 2018.

[116] M. Nicholl, E. Berger, R. Margutti, *et al.*, "The Superluminous Supernova SN 2017egm in the Nearby Galaxy NGC 3191: A Metal-rich Environment Can Support a Typical SLSN Evolution," *The Astrophysical Journal*, vol. 845, no. 1, p. L8, Aug. 2017.

[117] A. A. Zdziarski and R. Svensson, "Absorption of X-rays and gamma rays at cosmological distances," *The Astrophysical Journal*, vol. 344, p. 551, Sep. 1989.

[118] K. Bhirombhakdi, R. Chornock, R. Margutti, *et al.*, "Where is the Engine Hiding Its Missing Energy? Constraints from a Deep X-Ray Non-detection of the Superluminous SN 2015bn," *The Astrophysical Journal*, vol. 868, no. 2, p. L32, Sep. 2018.

[119] R. Margutti, R. Chornock, B. D. Metzger, *et al.*, "Results from a Systematic Survey of X-Ray Emission from Hydrogen-poor Superluminous SNe," *The Astrophysical Journal*, vol. 864, no. 1, p. 45, Aug. 29, 2018.

[120] A. J. Levan, A. M. Read, B. D. Metzger, *et al.*, "Superluminous x-rays from a superluminous supernova," *The Astrophysical Journal*, vol. 771, no. 2, p. 136, Jul. 2013.

[121] B. Margalit, B. D. Metzger, E. Berger, *et al.*, "Unveiling the engines of fast radio bursts, superluminous supernovae, and gamma-ray bursts," *Monthly Notices of the Royal Astronomical Society*, vol. 481, no. 2, pp. 2407–2426, Dec. 2018.

[122] T. Eftekhari, E. Berger, B. Margalit, *et al.*, "A Radio Source Coincident with the Superluminous Supernova PTF10hgi: Evidence for a Central Engine and an Analog of the Repeating FRB 121102?" *The Astrophysical Journal*, vol. 876, no. 1, p. L10, Apr. 30, 2019.

[123] N. Renault-Tinacci, K. Kotera, A. Neronov, *et al.*, "Search for Gamma-Ray Emission from Superluminous Supernovae with the Fermi-Lat," *Astronomy and Astrophysics*, vol. 611, A45, Aug. 29, 2018.

[124] S. Bose, S. Dong, A. Pastorello, *et al.*, "Gaia17biu/SN 2017egm in NGC 3191: The closest hydrogen-poor superluminous supernova to date is in a "normal", massive, metal-rich spiral galaxy," *The Astrophysical Journal*, vol. 853, no. 1, p. 57, Aug. 2, 2017.

[125] Q. Yuan, N.-H. Liao, Y.-L. Xin, *et al.*, "*Fermi* Large Area Telescope Detection of Gamma-Ray Emission from the Direction of Supernova iPTF14hls," *The Astrophysical Journal*, vol. 854, no. 2, p. L18, Feb. 14, 2018.

[126] S.-Q. Xi, R.-Y. Liu, X.-Y. Wang, *et al.*, "A Serendipitous Discovery of GeV Gamma-Ray Emission from Supernova 2004dj in a Survey of Nearby Star-forming Galaxies with Fermi-LAT," *The Astrophysical Journal*, vol. 896, no. 2, p. L33, Jun. 17, 2020.

[127] M. L. Ahnen, S. Ansoldi, L. A. Antonelli, *et al.*, "Very-high-energy gamma-ray observations of the Type Ia Supernova SN 2014J with the MAGIC telescopes," *Astronomy and Astrophysics*, vol. 602, p. 31, Feb. 24, 2017.

[128] H. Abdalla, F. Aharonian, F. Ait Benkhali, *et al.*, "Upper limits on very-high-energy gamma-ray emission from core-collapse supernovae observed with H.E.S.S.," *Astronomy and Astrophysics*, vol. 626, A57, Jun. 1, 2019.

[129] The H.E.S.S. Collaboration, "The exceptionally powerful TeV γ-ray emitters in the Large Magellanic Cloud," *Science*, vol. 347, no. 6220, pp. 406–412, Jan. 23, 2015.

[130] Planck Collaboration, P. A. R. Ade, N. Aghanim, *et al.*, "*Planck* 2015 results: XIII. Cosmological parameters," *Astronomy & Astrophysics*, vol. 594, A13, Oct. 2016.

[131] M. Nicholl, E. Berger, R. Margutti, *et al.*, "Superluminous Supernova Sn 2015bn in the Nebular Phase: Evidence for the Engine-Powered Explosion of a Stripped Massive Star," *The Astrophysical Journal*, vol. 828, no. 2, p. L18, Sep. 8, 2016.

[132] M. Nicholl, E. Berger, S. J. Smartt, *et al.*, "SN 2015bn: A Detailed Multi-Wavelength View of a Nearby Superluminous Supernova," *The Astrophysical Journal*, vol. 826, no. 1, p. 39, Jul. 2016.

[133] T. Weekes, H Badran, S. Biller, *et al.*, "VERITAS: The Very Energetic Radiation Imaging Telescope Array System," *Astroparticle Physics*, vol. 17, no. 2, pp. 221–243, May 2002.

[134] J. Holder, R. W. Atkins, H. M. Badran, *et al.*, "The First VERITAS Telescope," *Astroparticle Physics*, vol. 25, no. 6, pp. 391–401, Jul. 2006.

[135] M. Nicholl, "SuperBol: A User-friendly Python Routine for Bolometric Light Curves," *Research Notes of the AAS*, vol. 2, no. 4, p. 230, Dec. 13, 2018.

[136] M. Nievas Rosillo, "The throughput calibration of the VERITAS telescopes," *arXiv e-prints*, Aug. 1, 2021.

[137] W. D. Arnett, "Type I supernovae. I - Analytic solutions for the early part of the light curve," *The Astrophysical Journal*, vol. 253, p. 785, Feb. 1982.

[138] J. Guillochon, J. Parrent, L. Z. Kelley, *et al.*, "An Open Catalog for Supernova Data," *The Astrophysical Journal*, vol. 835, no. 1, p. 64, May 3, 2016.

[139] S. S. Komissarov, "Magnetic Dissipation in the Crab Nebula," *Monthly Notices of the Royal Astronomical Society*, vol. 428, no. 3, pp. 2459–2466, Jan. 2013.

[140] Y. E. Lyubarsky, "The Termination Shock in a Striped Pulsar Wind," *Monthly Notices of the Royal Astronomical Society*, vol. 345, no. 1, pp. 153–160, Oct. 2003.

[141] B. Margalit, B. D. Metzger, T. A. Thompson, *et al.*, "The GRB-SLSN connection: Misaligned magnetars, weak jet emergence, and observational signatures," *Monthly Notices of the Royal Astronomical Society*, vol. 475, no. 2, pp. 2659–2674, May 2018.

[142] J. Dexter and D. Kasen, "Supernova light curves powered by fallback accretion," *Astrophysical Journal*, vol. 772, no. 1, p. 30, Jul. 2013.

[143] T. J. Moriya, B. D. Metzger, and S. I. Blinnikov, "Supernovae Powered by Magnetars that Transform into Black Holes," *The Astrophysical Journal*, vol. 833, p. 64, Dec. 1, 2016.

[144] N. Smith and S. P. Owocki, "On the Role of Continuum-driven Eruptions in the Evolution of Very Massive Stars and Population III Stars," *The Astrophysical Journal*, vol. 645, no. 1, pp. L45–L48, Jul. 2006.

[145] R. A. Chevalier and C. M. Irwin, "Shock breakout in dense mass loss: Luminous supernovae," *Astrophysical Journal Letters*, vol. 729, p. L6, 1 PART II Mar. 2011.

[146] T. J. Moriya, K. Maeda, F. Taddia, *et al.*, "An analytic bolometric light curve model of interaction-powered supernovae and its application to type IIn supernovae," *Monthly Notices of the Royal Astronomical Society*, vol. 435, no. 2, pp. 1520–1535, Jul. 9, 2013.

[147] N. Smith, W. Li, R. J. Foley, *et al.*, "SN 2006gy: Discovery of the Most Luminous Supernova Ever Recorded, Powered by the Death of an Extremely Massive Star like η Carinae," *The Astrophysical Journal*, vol. 666, no. 2, pp. 1116–1128, Sep. 2007.

[148] M. Nicholl, P. K. Blanchard, E. Berger, *et al.*, "An Extremely Energetic Supernova from a Very Massive Star in a Dense Medium," *Nature Astronomy*, vol. 4, pp. 893–899, Apr. 13, 2020.

[149] E. Sorokina, S. Blinnikov, K. Nomoto, *et al.*, "Type I Superluminous Supernovae As Explosions Inside Non-Hydrogen Circumstellar Envelopes," *The Astrophysical Journal*, vol. 829, no. 1, p. 17, Sep. 2016.

[150] A. Kozyreva, M. Gilmer, R. Hirschi, *et al.*, "Fast evolving pair-instability supernova models: Evolution, explosion, light curves," *Monthly Notices of the Royal Astronomical Society*, vol. 464, no. 3, pp. 2854–2865, Jan. 2017.

[151] D. Milisavljevic, R. Margutti, A. Kamble, *et al.*, "Metamorphosis of SN 2014c: Delayed Interaction Between a Hydrogen Poor Core-Collapse Supernova and a Nearby Circumstellar Shell," *Astrophysical Journal*, vol. 815, no. 2, p. 120, Dec. 20, 2015.

[152] L. Yan, R. Quimby, E. Ofek, *et al.*, "Detection of Broad Hα Emission Lines in the Late-Time Spectra of a Hydrogen-Poor Superluminous Supernova," *Astrophysical Journal*, vol. 814, no. 2, p. 108, Dec. 2015.

[153] L. Yan, R. Lunnan, D. A. Perley, *et al.*, "Hydrogen-poor Superluminous Supernovae with Late-time H α Emission: Three Events From the Intermediate Palomar Transient Factory," *The Astrophysical Journal*, vol. 848, no. 1, p. 6, Oct. 5, 2017.

[154] X. Chen, S. Kou, and X. Liu, "A New Method to Classify Type IIP/IIL Supernovae Based on their Spectra," *The Astrophysical Journal*, vol. 890, no. 2, p. 177, Nov. 7, 2018.

[155] H. Kuncarayakti, K. Maeda, C. J. Ashall, *et al.*, "SN 2017dio: A Type-Ic Supernova Exploding in a Hydrogen-rich Circumstellar Medium," *The Astrophysical Journal*, vol. 854, no. 1, p. L14, Feb. 9, 2018.

[156] J. C. Mauerhan, A. V. Filippenko, W. K. Zheng, *et al.*, "Stripped-envelope supernova SN 2004dk is now interacting with hydrogen-rich circumstellar material," *Monthly Notices of the Royal Astronomical Society*, vol. 478, no. 4, pp. 5050–5055, Mar. 19, 2018.

[157] D. Pooley, W. H. G. Lewin, D. W. Fox, *et al.*, "X-Ray, Optical, and Radio Observations of the Type II Supernovae 1999em and 1998S," *The Astrophysical Journal*, vol. 572, no. 2, pp. 932–943, Jun. 20, 2002.

[158] P. Chandra, R. A. Chevalier, N. Chugai, *et al.*, "Radio and X-ray observations of SN 2006jd: Another strongly interacting type IIn supernova," *Astrophysical Journal*, vol. 755, no. 2, p. 110, Aug. 20, 2012.

[159] P. Chandra, R. A. Chevalier, N. Chugai, *et al.*, "X-Ray and Radio Emission from Type Iin Supernova SN 2010jl," *Astrophysical Journal*, vol. 810, no. 1, p. 32, Sep. 1, 2015.

[160] R. A. Chevalier and C. Fransson, "Circumstellar Emission from Type Ib and Ic Supernovae," *The Astrophysical Journal*, vol. 651, no. 1, pp. 381–391, Nov. 2006.

[161] K. Murase, T. A. Thompson, B. C. Lacki, *et al.*, "New class of high-energy transients from crashes of supernova ejecta with massive circumstellar material shells," *Physical Review D - Particles, Fields, Gravitation and Cosmology*, vol. 84, no. 4, p. 43 003, Aug. 2011.

[162] E. Steinberg and B. D. Metzger, "The Multidimensional Structure of Radiative Shocks: Suppressed Thermal X-Rays and Relativistic Ion Acceleration," *Monthly Notices of the Royal Astronomical Society*, vol. 479, no. 1, pp. 687–702, Sep. 2018.

[163] K. Fang, B. D. Metzger, K. Murase, *et al.*, "Multimessenger Implications of AT2018cow: High-energy Cosmic-Ray and Neutrino Emissions from Magnetar-powered Superluminous Transients," *The Astrophysical Journal*, vol. 878, no. 1, p. 34, Jun. 2019.

[164] K. Murase, A. Franckowiak, K. Maeda, *et al.*, "High-energy Emission from Interacting Supernovae: New Constraints on Cosmic-Ray Acceleration in Dense Circumstellar Environments," *The Astrophysical Journal*, vol. 874, no. 1, p. 80, Mar. 2019.

[165] S. Prajs, M. Sullivan, M. Smith, *et al.*, "The volumetric rate of superluminous supernovae at $z \sim 1$," *Monthly Notices of the Royal Astronomical Society*, vol. 464, no. 3, pp. 3568–3579, Jan. 21, 2017.

[166] M. McCrum, S. J. Smartt, A. Rest, *et al.*, "Selecting superluminous supernovae in faint galaxies from the first year of the Pan-STARRS1 medium deep survey," *Monthly Notices of the Royal Astronomical Society*, vol. 448, no. 2, pp. 1206–1231, Apr. 2015.

[167] M. Nicholl, P. K. G. Williams, E. Berger, *et al.*, "Empirical Constraints on the Origin of Fast Radio Bursts: Volumetric Rates and Host Galaxy Demographics as a Test of Millisecond Magnetar Connection," *The Astrophysical Journal*, vol. 843, no. 2, p. 84, Jul. 2017.

[168] C. A. Kierans, "AMEGO: Exploring the extreme multi-messenger universe," in *Space Telescopes and Instrumentation 2020: Ultraviolet to Gamma Ray*, J.-W. A. den Herder, K. Nakazawa, and S. Nikzad, Eds., Online Only, United States: SPIE, Dec. 13, 2020, p. 320, ISBN: 978-1-5106-3675-0 978-1-5106-3676-7.

[169] N. Park, "Performance of the VERITAS experiment," in *Proceedings of Science*, ser. International Cosmic Ray Conference, vol. 34, Jul. 2015, p. 771.

[170] C. T. A. Observatory and C. T. A. Consortium, *CTAO Instrument Response Functions - version prod3b-v2*, version prod3b-v2/v1.0.0, Apr. 5, 2016.

[171] J. Knödlseder, M. Mayer, C. Deil, *et al.*, "GammaLib and ctools: A software framework for the analysis of astronomical gamma-ray data," *Astronomy and Astrophysics*, vol. 593, A1, Sep. 2016.

[172] V. Fioretti, A. Bulgarelli, and F. Schüssler, "The Cherenkov Telescope array on-site integral sensitivity: Observing the Crab," *Ground-based and Airborne Telescopes VI*, vol. 9906, 99063O, Jul. 2016.

[173] A. Clocchiatti and J. C. Wheeler, "On the Light Curves of Stripped-Envelope Supernovae," *The Astrophysical Journal*, vol. 491, no. 1, pp. 375–380, Dec. 10, 1997.

[174] E. Chatzopoulos, J. Craig Wheeler, and J. Vinko, "Generalized semi-analytical models of supernova light curves," *Astrophysical Journal*, vol. 746, no. 2, p. 121, Feb. 2012.

[175] B. Warner, *Cataclysmic Variable Stars*, ser. Cambridge Astrophysics Series 28. Cambridge ; New York: Cambridge University Press, 1995, 572 pp., ISBN: 978-0-521-41231-5.

[176] M. Ermann, M. Ajello, A. Albert, *et al.*, "Fermi establishes classical novae as a distinct class of gamma-ray sources: The Fermi-LAT collaboration," *Science*, vol. 345, no. 6196, pp. 554–558, Aug. 2014.

[177] C. C. Cheung, P. Jean, S. N. Shore, *et al.*, "*FERMI*- LAT GAMMA-RAY DETECTIONS OF CLASSICAL NOVAE V1369 CENTAURI 2013 AND V5668 SAGITTARII 2015," *The Astrophysical Journal*, vol. 826, no. 2, p. 142, Jul. 27, 2016.

[178] A. Franckowiak, P. Jean, M. Wood, *et al.*, "Search for gamma-ray emission from Galactic novae with the *Fermi* -LAT," *Astronomy & Astrophysics*, vol. 609, A120, Jan. 2018.

[179] K. L. Li, B. D. Metzger, L. Chomiuk, *et al.*, "A nova outburst powered by shocks," *Nature Astronomy*, vol. 1, no. 10, pp. 697–702, Sep. 2017.

[180] E. Aliu, S. Archambault, T. Arlen, *et al.*, "Veritas Observations of the Nova in V407 Cygni," *The Astrophysical Journal*, vol. 754, no. 1, p. 77, Jul. 20, 2012.

[181] M. L. Ahnen, S. Ansoldi, L. A. Antonelli, *et al.*, "Very high-energy γ -ray observations of novae and dwarf novae with the MAGIC telescopes," *Astronomy & Astrophysics*, vol. 582, A67, Oct. 2015.

[182] T. Kato, "WZ Sge-type dwarf novae," *Publications of the Astronomical Society of Japan*, vol. 67, no. 6, p. 108, Dec. 4, 2015.

[183] S. J. Wagner and H. E. S. S. Collaboration, "H.E.S.S. observations of soft spectrum VHE gamma-ray emission from the recurrent nova RS Ophiuchi," *The Astronomer's Telegram*, vol. 14857, p. 1, Aug. 1, 2021.

[184] M. Collaboration, V. A. Acciari, S. Ansoldi, *et al.*, "Gamma rays reveal proton acceleration in thermonuclear novae explosions," Feb. 15, 2022.

[185] K.-L. Li, "Fermi-lat detection of TCP j18573095+1653396 (=Nova her 2021)," *The Astronomer's Telegram*, vol. 14705, p. 1, Jun. 2021.

[186] K. Zhirkov, Y. Kechin, V. Lipunov, *et al.*, "MASTER OT J030227.28+191754.5 - 10 mag outburst detection during an inspect of IceCube-211125A," *The Astronomer's Telegram*, vol. 15067, p. 1, Nov. 1, 2021.

[187] E. O. Waagen, "Nova in perseus: N per 2020 = TCP j04291884+4354232 = TCP j04291888+4354233," *AAVSO Alert Notice*, vol. 726, p. 1, Nov. 2020.

[188] U. Munari, P. Ochner, P. Valisa, *et al.*, "Rapid evolution of Nova Per 2020 on the rise toward optical maximum," *The Astronomer's Telegram*, vol. 14229, p. 1, Nov. 2020.

[189] U. Munari, F. Castellani, S. Dallaporta, *et al.*, "Classification of TCP J04291884+4354232 as a classical nova," *The Astronomer's Telegram*, vol. 14224, p. 1, Nov. 1, 2020.

[190] S. Borthakur, V. Kumar, V. Joshi, *et al.*, "'"Reverse hybrid" behavior of nova per 2020 = TCP j04291888+4354233," *The Astronomer's Telegram*, vol. 14230, p. 1, Nov. 2020.

[191] D. Chochol, L. Hambalek, R. Komzik, *et al.*, "Post-maximum spectroscopy of the classical nova V1112 Per (Nova Per 2020)," *The Astronomer's Telegram*, vol. 14243, p. 1, Dec. 2020.

[192] D. P. K. Banerjee, M. Shahbandeh, C. E. Woodward, *et al.*, "Near-infrared spectroscopy of V1112 per (nova per 2020)," *The Astronomer's Telegram*, vol. 14256, p. 1, Dec. 2020.

[193] I. Albanese, A. Farina, V. Andreoli, *et al.*, "Spectroscopic follow-up observations of Nova Herculis 2021," *The Astronomer's Telegram*, vol. 14718, p. 1, Jun. 1, 2021.

[194] E. Aydi, K. V. Sokolovsky, L. Chomiuk, *et al.*, "Multi-wavelength follow up of the very fast Nova Herculis 2021 (TCP J18573095+1653396)," *The Astronomer's Telegram*, vol. 14710, p. 1, Jun. 1, 2021.

[195] D. D. Balam, D. Bohlender, P. Koubsky, *et al.*, "H-alpha Spectroscopy of Nova V1674 Her," *The Astronomer's Telegram*, vol. 14740, p. 1, Jun. 1, 2021.

[196] J. J. Drake, J.-U. Ness, K. L. Page, *et al.*, "The Remarkable Spin-down and Ultrafast Outflows of the Highly Pulsed Supersoft Source of Nova Herculis 2021," *The Astrophysical Journal Letters*, vol. 922, no. 2, p. L42, Dec. 1, 2021.

[197] C. E. Woodward, R. M. Wagner, S. Starrfield, *et al.*, "Further Optical Spectroscopic Observations of V1674 Herculis," *The Astronomer's Telegram*, vol. 14723, p. 1, Jun. 1, 2021.

[198] P. Ochner, V. Andreoli, A. Farina, *et al.*, "Strong UV Neon lines in the spectrum of Nova Herculis 2021," *The Astronomer's Telegram*, vol. 14805, p. 1, Jul. 1, 2021.

[199] U. Munari, "[FeX] and [FeXI] coronal lines now present in Nova Her 2021," *The Astronomer's Telegram*, vol. 14824, p. 1, Aug. 2021.

[200] U. Munari, P. Valisa, and S. Dallaporta, "Spectroscopic classification of TCP J18573095+1653396 as a nova bordering naked-eye brightness," *The Astronomer's Telegram*, vol. 14704, p. 1, Jun. 1, 2021.

[201] K. L. Page, M. Orio, K. V. Sokolovsky, *et al.*, "Swift detection of super-soft X-ray emission from V1674 Her," *The Astronomer's Telegram*, vol. 14747, p. 1, Jul. 2021.

[202] P. Kuin, S. Starrfield, M. Orio, *et al.*, "Swift UVOT photometry and spectra from V1674 her," *The Astronomer's Telegram*, vol. 14736, p. 1, Jun. 2021.

[203] P. Mroz, K. Burdge, J. van Roestel, *et al.*, "An 8.4 min period in the archival ZTF light curve of Nova Herculis 2021," *The Astronomer's Telegram*, vol. 14720, p. 1, Jun. 1, 2021.

[204] S. Pei, G. J. M. Luna, M. Orio, *et al.*, "NICER observations of nova her 2021," *The Astronomer's Telegram*, vol. 14798, p. 1, Jul. 2021.

[205] J. Patterson, M. Epstein-Martin, T. Vanmunster, *et al.*, "The orbital and pulse periods of V1674 herculis," *The Astronomer's Telegram*, vol. 14856, p. 1, Aug. 2021.

[206] T. J. Maccarone, A. Beardmore, K. Mukai, *et al.*, "X-ray pulsations from nova her 2021," *The Astronomer's Telegram*, vol. 14776, p. 1, Jul. 2021.

[207] C. E. Woodward, D. P. K. Banerjee, T. R. Geballe, *et al.*, "Near-infrared Studies of Nova V1674 Herculis: A Shocking Record Breaker," *The Astrophysical Journal Letters*, vol. 922, no. 1, p. L10, Nov. 1, 2021.

[208] Z. Paragi, U. Munari, J. Yang, *et al.*, "E-EVN observations of V1674 her," *The Astronomer's Telegram*, vol. 14758, p. 1, Jul. 2021.

[209] K. Sokolovsky, E. Aydi, L. Chomiuk, *et al.*, "VLA radio detection of Galactic novae V1674 Her and V1405 Cas," *The Astronomer's Telegram*, vol. 14731, p. 1, Jun. 1, 2021.

[210] K.-L. Li, "Erratum to ATel #14705: Fermi-lat detection of TCP j18573095+1653396 (=Nova her 2021)," *The Astronomer's Telegram*, vol. 14707, p. 1, Jun. 2021.

[211] IceCube Collaboration, "IceCube-211125A: IceCube observation of a high-energy neutrino candidate track-like event," *GRB Coordinates Network*, vol. 31126, p. 1, Nov. 1, 2021.

[212] R. Stein, V. Karambelkar, M. M. Kasliwal, *et al.*, "Classification of AT2021afpi, a possible counterpart to IC211125A, as a classical nova," *The Astronomer's Telegram*, vol. 15069, p. 1, Nov. 1, 2021.

[213] K. Taguchi, M. Shibata, Y. Masayuki, *et al.*, "Spectroscopic and Photometric follow-up of MASTER OT J030227.28+191754.5: A Possible "Narrow-lined He Nova" or Large-amplitude Dwarf Nova," *The Astronomer's Telegram*, vol. 15072, p. 1, Nov. 1, 2021.

[214] K. Isogai, Y. Tampo, M. Yamanaka, *et al.*, "Spectroscopic and Photometric confirmation of MASTER OT J030227.28+191754.5 as a very large-amplitude WZ Sge-type dwarf nova," *The Astronomer's Telegram*, vol. 15074, p. 1, Nov. 1, 2021.

[215] H. Ayala, "HAWC observations of AT2021afpi / MASTER OT J030227.28+191754.5 (discovered during follow-up observations of IceCube-211125A)," *The Astronomer's Telegram*, vol. 15079, p. 1, Nov. 1, 2021.

[216] ——, "Update on HAWC observations of AT2021afpi / MASTER OT J030227.28+191754.5 (discovered during follow-up observations of IceCube-211125A)," *The Astronomer's Telegram*, vol. 15088, p. 1, Dec. 1, 2021.

[217] A. Coleiro, D. Dornic, and ANTARES Collaboration, "Search for counterpart to IceCube-211125A with ANTARES," *The Astronomer's Telegram*, vol. 15065, p. 1, Nov. 1, 2021.

[218] K. Sarneczky, J. Vinko, and L. Kiss, "Prediscovery detection of AT2021afpi/MASTER OT J030227.28+191754.5, 8 hours before the IceCube-211125A neutrino event," *The Astronomer's Telegram*, vol. 15081, p. 1, Dec. 1, 2021.

[219] V. S. Paliya, "Classical nova AT2021afpi, a possible EM counterpart to IC211125A, is in X-ray outburst," *The Astronomer's Telegram*, vol. 15073, p. 1, Nov. 1, 2021.

[220] D. B. Fox, "Dwarf Nova AT2021afpi: X-ray Observations," *The Astronomer's Telegram*, vol. 15087, p. 1, Dec. 1, 2021.

[221] V. V. Neustroev, J. P. Osborne, and K. L. Page, "Swift follow-up observations of AT2021afpi / MASTER OT J030227.28+191754.5," *The Astronomer's Telegram*, vol. 15115, p. 1, Dec. 1, 2021.

[222] J. Quinn, VERISTAS Collaboration, B. Metzger, *et al.*, "VERITAS observations of AT2021afpi / MASTER OT J030227.28+191754.5 (discovered during follow-up observations of IceCube-211125A)," *The Astronomer's Telegram*, vol. 15078, p. 1, Nov. 1, 2021.

[223] F. Aharonian, A. Akhperjanian, J. Barrio, *et al.*, "Evidence for TeV gamma ray emission from Cassiopeia A," *Astronomy & Astrophysics*, vol. 370, no. 1, pp. 112–120, Apr. 2001.

[224] E. Feigelson and P. Nelson, "Statistical methods for astronomical data with upper limits. I-Univariate distributions," *The Astrophysical Journal*, vol. 293, pp. 192–206, 1985.

[225] D. Helsel, "Much Ado About Next to Nothing: Incorporating Nondetects in Science," *The Annals of Occupational Hygiene*, Dec. 23, 2009.

[226] C. Deil, R. Zanin, J. Lefaucheur, *et al.*, "Gammapy - A prototype for the CTA science tools," vol. 301, p. 766, Jan. 1, 2017.

[227] G. Vianello, R. J. Lauer, P. Younk, *et al.*, "The Multi-Mission Maximum Likelihood framework (3ML)," version 1, 2015.

[228] L. Chomiuk, B. D. Metzger, and K. J. Shen, "New Insights into Classical Novae," *Annual Review of Astronomy and Astrophysics*, vol. 59, no. 1, pp. 391–444, Sep. 8, 2021.

[229] B. D. Metzger, T. Finzell, I. Vurm, *et al.*, "Gamma-ray novae as probes of relativistic particle acceleration at non-relativistic shocks," *Monthly Notices of the Royal Astronomical Society*, vol. 450, no. 3, pp. 2739–2748, Jul. 1, 2015.

[230] D. P. K. Banerjee, V. Joshi, G. C. Anupama, *et al.*, "Dust formation in V1112 per (nova per 2020)," *The Astronomer's Telegram*, vol. 14338, p. 1, Jan. 2021.

[231] J. Wang, C. Gao, L. P. Xin, *et al.*, "Spectroscopy of Nova V1674 Her on 2021 June 17," *The Astronomer's Telegram*, vol. 14737, p. 1, Jun. 1, 2021.

[232] C. E. Woodward, D. P. K. Banerjee, R. M. Wagner, *et al.*, "Near Infrared Spectroscopy of V1674 Herculis," *The Astronomer's Telegram*, vol. 14728, p. 1, Jun. 1, 2021.

[233] C. E. Woodward, D. P. K. Banerjee, A. Evans, *et al.*, "Near Infrared Coronal Line Emission in nova V1674 Herculis," *The Astronomer's Telegram*, vol. 14741, p. 1, Jun. 1, 2021.

[234] ——, "The Suite of Strong Near Infrared Coronal Line Emission in nova V1674 Herculis," *The Astronomer's Telegram*, vol. 14765, p. 1, Jul. 1, 2021.

[235] M. Kadler, F. Eppel, J. Hessdoerfer, *et al.*, "TELAMON Detection of a High-State Compact Radio Source and Gamma-Bright AGN Positionally Coincident with Two IceCube Bronze Neutrino Events (IceCube-191231A and IceCube-211125A)," *The Astronomer's Telegram*, vol. 15076, p. 1, Nov. 1, 2021.

[236] S. Paiano, A. Treves, R. Falomo, *et al.*, "Optical spectroscopy of 4FGLJ0258.1+2030: Possible counterpart of the two neutrino events IceCube-191231A and IceCube-211125A," *The Astronomer's Telegram*, vol. 15085, p. 1, Dec. 1, 2021.

[237] S. Reusch and R. Stein, "Observations of radio sources J0258+2030 and J0245+2405, possible counterparts to IceCube-211125A, with the Zwicky Transient Facility," *The Astronomer's Telegram*, vol. 15080, p. 1, Nov. 1, 2021.

[238] R. A. Downes and H. W. Duerbeck, "Optical Imaging of Nova Shells and the Maximum Magnitude-Rate of Decline Relationship," *The Astronomical Journal*, vol. 120, no. 4, pp. 2007–2037, Oct. 2000.

[239] C. A. L. Bailer-Jones, J. Rybizki, M. Fouesneau, *et al.*, "Estimating Distance from Parallaxes. IV. Distances to 1.33 Billion Stars in *Gaia* Data Release 2," *The Astronomical Journal*, vol. 156, no. 2, p. 58, Jul. 20, 2018.

[240] C. A. L. Bailer-Jones, J. Rybizki, M. Fouesneau, *et al.*, "Estimating Distances from Parallaxes. V. Geometric and Photogeometric Distances to 1.47 Billion Stars in Gaia Early Data Release 3," *The Astronomical Journal*, vol. 161, no. 3, p. 147, Mar. 1, 2021.

[241] G. Morlino and D. Caprioli, "Strong evidence for hadron acceleration in Tycho's supernova remnant," *Astronomy & Astrophysics*, vol. 538, A81, Feb. 2012.

[242] G. D. Lafferty, T. R. Wyatt, I. N. Physics, *et al.*, "Where to stick your data points: The treatment of measurements within wide bins," *Nuclear Inst. and Methods in Physics Research, A*, vol. 355, no. 2-3, pp. 541–547, Feb. 1995.

Appendix A: Physics Derivations

A.1 Frank-Tamm Formula

We are interested in calculating the power spectrum of a radiating particle in a medium with a dielectric constant:

$$n(\omega) = \sqrt{\epsilon(\omega)} \tag{A.1}$$

Work through the Maxwell's equations to get radiation as a function of this dielectric constant. Begin with a Fourier transform of the Maxwell equations:

$$(k^2 - \frac{\omega^2}{c^2}\epsilon(\omega))\phi(\vec{k},\omega) = \frac{4\pi}{\epsilon(\omega)}\rho(\vec{k},\omega) \tag{A.2}$$

$$(k^2 - \frac{\omega^2}{c^2}\epsilon(\omega))\vec{A}(\vec{k},\omega) = \frac{4\pi}{c}\vec{J}(\vec{k},\omega) \tag{A.3}$$

Assuming a moving point charge, where $\vec{v}$ is the velocity of the charge and e the magnitude of the charge,

$$\rho(\vec{x},t) = ze\delta(\vec{x} - \vec{v}t)$$
$$\vec{J}(\vec{x},t) = \vec{v}\rho(\vec{x},t)$$

Transforming these functions to Fourier space with frequency ω and wavenumber $\vec{k}$

$$\rho(\vec{x},t) \rightarrow \frac{ze}{2\pi}\delta(\omega - \vec{k}\cdot\vec{v})$$
$$\vec{J}(\vec{x},t) \rightarrow \vec{v}\rho(\vec{k},\omega) = \frac{ze\vec{v}}{2\pi}\delta(\omega - \vec{k}\cdot\vec{v})$$

Expanding A.2 and A.3:

$$(k^2 - \frac{\omega^2}{c^2}\epsilon(\omega))\phi(\vec{k},\omega) = \frac{4\pi}{\epsilon(\omega)}\left[\frac{ze}{2\pi}\delta(\omega - \vec{k}\cdot\vec{v})\right]$$
$$(k^2 - \frac{\omega^2}{c^2}\epsilon(\omega))\vec{A}(\vec{k},\omega) = \frac{4\pi}{c}\left[\vec{v}\rho(\vec{k},\omega)\right] = \frac{4\pi}{c}\left[\vec{v}\frac{ze}{2\pi}\delta(\omega - \vec{k}\cdot\vec{v})\right]$$

$$\begin{aligned}
\phi(\vec{k},\omega) &= \frac{1}{(k^2 - \frac{\omega^2}{c^2}\epsilon(\omega))}\frac{4\pi}{\epsilon(\omega)}\left[\frac{ze}{2\pi}\delta(\omega - \vec{k}\cdot\vec{v})\right] \\
&= \frac{2ze}{\epsilon(\omega)}\frac{\delta(\omega - \vec{k}\cdot\vec{v})}{(k^2 - \frac{\omega^2}{c^2}\epsilon(\omega))} \\
\vec{A}(\vec{k},\omega) &= \frac{1}{(k^2 - \frac{\omega^2}{c^2}\epsilon(\omega))}\frac{4\pi}{c}\left[\vec{v}\frac{ze}{2\pi}\delta(\omega - \vec{k}\cdot\vec{v})\right] \\
&= \frac{2ze\vec{v}}{c}\frac{\delta(\omega - \vec{k}\cdot\vec{v})}{(k^2 - \frac{\omega^2}{c^2}\epsilon(\omega))} \\
&= \epsilon(\omega)\frac{c}{\vec{v}}\phi(\vec{k},\omega)
\end{aligned}$$

With $\vec{A}(\vec{v},\omega)$ and $\phi(\vec{k},\omega)$, we can find $\vec{E}(\vec{v},\omega)$ and $\vec{B}(\vec{v},\omega)$ using the proper choice of gauge and

field equations:

$$
\begin{aligned}
\vec{E} &= -\nabla\phi - \frac{1}{c}\frac{\partial \vec{A}}{\partial t} \\
E(\vec{k},\omega) &= -i\vec{k}\phi + \frac{i}{c}\omega\vec{A}(\vec{k},\omega) \\
&= -i\vec{k}\frac{2ze}{\epsilon(\omega)}\frac{\delta(\omega-\vec{k}\cdot\vec{v})}{k^2-\frac{\omega^2}{c^2}\epsilon(\omega)} + \frac{i\omega}{c}\frac{2ze\vec{v}}{c}\frac{\delta(\omega-\vec{k}\cdot\vec{v})}{(k^2-\frac{\omega^2}{c^2}\epsilon(\omega))} \\
&= \left(\frac{-\vec{k}}{\epsilon(\omega)} + \frac{\omega\vec{v}}{c^2}\right)\left[2zei\frac{\delta(\omega-\vec{k}\cdot\vec{v})}{k^2-\frac{\omega^2}{c^2}\epsilon(\omega)}\right] \\
&= \left(-\vec{k} + \frac{\epsilon(\omega)\omega\vec{v}}{c^2}\right)\left[i\frac{2ze}{\epsilon(\omega)}\frac{\delta(\omega-\vec{k}\cdot\vec{v})}{k^2-\frac{\omega^2}{c^2}\epsilon(\omega)}\right] \\
&= i\left(-\vec{k} + \frac{\epsilon(\omega)\omega\vec{v}}{c^2}\right)\phi(\vec{k},\omega) \\
\vec{B} &= \nabla\times\vec{A} \\
&= i\epsilon(\omega)\vec{k}\times\frac{\vec{v}}{c}\phi(\vec{k},\omega)
\end{aligned}
$$

Now we have the electric fields in terms of the potentials in Fourier space and can integrate away the propagation vector $\vec{k}$.

$$
\begin{aligned}
\vec{E}(w) &= \int \frac{d^3k}{(2\pi)^{3/2}}e^{i\vec{k}\cdot\vec{x}}\vec{E}(\vec{k},\omega) \\
&= \frac{-i2ze}{\epsilon(\omega)(2\pi)^{3/2}}\int d^3k e^{i\vec{k}\cdot\vec{x}}\left(-\vec{k} + \frac{\epsilon(\omega)\omega\vec{v}}{c^2}\right)\frac{\delta(\omega-\vec{k}\cdot\vec{v})}{(k^2-\frac{\omega^2}{c^2}\epsilon(\omega))}
\end{aligned}
$$

Solve this integral by choosing an impact distance b to place the radiating particle, $\vec{x} = (0, b, 0)$. Simplify further with variable $\lambda^2 \equiv \frac{\omega^2}{\vec{v}^2} - \frac{\omega^2}{c^2}\epsilon(\omega) = \frac{\omega^2}{\vec{v}^2}(1-\beta^2\epsilon(\omega))$. First integrate parallel to $\vec{v}$, along direction 1.

$$
\begin{aligned}
E_1 &= \frac{-i2ze}{\epsilon(\omega)(2\pi)^{3/2}} \int d^3k e^{ik_2 b} \left(-k_1 + \frac{\epsilon(\omega)\omega v}{c^2}\right) \frac{\delta(\omega - k_1 v)}{(k^2 - \frac{\omega^2}{c^2}\epsilon(\omega))} \\
&= \frac{-i2ze}{\epsilon(\omega)(2\pi)^{3/2}} \int dk_1 k_2 k_3 e^{ik_2 b} \left(-k_1 + \frac{\epsilon(\omega)\omega v}{c^2}\right) \frac{\delta(\omega - k_1 v)}{(k^2 - \frac{\omega^2}{c^2}\epsilon(\omega))} \\
\delta(\omega - k_1 v) &= \frac{1}{v}\delta(k_1 - \frac{\omega}{v}) \\
\frac{1}{v\epsilon(\omega)}(\frac{\epsilon\omega v}{c^2} - \frac{\omega}{v}) &= \frac{\omega}{\epsilon v^2}(\frac{\epsilon v^2}{c^2} - 1) \\
&= \frac{\omega}{v^2}(\frac{v^2}{c^2} - \frac{1}{\epsilon}) \\
&= \frac{\omega}{v^2}(\beta^2 - \frac{1}{\epsilon}) = -\frac{\omega}{v^2}\left(\frac{1}{\epsilon(\omega)} - \beta^2\right) \\
E_1 &= -\frac{i2ze}{(2\pi)^{3/2}}\frac{\omega}{v^2}\left(\frac{1}{\epsilon(\omega)} - \beta^2\right) \int_{-\infty}^{\infty} dk_2 e^{ibk_2} \int_{-\infty}^{\infty} \frac{dk_3}{k_2^2 + k_3^2 + \lambda^2}
\end{aligned}
$$

The integral over k_1 is a a simple application of the dirac delta in all the k_1 positions. The integral over k_3 is a simple contour integral with a pole at k_3 which equals $\frac{\pi}{\sqrt{\lambda^2+k_2^2}}$. The remaining integral over k_2 is a modified Bessel function

$$
\begin{aligned}
E_1 &= -\frac{ize\omega}{v^2\sqrt{2\pi}}\left(\frac{1}{\epsilon(\omega)} - \beta^2\right) \int_{-\infty}^{\infty} dk_2 \frac{e^{ibk_2}}{\sqrt{\lambda^2 + k_2^2}} \\
&= -\frac{ize\omega}{v^2}\left(\frac{2}{\pi}\right)^2 \left(\frac{1}{\epsilon(\omega)} - \beta^2\right) K_0(\lambda b)
\end{aligned}
$$

The final set is

$$E_2(\omega) = \frac{ze}{v}\left(\frac{2}{\pi}\right)^{1/2} K_1(\lambda b) \tag{A.4}$$

$$E_3 = 0 \tag{A.5}$$

$$B_1 = B_2 = 0 \tag{A.6}$$

$$B_3 = \epsilon(\omega)\beta E_2(\omega) \tag{A.7}$$

We can now consider the radiated energy dE per particle traversed distance dx_{particle}. It can be expressed through the electromagnetic energy flow P_a through the surface of an infinite cylinder of radius a around the path of the moving particle, which is given by the integral of the Poynting vector $S = c/(4\pi)[E \times H]$ over the cylinder surface:

$$\begin{aligned}\left(\frac{dE}{dx_{particle}}\right)_{rad} &= \frac{1}{v}P_a \\ &= -\frac{c}{4\pi v}\int_{-\infty}^{\infty} 2\pi a B_3 E_1 dx \\ &= -\frac{ca}{2}\int_{-\infty}^{\infty} B_3(t)E_1 dt \\ &= -ca\text{Re}\left[\int_0^{\infty} B_3^*(\omega)E_1(\omega)d\omega\right]\end{aligned}$$

To go into the domain of Cherenkov radiation, we now consider perpendicular distance b much greater than atomic distances in a medium, that is, $|\lambda b \gg 1|$. With this assumption we can expand the Bessel functions above into their asymptotic form:

$$E_1 \to \frac{ize\omega}{c^2}\left(1 - \frac{1}{\beta^2\epsilon(\omega)}\right)\frac{e^{-\lambda b}}{\sqrt{\lambda b}}$$

$$E_2 \to \frac{ze}{v\epsilon(\omega)}\sqrt{\frac{\lambda}{b}}e^{-\lambda b}$$

Then

$$\left(\frac{dE}{dx_{particle}}\right)_{rad} = \mathrm{Re}\left[\int_0^\infty \frac{z^2e^2}{c^2}\left(-i\sqrt{\frac{\lambda^*}{\lambda}}\right)\omega\left(1-\frac{1}{\beta^2\epsilon(\omega)}\right)e^{-(\lambda+\lambda^*)a}d\omega\right]$$

If λ has a positive real part (usually true), the exponential will cause the expression to vanish rapidly at large distances, meaning all the energy is deposited near the path. However, this isn't true when λ is purely imaginary - this instead causes the exponential to become 1 and then is independent of a, meaning some of the energy escapes to infinity as radiation - this is Cherenkov radiation.

λ is purely imaginary if $\epsilon(\omega)$ is real and $\beta^2\epsilon(\omega) > 1$. That is, when $\epsilon(\omega)$ is real, Cherenkov radiation has the condition that $v > \frac{c}{\sqrt{\epsilon(\omega)}} = \frac{c}{n}$. This is the statement that the speed of the particle must be larger than the phase velocity of electromagnetic fields in the medium at frequency ω in order to have Cherenkov radiation. With this purely imaginary λ condition, $\sqrt{\frac{\lambda^*}{\lambda}} = i$ and the integral can be simplified to:

$$\begin{aligned}\left(\frac{dE}{dx_{particle}}\right)_{rad} &= \frac{z^2e^2}{c^2}Re\left[\int_{\epsilon(\omega)>\frac{1}{\beta^2}}\omega\left(1-\frac{1}{\beta^2\epsilon(\omega)}\right)d\omega\right] \\ &= \frac{z^2e^2}{c^2}\int_{v>\frac{c}{n(\omega)}}\omega\left(1-\frac{c^2}{v^2n^2(\omega)}\right)d\omega\end{aligned}$$

This can be simplified to the power spectrum for Cherenkov radiation:

$$\frac{d^2E}{dxd\omega} = \frac{z^2e^2}{c^2}\omega\left(1-\frac{c^2}{v^2n^2(\omega)}\right) \tag{A.8}$$

The total energy from Cherenkov radiation for $\beta n > 1$,

$$\left(\frac{dE}{dx}\right)_{Cherenkov} = \frac{z^2e^2}{c^2}\left[\int_0^\infty \omega\left(1-\frac{1}{\beta^2\epsilon(\omega)}\right)d\omega\Theta(n(\omega)-\beta^{-1})\right] \tag{A.9}$$

For universal index of refraction ($n(\omega) \equiv n$)

$$\left(\frac{dE}{dx}\right)_{n=const} = \frac{z^2e^2}{c^2}\left(1 - \frac{1}{\beta^2 n^2}\right)\int_0^\infty \omega d\omega$$

The integral on the right side diverges, so adopting a constant index of refraction results in an unphysical result. Instead, we demand a maximum frequency for each particle velocity:

$$n(\omega < \omega_{max}^{(\beta)}) = \beta^{-1}$$
$$n(\omega < \omega_{max}^{(1)}) \leq 1$$

A.2 Dielectric constant for an oscillating particle

Assume a charged particle in simple harmonic motion

$$\ddot{x} + \gamma\dot{x} + \omega_j^2 x = \frac{e}{m}E_0 e^{-i\Omega t}$$

Taking the Fourier transform of this equation, solving for the frequency-space electric field and then taking the inverse transform, we obtain

$$\begin{aligned}
x(t) &= \int \frac{d\omega}{\sqrt{2\pi}}\tilde{x}(\omega)e^{i\omega t} \\
x(\omega) &= \int \frac{dt}{\sqrt{2\pi}}x(t)e^{-i\omega t} \\
E(t) &= \int \frac{d\omega}{\sqrt{2\pi}}\tilde{x}(\omega)\left[-\omega^2 + i\omega\gamma + \omega_j^2\right]e^{i\omega t} \\
&= \int \frac{d\omega}{\sqrt{2\pi}}\tilde{E}(\omega)e^{i\omega t} \\
&= \frac{e}{m}E_0 e^{-i\Omega t} \\
\int \frac{d\omega}{\sqrt{2\pi}}e^{i\omega t}\left[\int \frac{dt}{\sqrt{2\pi}}\left(\frac{e}{m}E_0 e^{-i\omega t}\right)e^{-i\omega t}\right] &= \int \frac{d\omega}{\sqrt{2\pi}}e^{i\omega t}\left[\delta(\Omega + \omega)\right]
\end{aligned}$$

Solving

$$\begin{aligned}\tilde{x}\left[-\omega^2+\omega_j^2+i\gamma\omega\right] &= \frac{e}{m}E_0\int\frac{dt}{\sqrt{2\pi}}e^{-i(\omega+\Omega)t}\\ &= \frac{e}{m}E_0\sqrt{2\pi}\delta(\omega+\Omega)\\ \tilde{x}(\omega) &= \frac{\frac{e}{m}E_0\sqrt{2\pi}\delta(\omega+\Omega)}{-\omega^2+\omega_j^2+i\gamma\omega}\end{aligned}$$

Using the polarization of this system, I can find the dielectric constant directly:

$$\begin{aligned}\vec{P} &= \sum_j en_j x\\ \tilde{\vec{P}}(\omega) &= \sum_j en_j\tilde{x}\\ &= \sum_j\frac{\frac{e^2}{m}n_jE_0\sqrt{2\pi}\delta(\omega+\Omega)}{-\omega^2+\omega_j^2+i\gamma\omega}\end{aligned}$$

Then this form can be used to pull out the constant by assuming a linear relation to the displacement, which is the assumption of a linear dielectric

$$\begin{aligned}\vec{D}(\vec{x},t) &= \varepsilon(\vec{x},t)\vec{E}(\vec{x},t)+\vec{P}(\vec{x},t)\\ \vec{D}(\omega) &\to \varepsilon(\omega)\vec{E}(\omega)\\ &= \varepsilon_0(1+\tilde{X})\vec{E}(\omega)\\ \tilde{\varepsilon}_j(\omega) &= \varepsilon_0\left(1+\sum_j\frac{\frac{e^2}{m}E_0\sqrt{2\pi}\delta(\omega+\Omega)}{-\omega^2+\omega_j^2+i\gamma\omega}\right)\end{aligned}\tag{A.10}$$

The atomic type process leads to this form of the dielectric constant, which can diverge if $w_j \to 0$ or $\gamma \to 0$. These are values dependent on the material in the atmosphere. A material with large dielectric constant can lower the energy loss rate of equation A.9.

Appendix B: Novae Optical Data

In Tables B.1 and B.2 are the mean optical values averaged linearly over 1 day bins. Data from AAVSO in V band.

Table B.1: Nova Per 2020 Optical results. Linear Mean over 1 day bins using AAVSO data.

Date	Mean V (app)	V (app) Error
2 459 183.47	9.28	0.03
2 459 184.18	8.78	0.06
2 459 186.17	8.74	0.00
2 459 186.65	8.56	0.00
2 459 188.28	8.54	0.00
2 459 189.25	8.47	0.00
2 459 190.98	8.29	0.00
2 459 191.99	8.41	0.00
2 459 193.11	9.92	0.01
2 459 194.23	8.81	0.00
2 459 194.82	8.77	0.00
2 459 196.83	8.54	0.01
2 459 197.61	8.98	0.01
2 459 199.51	9.54	0.00
2 459 200.92	9.57	0.01
2 459 202.75	9.62	0.01
2 459 203.94	9.58	0.01
2 459 205.71	9.51	0.00
2 459 206.09	9.51	0.00
2 459 208.14	9.69	0.00
2 459 210.29	9.73	0.00
2 459 211.74	9.71	0.02
2 459 212.84	9.89	0.00
2 459 214.19	10.14	0.01
2 459 215.29	10.19	0.01

Table B.2: Nova Her 2021 Optical results. Linear Mean over 1 day bins using AAVSO data.

Date	Mean V (app)	V (app) Error
2 459 381.68	6.99	0.15
2 459 383.01	8.56	0.03
2 459 384.04	9.09	0.01
2 459 385.43	9.80	0.00
2 459 386.66	10.18	0.00
2 459 388.22	10.47	0.00
2 459 388.97	10.64	0.00
2 459 390.50	10.95	0.00
2 459 391.44	11.08	0.00
2 459 392.90	11.43	0.01
2 459 393.95	11.62	0.00
2 459 395.26	11.86	0.00
2 459 396.33	11.99	0.01
2 459 397.99	11.99	0.04
2 459 399.32	12.33	0.02
2 459 400.09	12.54	0.01
2 459 401.23	12.71	0.01
2 459 402.54	12.89	0.01
2 459 403.97	12.90	0.01
2 459 405.07	13.15	0.00

Table B.3: AT2021afpi Optical results. Linear Mean over 1 day bins using AAVSO data.

Date	Mean V (app)	V (app) Error
2 459 548.50	12.43	0.00
2 459 548.60	12.46	0.04
2 459 549.50	12.82	0.00
2 459 550.50	12.86	0.00
2 459 550.70	13.04	0.00
2 459 551.70	13.07	0.00
2 459 552.20	13.14	0.00
2 459 552.40	13.26	0.05
2 459 553.70	13.31	0.01
2 459 554.60	13.36	0.01
2 459 559.50	13.52	0.05
2 459 569.50	14.49	0.01
2 459 570.50	14.49	0.01
2 459 581.47	14.93	0.05
2 459 583.47	14.84	0.08
2 459 585.50	14.84	0.05
2 459 595.25	15.04	0.01

Appendix C: Fluxes

C.1 Photon Flux

C.1.1 Differential photon flux

Differential photon flux will be the main descriptor of the model in question. This is the term:

$$\frac{dN}{dE} = M(E) \quad \left(\mathrm{ph\,cm^{-2}s^{-1}MeV^{-1}}\right) \tag{C.1}$$

Models

This model $M(E)$ can be any of the following words/expressions:

Powerlaw

$$M(E) = k_0 \left(\frac{E}{E_0}\right)^{\gamma}$$

k_0 = Prefactor ($\mathrm{ph\,cm^{-2}s^{-1}MeV^{-1}}$)

γ = Index

E_0 = PivotEnergy (MeV)

Exponentially cut-off power law

$$M(E) = k_0 \left(\frac{E}{E_0}\right)^{\gamma} \exp\left(\frac{-E}{E_{cut}}\right)$$

k_0 = Prefactor ($\mathrm{ph\,cm^{-2}s^{-1}MeV^{-1}}$)

γ = Index

E_0 = PivotEnergy (MeV)

E_{cut} CutoffEnergy (MeV)

Super exponentially cut-off power law

$$M(E) = k_0 \left(\frac{E}{E_0}\right)^{\gamma} \exp\left(-\left(\frac{E}{E_{cut}}\right)^{\alpha}\right)$$

k_0 = Prefactor (ph cm^{-2}s^{-1}MeV^{-1})

γ = Index1

α = Index2

E_0 = PivotEnergy (MeV)

E_{cut} CutoffEnergy (MeV)

Broken power law

$$M(E) = k_0 \begin{cases} \left(\frac{E}{E_b}\right)^{\gamma_1} & E < E_b \\ \left(\frac{E}{E_b}\right)^{\gamma_2} & \text{otherwise} \end{cases}$$

k_0 = Prefactor (ph cm^{-2}s^{-1}MeV^{-1})

γ_1 = Index1

γ_2 = Index2

E_b= BreakEnergy (MeV)

Smoothly broken power law

$$M(E) = k_0 \left(\frac{E}{E_0}\right)^{\gamma_1} \left[1 + \left(\frac{E}{E_b}\right)^{\frac{\gamma_1-\gamma_2}{\beta}}\right]^{-\beta}$$

k_0 = Prefactor (ph cm^{-2}s^{-1}MeV^{-1})

γ_1 = Index1

E_0 = PivotEnergy (MeV)

γ_2 = Index2

E_b= BreakEnergy (MeV)

β = BreakSmoothness

Log parabola

$$M(E) = k_0 \left(\frac{E}{E_0}\right)^{\gamma+\eta \log(E/E_0)}$$

k_0 = Prefactor (ph cm^{-2}s^{-1}MeV^{-1})

γ = Index

E_0 = PivotEnergy (MeV)

η = Curvature

In all of these cases, the 'action' happens with unitless terms - note how the energy variable is divided out by the pivot energy (or cutoff energy, etc), so that the unit of the expression is fully enclosed by the Normalization or Prefactor variable only.

In general, I will use one of two forms $\left(\text{ph cm}^{-2}\text{s}^{-1}\text{MeV}^{-1}\right)$ for *Fermi*-LAT work or $\left(\text{ph m}^{-2}\text{s}^{-1}\text{TeV}^{-1}\right)$ for VERITAS. I will use the *Fermi*-LAT version for rest of this note, which is in $\left(\text{ph cm}^{-1}\text{s}^{-1}\text{MeV}^{-1}\right)$.

C.1.2 Index

Noting the form of equations above in section C.1.1, it is clear that many have an exponent on the energy term. In this case, we are representing the differential photon flux, so the index label can be labeled as 'photon index'.

In some cases, authors or software may refer to 'energy index'; this is the effective exponent on energy term when writing the differential energy flux, shown below in section C.2.1, which is 'photon index' + 1. Note the sign - usually only the number is referred to while the sign is ignored. Energy index is the more positive value, so obviously the number is closer to zero.

Per convention, the index specifies the "softness" or "hardness" of a source. A spectrum that is "softening" has a index that is becoming more negative, while "hardening" is becoming more positive. A soft source, which could have an index > 2, has a very steep spectrum so that the majority of events detected are at the lower energy range of the analysis.

C.1.3 Integral photon flux

Integral photon flux is described with the energy bin edges. This is generally used while referring to the instrument - e.g. VERITAS sees Crab at 6 photons min^{-1} means the Crab's integral photon flux with the VERITAS effective area implied in the statement.

$$\int_{E_{min}}^{E_{max}} \frac{dN}{dE} dE = \int_{E_{min}}^{E_{max}} M(E) dE \quad \left(\mathrm{ph\,cm^{-2}s^{-1}}\right) \tag{C.2}$$

Sometimes, this value is just called the *photon flux*. I prefer not to use this less descriptive form, and will always overdescribe, therefore this is the *integral photon flux*. In certain contexts, the unit for this integral photon flux will still contain the MeV^{-1} because it is to make clear that it is for a certain energy bin; this is unclear and should be avoided because it can be confused with the units for differential photon flux.

If using the VERITAS units ph $\mathrm{m^{-2}s^{-1}TeV^{-1}}$, simply multiply this evaluated result by $(1 \times 10^{-4}) \times (1 \times 10^{-6})$ to convert cm to meters and MeV to TeV.

C.2 Energy Flux

The energy flux is a more useful value that can be used within discussion of physics - such as the energy deposited by a process or the value input for a calculation of total luminosity.

C.2.1 Differential Energy Flux

This term is used sometimes in plots, but it is a rarely used term.

$$\frac{dN}{dE} E = E \times M(E) \quad \left(\mathrm{cm^{-2}s^{-1}}\right) \tag{C.3}$$

Converting these units from CTools to VERITAS is easy: simply multiply this evaluated result by $1 \times 10^{-4} \times 1 \times 10^{-6}$ to convert meters and TeV.

C.2.2 Integral Energy Flux

This expression refers to the total amount of energy deposited within an energy range, which now is integrated. This is much more useful to physics because it can be converted to Luminosity for a given astrophysical source with known distance (i.e. Flux = $\frac{L}{4\pi d^2}$).

$$\int_{E_{min}}^{E_{max}} \frac{dN}{dE} E\, dE = \int_{E_{min}}^{E_{max}} M(E) E\, dE \quad \left(\text{erg}\,\text{cm}^{-2}\text{s}^{-1}\right) \tag{C.4}$$

The units now have a new energy term *ergs*, which is by convention in the astro community. With this, we have to convert the value *after* the integral, simply with MeVtoErg = 1.60×10^{-6} or TeVtoErg = 1.60. Again, for VERITAS we can multiply this evaluated result by 1×10^{-4} to convert meters. However, we have to do the integral in TeV, which means conversion of the energy bounds and model/differential photon flux prefactor. Once meters and TeV is converted inside the integral, we can then apply TeVtoErg at the end after the integral.

Sometimes, this integral expression is referred to simply as *energy flux*. This is more common than using energy flux to mean differential energy flux. To be safe, explicitly say integral or differential every time.

C.3 Spectra

In most cases, spectral plots do not use any of these forms and instead convert energy fluxes to a form that is more clear for visually finding bumps and inspecting spectral shapes. Following the convention set by cosmic ray astronomy, (Fermi acceleration with respect to energy has the form of $\frac{dN}{dE} \propto E^{-p}$ for $p \geq 2$ and is the dominant process in many of these astrophysical systems) it is convention to plot

$$\frac{dN}{dE}|_{E_{mean}} \times E_{mean}^2 \quad \left(\text{erg}\,\text{cm}^{-2}\text{s}^{-1}\right) \tag{C.5}$$

Note that this is a differential photon flux, evaluated at E_{mean}, times E_{mean}^2. In many cases (but not always; VEGAS uses the mean energy defined in [242]), the energy for which the $\frac{dN}{dE}$ is evaluated

at is the geometric mean energy

$$E_{mean} = \sqrt{E_{min} \times E_{max}} \tag{C.6}$$

Note that the units for this plot are the same as the integral energy flux, which can lead to confusion.

For conversions: use the proper prefactor units (either in square centimeters or square meters, MeV or TeV) for your instrument and then multiply result by either MeVtoErg or TeVtoErg.

C.4 Uncommon Quantities

Although the following quantities are uncommon in high-energy astrophysics in general, they may occur in particular contexts.

C.4.1 Jansky

The jansky (Jy) is a non-SI unit of spectral flux density most commonly used in radio astronomy. It describes the emission from a source as a density of energy flux per frequency. This is useful for the radio band in which power is received over a detector bandwidth, as opposed to detecting individual photons. The unit is normalized to a small value useful for describing the weak fluxes from typical astronomical radio sources. In cgs units,

$$1 \text{ Jy} = 10^{-23} \text{ erg cm}^{-2} \text{ s}^{-1} \text{ Hz}^{-1} \tag{C.7}$$

To convert a flux density S in janskys to energy flux, integrate S over the frequency range being measured. To convert the energy bounds E_{min}, E_{max} in TeV to frequency bounds ν_{min}, ν_{max} in Hz, multiply by $\approx 2.41799 \times 10^{26}$ Hz TeV^{-1} [This comes from $E = h\nu$, where h is Planck's constant in the proper units. Convert by multiplying or dividing.]. Then the integral energy flux is obtained by

$$10^{-23} \int_{\nu_{\text{min}}}^{\nu_{\text{max}}} S(\nu) d\nu \quad \left(\text{erg cm}^{-2} \text{ s}^{-1}\right) \tag{C.8}$$

In the case of VERITAS observations that are used in this Jansky context, use the energy range of the analysis. For example, some theoretical models predict flux density that needs to be converted to a flux observable with VERITAS, so convert with equation above but use the energy ranges applicable to that analysis.

C.4.2 Fluence

Fluence refers to the energy received per unit area, or equivalently, the energy flux integrated over time. This is a useful unit when studying transient events, in which the emission lasts for a short period of time. To calculate the fluence $\mathcal{F}$, integrate the energy flux F over the observation time.

$$\mathcal{F} = \int_{t_{\text{start}}}^{t_{\text{end}}} F(t)dt \quad \left(\text{erg cm}^{-2}\right) \tag{C.9}$$

C.5 Useful Integrals

$$\int_{x_1}^{x_2} k_0 \left(\frac{x}{x_0}\right)^{-\gamma} \text{dx} = \frac{k_0 x_0}{\gamma - 1}\left[\left(\frac{x_1}{x_0}\right)^{1-\gamma} - \left(\frac{x_2}{x_0}\right)^{1-\gamma}\right] \tag{C.10}$$

$$= \frac{k_0}{\gamma - 1}\left[x_1\left(\frac{x_1}{x_0}\right)^{-\gamma} - x_2\left(\frac{x_2}{x_0}\right)^{-\gamma}\right] \tag{C.11}$$

$$\int_{x_1}^{x_2} k_0 x \left(\frac{x}{x_0}\right)^{-\gamma} \text{dx} = \frac{k_0 x_0^2}{\gamma - 2}\left[\left(\frac{x_1}{x_0}\right)^{2-\gamma} - \left(\frac{x_2}{x_0}\right)^{2-\gamma}\right] \tag{C.12}$$

$$= \frac{k_0}{\gamma - 2}\left[x_1^2\left(\frac{x_1}{x_0}\right)^{-\gamma} - x_2^2\left(\frac{x_2}{x_0}\right)^{-\gamma}\right] \tag{C.13}$$

Appendix D: SCT Optics

D.1 Optical System Parameters

See Table D.1 for all optical system parameters.

D.2 Optical Software Technical Diagrams

The software is organized as follows in Figures D.1 and D.2. The method, members and types are defined for each server and client programs. An example of three GUI screen-shots are in Figure D.3.

Most of the outward-facing system control components are defined within the controller objects. Controllers are initialized in CommunicationInterface:

1. Device::Identity are initialized
2. Controllers per device are initialized and added to a shared controller map
3. Relationships between controllers are defined

NodeManager creates

1. Objects (the buttons on the GUI)
2. Objects hold the beginCall or operate method, which interfaces with the controller.
3. Folders

- Controller types (each defining a device or composite device):
  - Actuator

Table D.1: Characteristics of the prototype Schwarzschild-Couder Telescope. Table from [84].

Quantity	Value/Summary	Units
Optic Design (non-diffraction limited)	Schwarzschild-Couder	
Main and Effective Aperture Size	9.66 / 7.82	m
System Effective Focal Length	5.59	m
Number of Mirrors or Reflecting Surfaces	2	
Separation between Primary and Secondary Mirrors	8.39	m
Separation between Secondary Mirror and Focal Plane	1.86	m
Primary Mirror (M1) Radius Max & Min	4.83 / 2.19	m
Number of Mirror Segments in M1	48 = 16 (P1) + 32 (P2)	
Average Area of M1 Mirror Segment	1.2	m^2
Average Weight of M1 Hybrid Mirror Segment	24	kg
Weight of M1 Mirror Segment Positioning System	19	kg
Secondary Mirror (M2) Radius Max & Min	2.71 / 0.40	m
Number of Mirror Segments in M2	24 = 8 (S1) + 16 (S2)	
Average Area of M2 Mirror Segment	0.94	m^2
Average Weight of M2 Hybrid Mirror Segment	19	kg
Weight of M2 Mirror Segment Positioning System	18	kg
Total Light Collecting Area on-axis & at 4 deg off-axis	50.31 / 47.73	m^2
Vignetting at the FoV Edge	-5.17	%
Wavelength Range of Cherenkov Photons	250 - 800	nm
M1 Mirror Segment Replication Technology	Cold Glass Slumping	
M2 Mirror Segment Replication Technology	Hot/Cold Glass Slumping	
M1 & M2 Mirror Surface Vacuum Deposition Coating	Al/Cr/SiO_2/HfO_2/SiO_2	
Mirror Segment Actuators Precision and Range	0.003 / 51	mm
Mirror Segment Positioning Degrees of Freedom	6	
Telescope total Moving Mass	30	ton
M1 OSS with Mirrors/Baffles	6.5	ton
M2 OSS with Mirrors/Baffles	3.5	ton
Camera & Camera Support Structure	6	ton
Counterweights	14	ton
Telescope Mass and Type of Material for Support Structure	75 (steel)	ton
Type of mount used for pointing	Alt- azimuth	
Azimuth allowed range	[-270, +270]	deg
Elevation allowed range	[-5, +91]	deg
Camera Diameter	0.78	m
Camera Field of View (FoV) Diameter	8	deg
Camera FoV solid angle	50.35	deg^2
Focal Plane Figure	Parabolic	
Focal Plane Sag at the FoV Edge	-22	mm
Focal Plane Plate Scale	1.625	mm/arcmin
Characteristic photon incidence angle	51.25	deg
PSF at the FoV edge ($2 \times$ MAX[RMS])	3.8-4.5	arcmin

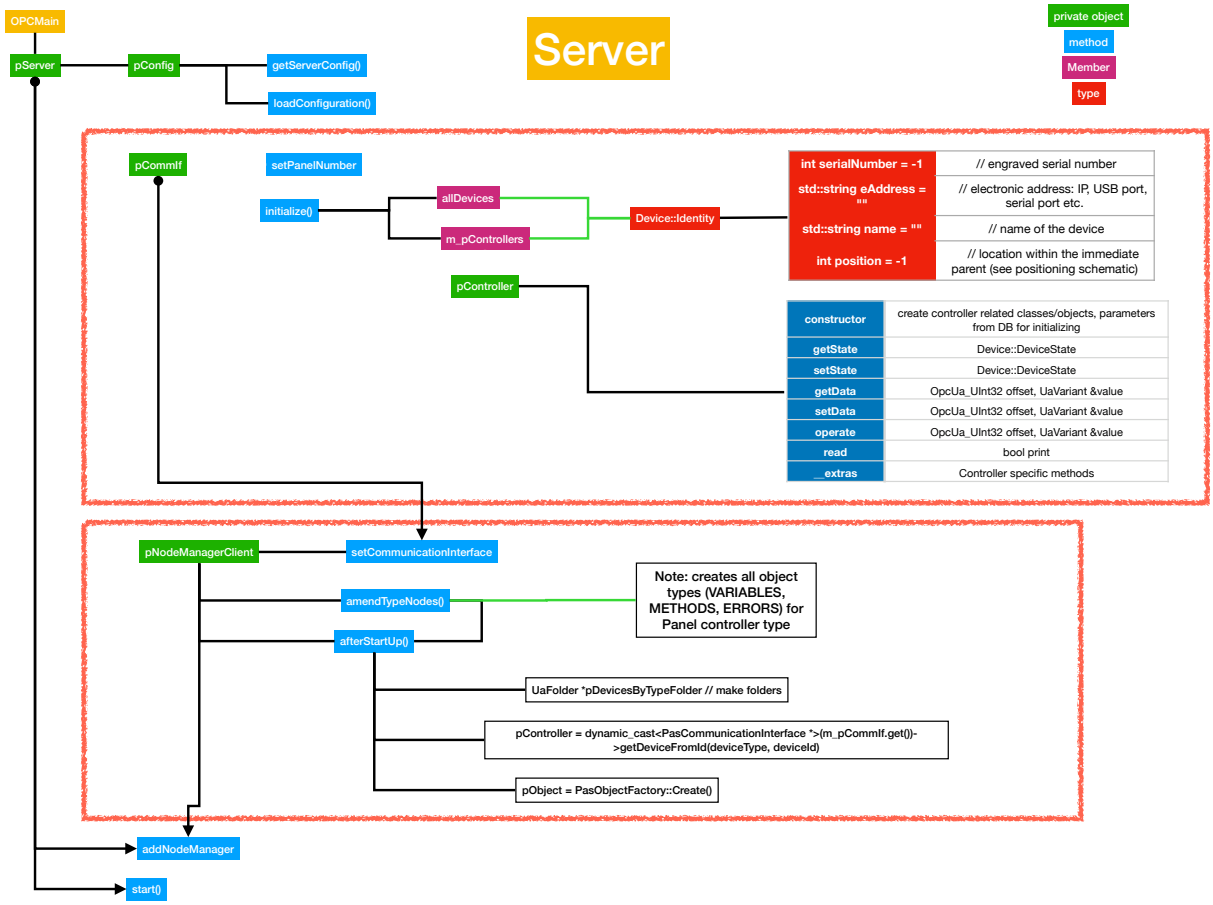

Figure D.1: Server diagram.

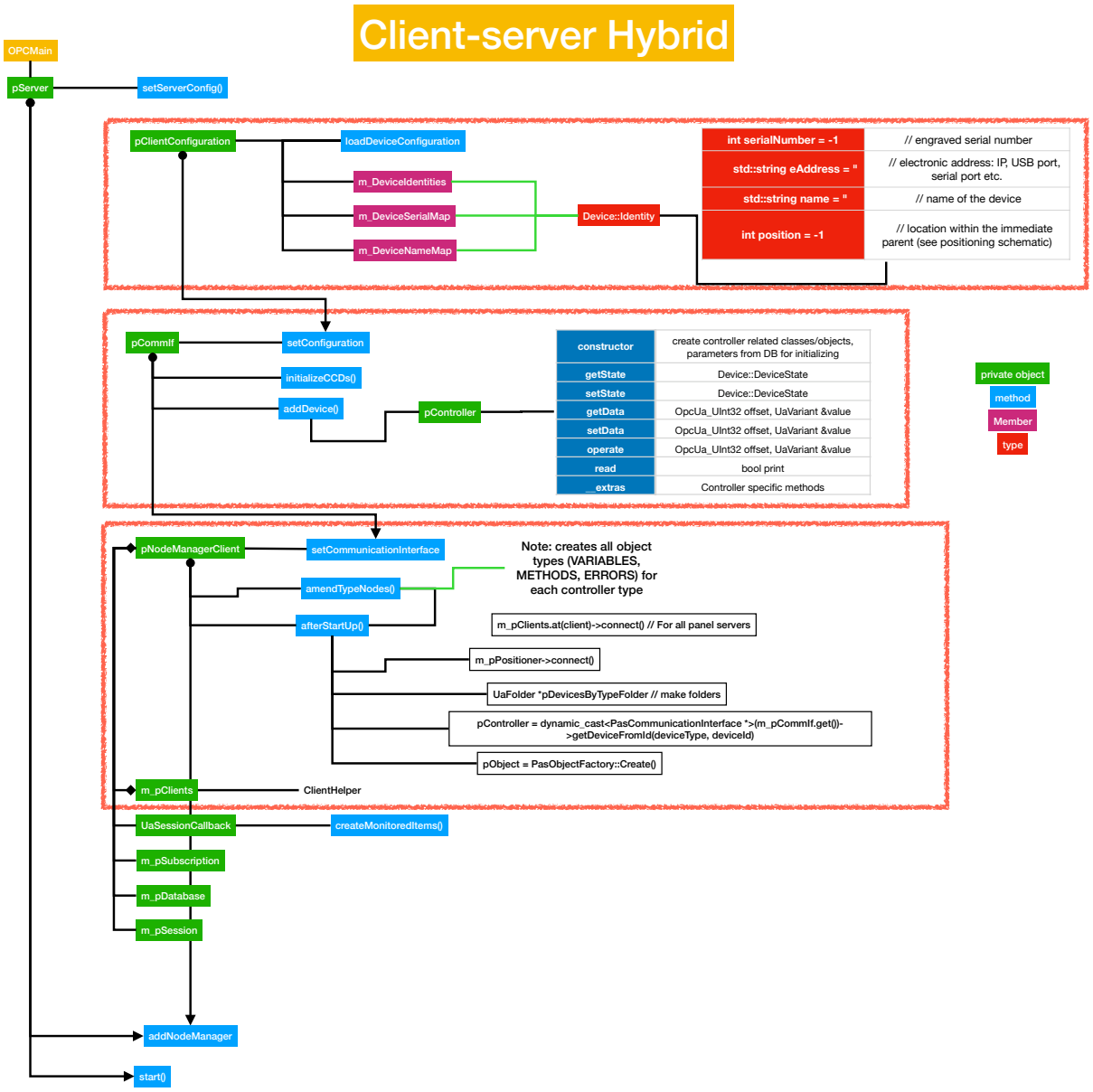

Figure D.2: Client diagram.

  - MPES
  - Panel
  - Edge
  - Mirror
  - Positioner
  - GlobalAlignment
  - CCD
  - PSD
  - Autocollimator
  - FocalPlaneImage
  - OpticalTable
  - Skycam
  - OpticalAlignment

- General Methods in all controllers
  - getData/setData
  - getErrors/setErrors
  - getState/setState
  - operate()

- Specific methods within each controller - e.g. ReadMPES() or MoveDeltaLength().

- These methods are effectively duplicated from server to client, where client version simply makes call to the server version

  - Extra features in client methods to handle devices across different servers, such as multiple MPES in an edge, or edges in a mirror. Also helpful printouts to log to client output.

- Methods in controller either compute with data in that controller class or trigger hardware action.

1. Actuator
    - MoveDeltaLength/MoveToLength
    - ForceRecover
    - Stop
2. MPES
    - Read
    - Set Exposure
3. Panel
    - FindHome
    - MoveDeltaLength/MoveToLength/MoveToCoords/MoveDeltaCoords
    - ReadPosition
4. Positioner
    - Initialize
    - Move
    - SetEnergy
    - Stop
5. CCD

- Read
- save single image
- StartMonitoring/StopMonitoring

6. PSD
    - Read
7. FocalPlaneImage
    - Read
    - save single image
    - AnalyzeSinglePanelImage/AnalyzePatternImage. Output to .dat file with image centroids.
    - CalcPatternToCenter/ CalcCenterToPattern/ CalcPanelToPattern/ CalcPanelToCenter. Imports .dat centroid file, outputs panel motion file in template form.
8. GR Cam
    - MoveGRCam
    - InsertPSD...RemovePSD (reposition PSD angle...?)
9. AutoCollimator
    - Read
10. SkyCam
    - Read - save single image
    - SetExposure/SetGain/SetFrameRate - this updates DB for these params
    - StartMonitoring/StopMonitoring - starts python script for monitoring

11. Edge
    - Align
    - FindMatrix
    - Read
12. Mirror
    - AlignRing/ AlignSector/AlignSequentialRecursive
    - CheckStatus
    - LoadAlignmentOffset/LoadDeltaCoords/LoadPosition
    - MoveDeltaCoords/MoveToCoords
    - ReadPosition/ReadSensors/ReadSensorsParallel
    - SaveAlignmentOffset/SavePosition
    - SelectAll
    - TestActuators/TestSensors
13. GlobalAlignment
    - StartPSDTracking/StopPSDTracking (has platform motion for OTs)
    - StartAllLogging
14. OpticalAlignment
    - MoveFocusToPattern (Defocus)- use some default motions for all panel (0th order, static motions)
    - Tells panels to move directly
    - MovePatternToFocus - use some default motions for all panel (0th order, static motions)
    - MoveForCalibration - Tells panels to move directly, uniformly in same Rx/Ry/z.

- GetResponseMatrix. Input: all centroid files from calibration motion
- CalibrateFirstOrderCorr - needs some intervention/quality check on image.

15. OpticalTable

- FindMatrix
- Align
- StepAll

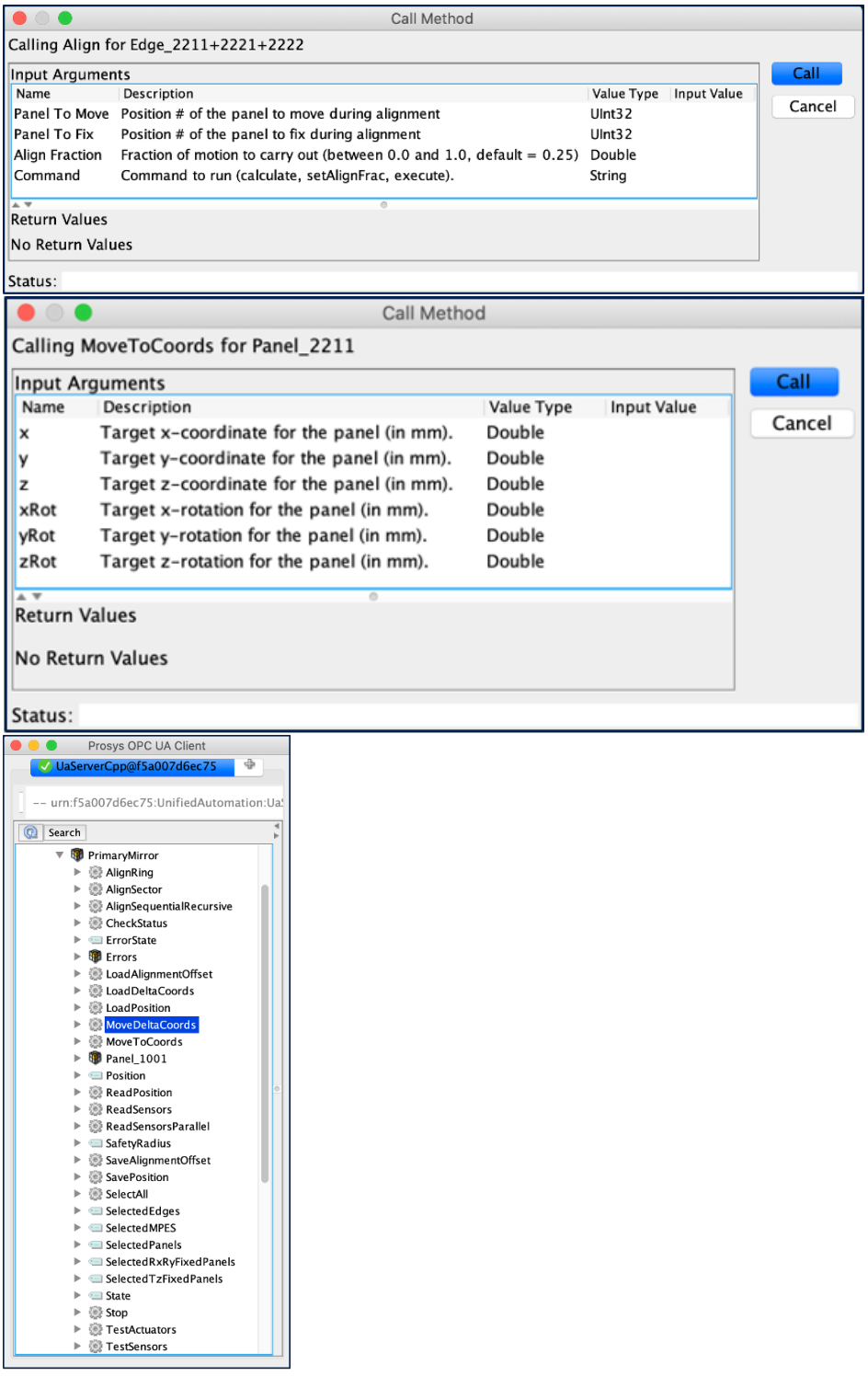

Figure D.3: Screenshots of a few graphical user interface components of the alignment software. The MoveToCoords and Align methods GUIs each have 'Call' button and parameter inputs. The PrimaryMirror device tree is shown at the top, with the child device Panel_1001 included.